Vibrational Spectroscopy of Proteins

DI Andreas Schwaighofer

AIT Austrian Institute of Technology

University of Natural Resources and Life Sciences

A thesis submitted for the degree of

Dr. nat. techn. (naturalium technicarum)

October 2013

Supervisor: Univ. Prof. Dr. Erik Reimhult
Institute for Biologically inspired materials

Meinen Eltern

Acknowledgements

Foremost, my sincere thanks go to my supervisor at the University of Natural Resources and Life Sciences, Univ. Prof. Dr. Erik Reimhult, for accepting me as his PhD student and his ongoing support during the last three years.

I also would like to express my gratitude to my supervisor at the Austrian Institute of Technology, Dr. Christoph Nowak, for his support and guidance throughout my doctoral studies. I appreciate the involvement in exciting and challenging projects as well as the independence to develop my own approaches. Furthermore, I am deeply grateful for the opportunity to attend several scientific conferences and workshops.

I acknowledge the assistance and expertise of Dr. Renate Naumann, particularly in the Cytochrome *c* Oxidase project and during the first year of my dissertation.

Moreover, I thank the following people for their general support during the last three years or contributions to a particular project: Dieter Baurecht, Pinar Frank, David Hildenbrandt, Wolfgang Knoll, Caroline Kotlowski, Melanie Larisika, Vedran Nedelkovski, Georg Ramer, Bernhard Siebenhofer, Johannes Srajer and Christoph Steininger.

I am thankful to my significant other, Ines for celebrating the ups and easing the downs.

Last but not least, I would like to thank my family, in particular my parents, Brigitte and Anton for their never-ending support.

Abstract

Two important steps for the development of a biosensor are the immobilization of the biological component (e.g. protein) on a surface and the enhancement of the signal to improve the sensitivity of detection. To address these subjects, the present work describes Fourier transform infrared (FTIR) investigations of several proteins bound to the surface of an attenuated total reflection (ATR) crystal. Furthermore, new nanostructured surfaces for signal enhancement were developed for use in FTIR microscopy.

The mitochondrial redox-protein cytochrome *c* oxidase (C*c*O) was incorporated into a protein-tethered bilayer lipid membrane (ptBLM) on an ATR crystal featuring a roughened two-layer gold surface for signal enhancement. Electrochemical excitation by periodic potential pulses at different modulation frequencies was followed by time-resolved FTIR spectroscopy. Phase sensitive detection was used for deconvolution of the IR spectra into vibrational components. A model based on protonation-dependent chemical reaction kinetics could be fitted to the time evolution of IR bands attributed to several different redox centers of the C*c*O.

Further investigations involved the odorant binding protein 14 (OBP14) of the honey bee (*Apis mellifera*), which was studied using ATR-FTIR spectroscopy and circular dichroism. OBP14 was found to be thermally stable up to 45 °C, thus permitting the potential application of this protein for the fabrication of biosensors. Thermal denaturation measurements showed that odorant binding increases the thermal stability of the OBP-odorant complex.

In parallel, plasmonic nanostructures were fabricated that enhance the absorbance in FTIR microscopy measurements. The nanostructures are composed of an array of round-shaped insulator and gold discs on top of a continuous gold layer. Enhancement factors of up to ∼125 could be observed with self-assembled monolayers of dodecanethiol molecules immobilized on the gold surface. Such structures could in the future greatly aid the study of membrane proteins in ptBLMs.

Kurzfassung

Zwei wichtige Schritte für die Entwicklung von Biosensoren sind die Immobilisierung der biologischen Komponente (zB. Protein) auf einer Oberfläche sowie die Verstärkung des Detektionssignals zur Erhöhung der Empfindlichkeit. Die vorliegende Arbeit widmet sich dieser Thematik. Es wurden mehrere Proteine mit Fourier Transform Infrarot Spektroskopie unter abgeschwächter Totalreflektion (ATR-FTIR) untersucht, bei der die Proteine an der Oberfläche eines Kristalls immobilisiert waren. Daneben wurde eine nanostrukturierte Oberfläche entwickelt und für die Signalverstärkung in der FTIR Mikroskopie verwendet.

Der vierte Komplex der Atmungskette, die Cytochrome *c* Oxidase (C*c*O) wurde in ein biomimetisches Membransystem (ptBLM) eingebettet und auf einem ATR-Kristall immobilisiert. Eine aufgeraute Goldschicht auf dem Kristall verursachte eine Oberflächenverstärkung des IR Signals und ermöglichte gleichzeitig die elektrochemische Anregung des Proteins mit periodischen Spannungspulsen. Die Anregung mit verschiedenen Modulationsfrequenzen erlaubte die Dekonvolution des IR Spektrums mit phasensensitiver Detektion in einzelne Banden. Die so identifizierten Banden wurden Redoxzentren in der C*c*O zugeordnet und deren zeitliche Änderung mit Hilfe von Modellrechnungen analysiert.

Zudem wurde das Duftstoff-bindende Protein 14 (OBP14) der Honigbiene (*Apis Mellifera*) mit ATR-FTIR Spektroskopie und Circulardichroismus untersucht. Thermostabilitätsmessungen zeigten, dass dieses Protein bis 45 °C stabil ist, was einen prinzipiellen Einsatz in Biosensoren ermöglicht. Durch die Ausbildung eines OBP-Duftstoff Komplexes wird die thermische Stabilität weiter erhöht.

In einem weiteren Projekt wurden plasmonische Nanostrukturen für die Oberflächenverstärkung in FTIR Mikroskopie entwickelt. Die Struktur besteht aus einem Array von Nichtleiter- und Goldscheiben auf einer durchgehenden Goldschicht. Bei Messungen von Alkanthiol Monoschichten konnten Verstärkungsfaktoren von bis zu ∼125 beobachtet werden. Diese Strukturen können zur Untersuchung von Proteinen in ptBLMs eingesetzt werden.

Contents

Motivation

Biosensors are analytical devices incorporating a biological sensing element, e.g. immobilized enzymes [1]. In the "Biosensor Technologies" group at the Austrian Institute of Technology, the focus of research is the development of biosensing elements as well as the structural and functional investigation of immobilized proteins.

The aim of the present work is to study functional proteins tethered to the surface of an attenuated total reflection (ATR) crystal with Fourier transform infrared (FTIR) spectroscopy. While many biosensor strategies only address binding kinetics and affinities, ATR-FTIR spectroscopy has the potential to probe structure and thereby function at high time-resolution of biomolecules on the sensor surface. To improve the sensitivity of FTIR spectroscopy, plasmonic nanostructures on the surface can be used for signal enhancement. Therefore, a further aim was to advance plasmonic nanostructures for signal enhancement using FTIR microscopy. Both, immobilization of the biological component (e.g. protein) on a surface as well as signal enhancement for improving the sensitivity are important steps for the development of biosensors capable to analyze the real-time function of proteins.

Cytochrome *c* Oxidase (C*c*O) is the final redox center in the mitochondrial respiratory chain. Its purpose is to use the energy gained by the reduction of oxygen to water to pump protons against a difference of electrochemical potentials across the mitochondrial inner membrane. This pumping is achieved by coupling a number of electron and proton transfer steps. Even though the structure and overall reaction is known for more than thirty years [2, 3], the mechanism of this redox-driven proton pump is not fully resolved yet. In order to elucidate the structure-function relationship of C*c*O, the protein needs to be studied under turnover conditions in its native environment, a bilayer lipid membrane.

Motivation

Our group established a biomimetic membrane system optimized for this purpose [4–6]. In this protein-tethered bilayer lipid membrane (ptBLM), the protein is tethered to a surface via linker molecules. After immobilization of the protein on the surface, it is reconstituted into a lipid bilayer by in situ dialysis. A key feature of the ptBLM is the orientational control of the incorporated membrane protein due to the position of the genetically engineered his-tag. It allows the controlled attachment of C*c*O to an electrochemical working electrode with the first redox center (Cu_A) directed towards the surface. Electrochemical electron injection to C*c*O via the linker allows kinetic analysis of electron transfer within the protein. Potentiometic titrations employing Raman spectroscopy demonstrated intact redox site structures and electron transfer between the electrode and the immobilized enzyme [4]. Electrochemical investigations involving cyclic voltammetry revealed that electron transfer between the four redox centers takes place sequentially in C*c*O incorporated in the ptBLM as opposed to independent electron transfer when employing redox mediators [7].

While Raman spectroscopy is sensitive to changes in the redox states of the heme centers in the C*c*O, infrared (IR) spectroscopy provides information of the conformational changes in the protein during electron transfer. For IR investigations of C*c*O immobilized in the ptBLM, a nanostructured gold surface was developed for signal enhancement [8]. The gold film evaporated on an ATR crystal acts as a working electrode for electrochemical excitation of C*c*O, whereas the nanostructured gold layer on top generates a surface enhancement effect for IR spectroscopy. Cyclic voltammetry measurements indicated that C*c*O is transferred from the inactivated state to the activated state by performing several cyclic voltammetry cycles under aerobic conditions, accompanied with a shift of the redox potentials to more negative values [7, 9]. Conformational changes of the protein corresponding to these two states have been shown by potentiometric titrations with IR detection [10].

The goal of the first part of this thesis is to perform time-resolved IR measurements of C*c*O under turnover conditions with electrochemical excitation. Earlier works involving time-resolved investigations of this protein utilized CO-photodissociation [11]. This photo-induced electron transfer only provides one electron at a time, thus it is impossible to observe the entire enzymatic cycle. Employing electrochemical excitation of C*c*O incorporated in a ptBLM with the first redox center directed towards the surface, modulation can be achieved by application of periodic potential pulses, thus

permitting a large variety of modulation amplitudes and frequencies.

The second part of the thesis deals with the investigation of odorant binding proteins (OBPs), which are the object of growing interest as biosensing elements for the fabrication of odorant sensors based on the olfactory system [12–14]. Applications are manifold and include disease diagnostics [15], food safety [16], and environmental monitoring [17]. Currently, so-called electronic noses are based on metal oxides and conducting polymers, but biomimetic sensors promise to show higher sensitivity and selectivity combined with lower detection limits and faster response time [18, 19]. OBPs are small acidic proteins present in very high concentrations at the interface between olfactory receptors and external environment [20]. Their physiological role has not been clarified yet, but they have been associated with transfer of the odorant molecules to the receptor proteins. Odorants commonly are lipophilic molecules and need to be carried through the aqueous olfactory mucus of vertebrates respectively the sensillar lymph of insects to the membrane-bound olfactory receptors [15].

The objective of this project is to study the effect of odorant binding on the thermal stability of OBP14 of the honey bee by using IR spectroscopy and circular dichroism measurements. Despite a common name, OBPs of insects and those of mammals are completely different in structure and research interest in insect OBPs did not arise until fairly recently. Mammal OBPs and their structural changes upon odorant binding have been thoroughly investigated using IR spectroscopy and an increase in thermal stability of the OBP-odorant complex has been revealed [21–24]. These findings agree with reports of stabilizing effects of proteins upon ligand binding for a large variety of systems [25, 26]. The aim is to reveal the changes in thermostability of OBP14 in the presence of different odorants by performing thermal denaturation measurements using IR spectroscopy and circular dichroism measurements. Varying transition temperatures of the OBP-odorant complex could give a rough estimate of the affinity of various odorants to OBP14.

A fundamental factor for the sensitivity of a biosensor is the magnitude of the detected signal generated by the species of interest relative to the background noise. The evolving field of life sciences has led to a growing need of sensitive spectroscopic techniques for biosensing, biochemical analytics and biomolecular diagnostics [27]. Optically ac-

tive nanostructures are powerful analytical tools based on two of their inherent key features. Firstly, the local field enhancement around the nanostructures allows detection of very few molecules, enabling low limits of detection down to single molecules [28, 29]. Secondly, substrates decorated with nanoparticles provide much larger surface areas than their macroscopic dimensions indicate and therefore provide a higher signal for the same-sized surface. Early studies exploring the signal enhancement effect utilized rough metal surfaces or films with metal islands for use in surface-enhanced Raman spectroscopy (SERS) and surface-enhanced infrared absorption spectroscopy (SEIRAS) [30]. Limited enhancement and repeatability issues [31] of these randomly arranged structures led to the fabrication of periodic arrays of nanoparticles on a supporting surface. This approach offers a higher reproducibility due to employment of nanolithographic fabrication methods and a more accurate tunability of the resonance position [32]. Numerous studies exploring different nanoparticle sizes, shapes and arrangements have been published in recent years [33, 34].

The goal of this part of the thesis is to establish a plasmonic nanostructured surface that exhibits signal enhancement for both, SERS and SEIRAS measurements. Due to the inherently different mechanisms of interaction between light and molecules for Raman and IR spectroscopy, a structure for both methodologies is difficult to achieve. The maximum electromagnetic enhancement for plasmonic nanostructures has been typically found in the UV-VIS region [35]. In recent years, there has evolved a growing interest in plasmonic devices for IR spectroscopy and it has been shown that by tuning the structure and composition of the nanoparticles, the region of electromagnetic enhancement can be shifted to the IR range [36]. A remarkable improvement in this direction has been achieved by insertion of a thin dielectric spacer layer between the metallic nanoparticle array and a conducting surface [37]. In the here developed nanostructured surface, this conducting surface supporting the nanoparticles can be employed as a working electrode for spectro-electrochemical methods.

I Theoretical Background

1.1 Vibrational Spectroscopy

Spectroscopy is the study of the interaction of matter with radiation energy [38]. Depending on the energy range of the irradiated light, different transitions are excited in a molecule. Figure 1.1 provides an overview of the different types of electromagnetic waves and induced quantum transitions. In spectroscopy, electromagnetic energy is commonly characterized either by the wavelength λ, by its frequency f (number of oscillations per seconds) or the wavenumber ν (number of waves per cm). The infrared (IR) range is known to excite molecular vibrational transitions and is subdivided in three sections:

	ν/cm^{-1}	$\lambda/\mu\mathrm{m}$
• Near IR (NIR):	10 000 - 4000	1 - 2.5
• Mid IR (MIR):	4000 - 400	2.5 - 25
• Far IR (FIR):	400 - 40	25 - 250

Within the MIR region, fundamental frequencies of normal stretching and bending modes of intramolecular transitions are observed. In NIR, overtone vibrations and combinations of MIR vibrations are induced. FIR contains information about vibrations of heavy atoms and weak bonds such as hydrogen bonds [39, 40].

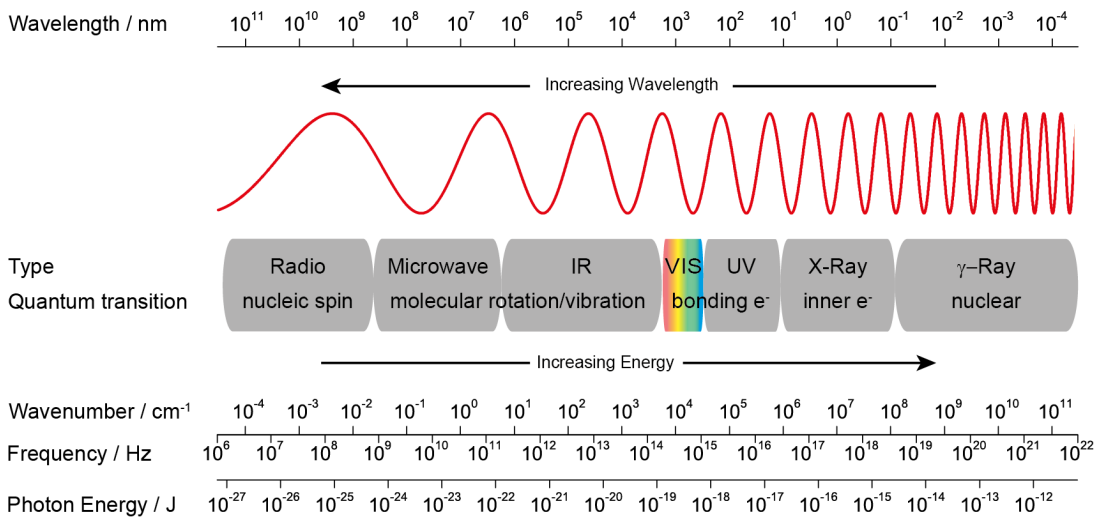

Figure 1.1: Types of electromagnetic waves and their corresponding quantum transitions.

1.1.1 Molecular Vibrations

Analytical methods for the investigation of molecular vibrations are IR and Raman spectroscopy. Molecules with N atoms have 3N degrees of motional freedom. Three of these involve moving all atoms in the same translational direction and another three represent rotations about one of the principal axes. The remaining 3N-6 degrees of freedom give the number of vibrational modes, i.e. motions that change the distance of a chemical bond or the angle between them. All vibrations in a molecule result from superposition of these 3N-6 normal vibrations. Linear molecules have an additional vibrational mode, since one of the degrees of freedom is lost (rotation of a molecule about one axis does not involve the displacement of atoms), resulting in 3N-5 modes [39, 40].

Possible vibrations of the methylene group are illustrated in Figure 1.2. Stretching vibrations involve the change of a bond length and occur at higher wavenumber regions than bending vibrations, where the bond angle is varied. According to the harmonic

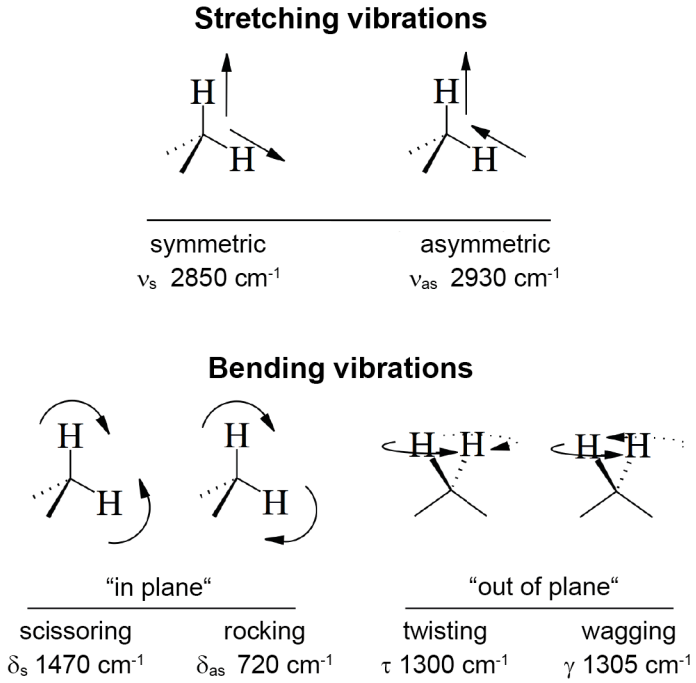

Figure 1.2: Stretching and bending vibrational modes for a CH_2 group. Figure adapted from ref. [41].

oscillator model obeying Hooke's law, the vibrational energy states $V_{i\nu}$ can be described by

$$V_{i\nu} = h\nu_i \left(\upsilon_i + \frac{1}{2} \right) , \tag{1.1}$$

where h is the Planck's constant, ν_i is the fundamental frequency and υ_i is the vibrational quantum number of the i^{th} mode. For strictly harmonic vibrational modes, only transitions with $\upsilon_i \pm 1$ would be allowed. In practice, also overtones and combinations of normal vibrations occur, thus $V_{i\nu}$ must be described by an anharmonic (Morse-type) potential function, as depicted in Figure 1.3 [39].

In IR spectroscopy, the sample molecule is irradiated with a continuous spectrum of infrared light. According to quantum mechanics the molecule can take up an amount of energy to reach the first vibrationally excited state, i.e. $h\nu_{\mathrm{Abs}}$ in Figure 1.3A. Consequently, the spectrum of the remaining radiation shows an absorption band at the frequency $h\nu_{\mathrm{Abs}}$. According to the selection rule for IR spectroscopy, a vibration is infrared active only if the dipole moment μ changes along the normal coordinate q.

$$\left(\frac{\partial \mu}{\partial q} \right)_0 \neq 0 \tag{1.2}$$

The approximate location of an IR band in the spectrum is governed by the masses involved in a vibration as well as the type of bonding (single, double, triple). Further, the exact position is determined by electron donating or withdrawing effects of the

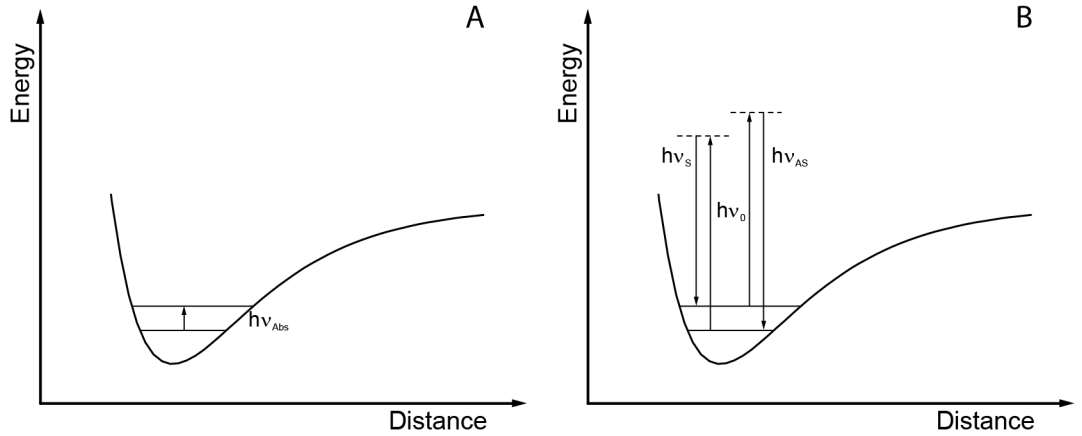

Figure 1.3: Excitation of a vibrational state. (A) Infrared absorption of a vibration with the energy $h\nu_{\mathrm{Abs}}$. (B) Stokes and anti-Stokes scattering. Figure adapted from ref. [40].

environment as well as coupling with other vibrations. In accordance with Equation 1.2, the intensity of absorption increases with increasing polarity of the vibrating bonds [42].

Raman spectroscopy provides complementary information of molecular vibrations, since in this case, the mechanism of interaction between light and molecules is principally different to IR spectroscopy. The sample is illuminated with the beam of a monochromatic radiation with the energy $h\nu_0$ (usually a laser in the NIR-VIS-UV region). The potential energy of molecules that interact with the photons is raised to a virtual state above the ground state (see Figure 1.3B). Most of the molecules return immediately to the ground state through the emission of a photon. Since the energy of these emitted photons is identical to the incident light, this process is a form of elastic scattering and is called Rayleigh scattering. A small fraction of the stimulated molecules fall back to an excited vibrational mode, emitting photons with the energy $h\nu_S$, that is lower than the energy of the incident light (Figure 1.3B). This phenomenon is referred to as Stokes Raman scattering. The energy difference $h\nu_0$ - $h\nu_S$ is in the MIR range and provides information about the stimulated vibrational modes. Molecules that are in an excited vibrational state at the time of laser illumination undergo the same excitation to a virtual state. Again, the majority of molecules exhibits Rayleigh scattering, but a small fraction will drop down to the ground vibrational state, emitting photons with the energy $h\nu_{AS}$, that is higher than the energy of the incident light (Figure 1.3B). This process is called anti-Stokes scattering and also here, from the energy difference $h\nu_0$ - $h\nu_{AS}$, information about the molecule vibration can be derived. The selection rule states that a molecular vibration can only be observed in the Raman spectrum, if there is a change of the polarizability α with the normal coordinate of the vibration q [39, 40].

$$\left(\frac{\partial\alpha}{\partial q}\right)_0 \neq 0 \tag{1.3}$$

1.1.2 Fourier Transform Infrared Spectroscopy

Early MIR spectrometers were dispersive instruments, where the infrared beam was dispersed by a grating or a prism and the spectrum was recorded by stepwise scanning of the different wavenumbers. Spectra acquisition was slow and thus a major problem was to maintain the stability of the sample that was exposed to the IR beam for a

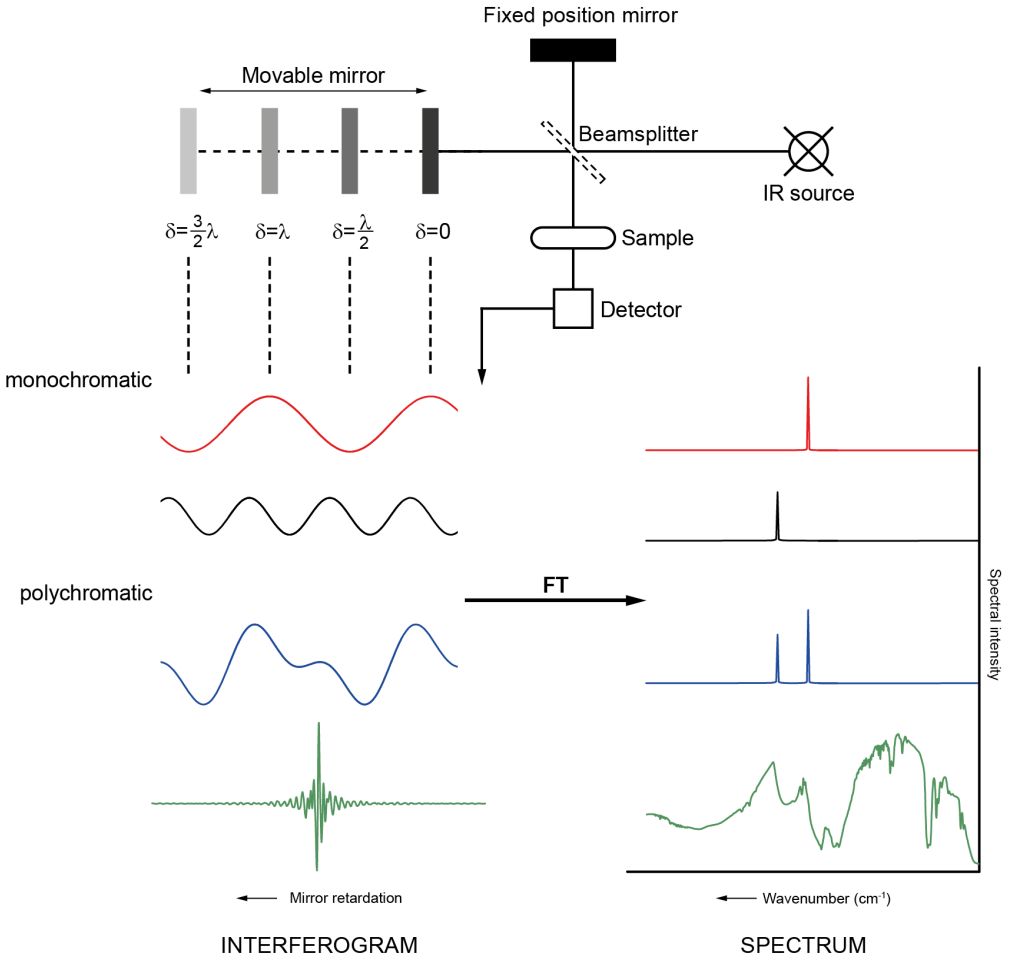

Figure 1.4: Major components of a FTIR spectrometer and working principle of a Michelson-interferometer. Examples show interferograms (left) and spectra (right) of two monochromatic waves and their cumulative curve as well as a continuous light source. Figure adapted from refs. [43, 44].

long period of time during measurement [45]. After the development of the fast Fourier transform algorithm in the 1960s [46], it was feasible to employ the interferometer for IR spectroscopy, which was conceived by Michelson in 1891 [47]. The working mechanism of the Michelson-interferometer is shown in Figure 1.4. A light beam from an infrared source is directed towards a beamsplitter. 50 % of the incident light is directed to a fixed position mirror and 50 % is transmitted to a movable mirror that can be translated back and forth. The reflected beams merge again at the beamsplitter, from where the light is directed through the sample and propagates to the detector. If the distance

of the beamsplitter to the fixed mirror matches the one of the movable mirror, the two beams have travelled the same distance, which results in constructive interference and high intensity at the detector (see Figure 1.4). Upon motion of the movable mirror, the optical path lengths become unequal, which is referred to as retardation δ. Mirror displacement of a distance x yields the retardation $\delta = 2\mathrm{x}$, since the light has to travel the distance back and forth to arrive at the beamsplitter again. If the mirror is shifted by a distance equal to one quarter of the radiation wavelength ($\mathrm{x} = \lambda/4$), the retardation becomes $\delta = \lambda/2$ resulting in destructive interference of the two rays at the beamsplitter [44]. The generated interferogram of monochromatic light can be described as an infinitely long cosine wave (red and black lines in Figure 1.4). When considering polychromatic light (blue line), it is possible to treat each frequency as a separate cosine function and to add the cosine waves to obtain the interferogram, which is mathematically described by

$$B(\delta) = \int_0^\infty I(\nu)\ cos(2\pi\delta\nu)\,\mathrm{d}\nu\,, \tag{1.4}$$

with $B(\delta)$ denoting the intensity (brightness) at the detector as a function of the retardation and $I(\nu)$ is the intensity as a function of wavenumber. A typical interferogram of a sample irradiated by a continuum light source is shown in Figure 1.4 (green line). At zero retardation ($\delta = 0$), all wavelengths exhibit constructive interference yielding the maximum intensity (center burst). The IR spectrum (intensity versus wavenumber) corresponding to the recorded interferogram (intensity versus time) is calculated by Fourier transformation [44]:

$$I(\nu) = \int_{-\infty}^{+\infty} B(\delta)\ cos(2\pi\nu\delta)\,\mathrm{d}\delta\,. \tag{1.5}$$

After obtaining an interferogram of the reference (I_R) and the sample (I_S), the absorption A of an analyte is calculated by

$$A = -log\left(\frac{I_S}{I_R}\right). \tag{1.6}$$

A striking advantage of FTIR compared to dispersive instruments is the simultaneous detection of all wavenumbers (Fellgett or multiplex advantage), which results in

dramatically lower acquisition times. A further highlight is the increased light throughput, since there is no need for a slit to achieve resolution (Jacquinot or throughput advantage). With the higher radiation power on the detector, greater signal-to-noise ratios (SNR) can be achieved. The Connes (or calibration) advantage describes the high wavenumber precision achieved by a laser that continuously determines the exact position of the movable mirror. This allows for fast and precise signal averaging by co-adding a multitude of scans for one spectrum, thus improving the SNR [44, 45, 48].

1.1.3 Infrared Spectroscopy of Proteins

Infrared spectroscopy is very sensitive to the chemical composition and architecture of molecules. This makes it a valuable tool for the investigation of protein structure and molecular mechanisms of protein reactions [42].

Absorption bands of proteins in the IR spectrum are caused by vibrations of the CONH peptide group. *N*-methylacetamide (Figure 1.5) is the smallest molecule containing a *trans* peptide group thus providing a good example for the demonstration of the normal modes of polypeptide backbone vibrations. Currently, there are known 9 characteristic IR bands of the peptide groups that are referred to as amide bands (see Table 1.1).

The amide I band is most commonly used for determination of the secondary structures of proteins. Approaches include fitting the amide I band with component bands or using a calibration set of spectra from proteins with known structure to perform pattern-recognition calculation [49]. Usually, band narrowing techniques like Fourier-self deconvolution or first-derivative spectra are used to identify the band component positions in the recorded spectrum [50]. For analysis of protein spectra with modu-

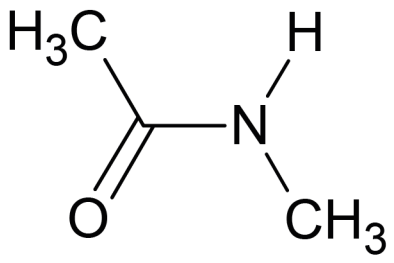

Figure 1.5: Structure of *N*-methylacetamide.

lated excitation, also phase sensitive detection is a feasible option for separation of overlapping bands [51].

Since the OH-bending band overlaps with the amide I band in the IR spectrum at $\sim$1640 cm^{-1}, measurements of proteins are often performed in D_2O solution. The OD-bending band is located at $\sim$1200 cm^{-1}, thus creating a region of relatively low absorbance between 1500 and 1800 cm^{-1}. Upon solvent exchange, the amide II band (predominantly originating from N–H vibrations) is shifted from $\sim$1550 to $\sim$1450 cm^{-1}. Since the amide I band is mainly composed of C=O vibrations, its shift is relatively small (5-10 cm^{-1}) compared to the amide II band [52]. Secondary structure analysis of the amide I band can be performed in D_2O solution, although it is necessary to demonstrate that D_2O does not alter the secondary structure of the protein [52]. It was reported that exposure of proteins to D_2O leads to changes in structure [53] such

Table 1.1: Characteristic amide infrared bands of proteins [45, 50].

Designation	Approximate frequency (cm^{-1})	Nature of vibration
A	3300	N–H stretching, in resonance with overtone (2 × amide II)
B	3100	
I	1650	80 % C=O stretching; 10 % C–N stretching; 10 % N–H bending
II	1550	60 % N–H bending; 40 % C–N stretching
III	1300	30 % C–N stretching; 30 % N–H bending; 10 % C=O stretching; 10 % O=C–N bending; 20 % other
IV	625	40 % O=C–N; 60 % other
V	725	N–H bending
VI	600	C=O bending
VII	200	C–N torsion

Table 1.2: Assignments of amide I band positions to secondary structure components [42].

Secondary Structure	Band position in H_2O (cm^{-1})		Band position in D_2O (cm^{-1})	
	Average	Extremes	Average	Extremes
α-helix	1654	1648-1657	1652	1642-1660
β-sheet	1633	1623-1641	1630	1615-1638
β-sheet	1684	1674-1695	1679	1672-1694
Turns	1672	1662-1686	1671	1653-1691
Disordered	1654	1642-1657	1645	1639-1654

as altered salt bridges [42] and protein denaturation [54, 55], as well as changes in their function [56], particularly in proteins with internal electron transfer [57, 58]. Assignments of amide I band positions to secondary structure in H_2O and D_2O are collected in Table 1.2.

1.1.4 ATR-IR Spectroscopy

Attenuated total reflection (ATR) spectroscopy was introduced by Harrick and Fahrenfort in the 1960s [59, 60]. Advantages of this mechanically stable and robust technique are its quick and facile sample preparation as well as the potential non-invasive nature. During the past few decades, ATR has gradually replaced other sampling methods for solid and liquid samples and now is routinely used in industrial and research laboratories [61]. ATR-IR spectroscopy allows both, quantitative and qualitative sample analysis and current fields of application include biology, medicine, forensics, process analytics and organic chemistry.

1.1.4.1 The Principle of total internal Reflection

IR light passing through a medium of optical high density (n_1) is totally reflected at the interface to a medium of lower optical density (n_2). The light rays do not propagate into the less dense medium, however, an evanescent field forms at the interface extending into the medium of lower density, as depicted in Figure 1.6A. Within this evanescent field, the light can interact with samples placed at the surface of the first medium, thus enabling IR absorption measurements. This total internal reflection is a special case of

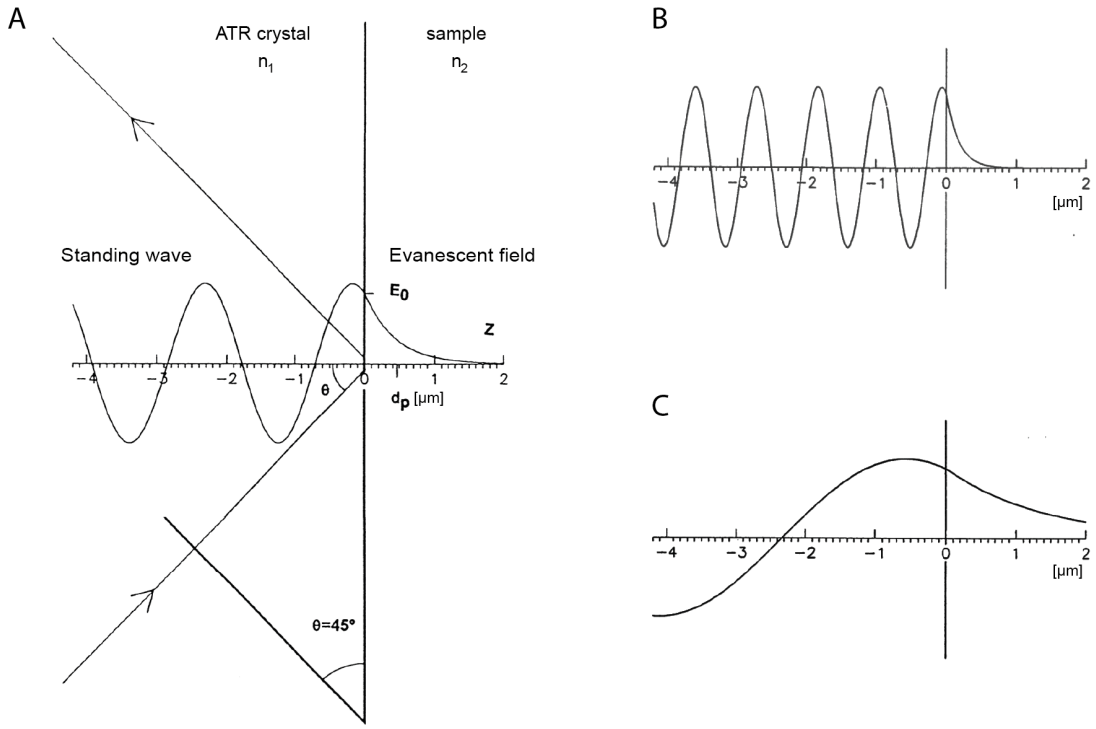

Figure 1.6: Frequency dependence of the penetration depth of the evanescent wave. (A) Side view of an ATR crystal with details of the electric field at the point of reflection at a light frequency of $1650\,\mathrm{cm}^{-1}$. The standing wave exists within the ATR crystal while the evanescent wave decays outside the crystal with the penetration depth d_p. (B) Details of the standing wave and evanescent field intensity at higher ($4000\,\mathrm{cm}^{-1}$) and (C) lower ($800\,\mathrm{cm}^{-1}$) wavenumbers. Figure adapted from ref. [62].

reflection of an electromagnetic wave at the interface between two media [61]. Above the critical angle θ_c

$$\theta_c = arcsin\left(\frac{n_2}{n_1}\right), \tag{1.7}$$

which depends on the refractive index of the ATR crystal n_1, the light beam is completely reflected when it meets the interface. The angle of incident light θ_i is equal to the angle of reflected light θ_r. Figure 1.7 displays the electric field components of linearly polarized light. In the case of parallel polarized light, indicated by the symbol $\parallel$, the indices p or pp as well as the acronym TM (transverse magnetic), the electric vector is parallel and the magnetic vector is orthogonal to the plane of incidence, respectively. Light polarized perpendicular to the plane of incidence is often referred to

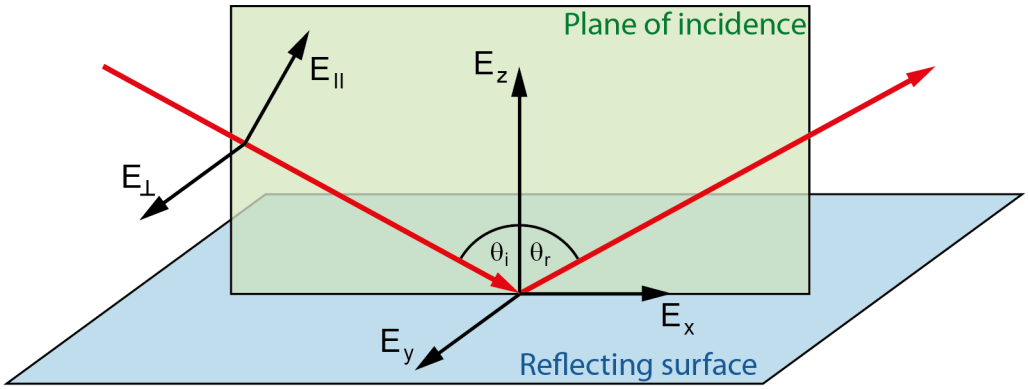

Figure 1.7: Schematic representation of the coordinate system of a light beam reflected on a surface. The angle of incidence with respect to the normal is denoted by θ_i. $E_{\parallel}$, the electric field component of parallel polarized light can interact with the x- and z-components of the transition dipole moment of the sample (i.e. E_x and E_z). $E_{\perp}$, the electric field component of normal polarized light can only excite the y-component of the dipole moment (E_y). Figure adapted from refs. [63–66].

by the symbol $\perp$, the indices s (german: senkrecht) or vp as well as the acronym TE (transverse electric). Its electric vector is perpendicular and the magnetic vector is parallel to the plane of incidence, respectively [61].

According to Maxwell's equations, this superposition of incoming and reflected waves result in a standing wave within the ATR crystal projecting perpendicularly from the total reflecting surface. Figure 1.6 shows a schematic representation of this standing wave that can be mathematically described by

$$E = 2\ cos\left(\frac{2\pi z}{\lambda_e} + \phi\right), \tag{1.8}$$

where z is the coordinate on an axis normal to the interface and $\lambda_e = \lambda_1 / cos\,\theta$ with λ_1 the wavelength within the ATR crystal $\lambda_1 = \lambda / n_1$. θ is the angle of incidence of the beam and ϕ the phase shift [62]. The evanescent wave in the optically less dense medium beyond the reflecting surface decays exponentially with the distance from the interface. The time averaged field intensity is described by

$$E = E_0\ e^{-z/d_p}, \tag{1.9}$$

where E_0 denotes the time averaged electric field intensity at the interface in the optically less dense medium and d_p is the penetration depth of the evanescent field.

This measure indicates how far the standing wave extends into the optically less dense medium and is defined as the depth at which the electrical field falls to the $1/e$ of the electrical field at the interface. It is given by Equation 1.10 [61, 62].

$$d_p = \frac{\lambda_1}{2\pi\sqrt{sin^2\theta - \left(\frac{n_2}{n_1}\right)^2}} \tag{1.10}$$

Smaller angles of incidence and decreasing wavenumbers result in a larger penetration depth, as indicated in Figure 1.6A-C. Consequently, ATR spectra of the bulk medium, where the sample thickness is much bigger than d_p, show increasing intensity with decreasing wavenumbers. For thin films that exhibit a small layer thickness compared to d_p, there is no such effect [61, 65]. Another characteristic of total reflection is the Goos-Hänchen effect, that describes the displacement of the totally reflected beam along the plane of incidence by a fraction of the wavelength (schematically depicted in Figure 1.6A) [67].

1.1.4.2 Choice of the ATR Element

The material of the ATR crystal profoundly influences the outcome of an experiment. Various characteristics have to be considered before selecting the ATR element. Generally, they should be chemically inert in the experimental environment and insoluble in the intended sample. The crystal should provide good transmission in the spectral range of interest without any absorption bands of its own. Its refractive index needs to be higher than the sample. When the index matching is better between the sample and the ATR element, a higher penetration depth can be obtained (see Equation 1.10). Harder ATR materials allow applying more force to press the sample against the surface for better contact [61, 62]. It is of particular interest for investigations of biological systems that certain ATR devices can be directly functionalized with organic monolayers [68–70]. A list of common materials for ATR elements and their optical properties is given in Table 1.3.

Also geometric parameters affect the potential experimental use of the ATR element. According to Equation 1.10, the penetration depth increases as θ decreases. ATR crystals with a trapezoidal cross-section exhibit multiple internal reflections. The number of reflections N is inversely proportional to the thickness t and proportional to

the length l according to Equation 1.11.

$$N = \frac{l}{t}\, cot\, \theta \tag{1.11}$$

Table 1.3: Optical properties of common materials for ATR elements [61, 71–73].

Material	Usable range (cm^{-1})	Refractive index	Comments
SiO_2/Quartz	55 000 - 4000	1.43	Hard and inert
Al_2O_3/β-Alumina	55 000 - 1800	1.7	Very hard and inert
BaF_2	50 000 - 840	1.45	Water soluble
CaF_2	50 000 - 1140	1.41	Slightly soluble in water
$C_{diamond}$	45 000 - 2500 and 1650 - 200	2.4	Very hard
ZnSe	20 000 - 500	2.4	Toxic in contact with acids
Si	8300 - 660	3.5	Hard
Ge	5500 - 600	4.0	Insoluble in water
TlBr-TlI/KRS-5	20 000 - 250	2.4	Toxic, soft

1.1.5 Surface-enhanced Infrared Spectroscopy

The infrared absorption intensity of molecules is radically increased when they are adsorbed on rough metal surfaces, films with metal islands or metal particles. This phenomenon is referred to as surface-enhanced infrared absorption (SEIRA) and was discovered by Hartstein in 1980 [74]. IR enhancement factors of up to 1000 have been accomplished [75]. The SEIRA effect can be observed in the transmission, ATR and external-reflection modes [76]. Enhancement depends on the morphology of the surface. For example for films formed from ellipsoid islands, the largest enhancements can be achieved when the islands are closely spaced, but do not touch each other. Chemisorbed molecules generally show larger enhancement than physisorbed molecules. Enhancement is particularly high for the first monolayer directly linked to the surface, and decays abruptly within 5 nm from the surface, with an enhancing field up to 15-20 nm [77]. Vibrational modes exhibiting a dipole moment perpendicular to the surface

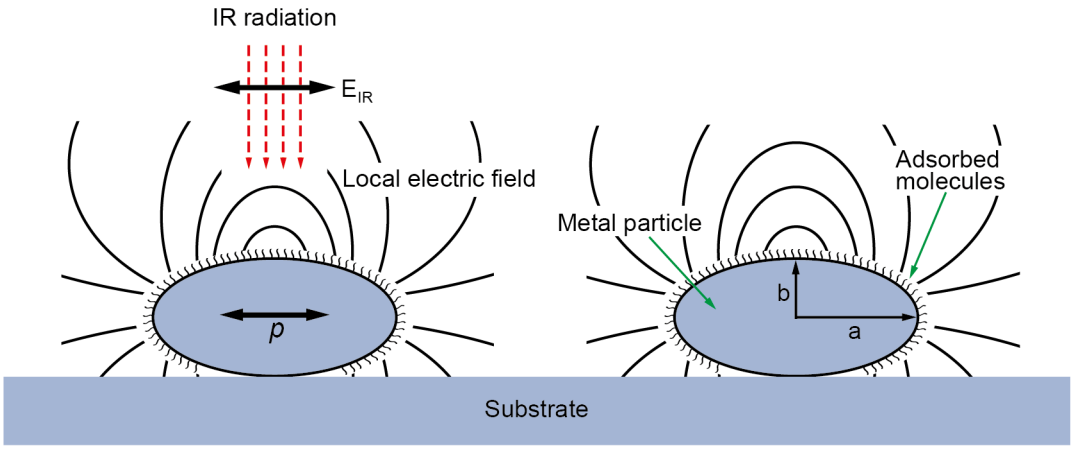

Figure 1.8: Schematic representation of the electromagnetic mechanism of SEIRA. Metal particles are modeled by elliptic sphaeroids. Incident IR radiation with the amplitude E_{IR} generates a strong local electric field that excites molecular vibrations of adsorbed molecules near the metal surface. Figure adapted from refs. [76, 80].

are preferentially enhanced, analogous to a surface selection rule in infrared reflection absorption spectroscopy (IRRAS) [30, 76].

Two mechanisms have been generally accepted to contribute to the signal enhancement of the SEIRA effect, the chemical and electromagnetic mechanism. The chemical mechanism plays a subordinate role for the magnitude of enhancement [78]. It is caused by interactions between adsorbed molecules as well as charge oscillations between molecular orbitals and the metal surface. Details of this enhancement mechanism are still unclear and not yet fully elucidated [76, 78].

The principle of the electrochemical mechanism has been thoroughly investigated and its contribution to the enhancement is considered to be predominant. It is well explained by the localized plasmon model with the metal island film approximated by elliptic spheroids, as depicted in Figure 1.8 [79]. The particles of the island film are much smaller than the wavelength of light and the dipole moment p induced at the metal particle is written as

$$p = \alpha\, V\, E_{\mathrm{IR}}\,, \tag{1.12}$$

where α and V are the polarizability and the volume of the metal particle, respectively and E_{IR} is the amplitude of the incident IR radiation [78, 79]. The induced dipole generates an electric field around the metal islands with the amplitude

$$E_{local} = \frac{2p}{l^3}\,, \tag{1.13}$$

with l as the distance from the center of the metal particle. The local electromagnetic field is much stronger than the incident field and excites the adsorbed molecules. The third power in the denominator of Equation 1.13 indicates the rapid decay of the local electric field within a short distance from the surface [78, 79]. Since E_{local} is normal to the substrate surface, only molecular vibrations exhibiting dipole changes perpendicular to the surface are excited, resulting in the surface selection rule mentioned above. In ATR measurements, the observed band intensities depend on the angle of incidence and the polarization of the infrared light [76].

1.1.6 Time-resolved Infrared Spectroscopy

Time-resolved FTIR (tr-FTIR) spectroscopy is used to obtain structural information of transient chemical species in dynamic systems such as ligand binding and dissociation, protein folding and reaction kinetics. The two prevalent recording modes for tr-FTIR spectroscopy are rapid-scan and step-scan. Using rapid-scan, processes with a time scale of milliseconds can be observed, step-scan measurements extend the time-resolution down to nanoseconds [81]. Step-scan is only applicable for reversible reactions, whereas rapid-scan can also be used for irreversible processes.

1.1.6.1 Rapid-Scan FTIR Spectroscopy

Data acquisition in the rapid-scan mode follows the same procedure of continuous scanning as in conventional static FTIR spectroscopy. Higher time-resolution is achieved by faster motion of the movable mirror in the Michelsen-interferometer. As depicted in Figure 1.9A, the data points of one interferogram are recorded consecutively and successive scans collect entire interferograms. The first interferogram (points 1-10) corresponds to the steady state of the sample just before excitation, and the second interferogram (points 11-20) just after excitation.

Recording of one scan involves the following steps of the mirror: *speedup - constant forward motion - slowdown - speedup - constant backward motion - slowdown.* Limitations for the time-resolution are the mirror velocity and the distance covered by the mirror. At these high time-resolutions, also the speedup and slowdown of the mirror contributes to the overall acquisition time. The covered distance of the mirror, and by that the

acquisition time for one scan can be reduced by lowering the resolution. The mirror velocity is constrained by mechanical characteristics [81].

Recently, a new interferometer design was introduced for ultra-rapid-scanning measurements, featuring an rotating optical element instead of the translational moving mirror [82]. The cube corner retroreflector achieves a sampling rate of up to 166 scans s^{-1}, in comparison with 25 scans s^{-1} of a conventional interferometer [81]. Further advantages of this novel interferometer are its high temperature stability and the compact design [83, 84].

1.1.6.2 Step-Scan FTIR Spectroscopy

Contrary to continuous scan FTIR, the step-scan technique decouples the time dependence of the IR measurement from the time dependence of the observed phenomenon [81]. Here, the mirror velocity is infinitely slow and retardation is obtained by discrete steps. The moving mirror is kept still at every retardation point, while data are collected. As shown in Figure 1.9B, the intensity data are collected in time-resolved columns at each retardation point. At the first retardation position (points 1-10), the

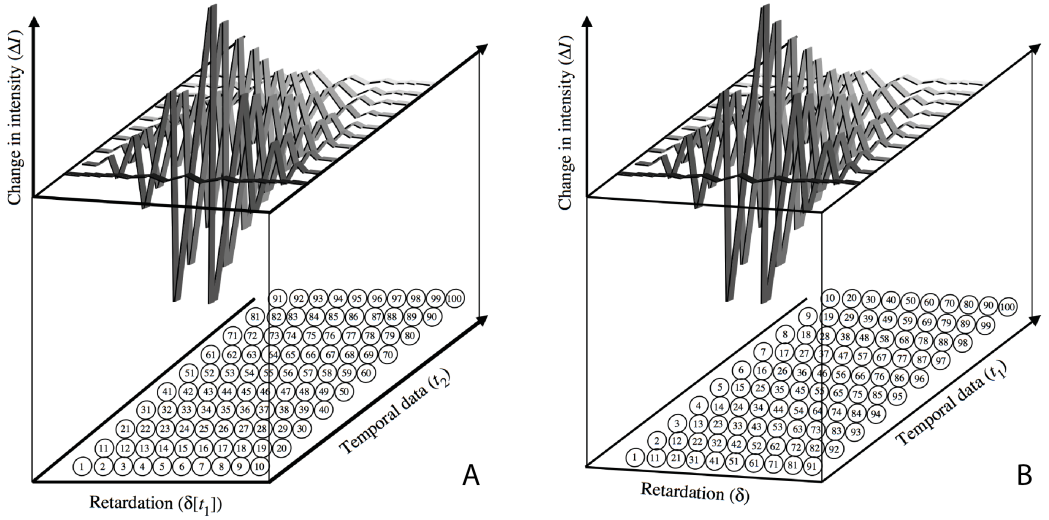

Figure 1.9: Data collection scheme for time-resolved interferograms. Numbered circles below the interferograms show the order of data sampling. (A) In rapid-scan FTIR spectroscopy, data collection proceeds in rows along the retardation axis. (B) Using step-scan FTIR spectroscopy, data is collected in columns along the temporal axis. Figure adapted from ref. [81].

observed reaction is restarted and the IR signal is recorded until the sample has fully relaxed. Multiple data points can be co-added at a constant retardation to increase the signal-to-noise ratio (SNR). When a desired SNR is reached, the mirror is moved to the next retardation point (points 11-20). A rigorous requirement for this acquisition mode is the repeatability and reproducibility of the observed sample reaction [85]. Given that condition, at each interferogram point spectral data acquisition is decoupled from the time domain, so any degree of spectral resolution as well as time-resolution with any SNR is theoretically possible [81]. A further prerequisite for the use of step-scan FTIR is the synchronization of sample excitation and data acquisition. Generally, an external pulse generator is used to trigger the excitation source of the sample, which is synchronized with the IR instrument. Limitations for the step-scan mode are the speed and sensitivity of detectors and amplifiers as well as the exact positioning of the mirror. An effective limitation for the spectral resolution and maximum obtainable number of co-additions is the memory in the FTIR instrument.

1.2 Biomimetic Membrane Systems

Membrane proteins play a vital role for the effective operation of every cell. It is estimated that approx. 30 % of human genes encode for membrane proteins [86]. Their functions include cell-cell interaction, signal transduction and transport of ions and nutrients [87]. Due to their large variety of functions, they are a preferred target for pharmaceuticals. Currently, more than 60 % of approved drugs affect membrane proteins [88]. Investigations of structure and function of membrane proteins is difficult, since they exhibit their native three dimensional structure and function only when embedded in a lipid bilayer [86]. To address this problem, various approaches to build artificial membrane systems have been taken. The first example were black lipid membranes (BLMs), where the bilayer is formed by applying lipid molecules dissolved in hydrophobic solvents onto a small aperture in a Teflon plate. This type of biomimetic membrane was primarily used for electrophysiological investigations e.g. for measuring the ion movement through ion channels [89]. A disadvantage of BLMs is the low stability of only a few hours.

This led to the development of solid-supported lipid bilayers (SLBs) that showed high stability even in the presence of high flow rates or vibrations [90]. SLBs are readily prepared by directly depositing lipid bilayers onto a solid surface, thus membrane areas of several square centimeters can be obtained. Attachment of the membrane to planar surfaces enabled the application of analytical methods such as interference fluorescence [91], Fourier transform infrared spectroscopy [92], surface plasmon resonance (SPR) [93] as well as quartz crystal microbalance (QCM) [94], that were impossible to carry out with earlier model systems.

However, a major drawback of SLBs is the proximity of the lipid molecules to the solid surface that acts as a supporting layer. Membrane-substrate distances of less than 1-2 nm may cause partial loss of function or even denaturation for proteins that protrude further from the membrane [95]. To avoid this problem, soft polymeric materials were used as a spacer between the substrate and the lipid membrane. Polymer-supported membranes employing regenerated cellulose have been used as a model system for the cell membrane [96]. A different approach to introduce an interstitial space separating the lipid bilayer from the surface is by using a macromolecular tether (tethered bilayer lipid membrane, tBLM). In this tethering strategy, a hydrophilic spacer molecule such

as oligo(ethylenoxide) is attached to the hydrophilic head group of the lipid molecule [97]. Adjusting the length of the tether molecule enables tuning of the membrane-substrate distance, whereas varying the lateral spacer density makes it possible to control the viscosity of the membrane [98]. Further-reaching demands in biomimetic membrane model systems led to the development of the protein-tethered bilayer lipid membrane (ptBLM).

1.2.1 Protein-tethered Bilayer Lipid Membrane

The driving force for the design of the ptBLM was the incorporation of membrane proteins in biomimetic bilayers in a defined orientation [6]. In this setup, the protein itself is tethered to the surface via linker molecules featuring an ion chelating nitrilotriacetic (NTA) acid group. Orientation of the protein relative to the surface is achieved by introducing a genetically engineered 6x his-tag at a predefined position of the recombinant protein. Complex binding of the his-tagged protein to the linker via a Ni^{2+} ion is based on the well-established concept of ion affinity chromatography [100]. After immobilization of the protein, it is reconstituted into a lipid bilayer by in situ dialysis,

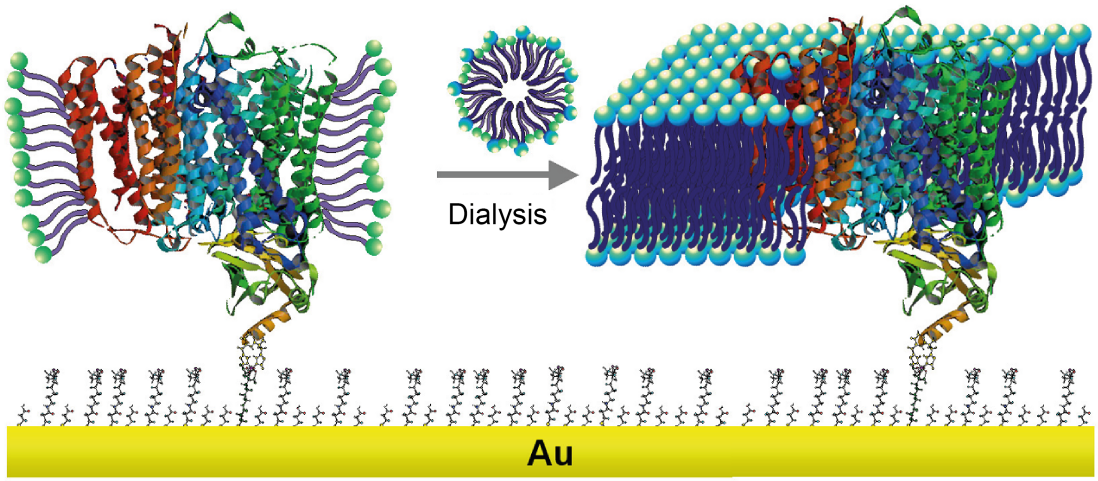

Figure 2.1: Schematic representation of the reconstitution of an immobilized protein into a lipid bilayer by in situ dialysis. (left) Cytochrome *c* oxidase dissolved in detergent molecules is attached to the surface via a NTA-linker by a genetically engineered his-tag to the protein. (right) The detergent molecules are substituted by lipid molecules, thus forming a lipid bilayer that is anchored to the surface by the protein. Figure adapted from ref. [99].

as depicted in Figure 2.1. This approach was successfully applied to study C*c*O in both configurations, with the cytochrome *c* binding site pointing away from the surface (his-tag at subunit I) [6, 101] and directed toward the surface (his-tag at subunit II) [4, 5, 9, 102–104] as well as to bacterial reaction centers [105].

As with other biomimetic membrane models, the linker molecule provides an interstitial space between the lipid bilayer and the surface that enables proper folding and full functionality of the membrane protein, particularly for proteins that feature extra-membraneous domains [106]. In investigations of redox-active membrane proteins such as the C*c*O, the linker also serves a second purpose, namely the electronic wiring of the protein to the electrode. In early attempts, the linker molecule was synthesized in situ on the gold surface by coupling the amino group of the nitrilotriacetic groups bearing ANTA to a *N*-hydroxy succinimide (NHS) functionalized surface, that is assembled on a gold or silver electrode via a thiol group [6]. Later, the linker molecule dithiobis-(nitriloacetic acid butylamidylpropionate) was synthesized ex situ, thus allowing a more effective control of the protein surface concentration by forming a mixed monolayer with a spacer molecule [9].

Adsorption of the linker on the gold surface as well as immobilisation of the protein have been followed by surface-enhanced infrared absorption spectroscopy (SEIRAS) [101]. Formation of the lipid bilayer were measured by SPR, QCM and electrochemical impedance spectroscopy (EIS) [6]. The electrical properties of the ptBLM analyzed by EIS are compatible with BLMs and tBLMs [106].

Enzymatic activity of C*c*O immobilized in a ptBLM has been demonstrated by cyclic voltammetry (CV) showing increased catalytic currents [7], whereas potentiometric titrations followed by SEIRAS [9] showed conformational changes of the protein as a consequence of electron transfer.

1.3 Cytochrome *c* Oxidase

1.3.1 The Respiratory Chain and its Role in the Human Body

Proteins of the respiratory chain are located in the cell membrane of prokaryotes and the inner mitochondrial membrane (IMM) of eukaryotes. As seen in Figure 3.1, the IMM forms a separate compartment within the mitochondrion called matrix. This matrix space is densely packed with metabolic enzymes required for the citric acid cycle, amino acid metabolism and urea synthesis [107]. Closely linked to products and intermediates of the citric acid cycle, proteins of the respiratory electron transfer chain use the energy gained by a series of redox reactions in order to produce a pH gradient across the IMM that finally drives the synthesis of adenosine triphosphate (ATP) in the ATP synthase. The respiratory electron transfer chain consists of the following four complexes:

- complex I NADH:ubiquinone oxidoreductase (NADH dehydrogenase)
- complex II Succinate:ubiquinone oxidoreductase (succinate dehydrogenase)
- complex III Cytochrome bc_1
- complex IV Cytochrome *c* oxidase

The respiratory electron transfer chain is the last step in the conversion of glucose into ATP. It is tightly intertwined with the citric acid cycle providing NADH, the substrate of complex I, and complex II is even a member of the citric acid cycle. Along complexes I-IV, the electrons pass at least ten intermediate redox systems with increasing standard redox potentials [108]. It has been found that there is a certain ratio of respiratory complexes. A single complex I is accompanied by approximately three complexes III and seven of complexes IV [109]. The membrane-soluble electron carrier UQH_2 transports electrons from complex I and II to complex III and water-soluble cytochrome *c* (cyt *c*) moves electrons from complex II to complex IV. Electron transfer in complex I, III and IV is coupled to proton translocation across the IMM with four, four and two protons pumped per each pair of electrons, respectively [110]. Notably, this proton pumping takes place "uphill" against an electrical and a pH gradient (see Figure 3.1), with high proton concentration in the intermembrane space (IMS) and low proton concentration in the matrix. This proton motive force is finally used by ATP

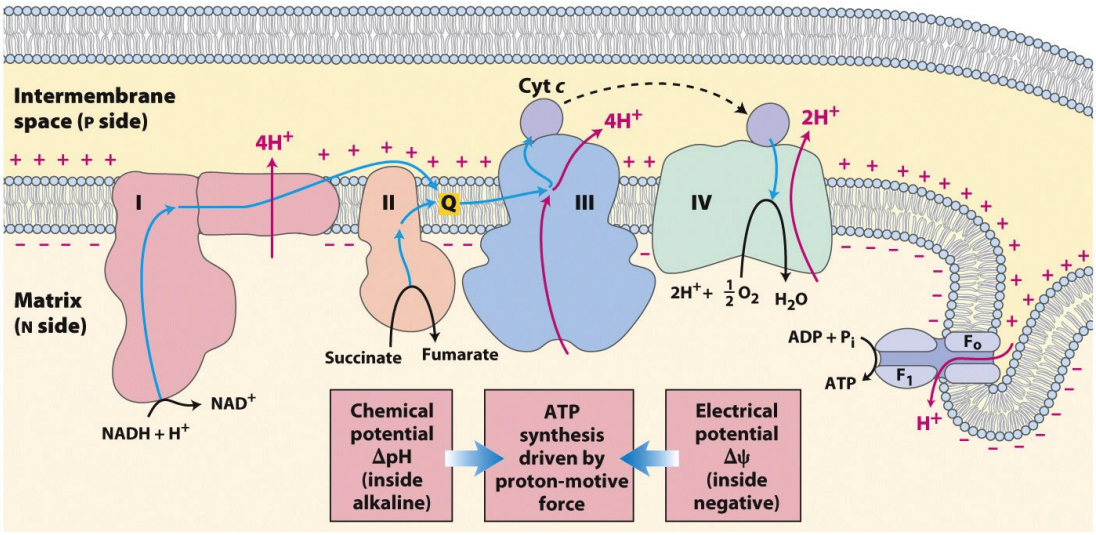

Figure 3.1: Mitochondrion with respiratory chain. The outer membrane forms the boundary with the cytoplasm and encloses the intermembrane space. This inner mitochondrial membrane forms the boundary to the matrix, where the citric acid cycle takes place. The IMM hosts the four respiratory chain complexes as well as the ATP synthase. Figure adapted from ref. [111].

synthase to form ATP. The overall reaction of the respiratory chain is expressed in Equation 3.1 [111].

$$\mathrm{NADH} + 11\,\mathrm{H^+_{Matrix}} + {}^1\!/_2\,\mathrm{O_2} \longrightarrow \mathrm{NAD^+} + 10\,\mathrm{H^+_{Matrix}} + \mathrm{H_2O} \tag{3.1}$$

With the efficiency of the ATP synthase of 0.25 produced ATP molecules per proton, the output of the respiratory chain is 2.5 ATP molecules per NADH [110]. Being the final product of the conversion of glucose, ATP serves as a ubiquitous energy unit in the living cell. The exergonic conversion of ATP to ADP or AMP is coupled to many endergonic reactions and processes.

1.3.2 Structure of the Cytochrome *c* Oxidase

1.3.2.1 Subunit Composition and Structure

Since C*c*O plays an important role in metabolism, its structure and mechanism have been subject of extensive research. After its first crystallization in 1961 [112], it took more than three decades to obtain high-resolution X-ray structures due to the general

difficulty of crystallizing membrane proteins. Atomic structure at 2.8 Å of *Paracoccus denitrificans* was revealed in 1995 [2], bovine C*c*O followed in 1996 [113], *Rhodobacter sphaeroides* in 2002 [114].

The common structural and functional feature of cytochrome *c* oxidases is a two subunit core that contains the four redox centers and is essential for the function of the enzyme [115]. Generally, bacterial C*c*Os only have one additional subunit, while eukaryotic oxidases possess a more complex structure. Bovine C*c*O, for example, consists of a dimer of 13 SUs with a combined molecular weight of 413 kDa. C*c*O of *Paracoccus denitrificans* with 4 SUs and a molecular weight of 134 kDa [116] as well as the protein of *Rhodobacter sphaeroides* with 4 SUs and 269 kDa are considerable smaller. According to X-ray crystallography, bacterial oxidases are identical to the ones of higher organisms with respect to electron and proton translocation pathways. Thus, due to their smaller sizes and better processability, bacterial oxidases are commonly used as model systems for mitochondrial C*c*Os of eukaryotes in experiments with the aim to elucidate the mechanism of the redox coupled proton pump.

Referring to C*c*O from *Paracoccus denitrificans*, the part of the protein that is integrated into the membrane has a trapezoidal form and contains 22 membrane-spanning segments, most of them helical (see Figure 3.2A). The width at the top (i.e. intermembrane space face) is ∼75 Å, at the bottom (i.e. matrix face) it corresponds to ∼90 Å. The height of the trapezoid is ∼55 Å, with a maximum height of ∼95 Å, as SU II is attached to the trapezoid on the top, thus protruding from the inner mitochondrial membrane into the periplasmatic space [2].

SU II is attached to the trapezoid on the top, thus protruding from the inner mitochondrial membrane into the periplasmatic space. Subunit I with its 12 transmembrane helices is largely embedded in the membrane and contains the latter three of the four redox centers of the protein. Heme *a*, heme a_3 and Cu_B are located about one third into the membrane depth from the intermembrane space face. Both hemes are oriented perpendicular to the membrane plane with an interplanar angle of 108° resulting in an edge-to-edge distance of 4.7 Å [117]. Two histidines provide the axial ligands for the low-spin heme *a*, whereas a histidine and a hydroxyl or water molecule pose as ligands for the high-spin heme a_3. According to ligand field theory, a high-spin split occurs, if the energy required to pair two electrons in a t_{2g} orbital is greater than the energy cost of placing an electron in an eg orbital (i.e. there is a small split between the eg and

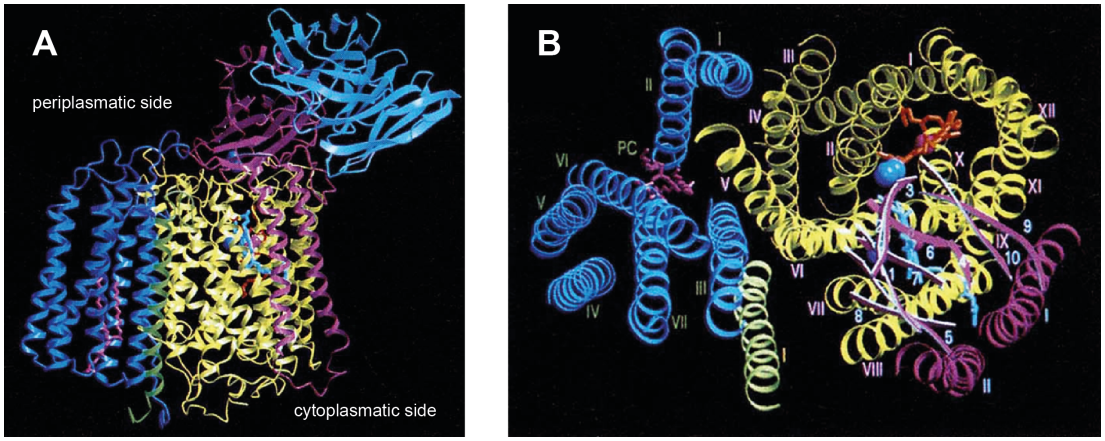

Figure 3.2: Cytochrome *c* oxidase from *Paracoccus denitrificans*. The polypeptide backbones of subunits I, II, III, IV are shown in yellow, magenta, blue and green, respectively. The cyan part denotes an antibody F_v fragment used for cocrystallization. (A) The whole protein viewed parallel to the membrane. (B) View of the protein along the membrane normal from the periplasmatic side. Transmembrane helices are indicated with Roman numbers. SU I contains heme *a* (red) and heme a_3 (cyan). Cu_A (blue) is situated in SU II near the β-barrel domain. Figure adapted from ref. [2].

t_{2g} orbitals), and vice versa. Thus, low-spin hemes are six-coordinated and high-spin hemes are five-coordinated [118, 119]. Cu_B is liganded by three histidines, situated 5.2 Å away from heme a_3, with which it forms the catalytic binuclear center (BNC), where oxygen binding and reduction take place [117]. Subunit II is L-shaped and consists of two N-terminal transmembrane helices that are followed by a hydrophilic, 10-stranded β-barrel domain. It protrudes into the periplasm and houses the first redox center, Cu_A. The two copper ions in a mixed-valence state ($Cu^I \bullet Cu^{II}$) are 2.6 Å apart.

Subunit III is fully embedded in the membrane and consists of seven transmembrane helices bundled in sets of two and five with a V-shape arrangement. It does not contain any cofactors associated with redox reactions. Subunit IV consists of a single transmembrane helix. Both, SU III and IV can be removed from the protein without losing its catalytic activity. However, it has been concluded that these SUs stabilize the integrity of the protein, since deletion of the gene coding for this SU lead to a partially assembled complex [115, 117]. Comparison of the bacterial protein explained above with mitochondrial bovine heart C*c*O reveals an amazing similarity of SUs I-III. The major difference are the 9 additional SUs, with two 13 SU monomers forming a functional dimer. X-ray measurements of bovine heart C*c*O also revealed

eight phospholipid and two cholate moieties within the protein. Both, bacterial and mitochondrial oxidases contain non-redox active metal ion binding sites. Manganese and magnesium ions have been revealed at the hydrophilic interface between SU I and II [120]. Discussed functions for these divalent ions are tethering together the two subunits or a role in a proton or water exit channel.

1.3.2.2 Proton and Electron Pathways

The reduction of oxygen to water takes place at the BNC, situated in the middle of the protein. For delivery of substrates (i.e. electrons, protons and oxygen) and release of product (water), especially designed pathways to the catalytic site have been identified.

Electron-transfer Pathways

C*c*O accepts electrons one by one from the water-soluble cyt *c* molecule at Cu_A, which is the first redox center in the protein. From there, the electrons are passed to heme *a*, (low-spin heme) and subsequently transferred to the BNC, consisting of heme a_3 (high-spin heme) and Cu_B, where the reduction of oxygen to water takes place. The rate of electron transfer depends on the difference of redox potential between donor and acceptor, their distance as well as their reorganization energy, according to electron transfer theory [121]. There are two conflicting theories about electron transfer in proteins. The first hypothesis states that electron transfer occurs specifically through bonds and thus can be modulated by conformational changes in the protein [122]. In the second theory [123, 124], a specific pathway through the protein is not necessary and electron transfer happens across multiple corridors defined by the optimal distance between donor and acceptor and the atomic density of the medium [125].

The electron transfer rate from cyt *c* to the bimetallic Cu_A has been found to be around $\sim$1x10^5 s^{-1} [126], and is modulated by a highly conserved Trp121 (the numbering of amino acids is based on the *Paracoccus denitrificans* enzyme) [127]. This high rate is facilitated by the tight binding of cyt *c* to the C*c*O. The interaction of numerous positively charged lysine residues on cyt *c* and negatively charged acidic amino acids on C*c*O causes a long-range electrostatic attraction and preorientation between the proteins. While Cu_A is situated near the membrane surface, the other redox centers are buried in the membrane (see Figure 3.3A). The distance from Cu_A to heme *a* is 19.5 Å, which is only 2.6 Å closer than heme a_3. The preference of electron transfer

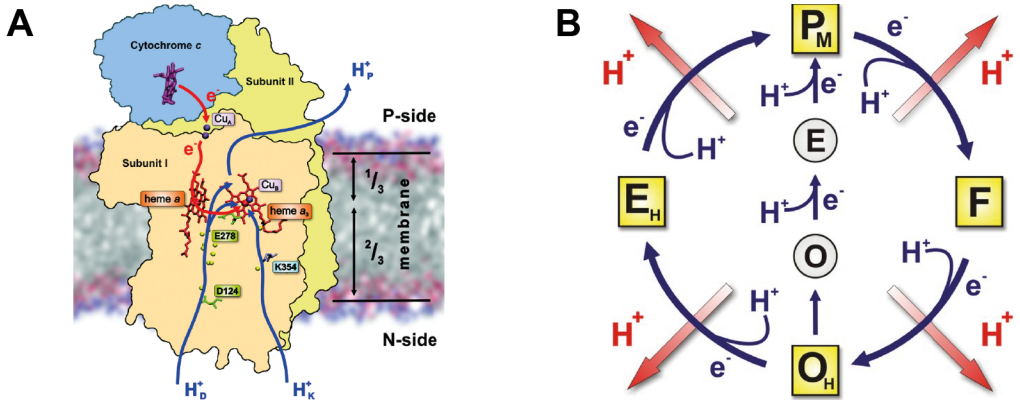

Figure 3.3: Electron and proton pathways in the C*c*O. (A) Relative arrangement of the redox centers within the C*c*O with attached cyt *c*. Electron transfer is indicated in red and proton pathways are shown in blue. The D channel begins at Asp124 and leads to Glu278, which acts as a gate between "pump site" or catalytic center. The K channel goes along Lys354 and leads to the catalytic site. (B) Proton pumping steps during the catalytic cycle of C*c*O. Each transition between active states (squares) is coupled to proton pumping. Reduction of relaxed states (circles) is not associated with proton pumping. Figures adapted from refs. [125, 133].

with heme *a* as an acceptor may be explained by a more favorable thermodynamical balance. It is known that this step is not coupled to a proton transfer and the mid-point redox potential of heme a_3 without proton transfer would be too low to allow electron transfer [128, 129]. The electron transfer rate for the reduction of heme *a* by Cu_A has been determined to be $1.1\text{x}10^5\,s^{-1}$ [130–132]. In the next step, heme *a* acts as an electron donor to heme a_3, which is at a distance of only 4.7 Å [2]. This reaction takes place at a slower pace with time constants in the range of 30 μs to 1 s, depending on the conditions under which the measurements are performed [125].

Proton-transfer Pathways

As mentioned before, the catalytic center is buried deep within the protein. In order to translocate protons within the protein, specific pathways are needed to ensure high rates of respiration. In C*c*O, proton pathways are needed for three particular reasons, as seen in Figure 3.3A. One pathway is required for delivering substrate protons to the catalytic center that chemically react to form water. A further pathway is needed for the uptake of four pumped protons from the matrix as well as an additional one for release of the protons to the IMS. Proton conductive structures within the pathways

are based on chains of hydrogen bonds between hydrogen-bonding protein side groups and water molecules.

At least two proton channels have been identified and confirmed by site-directed mutagenesis [134–137] and X-ray spectroscopy [2, 113, 114, 138]. Both of these pathways are situated in SU I and direct protons from the matrix to the BNC. The **D-pathway**, named after a highly conserved Asp124, is located near the surface of the protein on the matrix face. It starts at Asp124 and ends at Glu278, at a distance of $\sim$10 Å to the BNC [139]. This terminal glutamine is surrounded by an apolar cavity that is filled by several water molecules. It might be continuously filled throughout chemical water production at the BNC during turnover. This residue with its mobile water molecules is believed to hold a crucial role in directing incoming protons either to the BNC for chemical reaction or to a nearby Δ-propionate of heme a_3 for pumping [140, 141].

The **K-pathway** is named after Lys354 [135], the key residue of this channel, though not the beginning. It ends at the hydroxyethyl farnesly side chain of heme a_3 near the BNC [131]. Contrary to the D-channel, only few water molecules were found in this pathway, and the chain of hydrogen-bonds is interrupted by a hydrophobic gap. Studies involving site-directed mutagenesis of Lys354 did not substantially affect the catalytic cycle but stopped reduction of the BNC [142–144]. Consequently, it was proposed that the D-channel is solely responsible for translocation of pumped protons, whereas the K-channel is involved in uptake of chemical protons for water formation [2]. Recent results show that the D-pathway is used for the uptake of all four pumped protons and two of the chemical protons for water production (oxidative part of cycle) [145, 146]. The K-channel is responsible for the uptake of another two chemical protons (during the reductive part of the cycle) [144, 146].

An exit channel for pumped protons released out of the enzyme starts at the Δ-propionates of hemes and continues through highly mobile water molecules [147]. This highly hydrophilic region above the heme groups contains an extended hydrogen-bonded network of charged and polar amino acid residues.

Oxygen-transfer Pathways

Oxygen is a small, uncharged molecule and therefore able to permeate membranes. Accordingly, it can easily reach the catalytic site of the C*c*O even without a specific pathway. Even within the oxidase, it can move using conformational fluctuations.

However, uncontrolled diffusion would be too slow to maintain catalytic turnover of the oxidase. Thus, structures within the protein were proposed that lead oxygen to the catalytic center. X-ray crystal structures [113, 114] as well as experimental studies [148, 149] and theoretic examinations [140] revealed highly hydrophobic passages from the middle of the membrane to the BNC [125].

1.3.3 Catalytic Cycle and Mechanism of Proton Pumping

After the discovery of C*c*O in the 1920s, it took about 40 years of research to reveal that this protein produces and maintains a proton gradient across the IMM. Another 20 years later, the first comprehensive mechanistic cycle for the redox-driven proton pump was published by Wikström in 1989 [150]. After some refinements by Michel [151], the latest widely accepted catalytic cycle was suggested in 2000 [152]. Even though it describes the catalytic steps in principle, the exact structures and reaction parameters are not fully resolved yet. The overall reaction of C*c*O is shown in Equation 3.2.

$$4\,\text{cyt}\ c^{2+} + \text{O}_2 + 8\,\text{H}^+_{\text{Matrix}} \longrightarrow 4\,\text{cyt}\ c^{3+} + 2\,\text{H}_2\text{O} + 4\,\text{H}^+_{\text{IMS}} \tag{3.2}$$

Four electrons (obtained by reduced cyt *c*) are used to reduce one oxygen molecule to water. For every oxygen, four protons are taken up from the matrix reacting to two water molecules. Furthermore, parallel to this chemical reaction, four additional protons are pumped from the matrix to the IMS. The chemical reaction and proton translocation adds up to a proton gradient across the IMM of up to 4 pH units and a membrane potential of ∼50 mV.

A scheme of the latest proposed catalytic cycle with suggested structures is shown in Figure 3.4. In general, the cycle can be divided in a reductive part (**O**, **E**, **R**) and an oxidative part (**P**, **F**, **O**) [139]. In Figure 3.3B, the proton pumping steps during the catalytic cycle are shown. The predominant method for investigating the kinetics and intermediates of the catalytic cycle is optical absorbance spectroscopy. The redox centers at their reduced and oxidized states are characterized by distinct optical spectra that allowed the identification of up to 10 intermediates [125].

After expression and purification, the protein is usually in the **O** state, in which all redox centers are oxidized. This “as prepared” state is often referred to as the “resting” or “relaxed” form of the oxidase, which is inactive with respect to proton

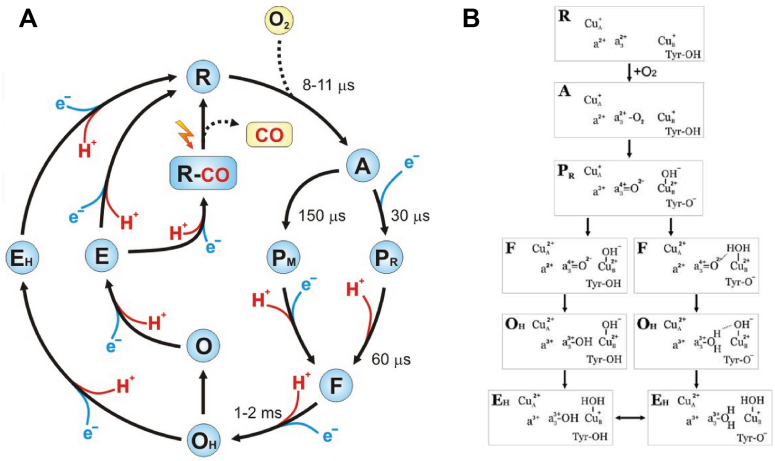

Figure 3.4: Catalytic cycle and proposed intermediates of C*c*O. (A) Catalytic cycle of C*c*O and (B) proposed structures of intermediates. The definitive structure is still unclear and thus leads to different possible configurations of the **F**, $\mathbf{O}_\mathrm{H}$ and $\mathbf{E}_\mathrm{H}$ state. Figures adapted from refs. [125, 133].

pumping. By periodic reduction and reoxidation (pulsing), a "pulsed" form of C*c*O is generated which is highly active with the ability to pump protons [153]. This active state is most likely identical to the $\mathbf{O}_\mathrm{H}$ state in the catalytic cycle [125].

Injection of one electron in the "resting" enzyme gains the one-electron reduced **E** state, where one electron is shared between heme a_3 and $\mathrm{Cu_B}$. This configuration is characterized by a distinct electron paramagnetic resonance (EPR) signal, originating from an oxidized heme a_3 in the presence of a reduced $\mathrm{Cu_B}$. This state can be created by several kinetic techniques like electron injection [131, 154, 155] or flash-induced chemical photoreduction [156], which takes several seconds. Thus, it is doubtful that the **E** state is a natural state during catalytic turnover because one complete cycle takes only several milliseconds.

The reduced **R** state can have two to four electrons in the redox centers and binds dioxygen. To maintain electroneutrality in the low-dielectric environment of the membrane, reduction of the redox centers is combined with proton uptake for charge compensation [128]. It was found that at least two of these protons are taken up by the K-pathway and probably are used for water production [142, 144, 146]. C*c*O in the **R** state with two electrons (mixed-valence) as well as four electrons (fully reduced) can

bind carbon monoxide to heme a_3. These CO adducts are broadly used as starting points to study the kinetics and intermediates of the catalytic cycle [11].

C*c*O with at least two electrons (reduced heme a_3 and Cu_B) can rapidly react with dioxygen to the ferrous-oxy **A** intermediate. It is rather unstable and decays fast, though it can be spectroscopically verified by its Raman spectrum that is similar to the one of oxygen-bound hemoglobin and myoglobin [125].

When there are two electrons present in the C*c*O at this point, compound **A** forms the mixed-valence peroxy intermediate $\mathbf{P}_M$. It is stable and without further injection of electrons, the reaction stops here. It was called "peroxy" because it was assumed that the oxygen bond was still intact with heme a_3 in a peroxy structure $Fe^{3+}_{a_3}$-O^-O^-. Later, it was found that the oxygen bond is already broken and heme a_3 is in the oxo-ferryl state $Fe^{4+}_{a_3}$=O while the other oxygen binds at the Cu_B (see Figure 3.4B) [157, 158]. For this cleavage of the oxygen bond, four electrons are necessary, three of which come from the BNC ($Fe^{2+}_{a_3}$•$Fe^{4+}_{a_3}$; $Cu_B{}^{I}$•$Cu_B{}^{II}$). The origin of the fourth proton is not definitely clarified yet, but it is assumed that it is donated by a nearby Tyr residue. Splitting of the oxygen bond also requires a proton. Measurements show that during this step, no proton gradient is built up [159], consequently this proton must come from within the enzyme rather than from the bulk solution, presumably from the same Tyr amino acid as the electron, thus forming a Tyr radical [158]. Oxygen addition to a fully reduced compound **A** leads to the peroxy intermediate $\mathbf{P}_R$. Kinetic measurements revealed that the structure of $\mathbf{P}_R$ and $\mathbf{P}_M$ are the same, with the oxygen bond already broken [160]. Here, however, only a proton is taken from the Tyr, leading to a deprotonated tyrosate anion instead of the radical.

The next reaction step, $\mathbf{P}_R \rightarrow \mathbf{F}$ is associated with proton pumping across the membrane (Figure 3.3A). The difference between the ferryl-oxo intermediate **F** and $\mathbf{P}_R$ is an additional proton which is taken up from the N-side of the membrane via the D-pathway. It is not fully resolved yet, if this proton binds to the tyrosate or the hydroxyl group at Cu_B (Figure 3.4B). In experiments, compound **F** can be obtained e.g. by flow-flash reactions from $\mathbf{P}_R$ [161] or electron injection into the $\mathbf{P}_M$ state [131]. It is easily detected by a characteristic peak in optical absorbance spectra [125].

The high-energy fully oxidized state $\mathbf{O}_H$, contrary to the relaxed **O** state is involved in proton pumping, by using the conserved energy released during the preceding redox reactions in the oxidative part [130]. $\mathbf{O}_H$ is unstable and in lack of further electrons

it may relax back into the inactive **O** state. These two states are not distinguishable with spectroscopic methods despite their energetic difference [162]. Reaction $\mathbf{F}\rightarrow\mathbf{O}_{\mathrm{H}}$ is associated with the uptake of an electron and a proton. The proton comes from the D-pathway and presumably goes to the BNC resulting in either a structure where both heme a_3 and $\mathrm{Cu_B}$ have hydroxide ligands or the two redox centers share a water and a hydroxide group [146]. The active one-electron intermediate $\mathbf{E}_{\mathrm{H}}$ is part of the catalytic cycle under turnover conditions. Transition $\mathbf{O}_{\mathrm{H}}\rightarrow\mathbf{R}$ initiates the reductive part of the cycle and is accompanied by electron and proton uptake. The following reaction to the reduced state **R** involves separation of the water molecules from the BNC, reception of an additional electron as well as proton pumping step [125].

As outlined above and depicted in Figure 3.3A, under turnover conditions, the four relatively stable intermediates $\mathbf{P}_{\mathrm{M}}$, **F**, $\mathbf{O}_{\mathrm{H}}$, $\mathbf{E}_{\mathrm{H}}$ are passed in the catalytic cycle. During each transition, a proton is pumped from the matrix to the IMS triggered by delivery of an electron to the enzyme [163]. Pumping of a proton is accompanied by uptake of a "chemical" proton that is used for water production. It is assumed that every proton pump cycle occurs by more or less the same mechanism, though it was found that the reductive part of the cycle is only linked to proton translocation when it is directly preceded by the oxidative part [164].

In a proposed sequence for proton pumping, the uptake of a "chemical" proton into the BNC forces a pre-pumped proton from a proton-loading site (PLS) into the IMS [165]. The structure and location of this PLS have not been unambiguously identified yet, but a propionate attached to heme a_3 has been suggested. First, the PLS receives a proton from the matrix upon reduction of heme *a*. The proton at the PLS causes an increase of redox potential at the BNC, thus being reduced by an electron coming from heme *a*. This electron transfer happens with similar kinetics as the loading of the proton loading site. In the next step, a "chemical" proton is taken up from the matrix into the BNC. Due to the shorter electron/proton distance it is drawn to the BNC rather than to the PLS. The arriving proton expels the proton from the PLS into the IMS by electrostatic repulsion. With the next electron accepted at heme *a* from $\mathrm{Cu_A}$, this proton pump cycle starts again. A prerequisite for this electrostatic mechanism is that the BNC, PLS and heme *a* are located closely together [164]. An ongoing point of discussion is the directionality of the proton pump and how leaking back of protons is prevented [139].

1.4 Odorant Binding Proteins and their Role in Olfaction

Odorants are mostly hydrophobic molecules with a relatively high vapor pressure and low molecular weight (150-250 $\mathrm{g\,mol^{-1}}$). This large repertoire comprises aliphatic and aromatic compounds with diverse chemical functional groups including aldehydes, esters, alcohols, alkenes and carboxylic acids [166]. The sophisticated mechanism of the olfactory system for discriminating this wide range of chemicals is rather complex and not fully resolved yet. Main aspects of the vertebrate and insect recognition system are described in the following section, with a focus on odorant binding proteins.

1.4.1 Principles of Odorant Recognition in Mammals and Insects

In combination with the other sensory systems, olfactory recognition plays an important role to generate a simplified internal representation of the complex external world [167]. Animals primarily rely on the olfactory sense to find food, trace predators and prey and mark their territory [166]. For insects, the olfactory system plays an even more important role for survival and reproduction than for mammals. Most insects depend on odorants for navigation, which requires the ability of the insects olfactory system to selectively detect and quickly inactivate (both in the millisecond time-scale) small amounts of odorants after they have been sensed [168].

The anatomy of the mammal olfactory system, here illustrated by the human organism, consists of an external nose and an inner nasal cavity (Figure 4.1A). Turbinate bones direct the inhaled air towards the olfactory epithelium. This mucous membrane contains a respiratory region that helps warming and humidifying the inspired air as well as an olfactory region where the olfactory receptor cells are located (Figure 4.1A). [19]. In the olfactory epithelium, more than 6-10 million olfactory receptor cells are present. They are bipolar neurons with an axon directly projecting into the olfactory bulb in the brain and at the other end, dendrites reach into the mucus [166]. These dendrites end in form of an olfactory knob which is the origin of five to fifty cilia that protrude into the olfactory epithelium. In the lipid bilayer sheath of the cilia, the chemosensory receptors are located, which are guanine nucleotide-binding protein (G-protein) coupled, seven domain transmembrane receptors (Figure 4.2A). Five types of G-protein-coupled chemosensory receptors are known in vertebrates: odorant receptors (ORs), trace amine-associated receptors (TAARs), two dissimilar vomeronasal

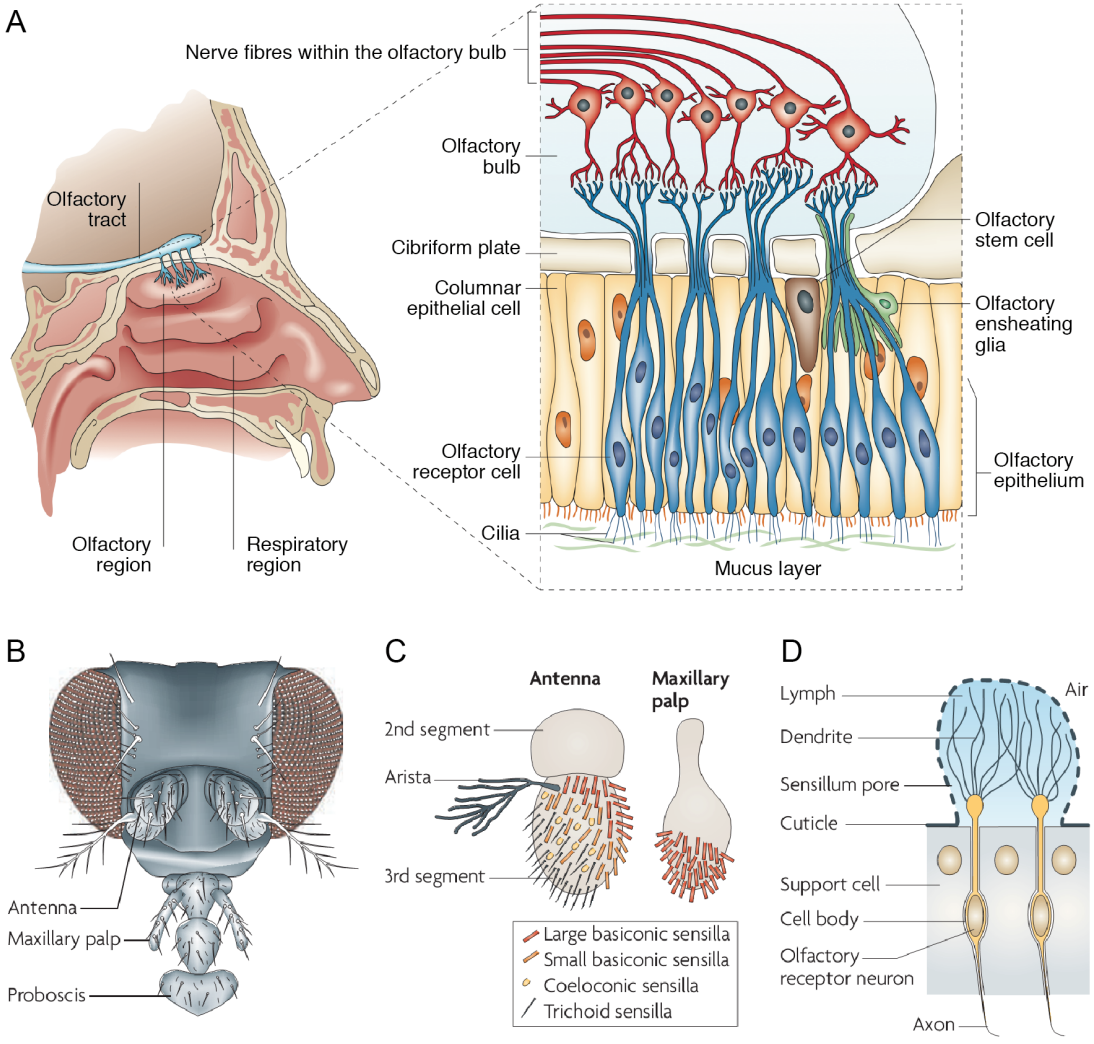

Figure 4.1: Anatomy of the mammal and insect olfactory system. (A) External human nose with the olfactory region in the inner nasal cavity. The olfactory receptor cell is situated in the olfactory epithelium with cilia protruding into the mucous layer. (B) In insects (here *D. melanogaster*), odorant sensing takes place in the maxillary palp and the third segment of the antenna. (C) The sensing areas are covered with three different types of sensilla. (D) One side of the odorant receptor cell extends into the sensillar lymph, while the other end forms an axon that converges into a glomerulus in the antennal lobe. Figure A adapted from ref. [169]; B, C and D adapted from refs. [170, 171].

receptors (V1R, V2R) and formyl peptide receptors (FPRs) [170]. The human genome contains more than 900 different olfactory receptor genes, two-thirds of which are non-functional (pseudo-genes). In the cilia of the odorant receptor cells, there are located about one million ORs. The surface dimensions of the cilia and accordingly the abundance of odorant receptors correlate with the sensitivity of the reception of smell. For example, the surface area of the human epithelium is estimated to be 10-20 cm^2, in the German shepherd it is approx. 7 m^2. Moreover, the concentration of ORs in dog's epithelium is 100 times higher than in humans, accounting for a much better sense of smell [172, 173].

The anatomy of the insect olfactory system (e.g. *Drosophila melanogaster*) is shown in Figure 4.1B-D. Olfaction takes place in the maxillary palp and the third segment of antennas. These regions are covered with sensory hairs (sensilla). In each sensillum, up to four olfactory receptor cells are located, that are morphologically similar to vertebrate receptor cells. Three kinds of sensilla (basiconic, coeloconic and trichoid) are discriminated according to their morphology and semiochemicals to which they respond. One side of the neuron extends into the sensillar lymph, while the other end forms an axon that converges into a glomerulus in the antennal lobe. Contrary to vertebrate olfactory receptor cells that contain only one type of OR, insect neurons host between two and four different receptors [170]. Whereas in vertebrates there are five types of chemosensory receptors, for insects three kinds were identified so far: general ORs that are unrelated to vertebrate ORs, gustatory receptors for the sense of taste and ionotropic receptors [170, 174].

The structure of ORs and signal transduction have been found to be fundamentally different for vertebrates and insects. Mammal ORs were first identified by Buck and Axel (Nobel Prize 2004) to be members of the superfamily of G protein-coupled receptors (GPCR) with seven membrane spanning domains. Each olfactory receptor cell contains one type of OR, and each OR is sensitive to a limited number of different odorants [19]. Cavities at the surface of ORs constitute potential binding sites for odorant binding proteins. Variations of binding sites allow the identification of a wide range of odorant classes. Odorant binding proteins (OBPs) help the predominantly hydrophobic odorants to get in contact with ORs located in the olfactory epithelium.

In mammals, binding of an odorant molecule to an OR induces the activation of a G protein signal cascade (see Figure 4.2A). Activation of the stimulatory G protein,

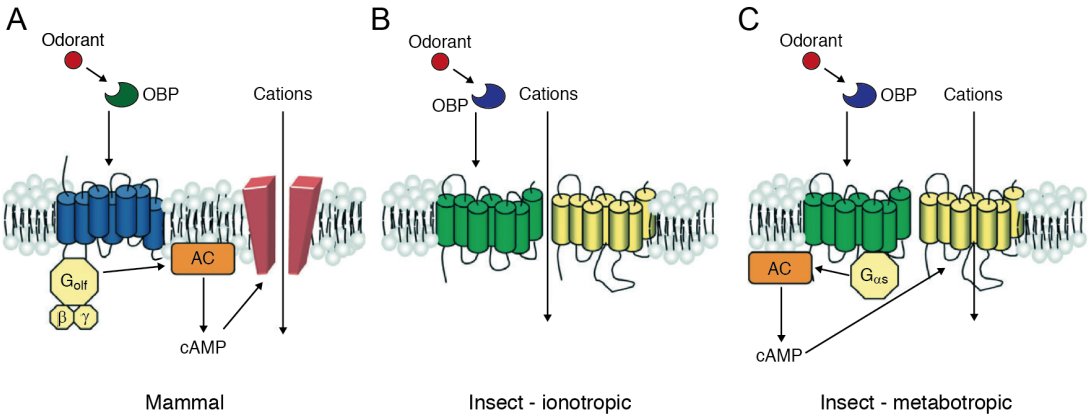

Figure 4.2: Models of signal transduction mechanisms in mammal and insect ORs. (A) Mammal ORs respond to odorant binding with a second messenger cascade that opens an off-site ion channel, leading to the polarization of the neuron. (B) In the ionotropic hypothesis for insects, Orco (yellow) acts as an odorant-gated ion channel that is directly opened by odorant binding. (C) In the alternative, metabotropic hypothesis, the ligand binding subunit (green) starts a cAMP cascade, that opens the CNG-like Orco ion channel. Figure adapted from ref. [175].

G_{olf} activates adenylate cyclase (AC), which increases the intracellular level of second messenger proteins (cyclic 3,5-adenosine monophosphate, cAMP; cyclic 3',5'-guanosine monophosphate, cGMP). Rising concentrations of the second messenger open the gated ion-protein channel (cyclic nucleotide-gated, CNG channel) that regulates the passage of extracellular inorganic ions (Na^+, Ca^{2+}), thus producing an action potential that travels down the axon to the brain [19, 170].

Adaptation and recovery are important processes of receptors. In the olfactory system, short- and long-term adaptation is achieved by changes of the cation concentration to adjust the sensitivity after completion of the response. Receptor recovery meaning response termination takes place at multiple phases of the signaling pathway. Mechanisms for recovery include phosphorylation of the odorant receptor, AC-inhibition or cAMP-hydrolysis [170].

Insect ORs share no structural homology with vertebrate ORs. The receptors contain seven transmembrane domains with an inverted topology as compared to conventional GPCRs, exhibiting a cytoplasmatic N-terminus and an extracellular C-terminus, as indicated in Figure 4.2 [167]. These heteromeric odorant receptors consist of a

binding unit and a well conserved coreceptor (Odorant receptor coreceptor, Orco).

After entering the sensillar lymph through pore tubules, odorants bind to odorant binding proteins. The OBP-odorant complex moves through the sensillar lymph and either directly activates the receptor (LUSH from *D. melanogaster*) or releases the odorant to the receptor (moth and mosquito OBP) [168]. The functionality and purpose of OBPs are not fully resolved yet, but they are thought of as a carrier that conveys the odorant to the receptor. For one particular OBP, LUSH from *D. melanogaster*, there exists evidence that the OBP-odorant complex itself activates the receptor [176]. In the current understanding, Orco acts as an odorant-gated ion channel that generates a fast and short hyperpolarization of the membrane [170, 174]. This ionotropic signaling is capable of providing a more direct and faster response to odorant sensing than the cAMP pathway, that may be necessary for the enhanced requirements of insects [177]. However, there is growing evidence, that Orco also can act as an metabotropic receptor and responds to cAMP that generates a slower but more prolonged sensing signal [178].

Since many insects depend on their olfactory sense for navigation, fast and sensitive detection of rapidly changing odorant concentrations requires a mechanism for signal inactivation. There are two proposed pathways for signal termination. It has been suggested that there is a scavenger molecule or molecular trap that inactivates stray odorant molecules [179]. However, this proposition lacks experimental evidence so far. A more profoundly documented and widely accepted hypothesis states that surplus odorants are inactivated by odorant degrading enzymes in the antenna [180–182].

1.4.2 Odorant Binding Proteins

OBPs are abundant small proteins found in the olfactory epithelium of vertebrates and the sensillar lymph of insects. Vertebrate OBPs belong to the superfamily of lipocalins and predominantly feature 8 antiparallel β-sheets forming a β-barrel structure, flanked by a α-helix at the C-terminus of the polypeptide chain, constituting a homodimer (see Figure 4.3A). This structure provides a hydrophobic binding pocket that can bind ligands at a size of 10-20 carbon atoms [19, 182]. Vertebrate OBPs have been investigated by FTIR spectroscopy to study the effects of odorant binding on thermal stability of the proteins [21–24]. These studies reported thermal stability of up to 85 °C, which is attributed to the stable β-barrel structure. An increased thermal stability has

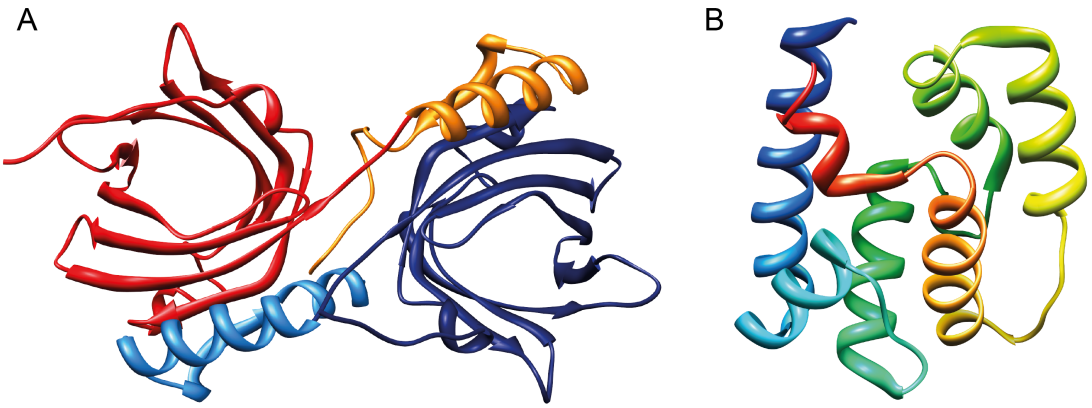

Figure 4.3: Examples for the secondary structure of mammal and insect OBPs. (A) Homodimeric structure of bovine OBP, with each monomer featuring a β-barrel (red, blue), similar to that of lipocalins. The α-helix (orange, light blue) of each monomer stacks against the β-barrel of the other monomer [183]. (B) OBP14 of the honey bee possesses a compact structure, mostly consisting of α-helical domains.

been observed after ligand binding and has been explained by the stabilizing effects of hydrophobic interactions and hydrogen bonds in the OBP-odorant complex.

The structure [184] and amino acid sequence [185] of insect OBPs are fundamentally different. OBPs of insects are classified in pheromone binding proteins, general odorant binding proteins and antennal specific proteins [182]. They are small acidic proteins ($\sim$13-16 kDa) with a three dimensional structure comprising α-helical domains that form a conical shaped cavity for odorants, as shown in Figure 4.3B [182]. Contrary to vertebrate OBPs that attach to the ligand as dimers, insect OBPs interact with the odorant as monomers. A further mutual structural motif among insect OBPs are the interlocked disulfide bridges. According to the number of Cys residues and disulfide bridges, OBPs are grouped into classical OBPs (6 Cys, 3 disulfide bridges), C-plus OBPs (6+2/3 Cys, 3 disulfide bridges), C-minus OBPs ($<$6 Cys, 2 disulfide bridges), and atypical OBPs ($\geq$6 Cys, 3 disulfide bridges) with a longer C-terminus, which are only found in blood sucking insects [186].

The functional role of OBPs for olfaction is not fully resolved yet. High concentrations (10 mM) of OBPs in olfactory dendrites and the high abundance of OBPs in the genome indicate important contributions [182, 187]. One proposed and meanwhile widely accepted hypothesis describes OBPs as a carrier for hydrophobic odorant

molecules through the aqueous mucus to the membrane, that holds the odorant receptor cells [168, 182]. There, the OBP-odorant complex either directly activates the OR or releases the odorant to interact with the OR [168]. Further potential functions may involve quenching high odorant concentrations before they cause long term receptor desensitation [188] as well as removing utilized odorants for degradation, thus enabling other odorant molecules to interact with the OR [19, 182].

1.4.3 Odorant Binding Protein 14 of the Honey Bee

The genome of the honey bee (*Apis mellifera* L.) comprises 21 OBPs [189], 13 of which are classified as classic OBPs (OBP1-13) as well as seven C-minus OBPs with four Cys residues (OBP15-21). OBP14, also a member of the C-minus class, features five cysteines. It has been identified in different tissues of adult bees, as well as in larvae [190]. OBP14 has 119 amino acid residues with a molecular weight of 13.5 kDa [191]. Typical for insect OBPs, its three dimensional structure is predominantly α-helical, with 6 helices forming the core structure of the protein. A notable feature of OBP14 is a 7^{th} α-helix at the C-terminus (see Figure 4.3B). In the protein core, a hydrophobic cavity with a volume of 415 Å^3 has been observed, that is suggested to be the binding site for odorants [191]. Using binding fluorescence studies, affinities of various odorants to OBP14 were determined. Citralva and eugenol were identified as high-affinity odorants, whereas geraniol showed lower affinity [190, 191]. The structural similarity of eugenol to 4-hydroxy-3-methoxycinnamyl alcohol, a component of queen the mandibular pheromone, may explain its high affinity to OBP14. IR and CD investigations of OBP14 confirm the predominantly α-helical structure of the protein [192]. In thermal denaturation experiments, transitions in the IR bands are observed around 55 °C, indicating a lower thermal stability than vertebrate OBP. In the presence of ligands, an increase of the denaturation temperature of up to 10 °C was found, attributed to stabilizing effects of non-covalent interactions between OBP14 and the odorant molecule.

II Publications

II. PUBLICATIONS

Phase Sensitive Detection in Modulation Excitation Spectroscopy applied to potential induced electron transfer in Cytochrome *c* Oxidase

Andreas Schwaighofer,[a] *Shelagh Ferguson-Miller,*[b] *Renate L.C. Naumann,*[a] *Wolfgang Knoll,*[a] *and Christoph Nowak*[a,c,*]

[a]Austrian Institute of Technology GmbH, AIT, Donau-City Str. 1, 1220 Vienna, Austria

[b]Biochemistry & Molecular Biology, Michigan State University, East Lansing, MI 48824, USA

[c]Center of Electrochemical Surface Technology, CEST, Viktor-Kaplan-Straße 2, 2700 Wiener Neustadt, Austria

*Corresponding Author; E-mail: c.nowak@ait.ac.at

ABSTRACT

Cytochrome *c* oxidase (C*c*O) from *R. sphaeroides* was investigated by Modulated Excitation Surface-Enhanced IR-Absorption Spectroscopy (ME-SEIRAS). Sequential electron transfer (ET) within C*c*O was initiated by electrochemical excitation. During modulated excitation by periodic potential pulses with frequencies between 20 Hz and 500 Hz, time-resolved IR spectra were measured by the Step-Scan technique with time-resolution in the millisecond time range. Conformational changes of the protein structure as a result of ET lead to rather complex SEIRA spectra with many overlapping bands embedded in a broad background signal. Phase sensitive detection (PSD) was used to separate single components within the broad band of overlapping structural bands in the amide I region. PSD is able to extract the periodic response of single components with the same frequency as the excitation from noise or from static background and therefore enhances the signal-to-noise ratio. Moreover, PSD enables validation of the fit model utilized for the deconvolution of overlapping bands by analyzing phase lags of single components acquired at different stimulation frequencies. Phase lags between the evaluated vibrational components and the modulated excitation increase with increasing excitation frequencies, which is an inherent prerequisite of this evaluation method.

Index headings: FTIR; Fourier transform infrared spectroscopy; SEIRAS; Surface-enhanced infrared-absorption spectroscopy; PSD; Phase sensitive detection; C*c*O; Cytochrome *c* oxidase; Band deconvolution; Modulation spectroscopy.

INTRODUCTION

Phase Sensitive Detection (PSD) had been found to be a very effective technique for sensitivity enhancement in combination with modulation spectroscopy. In the present work, modulated excitation Fourier transform infrared (ME-FTIR) spectroscopy is performed on C*c*O and the sequential ET within the protein is initiated by electrochemical excitation.[1,2] This method offers the possibility of modulating the excitation signal and measuring FTIR spectra in a large frequency range, particularly when used in combination with the Step-Scan technique. In earlier works, it has been demonstrated that the induced electron reaction is reversible and therefore suitable for modulated excitation experiments.[2] Conformational changes in protein secondary structure as a consequence of ET lead to SEIRA spectra with many overlapping bands embedded in a broad background signal. The goal of this work is to identify significant components within the amide I region using phase sensitive detection (PSD).[3,4] This method selectively highlights periodically changing signals stimulated by an external parameter, such as temperature,[5,6] pH,[4,7] concentration,[8,9] electric field,[10,11] pressure,[12] mechanical force,[13] radiant power[14] or absolute configuration.[15,16] PSD acts as a software lock-in amplifier and can be used in ME-FTIR spectroscopy without the need of any additional expensive hardware.[3,5] It can be applied offline after that the spectra have been obtained, which avoids complicated phase corrections and shortens the measuring time during data acquisition. Application of PSD converts the recorded tr-absorbance spectra into phase-resolved spectra and thereby (i) suppresses almost all frequency components of the noise and any constant background absorption and (ii) permits the selective detection of signals that show the same frequency as the stimulation. The resulting background compensation and the signal-to-noise ratio (SNR) are considerably better than those obtained by conventional difference spectroscopy. In particular, the characteristic increase of the phase lag with increasing excitation frequency permits the exclusive identification of components affected by

stimulation. Due to this inherent validation, spectra evaluation by PSD is considered to be more confident than evaluation by first-order derivatives or Fourier self-deconvolution (FSD), that significantly depends on the operator choice of two parameters.[5]

Fourier transform infrared (FTIR) spectroscopy has been proven as a powerful method for investigating protein dynamics. With its high sensitivity and characteristic marker bands for many molecules, IR spectroscopy provides a label-free environment for the investigation of molecular interaction and structural changes. In particular, time-resolved (tr-FTIR) methods promise to elucidate structure-function relationships even of large multi-redox center proteins such as the cytochrome *c* oxidase (C*c*O).[17-26] C*c*O is the fourth complex in the respiratory chain and is well characterized by FTIR methods; hence it poses an excellent model system for the present work. Our group established a method to immobilize membrane proteins in a biomimetic membrane system on an ATR crystal coated with a two-layer gold surface.[27] Incorporation of the protein in this protein-tethered bilayer lipid membrane (ptBLM) enables its investigation in a biomimetic environment that corresponds as closely as possible to the biological plasma membrane.[28] Direct electron injection into C*c*O has been shown to result in electron transfer (ET) along Cu_A/heme *a*/[heme a_3-Cu_B], the natural sequence of redox centers in the cytochrome *c* oxidase.[29] Induced electron transfer into C*c*O by electrochemical excitation has been investigated by fast-scan voltammetry and potentiometric titration followed by surface-enhanced IR-absorption spectroscopy (SEIRAS).[1,2,30] Employing electrochemical excitation, modulation can be achieved by application of periodic potential pulses, thus permitting a large variety of modulation amplitudes and frequencies.

The aim of this work is to demonstrate the convenient application of Phase Sensitive Detection to the amide I band in the FTIR spectrum of C*c*O to identifiy structural components that are involved in electron transfer through this large electron complex. To the best of our knowledge, PSD has been applied to this extent only to relatively small and simple molecules and proteins before.

EXPERIMENTAL SECTION

Solvents and Chemicals. Purified water was obtained from a Sartorius-Stedim system (Göttingen, Germany) with a resistivity of 18 MΩ cm. Argon (purity: 4.8) and oxygen (techn.) gas were obtained from Linde Gas GmbH (Stadl-Paura, Austria). Bio-Beads (20-50 mesh) were purchased from Bio-Rad Laboratories GmbH (Munich, Germany). 1,2-diphytanoyl-*sn*-glycero-3-phosphocholine (DiPhyPC, >99%) was provided by Avanti Polar Lipids (Alabaster, AL, US). Dodecyl-*β*-D-maltoside (DDM, ≥98%), was purchased from Sigma-Aldrich (Steinheim, Germany). All chemicals were used as purchased.

Preparation of the two-layer gold surface on the ATR crystal. Preparation of the ATR crystal was done as previously described.[11,27]

Immobilization of the protein. C*c*O was immobilized on the ATR crystal as described in detail.[1]

Cyclic voltammetry and activation of C*c*O. Prior to infrared measurements, up to 80 cyclic voltammetry cycles were performed on the immobilized C*c*O under aerobic conditions to transfer the protein from the inactivated to the activated conformational state.[2,31] Electrochemical measurements were performed with a potentiostat from Autolab (PGSTAT12 with GPES 4.9 from Metrohm, Herisau, Switzerland) in a three-electrode configuration with gold as the working electrode, a Ag|AgCl,KCl_{sat} reference and a platinum wire as the counter electrode. All electrode potentials are quoted versus the standard hydrogen electrode (SHE). Cyclic voltammetry measurements were done in PBS solution (0.05 M K_2HPO_4, 0.1 M KCl, pH 8) flushed with O_2 and with vertex potentials V_1 = +400 mV and V_2 = -800 mV at a sweep rate of 50 mVs^{-1}. As soon as the peak currents acquired constant positions and heights over a couple of cycles, indicating that the protein had been transferred to the activated conformational state,[2] the aerobic solution was exchanged with anaerobic PBS buffer. To establish anaerobic conditions, the PBS solution was flushed with argon for 20 minutes, after

which a chemical oxygen trap consisting of glucose (0.3% w/w), glucose oxidase (75 µg/ml) and catalase (12.5 µg/ml) was added.

ATR-SEIRA-Spectroscopy. The electrochemical cell was mounted on top of a trapezoid single reflection silicon ATR crystal. The IR beam of the FTIR spectrometer (VERTEX 70v, from Bruker, Ettlingen, Germany) was coupled into the crystal at an angle of incidence Θ = 60° by using the custom-made setup described previously.[27] All spectra were measured with parallel polarized light. Because the ATR element surface is coated with an electrical conductor, perpendicularly polarized light is unable to penetrate the conducting layer effectively. The total reflected IR beam intensity was measured with a liquid nitrogen-cooled photovoltaic mercury cadmium telluride (MCT) detector. IR measurements were done under anaerobic conditions at 28 °C. The sample unit was purged with dry, carbon dioxide-free air. FTIR spectra were recorded at 4 cm^{-1} resolution using Blackham-Harris 3-term apodization and a zero filling factor of 2. Due to small sample absorbances of the protein monolayer beside the large absorbance of water, interferograms were measured in double-sided mode and transformed into spectra using the Power phase correction mode. An optical filter (LWP < 2.966 cm^{-1}) was used to reduce the high folding limit to 3159 cm^{-1} and consequently, the number of necessary interferogram points to 2842. Spectra were analyzed using the software package OPUS 6.5 and OriginLab's Origin software.[32]

Principle of tr-ATR-SEIRA-Spectroscopy triggered by electrochemical potentials. The rectangular waveform used for modulated excitation was provided by a function generator (Agilent 33250A, Santa Clara, CA, US) that triggered the Autolab potentiostat and the spectrometer, as shown in Fig. 1. Potentials were periodically applied to the ptBLM on the gold film in the form of a square wave function to change the redox state of C*c*O from the fully oxidized (+400 mV) to the fully reduced state (-800 mV), as depicted in Fig. 2. Due to the charging of the Au/water interface, the range of potential actually affecting the enzyme lies between +200 mV and -600 mV.[33,34] FTIR measurements were triggered by the fast

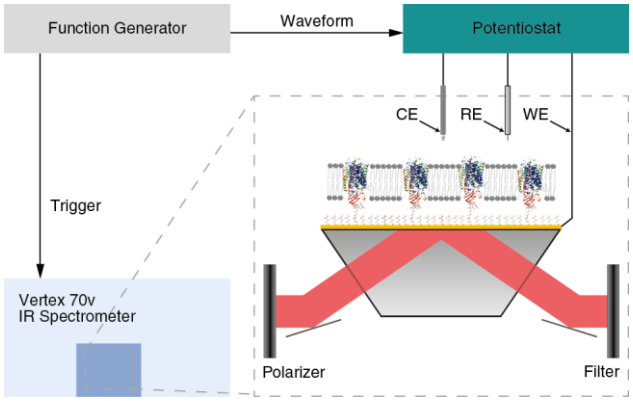

Fig 1. Setup for modulated excitation SEIRAS. The function generator provides the waveform that is applied to the protein layer by the potentiostat. Simultaneously, a trigger signal synchronizes the tr-SEIRAS measurements (CE: counter electrode, RE: reference electrode, WE: working electrode).

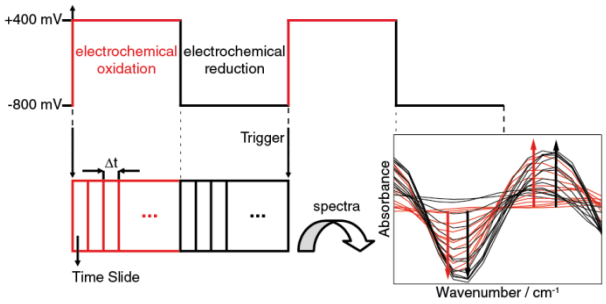

Fig 2. Principle of tr-SEIRAS measurements triggered by potential pulses. The trigger signal synchronizes the Step-Scan IR measurements and the beginning of each excitation period (potential jump from -800 mV to +400 mV). The relation between excitation frequency f, time-resolution Δt and number of time slides N_{TS} is given by $1/f = N_{TS} * \Delta t$.

potential change at the start of each period to record a succession of spectra that indicate changes of IR absorbances as a function of time. Absorbances were calculated using the fully reduced state of the protein as a reference. Spectra were recorded at frequencies of 20 Hz (period = 50 ms, time-resolution = 1000 µs, 30 co-additions.), 50 Hz (20 ms, 400 µs, 75 co-adds.), 100 Hz (10 ms, 200 µs, 150 co-adds.), 250 Hz (4 ms, 80 µs, 370 co-adds.) and 500 Hz

(2 ms, 40 µs, 700 co-adds.). These parameters result in 50 time slides per period for all excitation frequencies.

Principle of Phase Sensitive Detection (PSD). The analytical procedure of phase sensitive detection was applied to time-resolved spectra co-added during excitation cycles. PSD enables background elimination in absorbance spectra by separating the ac and dc components in the system response and by selectively detecting signals that respond t the fundamental frequency ω (i.e. excitation frequency) or higher harmonics.[3,4] PSD can be applied to systems that exhibit a reversible response to an external perturbation. In this study, PSD was used to improve the SNR of the measured spectra by distinguishing the weak system response of the protein monolayer from the large background absorption.

The time-dependent absorbance $A_i(\tilde{\nu},t)$ of all vibrational modes i can be described by Eq. 1,

$$A_i(\tilde{\nu},t) = \sum_{i=1}^{N} \left(A_{i,0}(\tilde{\nu}) + \sum_{k=1}^{\infty} A_{i,k}(\tilde{\nu}) \sin\left(k\omega t + \varphi_{i,k}\right) \right) \tag{1}$$

where k denotes the multiple of the fundamental ($k = 1$ fundamental frequency, $k > 1$ higher harmonics) and $\varphi_{i,k}$ indicates the phase lag of the k^{th} harmonic that is independent of the wavenumber and associated with the vibrational mode i. The left-hand part within the summation bracket corresponds to the stationary overall absorbance (dc-part) and the right-hand part corresponds to the modulated system response (ac-part). The phase-resolved absorbance spectrum $A_k^{\phi^{PSD}}(\tilde{\nu})$ with the operator-controlled phase angle ϕ_k^{PSD} is obtained by multiplication of $A_i(\tilde{\nu},t)$ by e.g. $\sin\left(k\omega t + \phi_k^{PSD}\right)$ followed by a normalized integration over the modulation period T. In this study, only the fundamental frequency ($k = 1$) was used for calculations. Therefore, k is omitted in all subsequent equations, and the phase-resolved absorbance spectrum of the fundamental is reduced to Eq. 2.

$$A^{\phi^{PSD}}(\tilde{\nu}) = \frac{2}{T}\int_0^T A_i(\tilde{\nu},t)\,\sin\left(\omega t + \phi^{PSD}\right)\mathrm{d}t \tag{2}$$

Straightforward calculation leads to Eq. 3, which describes the relation between the calculated phase-resolved spectrum, the searched amplitudes $A_i(\tilde{\nu})$ and the phase lags φ_i of the components i and where $A_i^{\phi^{PSD}}(\tilde{\nu})$ represents the phase-resolved absorbance of the vibrational mode i.

$$A^{\phi^{PSD}}(\tilde{\nu}) = \sum_{i=1}^{N} A_i^{\phi^{PSD}}(\tilde{\nu}) = \sum_{i=1}^{N} A_i(\tilde{\nu})\,\cos\left(\varphi_i - \phi^{PSD}\right) \tag{3}$$

As the absorbance of a single component will later be given by the evaluated peak area of the absorption of its vibrational mode (e.g. by curve-fitting) we can eliminate the dependency of the wavenumber using Eq. 4.

$$A_i = \int A_i(\tilde{\nu})\,\mathrm{d}\tilde{\nu} \tag{4}$$

Using Eq. 3 and 4, the wavenumber-independent phase-resolved absorbance of a vibrational mode i is then given by Eq. 5 as follows:

$$A^{\phi^{PSD}} = A_i\cos\left(\varphi_i - \phi^{PSD}\right) \tag{5}$$

Due to the characteristics of the cosine function, $A_i^{\phi^{PSD}}$ becomes maximum for $\varphi_i = \phi^{PSD}$, meaning that the absorbance of a component with the phase lag φ_i reaches its maximum in the phase-resolved spectrum with $\phi^{PSD} = \varphi_i$. This behavior permits the discrimination of overlapping bands (resulting from the absorbance of different components) in a set of phase-resolved spectra with the prerequisite that the phase lag of the selected bands is different. Therefore, the phase-resolved spectrum with $\phi^{PSD} = \varphi_i \pm 90$ results in zero absorbance for the vibrational mode A_i. A non-zero absorbance at this phase setting originates therefore only from other components.

As seen in Eq. 6, the tr-absorbance of one vibrational mode $A_i(t)$ can be expressed by $A_i^{0°}$ and $A_i^{90°}$, the phase-resolved spectra at $\phi^{PSD} = 0°$ and $\phi^{PSD} = 90°$, respectively

$$A_i(t) = \sum_{i=1}^{N} \left(A_i^{0°} \cos(\omega t) + A_i^{90°} \sin(\omega t) \right) \tag{6}$$

Finally, the amplitude and phase lag of the response of a vibrational mode are given by Eq. 7-9 and can therefore be calculated from the evaluated phase-resolved spectra $A_i^{0°}$ and $A_i^{90°}$.

$$A_i = \sqrt{A_i^{0°2} + A_i^{90°2}} \tag{7}$$

$$\cos(\varphi_i) = \frac{A_i^{0°}}{A_i}, \quad \sin(\varphi_i) = \frac{A_i^{90°}}{A_i} \tag{8}$$

$$\varphi_i = \arctan\left(\frac{A_i^{90°}}{A_i^{0°}}\right) \tag{9}$$

As depicted in Fig. 3, Eq. 8 can be combined to Eq. 9. However, because the result of the arctan function is only defined to be within -90° and 90°, the phase lags in the range of 0°–360° must be determined from Eq. 8 as reported by Baurecht et al..[3] We further assume the kinetic approach of Fringeli et al.,[4] which accounts for a reversible first-order reaction, whose rate constant is considered to change as a function of the magnitude of the excitation parameter. As a result, the relationship between the phase lag and the excitation frequency f is given by Eq. 10,

$$\tan(\varphi) = -2\pi f \tau_m \tag{10}$$

with the relaxation time τ_m.

Curve-fitting of PSD spectra. Curve-fitting of phase-resolved spectra was performed with OriginLab's Origin software[32] using the Levenberg-Marquardt algorithm and Lorentzian band shapes. In order to account for the modulated absorbance changes of abundant water molecules in the electric field, a H_2O-bending band ($\delta(H_2O)$) was added to the fit model. Therefore, fixed band parameters such as a band position of 1643 cm^{-1} and a full width at half

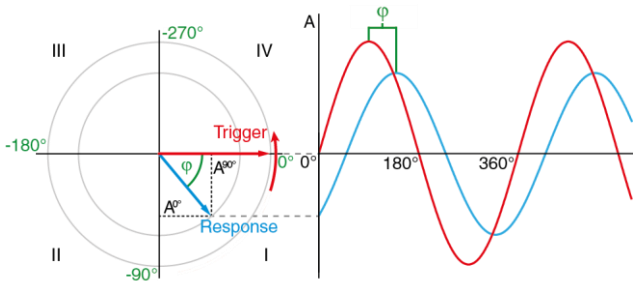

Fig 3. Schematic representation of the relationship between the excitation trigger (red), response signal (blue) and relative phase lag (green). The relative phase lag is indicated in negative digits, because the response exclusively occurs after the excitation. One excitation period is divided into 4 quadrants (roman numerals) in the polar coordinate system and the response vector of first-order reactions can only appear in the first and third quadrants (see text for details).

maximum (FWHM) of 80 cm^{-1}, evaluated from an independently measured spectrum of pure H_2O. The phase lags of the separated components were calculated according to Eq. 9. The corresponding band areas $A_i^{\phi^{PSD}}(\omega)$ were determined by curve-fitting the phase-resolved spectra at $\phi^{PSD} = 0°$ and $\phi^{PSD} = 90°$ of all five excitation frequencies ω. Initial values for band positions and FWHM were estimated by visual inspection of phase-resolved spectra using several different angles ϕ^{PSD}. Due to the high number of free parameters, the upper and lower limits were set in the fitting software to ±2 cm^{-1} for band positions. At this point, all other parameters i.e. FWHM and intensity were allowed to be fitted by the program. This first curve fit of the 10 phase-resolved spectra resulted in a slightly varying number and position of bands for each spectrum. Thus, in the second iteration, only the band positions that occurred in all fitted spectra (±1 cm^{-1}) were considered and averaged for further analysis, also FWHM values were averaged. Prior to the third iteration, bands that did not exhibit an increasing phase lag with increasing excitation frequency were excluded from the data set and the band position and FWHM values of the remaining components were retained. The final fit was

performed by only allowing the band intensity to be fitted. Phase lags calculated using that method are phase lags related to the trigger signal.

RESULTS AND DISCUSSION

C*c*O from *Rhodobacter sphaeroides* was immobilized on a two-layer gold film[27] deposited on an ATR crystal and reconstituted into a protein-tethered bilayer lipid membrane (ptBLM). The enzyme was then transferred to its activated state by several cyclic voltammetry cycles. SEIRA spectra were acquired under strictly anaerobic conditions in the Step-Scan mode by applying periodic potential pulses stepping between -800 mV to +400 mV. As it has been shown previously,[25,35] electron transfer within C*c*O occurs in the millisecond time scale. In this work, excitation frequencies in the range from 20 to 500 Hz and time-resolutions in the millisecond time range were used. This ensures best conditions to detect changes of vibrational components involved in this process by PSD. Each excitation frequency was measured with a new sample of C*c*O reconstituted into the ptBLM system. Tr-SEIRA spectra obtained after baseline correction (Fig. 4a) featured a broad band in the amide I region, similar to the prominent bands obtained previously in potentiometric titration experiments followed by SEIRAS.[2] In titration spectra, band analysis with Two-Dimensional (2D) spectra proved to be successful. However, in tr-SEIRAS, the spectra contained many more overlapping bands in addition to a high level of noise as seen in Fig. 4a. For further analysis and band deconvolution, phase-resolved spectra were calculated at different phase settings ϕ^{PSD} (Fig. 4b). The reduction of the noise in the PSD spectrum is immediately visible, because static signals as well as noise, that are not correlated to the modulation frequency, have been eliminated. This kind of noise reduction illustrates the advantage of PSD to other spectra evaluation techniques e.g. two-dimensional correlation spectroscopy, where static background and noise may distort the correlation spectra and therefore lead to inaccurate band assignments.[36,37]

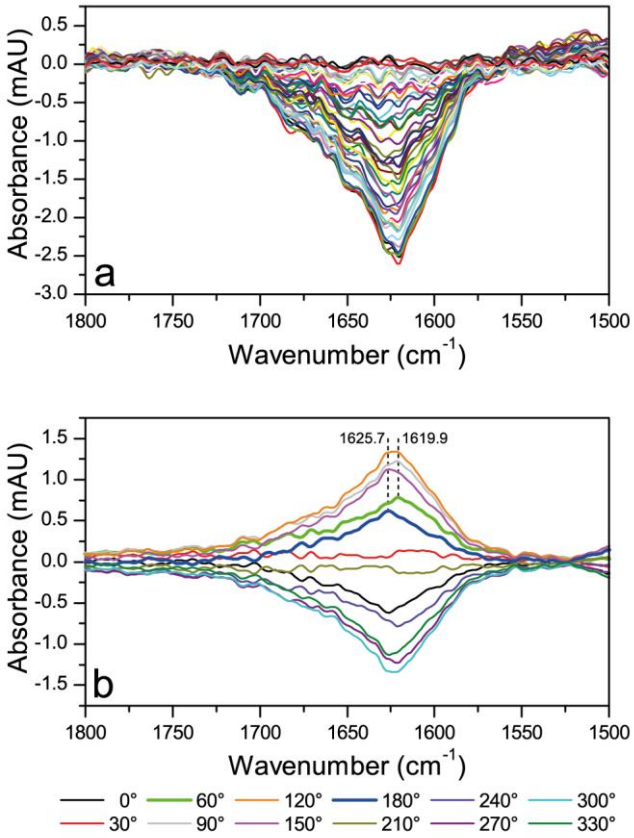

Fig 4. (**a**) Time-resolved and (**b**) phase-resolved FTIR-ATR absorbance spectra of the amide I region recorded with a modulation frequency of 100 Hz. The absorbance of the amide II band of the immobilized proteins was 2-2.5 mAU. (**a**) Tr-absorbance spectra were calculated using the fully reduced spectrum (first time slide) as reference. All 49 absorbance time slides are shown. (**b**) Phase-resolved spectra of the fundamental frequency with ϕ^{PSD}= 0,30,…,330°. The presence of different vibrational components at a certain wavenumber is indicated by a change of the band shape at different phase angles. Considering the bands at 1619.9 cm^{-1} and 1625.7 cm^{-1}, the absorbance of the first band is more pronounced at the phase angle of 60° (bold green line), while the absorbance of the latter band is more prominent at a phase angle of 180° (bold blue line).

The significant change in shape of the phase-resolved spectra at different phase angles clearly indicates the presence of several vibrational components with different phase lags, as outlined in the experimental section. Considering the bands at 1619.9 cm^{-1} and 1625.5 cm^{-1} in Fig. 4b, the absorbance of the first band is more prominent at the phase angle of 60° (bold

green line), whereas the absorbance of the latter band is more pronounced at a 180° phase angle (bold blue line). Even though the improved SNR reveals a large number of potential analytical bands, the selection of the valid vibrational bands was exclusively accomplished by evaluation of the progression of phase lags with increasing excitation frequencies as discussed further below.

Only the spectral features of the amide I region that is known to be particularly sensitive for conformational changes in proteins[38] were used for evaluation of vibrational components by PSD in the present study. The relative phase lags of the single components were calculated according to Eq. 9 after curve fitting the 0° and 90° phase-resolved spectra. A representative curve fit is shown in Fig. 5a. In the course of the incremental fitting procedure, it became apparent that water molecules also respond to the modulated excitation. Numerous FT-IR studies of proteins were conducted in D_2O rather than in H_2O in order to avoid interference of the H_2O bending band with the amide I band. However, it was reported that exposure of proteins to D_2O leads to changes in structure[39] such as altered salt bridges[40] and protein denaturation,[41,42] as well as changes in their function,[43] particularly in proteins with internal electron transfer.[44,45] Consequently, present measurements were carried out in aqueous buffer solution rather than D_2O buffer elsewhere used for FTIR investigations of proteins. Considering that the water molecule represents a strong dipole, small changes in orientation may have a significant impact on the IR spectrum. Effects on water bands by potential changes have been reported previously.[46,47]

Subtraction of H_2O bending bands in FTIR-spectra of proteins by the user is delicate, because it is prone to personal bias and uncertainty.[48] We believe that water subtraction by PSD is superior in this respect, because it is rather objective and free from the operator's judgement. For evaluation with PSD, water is treated as a species that responds to the potential modulation, and a fixed parameter set obtained by static IR measurements was included in the

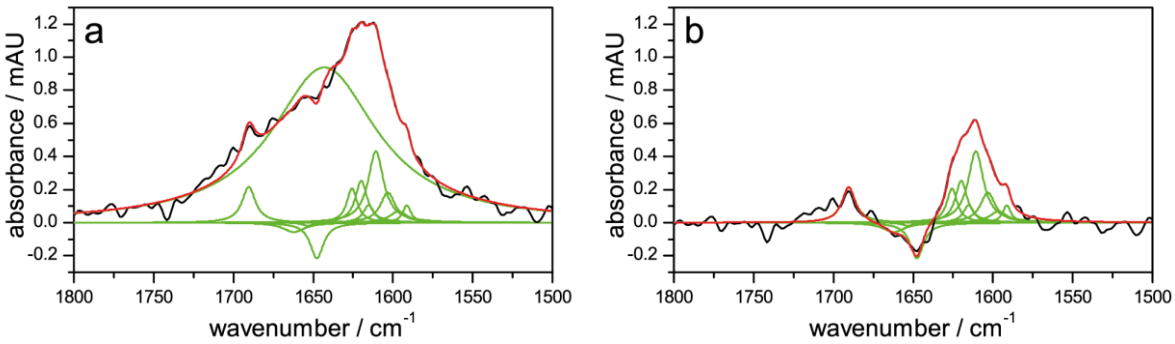

Fig 5. Curve fit of the 90° phase-resolved spectrum recorded with a modulation frequency of 20 Hz (**a**) with and (**b**) without the fitted water band (black: phase-resolved spectrum, green: curve-fitted vibrational components, red: sum of fitted components). The broad band in (**a**) with a maximum at 1643 cm^{-1} has been tentatively assigned to the H_2O-bending band. Positive and negative components within one phase-resolved spectrum appear when phase lags of the components are different in the range of 180°, e.g. one component increases and the other component decreases with increasing excitation parameter. In the region between 1700 cm^{-1} and 1750 cm^{-1}, bands could be fitted at certain phase-resolved spectra, but were excluded from the final parameter set because they did not show an increasing phase lag with increasing excitation frequencies.

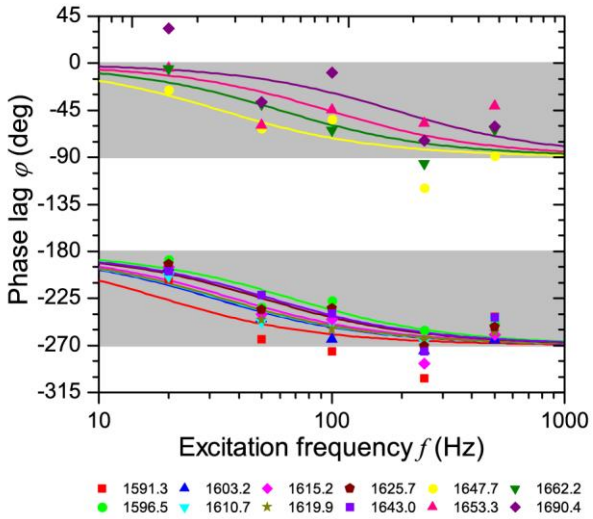

Fig. 6. Evaluated phase lags of the separated vibrational components in the amide I region. The lines indicate the progression of the phase lag with increasing excitation frequency by fitting the Eq. 10 to the data points. Grey areas indicate the first (0° – -90°) and third (-180° – -270°) quadrant as depicted in Fig. 3.

fitting procedure to account for the H_2O-bending band ($\delta(H_2O)$). As shown in Fig. 6, it shows the same phase lag increase as the other identified components.

The origin of the H_2O-bending band is assumed to be the water molecules in the submembrane space (i.e. the space between the membrane and the crystal) provided by the linker molecule in the ptBLM system.[1] The high absorbance of the H_2O-bending band in the ME-SEIRA spectra can be explained by an inherent characteristic of SEIRAS as the intensity of the surface-enhanced field in SEIRAS experiments decreases with the 6^{th} power of the distance from the crystal.[49] Therefore, vibrations of groups in the immediate vicinity of the ATR crystal yield a higher absorbance than vibrations of groups situated further away (at the same concentration of absorbing groups).

Subtraction of the $\delta(H_2O)$ band by PSD facilitates the evaluation of the absorbance of the components as shown in Fig. 5b in an example of the final fit result obtained from the 90° phase-resolved spectrum with a modulation frequency of 20 Hz. Fig. 5b clearly shows the low level of noise in the 10^{-4} AU range as compared to the absorbance of components. Positive and negative components in a phase-resolved spectrum indicate that phase lags of the components are different in the range of 180° e.g. positive bands in the 0° phase-resolved spectra indicate that the band increases at the first excitation half-period, a negative band in the 0° phase-resolved spectra indicates a decrease, respectively. The phase lag, however, can only be determined by considering both, the 0° and 90° phase-resolved spectra according to Eq. 9. The phase lags of the vibrational components as a function of the excitation frequency are shown in Fig. 6. Theory predicts that (i) phase lags of the vibrational components increase with increasing excitation frequency, (ii) phase lags are located within the first and the third quadrant for the response of first-order reactions to modulated excitation and (iii) phase lags should be different for individual vibrational components. Only the components matching all of these criteria were considered significant. In addition to criterion (ii), since the response signal cannot increase while the excitation signal decreases, the phase lags cannot lie within

the second and fourth quadrants. Components with phase lags in the third quadrant are in anti-phase compared to components in the first quadrant. At this point, it should be emphasized that due to the presence of the gold film evaporated on the ATR crystal, only the component of the transition dipole moments perpendicular to the metal surface can be detected.[50] Therefore, only changes in absorbance of vibrational modes with such components are observed. From Fig. 6, we can deduce that the phase lags are different for the individual vibrational components, as requested in (iii). In order to resolve individual vibrational components within an overlapping absorption band, it is essential that the difference in their phase lags is large. At relatively low frequencies, the difference of the phase lags is rather small, since all components (which have themselves faster reaction rates than the trigger) are able to respond immediately to the trigger. Therefore the amplitude of the changes is large in this frequency range. When the excitation frequencies become too high, the modulation amplitude decreases and all phase lags originating from the stimulation parameter end up at the same phase lag. Thus there is always an optimum frequency range where phase lags become maximum in modulated excitation experiments.[4] This is in good agreement with the data shown in Fig. 6, where the largest difference of phase lags is between 50 – 250 Hz, with smaller differences at lower and higher excitation frequencies. Accordingly, the optimum frequency range for band separation in the measurements was deduced to be between 50 – 250 Hz. Finally, vibrational components were identified and associated band parameters were collected in Table 1.

Although the primary aim of this work is to show the prospects of band separation by PSD, as a first insight into the kinetics of conformational changes, a fit for the progression of the obtained phase lags of every component with increasing excitation frequency is included in Fig. 6. The relation given in Eq. 10 only applies to a first-order reaction.[4] Since conformational changes due to electron transfer along redox centers exhibit kinetics of a

Table 1. Band parameters calculated by the fitting procedure and tentative band assignments of the evaluated vibrational components. (Numeration of the amino acid side chains refers to C*c*O from *Paracoccus denitrificans*). Band positions were allowed to vary within the margin of $\pm 1 cm^{-1}$.

Experimental		Literature			
band position [cm^{-1}]	FWHM [cm^{-1}]	band position [cm^{-1}]	redox center	tentative band assignment	Ref.
1591.3	6.2	1592	Cu_A	H, HisH; ν(C═C); H224, H181/R, Arg-H_5^+; $\nu_{as}(CN_3H_5^+)$; R473/D; Asp-COO^-; $\nu_{as}(COO^-)$; D178	51
1596.5	13.4	1594	heme *a*	His	52
1603.2	11.3	1603	Cu_A	amide I (β-sheet); ν(C═O)	51
1610.7	11.7	1606	heme *a*	ν(C═O) CHO heme *a*; ν_7 heme *a*; ring O^- Tyr	52
1615.2	8.1	1637-1613	---	amide I (β-sheet)	53
1619.9	9.1	1618	heme a_3	Y, Tyr-OH; ν(CC) ring; δ(CH); Y280/W; ν(CC), ν(C═C); W272, W164/vinyl; ν(C-C) /amide I (β-sheet), ν(C═O)	51
		1618	heme *a*/ heme a_3	$\nu(C_\alpha{=}C_\beta)$ vinyl group (heme a/a_3); amide I (β-sheet)	52
1625.7	8.0	1630	heme a_3	R, Arg-H_5^+; $\nu_s(CN_3H_5^+)$; R473/H, $HisH_2^+$; ν(C═C); H403/formyl; amide I (β-sheet); ν(C═O)	51
1643.0	80.0	1645	---	δ(HOH)	54
1647.7	10.1	1651	Cu_A	amide I (α-helical); ν(C═O)	51
1653.3	8.0	1655	heme a_3	amide I (α-helical); ν(C═O)	51
		1656	heme a_3	amide I (α-helical)	52
1662.2	16.4	1661	heme *a*	amide I (α-helical), ν(C═O)/amide I, turns; ν(C═O)	51
		1662	heme *a*/ heme a_3	ν(C═O) CHO-heme a_3; amide I (α-helical); $\nu_{as}(CN_3H_5)$ Arg	52
1690.4	10.3	1689	Cu_A	amide I (β-sheet); ν(C═O)	51

higher order, in our study, Eq. 10 can only give a rough estimate of the phase lag progression with increasing excitation frequency. Nevertheless, some conclusions can be derived from that. For example, the band at 1690.4 cm^{-1} in the first quadrant exhibits the smallest phase lag. This band can be assigned to the C=O stretching vibration, characteristic for β-sheets and has been tentatively attributed to changes in the Cu_A-redox center. Because this redox center is the first in the native electron pathway within the C*c*O, it is conceivable that Cu_A is reduced by

the electrochemical excitation prior to the ensuing redox centers. Moreover, increased flexibility of the β-sheet region has been shown by computational methods,[55,56] and has been confirmed by deuterium exchange analysis.[57] In the third quadrant, the band at 1596.5 cm^{-1} is the vibrational component with the lowest phase lag. This band has been assigned to one of the histidine residues of the porphyrin ring of heme *a*, which is the second electron center in C*c*O and the direct successor of Cu_A. Within the margin of error, the band with the next higher phase lag is the band at 1643.0 cm^{-1},which has been assigned to water. The H_2O-bending band is expected to have a small phase lag, because it is a small molecule and does not participate in protein dynamics.

CONCLUSION

In the present study, C*c*O was stimulated by modulated electrochemical excitation while simultaneously performing SEIRAS in the Step-Scan mode. Overlapping structural bands in tr-SEIRA spectra were deconvoluted and separated from large background noise by rigorous application of the analytical procedure of PSD. Hence, enhancement of SNR permitted the identification of vibrational components in the amide I region. Crucial in this context has been the elimination of the large water band present beneath the amide I band. Evaluation of phase lags revealed the characteristic increase with increasing excitation frequency. This inherent validation proved PSD to be superior to other band-identification techniques such as FSD or first-order derivative which depend significantly on the operator choice of initial parameters, while evaluation by PSD is based on standard analytical procedures and validated by theoretical constraints. The bands assigned to secondary structures can also be attributed to specific redox centers. After application of PSD to tr-SEIRA spectra of cytochrome *c*[11] and C*c*O, our group showed that this method is an excellent tool for band deconvolution and identification of modulated-excitation FTIR spectra. Further analysis of tr-SEIRA spectra of C*c*O with respect to redox kinetics will be presented in the near future.[34]

ACKNOWLEDGEMENTS

We gratefully acknowledge the invaluable advice and assistance of Prof. Dieter Baurecht, Institute of Physical Chemistry, University of Vienna, Austria. Partial support for this work was provided by ZIT, Center of Innovation and Technology of Vienna.

REFERENCES

1. C. Nowak, D. Schach, J. Gebert, M. Grosserueschkamp, R.B. Gennis, S. Ferguson-Miller, W. Knoll, D. Walz, R.L.C. Naumann. "Oriented immobilization and electron transfer to the cytochrome c oxidase". J. Solid State Electrochem. 2011. 15(1): 105-114.
2. C. Nowak, M.G. Santonicola, D. Schach, J. Zhu, R.B. Gennis, S. Ferguson-Miller, D. Baurecht, D. Walz, W. Knoll, R.L.C. Naumann. "Conformational transitions and molecular hysteresis of cytochrome c oxidase: Varying the redox state by electronic wiring". Soft Matter 2010. 6(21): 5523-5532.
3. D. Baurecht, U.P. Fringeli. "Quantitative modulated excitation Fourier transform infrared spectroscopy". Rev. Sci. Instrum. 2001. 72(10): 3782-3792.
4. U.P. Fringeli, D. Baurecht, H.H. Günthard. "Biophysical Infrared Modulation Spectroscopy". In: H. U. Gremlich and B. Yan, editors. Infrared and Raman Spectroscopy of Biological Materials New York: Marcel Dekker, 2001. pp. 143-192.
5. D. Baurecht, I. Porth, U.P. Fringeli. "A new method of phase sensitive detection in modulation spectroscopy applied to temperature induced folding and unfolding of RNase A". Vib. Spectrosc. 2002. 30(1): 85-92.
6. M. Muller, R. Buchet, U.P. Fringeli. "2D-FTIR ATR spectroscopy of thermo-induced periodic secondary structural changes of poly-(L)-lysine: A cross-correlation analysis of phase-resolved temperature modulation spectra". J. Phys. Chem. 1996. 100(25): 10810-10825.
7. M. Bieri, T. Burgi. "L-Glutathione chemisorption on gold and acid/base induced structural changes: A PM-IRRAS and time-resolved in situ ATR-IR spectroscopic study". Langmuir 2005. 21(4): 1354-1363.

8. T. Burgi, A. Baiker. "In situ infrared spectroscopy of catalytic solid-liquid interfaces using phase-sensitive detection: Enantioselective hydrogenation of a pyrone over Pd/TiO2". J. Phys. Chem. B 2002. 106(41): 10649-10658.

9. D. Baurecht, G. Reiter, N. Hassler, M. Schwarzott, U.P. Fringeli. "Application of Special FTIR ATR Techniques for Quantitative Structural Analysis of Thin Surface Layers". Chimia 2005. 59226-235.

10. M. Schwarzott, P. Lasch, D. Baurecht, D. Naumann, U.P. Fringeli. "Electric field-induced changes in lipids investigated by modulated excitation FTIR spectroscopy". Biophys. J. 2004. 86(1): 285-295.

11. C. Nowak, C. Luening, D. Schach, D. Baurecht, W. Knoll, R.L.C. Naumann. "Electron Transfer Kinetics of Cytochrome C in the Submillisecond Time Regime Using Time-Resolved Surface-Enhanced Infrared Absorption Spectroscopy". J. Phys. Chem. C 2009. 113(6): 2256-2262.

12. I. Noda, G.M. Story, C. Marcott. "Pressure-induced transitions of polyethylene studied by two-dimensional infrared correlation spectroscopy". Vib. Spectrosc. 1999. 19(2): 461-465.

13. Q. Wu, X. Lu, S. Yang, B. Zhang. "Dynamic double modulation with step scan FTIR spectroscopy on polyurethane film". Spectrosc. Spect. Anal. 2002. 22(1): 25-28.

14. M. Forster, K. Loth, M. Andrist, U.P. Fringeli, H.H. Günthard. "Kinetic study of the photooxidation of pyrocatechol by modulated electronic excitation IR and ESR spectroscopy (MEIR and MESR)". Chem. Phys. 1976. 17(1): 59-80.

15. R. Wirz, T. Burgi, A. Baiker. "Probing enantiospecific interactions at chiral solid-liquid interfaces by absolute configuration modulation infrared spectroscopy". Langmuir 2003. 19(3): 785-792.

16. R. Wirz, T. Burgi, W. Lindner, A. Baiker. "Absolute configuration modulation attenuated total reflection IR spectroscopy: An in situ method for probing chiral recognition in liquid chromatography". Anal. Chem. 2004. 76(18): 5319-5330.

17. J.A. Bailey, F.L. Tomson, S.L. Mecklenburg, G.M. MacDonald, A. Katsonouri, A. Puustinen, R.B. Gennis, W.H. Woodruff, R.B. Dyer. "Time-resolved step-scan Fourier transform infrared spectroscopy of the CO adducts of bovine cytochrome c oxidase and of cytochrome bo(3) from Escherichia coli". Biochemistry 2002. 41(8): 2675-2683.

18. D. Heitbrink, H. Sigurdson, C. Bolwien, P. Brzezinski, J. Heberle. "Transient Binding of CO to CuB in Cytochrome c Oxidase Is Dynamically Linked to Structural Changes around a Carboxyl Group: A Time-Resolved Step-Scan Fourier Transform Infrared Investigation". Biophys. J. 2002. 82(1): 1-10.

19. E. Pinakoulaki, U. Pfitzner, B. Ludwig, C. Varotsis. "The role of the cross-link His-Tyr in the functional properties of the binuclear center in cytochrome c oxidase". J. Biol. Chem. 2002. 277(16): 13563-13568.

20. S. Stavrakis, K. Koutsoupakis, E. Pinakoulaki, A. Urbani, M. Saraste, C. Varotsis. "Decay of the Transient CuB−CO Complex Is Accompanied by Formation of the Heme Fe−CO Complex of Cytochrome cbb3−CO at Ambient Temperature: Evidence from Time-Resolved Fourier Transform Infrared Spectroscopy". J. Am. Chem. Soc. 2002. 124(15): 3814-3815.

21. C. Koutsoupakis, E. Pinakoulaki, S. Stavrakis, V. Daskalakis, C. Varotsis. "Time-resolved step-scan Fourier transform infrared investigation of heme-copper oxidases: implications for O2 input and H2O/H+ output channels". Biochim. Biophys. Acta, Bioenerg. 2004. 1655347-352.

22. R.M. Nyquist, D. Heitbrink, C. Bolwien, R.B. Gennis, J. Heberle. "Direct observation of protonation reactions during the catalytic cycle of cytochrome c oxidase". Proc. Natl. Acad. Sci. U.S.A. 2003. 100(15): 8715-8720.

23. D. Okuno, T. Iwase, K. Shinzawa-Itoh, S. Yoshikawa, T. Kitagawa. "FTIR Detection of Protonation/Deprotonation of Key Carboxyl Side Chains Caused by Redox Change of the CuA-Heme a Moiety and Ligand Dissociation from the Heme a3-CuB Center of Bovine Heart Cytochrome c Oxidase". J. Am. Chem. Soc. 2003. 125(24): 7209-7218.

24. B. Rost, J. Behr, P. Hellwig, O.M.H. Richter, B. Ludwig, H. Michel, W. Mantele. "Time-resolved FT-IR studies on the CO adduct of Paracoccus denitrificans cytochrome c oxidase: Comparison of the fully reduced and the mixed valence form". Biochemistry 1999. 38(23): 7565-7571.

25. B.H. McMahon, M. Fabian, F. Tomson, T.P. Causgrove, J.A. Bailey, F.N. Rein, R.B. Dyer, G. Palmer, R.B. Gennis, W.H. Woodruff. "FTIR studies of internal proton transfer reactions linked to inter-heme electron transfer in bovine cytochrome c oxidase". Biochim. Biophys. Acta, Bioenerg. 2004. 1655(1-3): 321-331.

26. F. Tomson, J.A. Bailey, R.B. Gennis, C.J. Unkefer, Z.H. Li, L.A. Silks, R.A. Martinez, R.J. Donohoe, R.B. Dyer, W.H. Woodruff. "Direct infrared detection of the covalently

ring linked His-Tyr structure in the active site of the heme-copper oxidases". Biochemistry 2002. 41(48): 14383-14390.

27. C. Nowak, C. Luening, W. Knoll, R.L.C. Naumann. "A Two-Layer Gold Surface with Improved Surface Enhancement for Spectro-Electrochemistry Using Surface-Enhanced Infrared Absorption Spectroscopy". Appl. Spectrosc. 2009. 63(9): 1068-1074.

28. F. Giess, M. Friedrich, J. Heberle, R. Naumann, W. Knoll. "The Protein-Tethered Lipid Bilayer: A Novel Mimic of the Biological Membrane". Biophys. J. 2004. 87(5): 3213-3220.

29. D. Schach, C. Nowak, R.B. Gennis, S. Ferguson-Miller, W. Knoll, D. Walz, R.L.C. Naumann. "Modeling direct electron transfer to a multi-redox center protein: Cytochrome c oxidase". J. Electroanal. Chem. 2010. 649(1-2): 268-276.

30. K. Ataka, F. Giess, W. Knoll, R. Naumann, S. Haber-Pohlmeier, B. Richter, J. Heberle. "Oriented Attachment and Membrane Reconstitution of His-Tagged Cytochrome c Oxidase to a Gold Electrode: In Situ Monitoring by Surface-Enhanced Infrared Absorption Spectroscopy". J. Am. Chem. Soc. 2004. 126(49): 16199-16206.

31. M.G. Friedrich, J.W.F. Robertson, D. Walz, W. Knoll, R.L.C. Naumann. "Electronic Wiring of a Multi-Redox Site Membrane Protein in a Biomimetic Surface Architecture". Biophys. J. 2008. 94(9): 3698-3705.

32. OriginPro 8.6G, v8.6.0 SR3. OriginLab, Northampton, 2012.

33. D. Schach, Direct Electron Transfer to the Cytochrome c Oxidase investigated by Electrochemistry and Time-Resolved Surface-Enhanced Infrared Absorption Spectroscopy, Ph.D. Thesis (Johannes Gutenberg Universität Mainz, Mainz, 2011).

34. A. Schwaighofer, C. Steininger, D.M. Hildenbrandt, J. Srajer, C. Nowak, W. Knoll, R.L.C. Naumann. "Time-Resolved Surface-Enhanced IR-Absorption Spectroscopy of direct Electron Transfer to Cytochrome c Oxidase from R. sphaeroides". Biophys. J. 2013. under review

35. P. Brzezinski. "Internal Electron-Transfer Reactions in Cytochrome c Oxidase". Biochemistry 1996. 35(18): 5611-5615.

36. Z.W. Yu, J. Liu, I. Noda. "Effect of noise on the evaluation of correlation coefficients in two-dimensional correlation spectroscopy". Applied Spectroscopy 2003. 57(12): 1605-1609.

37. M.A. Czarnecki. "Interpretation of two-dimensional correlation spectra: Science or art?". Applied Spectroscopy 1998. 52(12): 1583-1590.

38. J.L.R. Arrondo, A. Muga, J. Castresana, F.M. Goñi. "Quantitative studies of the structure of proteins in solution by fourier-transform infrared spectroscopy". Prog. Biophys. Mol. Biol. 1993. 59(1): 23-56.

39. D.K. Das, T. Mondal, U. Mandal, K. Bhattacharyya. "Probing Deuterium Isotope Effect on Structure and Solvation Dynamics of Human Serum Albumin". ChemPhysChem 2011. 12(4): 814-822.

40. A. Barth. "Infrared spectroscopy of proteins". Biochim. Biophys. Acta, Bioenerg. 2007. 1767(9): 1073-1101.

41. J.L.R. Arrondo, F.M. Goñi. "Structure and dynamics of membrane proteins as studied by infrared spectroscopy". Prog. Biophys. Mol. Biol. 1999. 72(4): 367-405.

42. E. Rial, A. Muga, J.M. Valpuesta, J.-L.R. Arrondo, F.M. Goñi. "Infrared spectroscopic studies of detergent-solubilized uncoupling protein from brown-adipose-tissue mitochondria". Eur. J. Biochem. 1990. 188(1): 83-89.

43. A. Kohen, H.H. Limbach. Isotope Effects In Chemistry and Biology. Boca Raton: CRC Press, 2005.

44. R.P. Sheridan, E.T. Knight, L.C. Allen. "The effect of deuterium substitution on hydrogen bonds in redox proteins". Biopolymers 1984. 23(2): 195-200.

45. O. Farver, J.D. Zhang, Q.J. Chi, I. Pecht, J. Ulstrup. "Deuterium isotope effect on the intramolecular electron transfer in Pseudomonas aeruginosa azurin". Proc. Natl. Acad. Sci. U.S.A. 2001. 98(8): 4426-4430.

46. K. Ataka, T. Yotsuyanagi, M. Osawa. "Potential-dependent reorientation of water molecules at an electrode/electrolyte interface studied by surface-enhanced infrared absorption spectroscopy". J. Phys. Chem. 1996. 100(25): 10664-10672.

47. M. Osawa, A. Yamakata. "Structure and Behavior of Water at the Electrochemical Interface Studied by Surface-Enhanced Infrared Absorption Spectroscopy". Jpn. Anal. 2011. 60(1): 1-9.

48. J.R. Powell, F.M. Wasacz, R.J. Jakobsen. "An Algorithm for the Reproducible Spectral Subtraction of Water from the Ft-Ir Spectra of Proteins in Dilute-Solutions and Adsorbed Monolayers". Appl. Spectrosc. 1986. 40(3): 339-344.

49. M. Osawa. "Dynamic Processes in Electrochemical Reactions Studied by Surface-Enhanced Infrared Absorption Spectroscopy (SEIRAS)". Bull. Chem. Soc. Jpn. 1997. 702861-2880.

50. M. Osawa, K. Ataka, K. Yoshii, Y. Nishikawa. "Surface-Enhanced Infrared-spectroscopy-The Origin of the Absorption Enhancement and Band Selection rule in Infrared-spectra of Molecules adsorbed on fine Metal Particles". Appl. Spectrosc. 1993. 47(9): 1497-1502.

51. E.A. Gorbikova, K. Vuorilehto, M. Wikstrom, M.I. Verkhovsky. "Redox titration of all electron carriers of cytochrome c oxidase by Fourier transform infrared spectroscopy". Biochemistry 2006. 45(17): 5641-5649.

52. P. Hellwig, S. Grzybek, J. Behr, B. Ludwig, H. Michel, W. Mantele. "Electrochemical and Ultraviolet/Visible/Infrared Spectroscopic Analysis of Heme a and a3 Redox Reactions in the Cytochrome c Oxidase from Paracoccus denitrificans: Separation of Heme a and a3 Contributions and Assignment of Vibrational Modes". Biochemistry 1999. 38(6): 1685-1694.

53. E. Goormaghtigh, V. Cabiaux, J.-M. Ruysschaert. "Secondary structure and dosage of soluble and membrane proteins by attenuated total reflection Fourier-transform infrared spectroscopy on hydrated films". Eur. J. Biochem. 1990. 193(2): 409-420.

54. B. Stuart. Biological Applications of Infrared Spectroscopy. New York: Wiley, 1997.

55. L. Qin, J. Liu, D.A. Mills, D.A. Proshlyakov, C. Hiser, S. Ferguson-Miller. "Redox-Dependent Conformational Changes in Cytochrome c Oxidase Suggest a Gating Mechanism for Proton Uptake". Biochemistry 2009. 48(23): 5121-5130.

56. L. Buhrow, S. Ferguson-Miller, Leslie A. Kuhn. "From Static Structure to Living Protein: Computational Analysis of Cytochrome c Oxidase Main-chain Flexibility". Biophys. J. 2012. 102(9): 2158-2166.

57. L.S. Busenlehner, L. Salomonsson, P. Brzezinski, R.N. Armstrong. "Mapping protein dynamics in catalytic intermediates of the redox-driven proton pump cytochrome coxidase". Proc. Natl. Acad. Sci. U.S.A. 2006. 103(42): 15398-15403.

Progress in Reaction Kinetics and Mechanism, 2013, 38(1), 32–47
doi:10.3184/146867812X13558465325118

RESEARCH PAPER

A kinetic model of proton transport in a multi-redox centre protein: cytochrome *c* oxidase

Johannes Srajer[a,b], Andreas Schwaighofer[a], David M. Hildenbrandt[a], Asmorom Kibrom[a] and Renate L.C. Naumann[a*]

[a]*Austrian Institute of Technology GmbH, AIT, Donau-City Str. 1, 1220 Vienna, Austria*

[b]*CEST Center of Electrochemical Surface Technology, Viktor-Kaplan-Strasse 2, 2700 Wiener Neustadt, Austria*

**E-mail: renate.naumann@ait.ac.at*

ABSTRACT

We use chemical reaction kinetics to explore the stepwise electron and proton transfer reactions of cytochrome *c* oxidase (C*c*O) from *R. sphaeroides*. Proton transport coupled to electron transport (ET) is investigated in terms of a sequence of protonation-dependent second-order redox reactions. Thereby, we assume fixed rather than shifting dissociation constants of the redox sites. Proton transport can thus be simulated particularly when separate proton uptake and release sites are assumed rather than the same proton pump site for every ET step. In order to test these assumptions, we make use of a model system introduced earlier, which allows us to study direct ET of redox enzymes by electrochemistry. A four-electron transfer model of C*c*O had been developed before, according to which electrons are transferred from the electrode to Cu_A. Thereafter, electrons are transferred along the sequence heme *a*, heme a_3 and Cu_B. In the present investigation, we consider protonation equilibria of the oxidised and reduced species for each of the four centres. Moreover, we add oxygen/H_2O as the terminal (fifth) redox couple including protonation of reduced oxygen to water. Finally we arrive at a kinetic model comprising five protonation-dependent redox couples. The results from the simulations are compared with experimental data obtained in the absence and presence of oxygen. As a result, we can show that proton transport can be modelled in terms of protonation-dependent redox kinetics.

KEYWORDS: proton pump, protonation-dependent chemical reaction kinetics, second-order redox reaction, metalloprotein, master equation

1. INTRODUCTION

Cytochrome *c* Oxidase (C*c*O) is the final complex of the respiratory chain. Its purpose is to use the energy gained by the reduction of oxygen to water to pump protons against a difference of electrochemical potentials across the mitochondrial inner membrane. This pumping is achieved by coupling a number of electron (ET) and proton transfer (PT) steps. The stepwise transfer is under debate since C*c*O has been recognised as a proton pump more than three decades ago [1–3]. According to current view [2], the gradual increase of the p*K* value during each ET step leads to the transfer of a proton to the proton loading site (PLS), which is separated from the site where oxygen chemistry occurs [4–7]. After the transfer of a proton to the PLS, another proton is taken up for the chemical reaction in the catalytic site. Electrostatic repulsion from this second proton will then expel the proton out of the PLS. This view is hard to challenge experimentally, particularly since few methods are available to follow ET and HT steps during an entire catalytic cycle, see, however, [8]. A convenient way to study proton-coupled ET is chemical reaction kinetics initiated by electrochemistry [9–12]. In this study, we make use of a model system developed earlier, which permits direct ET to redox enzymes [13]. This system comprises C*c*O from *R. sphaeroides* tethered to an electrode via a his-tag attached to subunit (SU) II followed by reconstitution into a protein-tethered bilayer lipid membrane (ptBLM). The benefit of this system is the accessibility of the internal redox centres avoiding the diffusion limitation of mediators. A further advantage inherent in the geometry of the ptBLM is the hydrophilic layer between the electrode and the lipid membrane provided by the tether molecules. The experimental benefit is the sensitivity of the small interstitial reservoir (~0.2 nL cm^{-2}) to changes in proton concentration as a result of enzyme activity. Thus, this methodology presents a new approach to examine separately proton and electron transfer reactions in membrane proteins, see the schematics of the model system (Figure 1).

Previous studies have made it highly likely that electrons are transferred from the electrode directly to Cu_A. A sequential four-electron transfer model had been designed according to which electrons are then transferred along the sequence Cu_A, heme *a*, heme a_3 and Cu_B [14]. In the presence of oxygen, the enzyme displays enzymatic activity indicated by amplified electron as well as proton currents [15]. In the present investigation, we extend this four-electron transfer model in two steps. In the first step we consider protonation equilibria of the oxidised and reduced species for each of the four centres. In the second step we add oxygen/H_2O as the terminal (fifth) redox couple including protonation of reduced oxygen to water. Finally, we arrive at a kinetic model comprising five

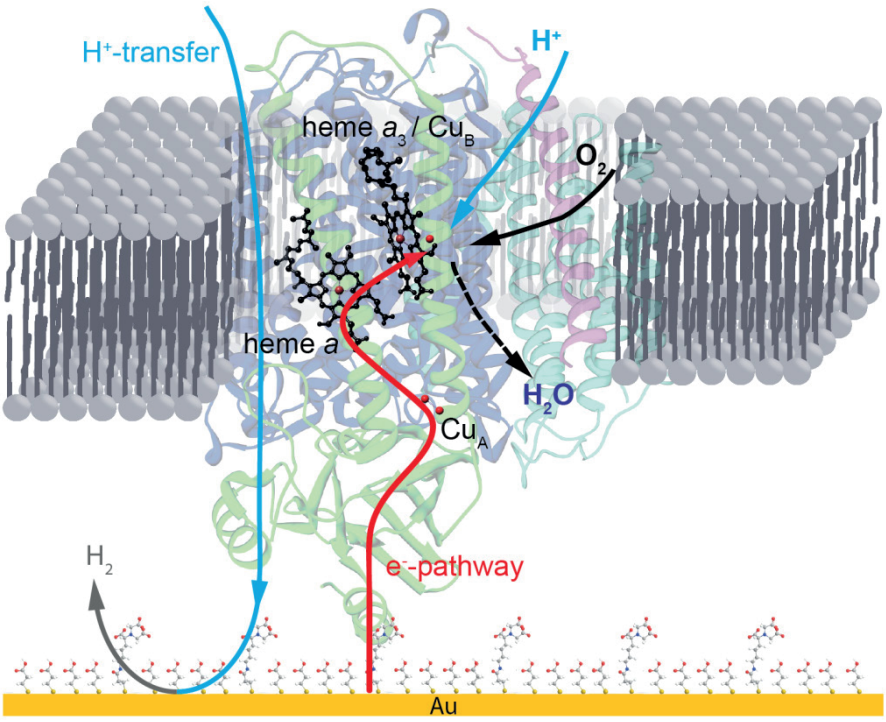

Figure 1 Model system of C*c*O from *R. sphaeroides*, immobilised through his-tag engineered to SU II on an Au electrode and reconstituted into a lipid bilayer.

redox couples describing a string of second-order reactions with protonations. The model will be tested using cyclic voltammetry data of the C*c*O in the absence and presence of oxygen.

2. KINETIC MODEL

The sequential four-electron transfer model of C*c*O, comprising the redox sites Cu_A, heme *a*, heme a_3 and Cu_B, has been developed before [14]. Each site is either in the reduced (r) or in the oxidised (o) state. The model therefore results in $2^4 = 16$ possible redox states of the enzyme. In order to simulate internal processes within the enzyme, time-dependent density functional theory is used, which is based on the local equilibrium assumption [16]. Recent developments show that this can also be applied to far-from-equilibrium dynamics under time-dependent driving signals such as cyclic voltammetry [17]. Instead of using an electrostatic approach calculating the Coulomb forces for a fixed spatial dilatation of the enzyme, we employ chemical reaction kinetics based on a modified Nernst equation, taking into account protonation equilibria. In our formulation we describe the behaviour of the enzyme by rate constants, standard redox potentials and acid dissociation constants.

2.1 General concepts

Since we are interested in dynamic processes within a single complex, it is suffvicient to define a probability P_i for every single redox state i (i=1,...,16) of the enzyme. The temporal evolution of this system is governed by the master equation

$$\frac{d}{dt}P_i = \sum_{j\neq i} k_{ij}P_i - k_{ji}P_j, \tag{1}$$

where k_{ij} and k_{ji} are the forward and backward reaction rates for the transition from redox state i into state j. The relation between these reaction rates is defined by the equilibrium constant $K = \frac{k_{ij}}{k_{ji}}$. Since we are dealing with a single complex, the condition

$$\sum_{i=1}^{16} P_i = 1 \tag{2}$$

holds at any time.

2.1.1 Redox reactions and protonation

Considering a single redox couple, protonation/deprotonation in the course of the transition from the oxidised to the reduced state can take place in four different ways, dependent on the dissociation constants K_m^o and K_m^r of the oxidised and reduced state, respectively (Figure 2).

Since spectroscopic methods distinguishing between protonated and deprotonated species are often not available, we adopted a concept developed by Walz for all kinds of redox processes associated with ligands [18]. This concept comprises total reduced and oxidised species as the sum of ligated and unligated species. Translated into the realm of protonations, this means considering total species as the sum of protonated and deprotonated species, resulting in Eqns (3) and (4) for the reduced and oxidised form, respectively.

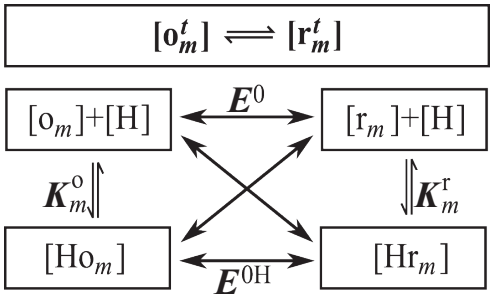

Figure 2 Reaction scheme of the transition from the oxidised to the reduced state of a single redox couple considering protonations of oxidised and reduced species. Black arrows show the possible transitions, with the standard redox potentials E^0 for the deprotonated species and E^{OH} for the protonated species.

$$[r_m^t] = [r_m] + [Hr_m] = [r_m](1 + 10^{pK_m^r - pH}) \tag{3}$$

$$[o_m^t] = [o_m] + [Ho_m] = [o_m](1 + 10^{pK_m^o - pH}) \tag{4}$$

Insertion of Eqns (3) and (4) into the Nernst equation yields

$$E = E_m^0 + \frac{RT}{nF}\ln\frac{[o_m^t]}{[r_m^t]} + \frac{RT}{nF}\ln\frac{1+10^{pK_m^r - pH}}{1+10^{pK_m^o - pH}}, \tag{5}$$

with E as the electrode potential, E^0 as the standard redox potential both defined in aqueous solution *versus* standard hydrogen electrode (SHE) as the reference point, T as the temperature, n as the number of electrons involved in this process and R and F are the universal gas and Faraday constants. According to Eqn (5), the electrode potential E depends not only on the ratio between the redox states, but also on pH and the pK values of the oxidised and reduced species. In the biochemical literature, the first and third terms are often combined to yield the midpoint potential E^m, defined by Eqn (6) [12,18].

$$E_m^m = E_m^0 + \frac{RT}{nF}\ln\frac{1+10^{pK_m^r - pH}}{1+10^{pK_m^o - pH}}, \tag{6}$$

Due to the second term in Eqn (6), the midpoint potential is pH-dependent.
We now proceed to consider the interaction between two such protonation-dependent redox couples, each one defined by the modified Nernst Eqn (5) (see Figure 3).
We begin with the second-order reaction equation written likewise in terms of total species

$$[r_l^t] + [o_m^t] \rightleftharpoons [o_l^t] + [r_m^t] \tag{7}$$

yielding the equilibrium constant of this reaction

$$K = \frac{k_{lm}}{k_{ml}} = \frac{[o_l^t][r_m^t]}{[r_l^t][o_m^t]} \tag{8}$$

which determines the ratio between the forward and backward reaction rates. Insertion of Eqn (5), that is valid for each of the single redox centres l and m, the equilibrium constant for this reaction becomes

$$K = \frac{k_{lm}}{k_{ml}} = e^{\frac{nF(E_m^0 - E_l^0)}{RT}} \frac{(1+10^{pK_l^o - pH})}{(1+10^{pK_l^r - pH})}\frac{(1+10^{pK_m^r - pH})}{(1+10^{pK_m^o - pH})} \tag{9}$$

From Eqns (8) and (9) the flow of electrons J_{lm} between centres l and m can

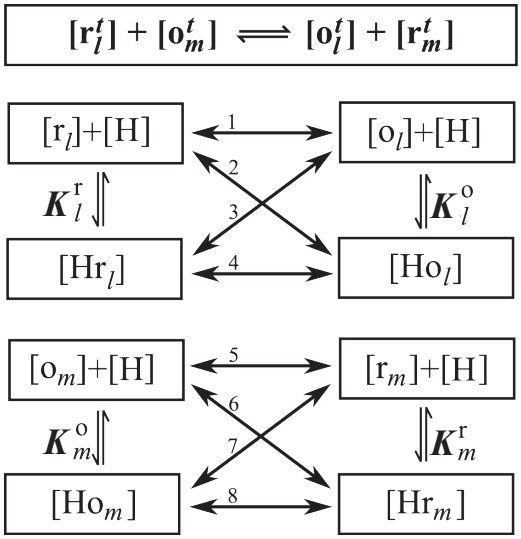

Figure 3 Scheme for second-order reaction using total species: Each redox centre has four different possibilities to undergo the transition (centre *l*: 1–4, centre *m*: 5–8), resulting in 16 different possible combinations.

be calculated, once the forward reaction rate has been identified, *e.g.* by independent measurements,

$$J_{lm} = \Gamma\ A\left(k_{lm}P_i - k_{lm}\ e^{\frac{nF(E_l^0 - E_m^0)}{RT}}\ \frac{(1+10^{pK_l^r - pH})}{(1+10^{pK_l^o - pH})}\frac{(1+10^{pK_m^o - pH})}{(1+10^{pK_m^r - pH})}P_j\right) \quad (10)$$

using Γ, the surface concentration of the enzyme and the surface area A. Note that in introducing Eqn (10), we are able to take into account the p*K* values of all of the species possibly involved in a second-order reaction given by Eqn (7).

2.1.2 Transition rates of protons

The number of protons taken up or released in a second-order reaction depends on the difference in magnitude of the dissociation constants of the reduced and oxidised species. Assuming the equilibrium condition for all kinds of protonations/deprotonations, we derive the probabilities of protons being taken up or released in a particular redox reaction. The transition rates of protons are then obtained by multiplying the flow of electrons calculated in Eqn (10) with these probabilities. For example, we can deduce from the dissociation constants that the probabilities of the reduced species to be in the deprotonated and protonated state are $\frac{1}{1+10^{pK^r - pH}}$ and $\frac{1}{1+10^{pH - pK^r}}$, respectively. Hence, the probability of a proton being associated in the course of reduction P_m^{up} of a single redox couple *m* can be expressed:

$$P_m^{up} = \frac{1}{1+10^{pK_m^o - pH}} \quad \frac{1}{1+10^{pH-pK_m^r}} \tag{11}$$

In the case of a second-order reaction, the probabilities of species being protonated or deprotonated have to be taken into account for both redox couples. This leads to the 16 different combinations depicted in Figure 3. For example, transition 1 combined with 6 and transition 2 with 8 yields an uptake of a proton. Transition 1 combined with 7 and transition 3 with 5 yields a release and transition 3 combined with 6 and transition 4 with 8 yields a concomitant ET and HT. The total number of protons in every transition is then obtained by the sum of the transition probabilities having the same result. For further details, see the Electronic Supplementary Information.

2.1.3 Electrode reactions

The treatment so far is only applicable to second-order chemical reactions. In our model system, however, Cu_A, the first redox centre is connected to the electrode. Hence, in this case, the rate of electron transfer to Cu_A depends on the applied potential E according to the Butler–Volmer equation [19]. Inserting midpoint potentials [Eqn (6)], in order to take into account the protonation constants of reduced and oxidised species, the current i^e resulting from the electron transfer to Cu_A can be written:

$$i^e = -FAk_e\Gamma \sum_{i\neq j} \left(P_i e^{\frac{F\alpha(E_1^0 - E)}{RT}} \left(\frac{1+10^{pK_1^r - pH}}{1+10^{pK_1^o - pH}}\right)^{\alpha} - P_j e^{\frac{-F(1-\alpha)(E_1^0 - E)}{RT}} \left(\frac{1+10^{pK_1^r - pH}}{1+10^{pK_1^o - pH}}\right)^{-(1-\alpha)} \right) \tag{12}$$

with the surface area A of the electrode, the standard rate constant k_e of the electron transfer, the surface concentration of the enzyme Γ and the charge transfer coefficient α. The reduction of Cu_A is a one-electron transfer process so that $n=1$ is already inserted in Eqn (12). The same formalism is also used for protons, which are reduced to hydrogen at the electrode. These protons are the so-called pumped protons, which arrive at the electrode in the course of enzyme turnover. Two electrons are used to reduce two protons to a hydrogen molecule H_2. The current i^H flowing in this process is calculated according to

$$i^H = -F \; A \; k_{e,H} \left([H] \; e^{\frac{F\alpha(E^0 - E)}{R\,T}} \right) \tag{13}$$

with the concentration of protons [H] in the aqueous phase, the rate constant $k_{e,H}$ and the standard potential E^0 of molecular hydrogen formation, which is shifted by 0.39 Volts *versus* SHE, due to kinetic limitations at the gold electrode [20]. The dependence on the partial pressure of H_2 is negligible due to the rapid

diffusion of H_2 into the surrounding air. Both electrode reactions contribute to the current measured in experiments $i^{exp} = i^{e} + i^{H}$. The ratio between the two kinds of currents yields the number of protons pumped per electron.

2.2 Electrochemical model system

The complete model system is depicted schematically in Figure 4. Under anaerobic conditions only the pathways indicated by electrochemical reduction are active as indicated by black arrows, whereas under aerobic conditions the model is expanded to take into account also enzymatic reoxidation indicated by green arrows. Taken under anaerobic conditions, the model comprises the electrochemical electron uptake by Cu_A coupled to a series of second-order electron exchange reactions to heme *a*, heme a_3 and Cu_B. This sequential four-ET model had already been discussed previously. The four redox centres can be present in reduced and oxidised states, indicated by the letters *r* and *o*, respectively. Electrons are taken up by the enzyme electrochemically, but only via the first electron acceptor, Cu_A [14].

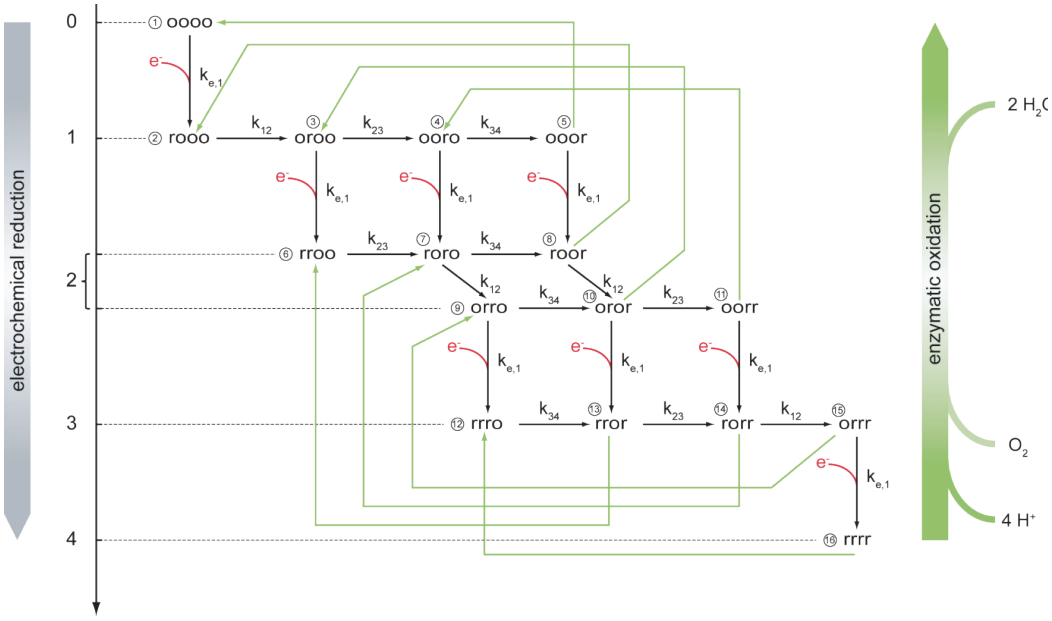

Figure 4 Kinetic scheme for sequential electron transfer in C*c*O under anaerobic and aerobic conditions. The four centres are arranged in the order Cu_A, heme *a*, heme a_3 and Cu_B, which can be present either in the reduced (r) or oxidised (o) state. All of the r and o states can be protonated or deprotonated. Hence, the enzyme can exist in 16 different redox states and 256 protonation states. Vertical arrows with red branches represent electron uptake from the electrode, while black horizontal arrows indicate second-order reactions between redox centres. Green arrows show enzymatic reoxidation under aerobic conditions. Oxidation steps start with Cu_B in the reduced state. Different oxidised states of the enzyme are thus restored.

Considering protonations, in principle all of the reduced and oxidised species can be protonated depending on their individual pK^r and pK^o values. This increases the number of possible redox and protonation states to 256 different states, which cannot be reflected in the schematic shown in Figure 4. In the presence of oxygen, the enzymatic turnover has to be taken into account. To this end, oxygen is considered as a fifth redox couple, exchanging electrons and protons in a further second-order reaction with reduced Cu_B. One-electron transfer steps are considered, thus dividing the reduction of one O_2 molecule into four steps consuming ½O + H yielding ½H_2O each. Four such steps yield one full cycle of the C*c*O, using four protons (H) and one oxygen molecule (O_2) to form two water molecules (2 H_2O). Even though this is still a simplified model, it enables us to simulate the sequential reduction of the redox centres coupled to reoxidation by oxygen, thus mimicking a full enzymatic cycle.

3. MATERIALS AND METHODS

3.1 Immobilisation of the protein

Immobilisation of C*c*O on template stripped gold (TSG) [21] electrodes was performed as described in detail by Nowak *et al*. [22]. Briefly, C*c*O from *Rhodobacter sphaeroides* with a his-tag engineered to the C-terminus of subunit II was expressed and purified according to Hiser and Ferguson-Miller [23]. TSG electrodes were provided with a self-assembled monolayer of a mixture of dithiobis (nitriloacetic acid butylamidyl propionate (DTNTA) and dithiobis (propionic acid) (DTP) in a mole ratio of 0.2. After loading the NTA-functionalised surface with Ni^{2+}, C*c*O dissolved in dodecyl β–D–maltoside (DDM)phosphate-buffer (0.05 M K_2HPO_4, 0.1 M KCl, pH = 8, 0.1% DDM) was adsorbed at a final concentration of 100 nM. Dialysis was performed *in situ* in a DiPhyPC solution (40 µM) in DDMphosphate buffer by adding biobeads (Bio-Rad Laboratories GmbH, Munich, Germany) to the lipid–detergent solution.

3.2 Electrochemical methods

Electrochemical measurements were performed using an Autolab instrument (PGSTAT302 with GPES 4.9) with an ECD-module amplifier for low-currents, an ADC750 module for rapid scan measurements and a SCAN-GEN module for analogue potential scanning. Cyclic voltammetry experiments were conducted with IR drop compensation. Measurements were performed in a buffer solution containing 0.05 M K_2HPO_4, 0.1 M KCl, pH = 8. Under anaerobic conditions, the buffer solution was flushed with Ar and an oxygen trap consisting of glucose (0.3% w/w), glucose oxidase (75 µg mL^{-1}) and catalase (12.5 µg mL^{-1}) was added. Under aerobic conditions the buffer solution was flushed with oxygen.

Thereafter, up to 30 CVs were taken until the CV had reached steady state regarding peak position and current density. All electrochemical measurements were taken in a three-electrode configuration with TSG as the working electrode, a Ag|AgCl,KCl_{sat} reference and a platinum wire as the counter electrode. All electrode potentials are quoted *versus* SHE.

3.3 Computational methods

The system of 16 differential equations, described by the master equation are solved numerically using the solver ode15s of the commercially available software package MATLAB R2011a®.

4. RESULTS AND DISCUSSION

In order to explore the impact of protonations on our four-electron transfer model (see Figure 4) we used the same data sets presented in the context of our previous studies [14,22]. CVs taken under strictly anaerobic conditions had shown peaks in the range of 200 – 600 mV, corresponding to midpoint potentials of redox centres known from equilibrium titrations (see Figure 5A) [24]. In an air-saturated solution, the enzyme had been shown to work under turnover conditions, indicated by two peaks appearing at around 200 mV and 500 mV exhibiting an increased current density (Figure 5B). These peaks had been attributed to repeated electron and proton transfer. Surprisingly, the electron transfer peak was shifted by more than 400 mV in the negative direction *versus* known midpoint potentials. Returning to anaerobic conditions, we had found that the peak at around – 200 mV persisted for a certain period of time (Figure 5C), before the enzyme relaxes back to the original anaerobic state (Figure 5A). We had deduced from these results that the enzyme undergoes a transition from a non-activated to an activated conformational state, equivalent to the transition from the resting to the pulsed state when the C*c*O reconstituted in liposomes is subjected to oxygen pulses [22]. The negative shift of the electron transfer peak had been confirmed by equilibrium potentiometric titrations of the activated enzyme followed by FTIR spectroscopy [15,22].

Electron and proton currents were calculated using Eqns (13) and (14). CVs were simulated based on triangularly-shaped changes of applied voltages as a function of time. Since a large number of parameters have to be considered, some of them were fixed to values adopted from previous studies such as electrochemical rate constants, surface concentrations of C*c*O, and forward reaction rates. Redox potentials were adopted from equilibrium potentiometric titrations followed by UV/VIS and FTIR measurements [24]. The list of all fixed parameters can be found in the supplementary information. Since the focus of

this study is protonation, we varied the dissociation constants of reduced and oxidised species according to Table 1.

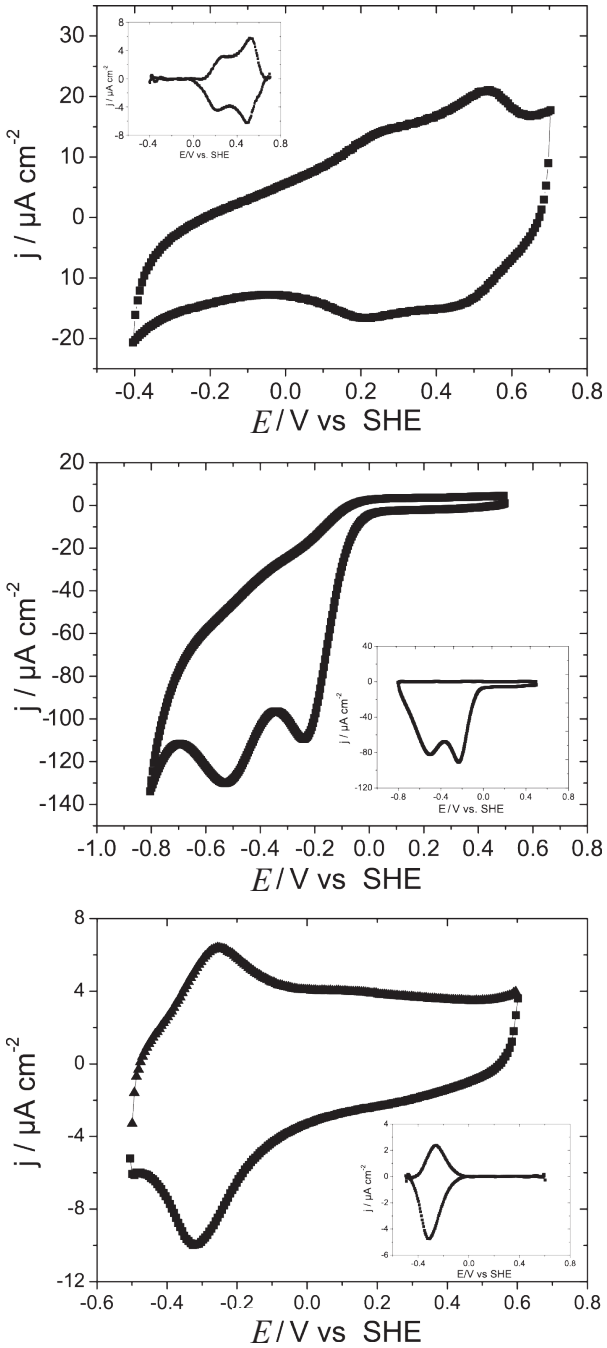

Figure 5 Experimentally measured CVs of C*c*O under anaerobic (A,C) and aerobic (B) conditions in the non-activated (A) and activated (B,C) state, respectively. The insets show baseline corrected signals, normalised to the same scan rate (50 mV s^{-1}) in order to exclude charging effects of the ptBLM and the electrochemical reduction of oxygen at the electrode.

In a first attempt to simulate the CVs of the non-activated anaerobic C*c*O (Figure 5A), pK^r values were estimated according to the mechanisms of proton uptake and release described in section 2.1.2. pK^o values are very hard to estimate and were therefore set to zero. Using parameter set V1 proton uptake and release is assumed in reactions between Cu_A and heme *a*, and between heme a_3 and Cu_B, respectively, whereas concomitant electron and proton transfer is assumed between heme *a* and heme a_3. E^m of Cu_A is assumed not to be pH-dependent. The first positive peak in Figure 5A corresponds to the redox potential of Cu_A of about 250 mV. The second positive peak located at 520 mV cannot be attributed to any of the known midpoint potentials of C*c*O [24]. Using the modified model taking into account parameter set V1 results in an additional peak shifted in the positive direction to 470 mV (Figure 6A) in good agreement with the measurement (Figure 5B). Previous modelling studies that do not consider protonations have not been able to describe this phenomenon [14]. Extending the model to include oxygen reduction (Figure 4) and keeping the parameter set V1 yields the simulated CV shown in Figure 6B. An overall catalytic current density 60 µA cm^{-2} is recognised as well as a current due to proton reduction at the electrode of about 30 µA cm^{-2}, which is in agreement with measured values. The proton current indicates proton pumping, which is the result of proton uptake and release in the reaction kinetics. The overshooting proton peak at a potential of about 65 mV (Figure 6B) is an artefact due to rapid changes of the pH in the interstitial volume of only 0.24 nL cm^{-2}, between the electrode and the lipid membrane [13]. Hence, we consider constant currents only, although peak-shaped currents are seen in the experiments. They are due to diffusion-based depletion of oxygen and protons, which have not been taken into account in the simulation (see Figure 6B).

Changing the parameter set to V2, thereby decreasing pK^r_3 of heme *a* to p$K^r_3 = 3$, we assume a further proton release step on the level of ET between heme *a* and a_3. As a result we still see electron and proton currents equal in magnitude under aerobic conditions, however, too high as compared to the measured data

Table 1 Variation of acid dissociation constants. Every redox centre has two acid dissociation constants for the reduced and the oxidised species, respectively

Variation	Cu_A		Heme *a*		Heme a_3		Cu_B	
no.	pK_1^r	pK_1^o	pK_2^r	pK_2^o	pK_3^r	pK_3^o	pK_4^r	pK_4^o
V1	0	0	10	0	10	0	3	0
V2	0	0	3	0	10	0	3	0
V3	0	0	3	0	10	0	9	0

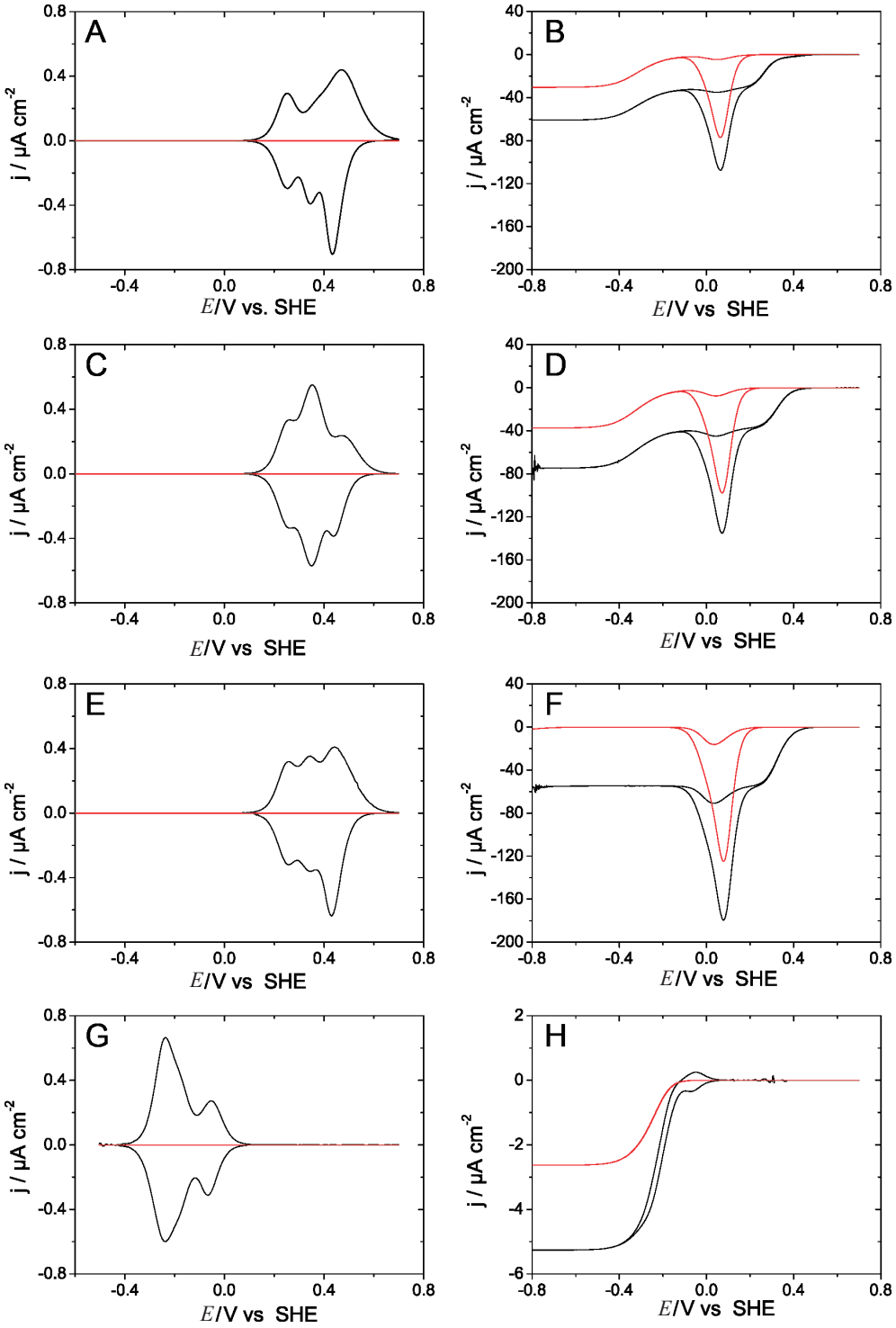

Figure 6 CVs simulated under anaerobic conditions (A,C,E,G) and under aerobic conditions (B,D,F,H). Different parameter sets for the acid dissociation constants are used, see Table 1 (V1 = A,B,G,H / V2 = C,D / V3 = E,F). The black lines represent the overall currents, while the red lines show currents resulting from proton reaction with the electrode. (G) and (H) show simulation results using the activated standard redox potentials for anaerobic and aerobic conditions respectively.

(Figure 6D). Also the simulated CV under anaerobic conditions do no longer compare favourably with the measured data. The peak due to reduction of Cu_A (262 mV) is still close to 250 mV, however, a prominent peak appears at 355 mV and a smaller one at 475 mV (Figure 6C). Further changing the parameter set to V3, thereby deliberately assuming pK^r_4 of Cu_B being $pKr_4 = 9$, attributed to the PLS in previous studies [5,6,25]. This parameter set results in no proton current at all, and an ET current of around 60 μA cm^{-2} density (Figure 6F). The anaerobic case shows again a peak at 259 mV due to Cu_A, however, two more positive peaks at 343 and 442 mV, different from the measured CV, exhibiting a single more positive peak at 520 mV (Figure 5B).

The best result so far has been obtained with parameter set V1, at least as far as proton and electron currents is concerned. This parameter set comprises ET occurring concomitantly with HT between heme *a* and heme a_3, an overall charge-balanced process. This would explain not only the fast ET rate measured between these redox centres but also that this ET does not seem to contribute to the generation of membrane potential of the C*c*O [8].

The negative shift of the ET and HT peaks under aerobic conditions, however, can only be simulated by assuming equilibrium potentials of the activated enzyme shifted to negative potentials, in agreement with our previous modelling and FTIR studies, see also the supplementary Information [14,22]. Using pK^r values according to the parameter setting V1 results in a simulated CV with ET and HP currents equal in magnitude and, both shifted to around – 200 mV (Figure 6H), in reasonable agreement with the measurement (Figure 5B). Peaks in the simulated CV under anaerobic conditions are equally shifted in the negative direction, which is consistent with respective measured CVs of the activated rather than the non-activated enzyme (Figure 6G).

For a more accurate determination of p*K* values including pK^o, we are currently working on an adequate parameter optimisation routine, in order to deal with the number of free parameters.

5. CONCLUSIONS

The simulations show that the concept of a string of second-order reactions including protonations appears to reflect the behaviour of the C*c*O, at least in principle, regarding catalytic currents as well as proton translocation. Notably, this concept is based on constant p*K* values and standard redox potentials rather than p*K* or E^0 changing in the course of a redox reaction as assumed in previous studies [4,6,7,26]. E^m may change as a function of pH, though. As far as p*K* and E^0 values are concerned, however, there is no reason to believe that the principles described by Eqns (9) and (10) work differently in a protein

as compared to an ordinary chemical reaction, see *e.g.* [9,12,27,28]. Proton pumping can thus be simulated particularly when separate proton uptake and release sites are assumed rather than the same proton pump site for every ET step. In this regard, there are similarities with another kinetic model also comprising four ET and four PT sites [25]. Different from this model, however, in order for pumping to take place in our model, the p*K* of the release site is required to be smaller than that of the uptake site (see parameter set V3 compared to V1). The low p*K* values could be due to a yet unidentified anionic group coupled to Cu_B reduction. A further requirement for an effective proton pumping is considering oxygen/H_2O as a fifth redox couple including the ionic product of water. This gives rise to a final ET and HT uptake rather than a separate chemical reaction. We have to bear in mind, however, that we are still using a simplified model, particularly regarding the reactions with oxygen. The net result, however, should be the same, at least as far as proton pumping is concerned.

ELECTRONIC SUPPLEMENTARY INFORMATION

The ESI is available through stl.publisher.ingentaconnect.com/content/stl/prk/supp-data

6. ACKNOWLEDGMENTS

We gratefully acknowledge the invaluable advice and assistance over the years of Prof. Dieter Walz, Biozentrum, University of Basel, Switzerland. Likewise, we thank Prof. Shelagh Ferguson-Miller and Carrie Hiser, Michigan State University, East Lansing MI 48824, USA, for inspiring discussions and for providing us with high-quality preparations of C*c*O from *R. sphaeroides*.

7. REFERENCES

[1] Wikstrom, M. and Verkhovsky, M.I. (2007) *Biochim. Biophys. Acta. Bioenerg.*, 1767, 1200 – 1214.

[2] Brzezinski, P. and Gennis, R. (2008) *J. Bioenerg. Biomembr.*, **40**, 521 – 531.

[3] Wikstrom, M.K.F. (1997) *Nature*, **266**, 271 – 273.

[4] Popovic, D.M. and Stuchebrukhov, A.A. (2004) *FEBS Lett.*, **566**, 126 – 130.

[5] Popovic, D.M. and Stuchebrukhov, A.A. (2012) *Biochim. Biophys. Acta. Bioenerg.*, **1817**, 506 – 517.

[6] Blomberg, M.R.A. and Siegbahn, P.E.M. (2012) *Biochim. Biophys. Acta. Bioenerg.*, **1817**, 495 – 505.

[7] Krab, K., Kempe, H. and Wikstrom, M. (2011) *Biochim. Biophys. Acta. Bioenerg.*, **1807**, 348–358.

[8] Belevich, I., Bloch, D.A., Belevich, N., Wikstrom, M. and Verkhovsky, M.I. (2007) *Proc. Natl. Acad. Sci. USA*, **104**, 2685–2690.

[9] Finklea, H.O. (2001) *J. Phys. Chem.*, **105**, 8685–8693.

[10] Jeuken, L.J.C., Jones, A.K., Chapman, S.K., Cecchini, G. and Armstrong, F.A. (2002) *J. Am. Chem. Soc.*, **124**, 5702–5713.

[11] Leger, C., Jones, A.K., Albracht, S.P.J. and Armstrong, F.A. (2002) *J. Phys. Chem. B.*, **106**, 13058–13063.

[12] Leger, C. and Bertrand, P. (2008) *Chemical Reviews*, **108**, 2379–2438.

[13] Friedrich, M.G., Robertson, J.W.F., Walz, D., Knoll, W. and Naumann, R.L.C. (2008) *Biophys. J.*, **94**, 3698–3705.

[14] Schach, D., Nowak, C., Gennis, R.B., Ferguson-Miller, S., Knoll, W., Walz, D. *et al.* (2010) *J. Electroanal. Chem.*, **649**, 268–276.

[15] Nowak, C., Laredo, T., Lipkowski, J., Gennis, R., Ferguson-Miller, S., Knoll, W. *et al.* (2011) *Metallomics*, **3**, 619–627.

[16] Reinel, D. and Dieterich, W.J. (1996) *Chem. Phys.*, **104**, 5234–5239.

[17] Einax, M., Solomon, G.C., Dieterich, W. and Nitzan, A. (2010) *J. Chem. Phys.*, **133**, 54102.

[18] Walz, D. (1979) *Biochim. Biophys. Acta.* **505**, 279–354.

[19] Bard, A.J. and Faulkner, L.R. (2001) *Electrochemical methods: fundamentals and applications*, 2nd ed. J. Wiley & Sons, New York.

[20] Kümmel, R. (1988) *Acta Hydrochim. Hydrobiol.*, **16**, 340.

[21] Naumann, R., Schiller, S.M., Giess, F., Grohe, B., Hartman, K.B., Karcher, I. *et al.* (2003) *Langmuir*, **19**, 5435–5443.

[22] Nowak, C., Santonicola, M.G., Schach, D., Zhu, J.P., Gennis, R.B., Ferguson-Miller, S. *et al.* (2010) C. *Soft Matter*, **6**, 5523–5532.

[23] Hiser, C., Mills, D.A., Schall, M. and Ferguson-Miller, S. (2001) *Biochemistry*, **40**, 1606–1615.

[24] Gorbikova, E.A., Vuorilehto, K., Wikstrom, M. and Verkhovsky, M.I. (2006) *Biochemistry*, **45**, 5641–5649.

[25] Smirnov, A.Y., Mourokh, L.G. and Nori, F. (2009) *J. Chem. Phys.*, **130**, 235105

[26] Popovic, D.M. and Stuchebrukhov, A.A. (2004) *J. Am. Chem. Soc.*, **126,** 1858–1871.

[27] Laviron, E. and Meunierprest, R. (1992) *J. Electroanal. Chem.*, **324**, 1–18.

[28] Meunierprest, R. and Laviron, E. (1992) *J. Electroanal. Chem.*, **328**, 33–46.

Time-Resolved Surface-Enhanced IR-Absorption Spectroscopy of direct Electron Transfer to Cytochrome *c* Oxidase from *R. sphaeroides*

Andreas Schwaighofer,[†#] Christoph Steininger,[†#] David M. Hildenbrandt,[†#] Johannes Srajer,[†§] Christoph Nowak[†§], Wolfgang Knoll[†] and Renate L.C. Naumann[†*]

[†]Austrian Institute of Technology GmbH, AIT, Donau-City Str. 1, 1220 Vienna, Austria

[§]Center of Electrochemical Surface Technology, CEST, Viktor-Kaplan-Straße 2, 2700 Wiener Neustadt, Austria

*Correspondence: Renate.Naumann@ait.ac.at

# These authors contributed equally to this work

ABSTRACT

Time-resolved surface-enhanced IR-absorption spectroscopy (tr-SEIRAS) triggered by electrochemical modulation has been performed on cytochrome *c* oxidase from *R. sphaeroides*. Single bands isolated from a broad band in the amide I region using phase sensitive detection were attributed to different redox centers. Their absorbances changing in the ms time scale could be fitted to a model based on protonation-dependent chemical reaction kinetics established previously. Substantial conformational changes of secondary structures coupled to redox transitions were revealed.

INTRODUCTION

Time-resolved Fourier transform infrared (tr-FTIR) spectroscopy is a powerful method to elucidate structure-function relationships even of large multi-redox center proteins such as the cytochrome *c* oxidase (C*c*O). In previous tr-studies, FTIR measurements were mostly triggered by photodissociation of CO adducts of C*c*O (1-10). Photodissociation of CO adducts has also been combined with oxidation of the enzyme by O_2 or caged O_2 (11-13), yielding real-time measurements of FTIR and UV/VIS spectra in the ms time scale (13). As an alternative to these approaches, we had introduced direct electron transfer (ET) or electronic wiring to C*c*O from *R. sphaeroides*, where the enzyme was immobilized in a strict orientation on the gold film of an ATR crystal, followed by reconstitution in a protein-tethered bilayer lipid membrane (ptBLM) (14-16). This allowed the application of surface-enhanced resonance Raman (SERR) and IR absorption (SEIRA) spectroscopy in the course of direct electrochemical reduction/oxidation of the C*c*O (17,18).

Direct ET to C*c*O also had been investigated by fast-scan voltammetry. Data were fitted to the sequential four ET model, according to which the enzyme undergoes direct ET to Cu_A coupled to the sequential electron exchange with the remaining four redox centers, heme *a*, heme a_3 and Cu_B (19). Changing to an oxygenated solution, the enzyme was shown to undergo a transition from a non-activated to an activated state and to become catalytically active (16-18). This finding was corroborated by potentiometric titrations on the C*c*O employing direct ET followed by SEIRA spectroscopy. 2D-correlations maps of these SEIRA spectra showed substantial conformational changes of the C*c*O being converted from the non-activated to the activated state (20). The sequential four ET model was later expanded to describe proton transport coupled to ET, considering acid dissociation constants of the oxidized and reduced form (pKr and pKo) of all four redox centers, respectively (21).

In the present work, we use this expanded model in order to analyze time-resolved SEIRA spectra of C*c*O incorporated in a ptBLM. We will be studying substrate-free, i.e. oxygen-free, four-electron transfer in the activated state of the enzyme. To this end, we use SEIRAS in the Step-Scan mode modulated by periodic potential pulses. The objective of this study is to receive information about vibrational modes of amino acids and peptide groups coupled to specific redox transitions. Vibrational components in the amide I region of the tr-SEIRA spectra had been identified and validated before by application of phase sensitive detection (22). Parameters such as band positions and full widths at half maximum (FWHM) values had thus been obtained, Table 1. These parameters will be used in the present study in order to deconvolute the highly overlapping bands in the tr-SEIRA spectra. Based on comparative IR and UV/VIS data found in

the literature (23), the deconvoluted components will be attributed to changes in specific redox centers. Absorbances plotted as a function of time will then be fitted to the extended model mentioned above (21). Fit parameters will be compared with the ones obtained in modelling studies of electrochemical data (19,21). Our results suggest that conformational changes coupled to redox transitions occur in the ms time scale dominated by the rate constant of electrochemical excitation. Thereby, secondary structures seem to undergo more substantial conformational changes than expected from previous FTIR studies (13).

Materials and Methods

Solvents and Chemicals

3-Mercaptopropyltrimethoxy-silane (MPTES, 95%) was purchased from ABCR GmbH (Karlsruhe, Germany). (C2-NTA) (≥95.0%) was obtained from Dojindo Laboratories (Kumamoto, Japan). 1,2-diphytanoyl-sn-glycero-3-phosphocholine (DiPhyPC, >99%) was provided by Avanti Polar Lipids (Alabaster, AL, US). Hydroxylamine hydrochloride ($NH_2OH{\cdot}HCl$, 99%), gold(III) chloride hydrate ($HAuCl_4{\cdot}xH2O$, 99.999%), 3,3'-dithiodipropionic acid (DTP, 99%) and dodecyl-β-D-maltoside (DDM, ≥98%) were purchased from Sigma-Aldrich (Steinheim, Germany).

Preparation of the two-layer gold surface on the ATR crystal

The preparation was done as previously described (22,24,25). Briefly, after modification with MPTES, the ATR crystal was provided with a 25 nm gold film by electrothermal evaporation (HHV Edwards Auto 306, Crawley, UK). Gold nanoparticles were grown on the gold film by immersing the crystal in 50 ml of an aqueous solution of hydroxylamine hydrochloride (0.4 mM), to which 500 µl of an aqueous solution of gold(III) chloride hydrate (0.3 mM) was added five times at 2-minutes intervals.

Immobilization of the protein

C*c*O was immobilized on the ATR crystal as described in detail by Schwaighofer et al. (22). C*c*O from *Rhodobacter sphaeroides* with a His-tag engineered to the C terminus of subunit II was expressed and purified according to Ferguson-Miller et al. (26). ATR crystals with the two-layer gold surface were immersed in a solution of 2.5 mM C2-NTA and 7.5 mM DTP in dry DMSO for 20 h. After chelating in 40 mM $NiCl_2$ in acetate buffer (50 mM, pH 5.5) and rinsing with purified water, C*c*O dissolved in DDM phosphate buffer (0.05 M K_2HPO_4, 0.1 M KCl, pH 8, 0.1% DDM) was adsorbed onto the NTA-functionalized surface at a final concentration of 100 nM. After 4-h adsorption time, the cell was rinsed with DDM phosphate buffer and 40 µM DiPhyPC in DDM phosphate buffer was added. Dialysis was performed by adding Bio-Beads to the lipid–detergent solution.

Cyclic voltammetry and activation of C*c*O

Electrochemical measurements were performed with a potentiostat from Autolab (PGSTAT12 with GPES 4.9 from Metrohm, Herisau, Switzerland) in a three-electrode configuration with gold as the working electrode, a Ag|AgCl,KCl_{sat} reference and a platinum wire as the counter electrode. All electrode potentials are quoted versus the standard hydrogen electrode (SHE). Cyclic voltammetry measurements were done in PBS solution (0.05 M K_2HPO_4, 0.1 M KCl, pH 8) with vertex potentials V_1 = +400 mV and V_2 = -800 mV at a sweep rate of 50 mVs^{-1}. Prior to infrared measurements, up to 20 cyclic voltammograms (CVs) were performed on the immobilized C*c*O under aerobic conditions to transfer the protein from the inactivated to the activated conformational state (16,17), indicated by a stationary state regarding peak currents and potentials (17). Thereafter, the aerobic solution was exchanged against an anaerobic PBS buffer, established by purging the buffer for 20 minutes with Ar and adding an oxygen trap consisting of glucose (0.3% w/w), glucose oxidase (75 µg/ml) and catalase (12.5 µg/ml).

tr-ATR-SEIRA-Spectroscopy modulated by electrochemical potentials

The electrochemical cell was mounted on top of a trapezoid single reflection silicon ATR crystal. The IR beam of the FTIR spectrometer (VERTEX 70v, from Bruker, Ettlingen, Germany) was coupled into the crystal at an angle of incidence Θ = 60° by using the custom-made setup described previously (24). All spectra were measured with parallel polarized light. The total reflected IR beam intensity was measured with a liquid nitrogen-cooled photovoltaic mercury cadmium telluride (MCT) detector. Measurements were done at 28 °C. FTIR spectra were recorded at 4 cm^{-1} resolution using Blackham-Harris 3-term apodization and a zero filling factor of 2. Because of the small absorbances of the protein monolayer in the presence of the large amount of water, interferograms were measured in double-sided mode and transformed into absorption spectra using the Power phase correction mode. An optical filter (LWP < 2.966 cm^{-1}) was used to reduce the high folding limit to 3159 cm^{-1} and consequently, the number of necessary interferogram points to 2842. The rectangular waveform used for the modulated excitation was provided by a function generator (Agilent 33250A, Santa Clara, CA, US) that triggered the Autolab potentiostat and the spectrometer. Potentials were periodically applied to the ptBLM on the gold film in the form of a square wave function to change the redox state of C*c*O from the fully oxidized (+400 mV) to the fully reduced state (-800 mV). Due to the charging of the Au/water interphase, the range of potentials actually affecting the enzyme deviates from the applied potential, see Fig S3. FTIR measurements were triggered by the fast potential change at the start of each period to record a succession of spectra that indicate the changes of IR absorbances as a function of time. Absorbances were calculated using the fully reduced state of the protein as a reference. Spectra were recorded at a frequency of 100 Hz (period = 10 ms, time-resolution = 200 µs, 150 co-additions). Spectra were analyzed using the software package OPUS 6.5.

Estimation of kinetic model parameters from tr-SEIRAS data

In our model system developed before (19,21) we employ chemical reaction kinetics to describe the sequential ET between redox centers, indicated by black arrows, which can each be in the reduced and oxidized state, denoted r and o, respectively (Fig. 1) Proton uptake and release

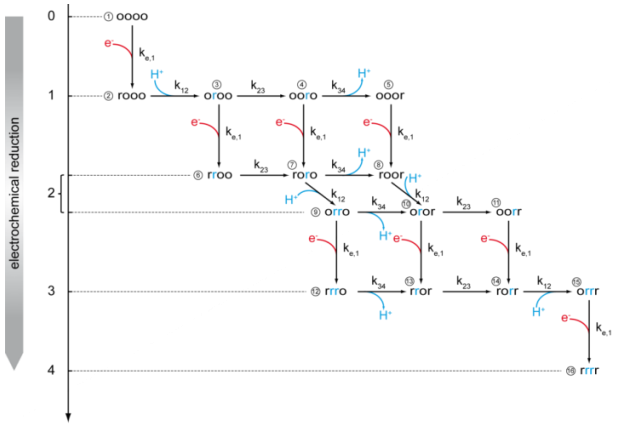

Figure 1: Kinetic scheme for sequential electron transfer in C*c*O under anaerobic conditions. The four centers are arranged in the order Cu_A, heme *a*, heme a_3 and Cu_B, which can be present either in the reduced (r) or oxidised (o) state. All of the r and o states can be protonated or deprotonated. Hence, the enzyme can exist in 16 different redox states and 256 protonation states. Vertical arrows with red branches represent electron uptake from the electrode, while black horizontal arrows indicate second-order reactions between redox centers. Blue arrows indicate proton uptake and release steps likely to occur as a consequence of second order ET reactions between redox centers.

indicated by blue arrows is considered in terms of independent acid dissociation constants for each of the different redox centers as identified in previous modeling studies (21). It has to be mentioned, however, that proton release would be prohibited in the absence of oxygen out of electrostatic reasons, whereas proton uptake is facilitated under both anaerobic and aerobic conditions. In the present study, electron uptake is provided by direct ET from an electrode to Cu_A or in other words, electrochemical modulation, followed exclusively under anaerobic conditions. That means the four redox centers are sequentially reduced and re-oxidized by applying alternatively positive and negative potential pulses (Fig. S3). Enzymatic turnover using oxygen cannot be expected. Changes of redox states are deduced from IR bands (Table 1) whose absorbances, A_i, change as a function of time. The temporal changes are then used to fit the model to the data. To this end, the model was further complemented to take into account deviation of the effective potential E_{eff} acting on the protein from the potential E, which is externally applied to the electrode. This deviation is attributed to the charging of the electrode/water interface and modeled by consecutive charging and "discharging" of an RC circuit with relaxation time τ with respect to the applied rectangular potential pulse, ΔE derived from vertex potentials $E_{p,0}$ and $E_{p,1}$ according to

$$\Delta E = E_{p,1} - E_{p,0} \tag{1}$$

$$E_{T/2} = E\left(t = \frac{T}{2}\right) = E_{p,1} - \Delta E \cdot e^{-\frac{T/2}{\tau}} - E_{p,0} \tag{2}$$

$$E_{eff}(t) = \begin{cases} E_{p,1} - \Delta E \cdot e^{-\frac{t}{\tau}} & for \quad 0 \le t \le \frac{T}{2} \\ E_{p,0} + E_{T/2} \cdot e^{-\frac{t-T/2}{\tau}} & for \quad \frac{T}{2} < t \le T \end{cases} \tag{3}$$

The kinetic model is based on a Master-equation approach, describing the time evolution of occupation probabilities of 24 = 16 possible redox states (conformations) of the enzyme (19,21). According to Beer-Lambert's law, the contributions of the redox states to the absorbance A_i at wavenumber ν and time t for a band associated with the i^{th} redox center are proportional to the overall probabilities of the oxidized and the reduced state of this center. The overall probabilities for the i^{th} center in the reduced and oxidized state can be derived from the conformation probabilities p_i (27):

$$A_i(\bar{\nu}, t) = k_{i,ox}(\bar{\nu})p_{i,ox}(t) + k_{i,red}(\bar{\nu})p_{i,red}(t) = k_{i,ox}(\bar{\nu}) + (k_{i,red}(\bar{\nu}) - k_{i,ox}(\bar{\nu}))p_{i,red}(t) \tag{4}$$

The proportionality constants $k_{i,red}(\bar{\nu})$ and $k_{i,ox}(\bar{\nu})$ are products of the effective optical path length, the concentration of protein, and the respective molar extinction coefficients. Since the absorbance $A_i(\bar{\nu}, 0)$ at the beginning of a potential pulse is chosen as a reference, the change in absorbance with time becomes (cf. Eq. 4)

$$\Delta A_i(\bar{\upsilon}, t) = \Delta A_i(\bar{\upsilon}) \cdot \left[p_{i,red}(t) - p_{i,red}(0)\right] + A_{i0}(\bar{\nu}). \tag{5}$$

The term $A_{i0}(\bar{\nu})$ is added in Eq. 5 to account for a possible deviation of $A_i(\bar{\nu}, 0)$ due to experimental scatter. In order to reduce the effect of experimental scatter for A_i at individual wavenumbers, $\Delta A_i(\bar{\nu}, t)$ is integrated over $\bar{\nu}$ thus yielding the band area.

Bayesian inference is used to obtain a set of parameters for which the best agreement of experimental and simulated data is achieved. Within this context we acquire maximum likelihood (MLE) as well as maximum a posteriori probability estimates (MAP) through use of Markov Chain Monte Carlo Simulation (28).

Due to ambiguities in the pH dependence of midpoint potentials, see ref (21), we chose as fitting parameters, the inherently pH-independent standard redox potentials E^0_{1-4} as well as the pK values of the reduced and oxidized form, pK^r_{1-4} and pK^o_{1-4} of the four centers, respectively, numerated in the order of sequential ET, Cu_A, heme *a*, heme a_3 and Cu_B. As for the kinetic parameters, we have to distinguish between electrochemical ET to Cu_A characterized by the electrochemical rate constant k_e, and chemical reaction kinetics between consecutive redox centers with rate constants $k_{l,m}$, described in the Supporting Material. Finally, τ, the time constant of charging the interface according to Eq. 2. has also to be included in the list of fitted parameters, table 2. Details on fitting assumptions and accuracies are discussed in the Supporting Information.

Both, the reaction kinetic model and the fitting routine were implemented using MATLAB R2010b. For details, see the supplementary information.

Results and Discussion

C*c*O from *Rhodobacter sphaeroides* was immobilized on the two-layer gold film deposited on an ATR crystal in a ptBLM and transferred to the activated state. Thereafter, the C*c*O was subjected to SEIRA measurements in the Step-Scan mode by applying periodic potential pulses stepping between -800 mV to +400 mV, at a modulation frequency of 100 Hz as described in the experimental section. Other excitation frequencies were also used, but 100 Hz had shown the best suitable condition, see Fig. S12. Tr-SEIRA spectra obtained after baseline correction (Fig. 2) showed a broad band in the amide I region, similar to the prominent bands obtained previously in potentiometric titration experiments followed by SEIRAS. However, in tr-SEIRAS, the spectra contained many more overlapping bands revealed by a treatment called phase sensitive detection (PSD), described in the supplementary information and in more detail in a separate publication (22). PSD also revealed a large water band at 1643 cm^{-1}, which had to be subtracted in order not to obscure the band evaluation due to the secondary structures, as seen in Fig. S13. The list of bands finally obtained is shown in Table 1 together with the parameters obtained from PSD such as band positions and full widths at half maximum (FWHM).

The format of the ptBLM is so far not suitable to conduct UV/VIS simultaneously with tr-SEIRAS measurements. However, we know from independent fast-scan voltammetry data, that direct ET does take place in the potential window used for the modulation (19). Moreover, electrochemical reduction of the heme centers had been demonstrated by surface-enhanced resonance Raman spectroscopy (SERRS) (16). Therefore, it is safe to assume that we have been able to follow conformational changes of secondary structures such as α-helices and β-sheets, coupled to redox changes and to be entitled to employ band assignments published by other groups (23), see table 1. Bands had been attributed to redox centers on the basis of UV/VIS measurements from simultaneously performed with FTIR measurements of C*c*O (23).

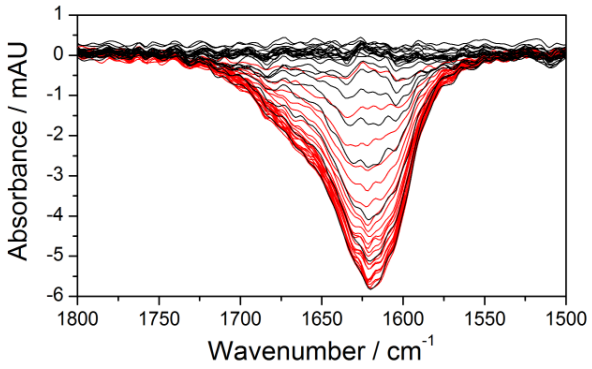

Figure 2: Tr-SEIRA spectra of the activated C*c*O under anaerobic conditions. Spectra of the first excitation half period (oxidation) are shown in red, those of the second half period (reduction) are indicated in black.

TABLE 1 Band parameters calculated by the PSD fitting procedure described in the supplementary information and in ref. (22) and tentative band assignments of the vibrational components on the basis of data from the literature, see references (*R. sphaeroides* numbering).

Experimental		Literature		
band position [cm^{-1}]	FWHM [cm^{-1}]	band position [cm^{-1}](ref)	redox center	tentative band assignment* (absorber; vibration type; tentative residue)
1591.3	6.2	1592(23)	Cu_A	H, HisH; ν(C═C); H224, H189 R, Arg-H_5^+; $\nu_{as}(CN_3H_5^+)$; R481 D, Asp-COO^-; $\nu_{as}(COO^-)$; D186
1596.5	13.4	1594(29)	heme *a*	His
1603.2	11.3	1603(23)	Cu_A	amide I, β-sheet; ν(C═O)
1610.7	11.7	1606(29)	heme *a*	ν(C═O) CHO heme *a* ν_{37} heme *a* ring O^- Tyr
1615.2	8.1	1637-1613(30)	---	amide I, β-sheet
1619.9	9.1	1618(23)	heme a_3	Y, Tyr-OH; ν(CC) ring; δ(CH); Y288 W; ν(CC), ν(C═C); W280, W172 vinyl; ν(C-C) amide I, β-sheet, ν(C═O)
		1618(29)	heme *a*/ heme a_3	$\nu(C_\alpha{=}C_\beta)$ vinyl group (heme a/a_3) amide I, β-sheet
1625.7	8.0	1630(23)	heme a_3	R, Arg-H_5^+; $\nu_s(CN_3H_5+)$; R481 H, $HisH_2^+$; ν(C═C); H411 amide I, β-sheet; ν(C═O)
1643.0	80.0	1645(31)	---	δ(HOH)
1647.7	10.1	1651(23)	Cu_A	amide I, α-helical; ν(C═O)
1653.3	8.0	1655(23)	heme a_3	amide I, α-helical; ν(C═O)
		1656(29)	heme a_3	amide I, α-helical
1662.2	16.4	1661(23)	heme *a*	amide I, α-helical; ν(C═O) amide I, turns; ν(C═O)
		1662(29)	heme *a*/ heme a_3	ν(C═O) CHO-heme a_3 amide I, α-helical $\nu_{as}(CN_3H_5)$ Arg
1690.4	10.3	1689(23)	Cu_A	amide I, β-sheet; ν(C═O)

*Numeration of the amino acid side chains refers to C*c*O from (*R. sphaeroides*). Band positions were allowed to vary within the margin of ±1cm^{-1}.

PSD-deconvoluted tr-SEIRA spectra are shown in Fig. 3. Band areas obtained from Fig. 3 were plotted as a function of time, see examples in Fig. 4 used for the fitting routine, all of which are negative bands. That means they represent reduced species, which gradually disappear in the first half period of the potential pulse going from -800 mV to +400 mV and re-appear in the second half period, when the potential changes in the opposite direction. Other bands including positive bands are shown in the supplementary information (Fig. S14A-F). Positive bands mean they

represent oxidized species that are formed while proceeding from the fully reduced to the fully oxidized state at -800 mV and at +400 mV, respectively. The bands at 1603, 1610 and 1625 cm^{-1}, assigned to Cu_A, heme a, and heme a_3, respectively, were selected to be fitted to the kinetic model of the C*c*O (21). Evaluation using PSD did not yield any bands attributed to Cu_B, because

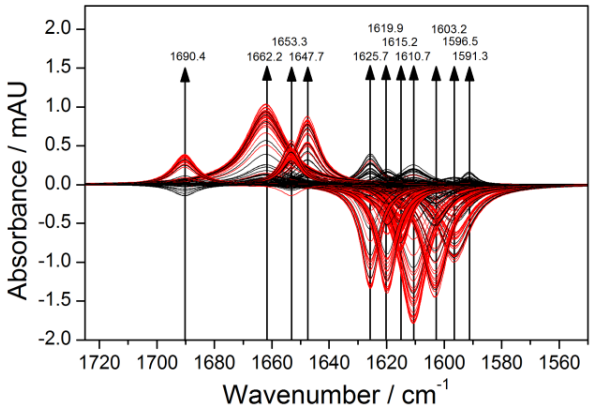

Figure 3: Simulated spectra of deconvoluted bands revealed by PSD at an excitation frequency of 100 Hz. Subtraction of OH bending band (see Fig. S13) reveals positive and negative bands that are attributed to oxidized and reduced species, respectively. Spectra obtained in the first and second excitation half period are shown in red and black, respectively.

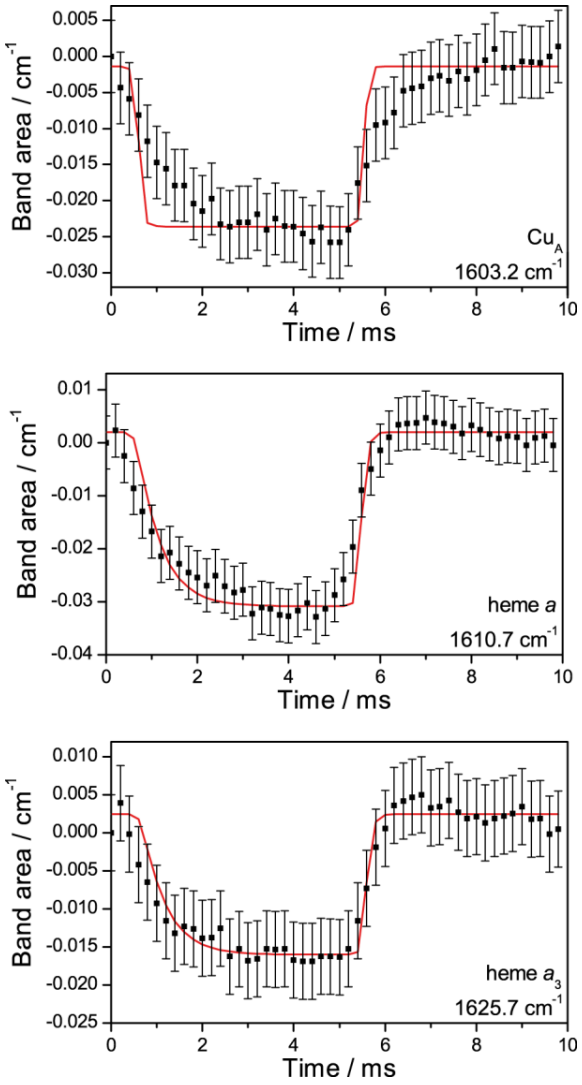

Figure 4: Plots of band areas vs. time (black squares) of the bands at 1603.2 (Cu_A), 1610.7 (heme *a*) and 1625.7 cm^{-1} (heme a_3). Fitted curves of band areas vs. time to the sequential four-electron ET model of C*c*O are given as solid, red lines. Uncertainties of the measurement are indicated as error bars.

they are generally expected to appear in the fingerprint region, where they are too small in the obtained spectra to be discriminated from noise. Even though only three of the four redox centers are observed in the experiments, reasonable fits were obtained using the four center model. For the fitted curves see also Fig. 4, fit parameters are shown in Table 2.

As seen in Fig. 4, different centers follow very similar time traces, which can be explained by the fact that the overall rate limiting factor is a combination of τ, the time constant of the charging current, and k_e, the electrochemical rate constant. Both are in the millisecond time scale and cannot be separated from each other experimentally and from the rate of ET between redox

TABLE 2 Set of model parameters isolated as maximum likelyhood estimation (MLE) by the fitting routine, compare table S4.

τ [ms]	0.55
k_e [s^{-1}]	536.36
E^0_1 [mV]	-192.1
E^0_2 [mV]	-202.3
E^0_3 [mV]	-127.7
E^0_4 [mV]	-443.7
pK^r_1	8.09
pK^r_2	9.29
pK^r_3	4.51
pK^r_4	1.49
pK^o_1	2.48
pK^o_2	5.38
pK^o_3	1.84
pK^o_4	0.78

centers. Due to this limitation, rate constants of ET between the redox centers have to be fixed to high values (see Table S1), while the overall rate is in ms time scale for all centers, (Fig 4). k_e and τ were found to be in larger and smaller, respectively, than values from previous fit results of cyclic voltammetry data (k_e = 370 s-1, τ ~ 1 ms) (19), although in the same order of magnitude. We explain the relatively poor fit of the Cu_A time trace as compared to the ones from heme *a* and a_3, by the inadequacies of the simplified reaction scheme, see for a discussion further below. However, taking into account all the parameters listed in table 2, the overall fit result turned out to be the one depicted in Fig. 4. The uncertainty of all the parameters has been deduced from histograms shown in the Supporting Material (Figs. S4-S11).

CONCLUSION

Results show that fitting the parameters of the expanded model of the C*c*O to the experimental data can be preformed with high accuracy. The most important fit results are the E^0 values of the four centers. E^0 values are apparently shifted to negative values compared to known midpoint potentials ref. (23), well in accordance with previous CV (16), and titration data followed by

SEIRAS (17) and SERRS (32). Modelling studies (19,21) had revealed a redox process at around −200 mV consuming four electrons, which can be observed even under anaerobic conditions but only following several enzyme turnovers in the presence of oxygen. We tentatively interpret this observation in terms of higher oxidation states of the C*c*O, e.g. the states P_M and F also called C_4 and C_3 according to the terminology recently introduced by Wikström (33), in which the subscript describes the number of oxidizing equivalents in the binuclear heme-copper center. Our studies seem to indicate that one of these states prevails for some time after returning to anaerobic conditions. Midpoint potentials of these states were reported by Wikstrom, to be $E_{m,7}$ = +817 and +762 mV, respectively, corrected for the difference in pH and membrane potential, corresponding to $E_{m,7}$ = +417 and +350 mV actually observed (34). These values fit perfectly well into the energy diagram of different states of the enzyme cycle between cytochrome *c* ($E_{m,7}$ = +260 mV) and oxygen ($E_{m,>7}$ = >+400 mV), whereas the values found in our measurements are out of this range. For example, our E^0 are much too negative to be reduced by cytochrome *c*. We have to consider, however, that there is a fundamental difference between the enzyme cycle under physiological (33) and electrochemical conditions. Using electrochemistry, C_4 or C_3 may well be reduced in a single step back to the reduced state R(C_0) including all the oxygen trapped there. This process may proceed at a potential different from the $E_{m,7}$ of transitions C_4/C_3 and C_3/C_2 as determined by equilibrium titrations mentioned above (34). The reason is, that under physiological conditions, the enzyme has to pass the fully oxidized state O_H (C_2), reduced step-wise by cytochrome *c* to obtain the reduced states E(C_1) and R(C_0), before oxygen can be absorbed. Under electrochemical conditions, on the other hand, we have evidence from Raman studies that at -200 mV both hemes are reduced to the $Fe^{(II+)}$ state and that oxygen bound to the BNC is fully reduced to H_2O, provided the enzyme had first been activated by several enzyme turnovers. The conclusion regarding oxygen is deduced from modelling studies of enzyme turnover using the model presented in Fig. 2 modified to include oxygen reduction (21). We conclude that the electrochemical result does not reflect the natural behaviour of the enzyme, nevertheless, it could give us a clue to the hypothetical metastable high-energy configuration of the binuclear center.

Electrochemical oxygen reduction and reoxidation at the gold electrode in the absence of C*c*O is a strongly kinetically-controlled process, with reduction and oxidation taking place at potentials well separated at around -400 and >+800 mV respectively, far away from the standard redox potential of oxygen ($E^{Ø}$ = +400 mV at pH=>>7) (35). In the presence of C*c*O, the reduction potental is shifted to -200 mV, indicating the facilitated oxygen reduction due to enzyme turnover. Indications of this process should disppear from the voltammogram or the SERR and SEIRA spectrum, when oxygen has been removed, which obviously is not the case. Hence we tentatively explain the apparent negative potentials in terms of a transient state of the general configuration C_4, which even after removal of oxygen from solution prevails on the enzyme for some time, to be electrochemically reduced back to the state C_0 thereby consuming four electrons. (The role of the tyrosin radical is deliberately not included in the discussion). Out of obvious reasons, our simplified reaction scheme does not include the C_4 state, but its existence is revealed by an apparent shift of all the E^0 values to negative values. This idea is supported by the fact that appearance and duration of this state not only depends on the number of turnovers needed for activation but also from the batch of C*c*O used for the measurements. Over the past years, we have investigated more than 20 batches of C*c*O from different labs and the enigmatic reduction step at -200 mV under anaerobic conditions had very different life times from zero to hours, whereas the continuous current under aerobic condtions indicating enzyme turnover gives

very stable and reproducible signals (see Fig. 4C,D and 4B in ref. (19), respectively.) The hypothesis of a metastable state was originally brought forward by Wikstrom, who considered the fully oxidized state O or C_2, to attain a high-energy configuration O_H after several turnovers (36). This may still apply to physiological conditions. However, using electrochemistry the transient state seems more likely to be represented by a kind of C_4 state. Further studies will be needed to verify this assumption.

Proton uptake and release had been considered due to differences in pK values between consecutive redox couples, e.g. $pK_2^r > pK_1^r$ and $pK_3^r > pK_4^r$, respectively. pK^r values found by fitting are in reasonable agreement with these assumptions (21), although their uncertainty is relatively high as seen by the histograms (Figs. S4-S11).

Further information can also be deduced from our tr-SEIRAS studies regarding conformational changes of secondary structures. Absorbances in the amide I region are relatively high, particularly in comparison to those in the fingerprint region, which are too small to be evaluated as a function of time. This is different from previous tr-FTIR studies (13) showing more evenly distributed absorbances in the region 1000-1800 cm^{-1}, however, in the course of the reaction of reduced C*c*O with oxygen. The prominent amide I bands in our spectra can partially be explained by the theory of SEIRAS, predicting that dipoles oriented perpendicular to the surface are subject to a particularly high surface-enhancement effect, while dipoles pointing in other directions are not detected (37,38). The proteins are arranged on the surface with the α-helices pointing in the z-direction, while strong dipoles are generated during sequential ET. These effects are enhanced by the pre-orientation of the C*c*O molecules within the ptBLM. Nevertheless, conformational changes appear substantial, particularly considering the absorbance of the unmodulated SEIRA spectrum of C*c*O (Fig. S15). This is well in agreement with our titration studies (17,20), although the distribution between the two kinds of secondary structures was quite different from the one found in the time-resolved study. As for the titration, the helical structures are more prominent, while in the tr-SEIRA spectra the β-sheets are more strongly represented, as see the bands at 1603, 1615, 1619, 1625 cm^{-1}, while the band at 1653 cm^{-1}, characteristic for α-helices is weak in comparison. These findings are well in agreement with the higher flexibility of β-sheets found in MD studies of high-resolution crystallographic structures (39,40). The greater rigidity of the α-helices, on the other hand, prevents these structures from following the excitation at high modulation frequencies, resulting in a lower absorbance of the respective IR-signals. Substantial conformational changes were also observed recently in separate high-resolution crystallography images of the reduced and oxidized form of C*c*O (41).

In summary, the time-resolution of electrochemically modulated Step-Scan measurements was found to be in the ms time scale, limited by electrochemical excitation. Hence kinetic constants of ET between redox centers cannot be deduced. In comparison, Gorbikova et al. (13) found a time-resolution of FTIR measurements in the time scale of seconds, however, using a mutant with a deliberately delayed time constant. Moreover, they investigated the reaction of reduced C*c*O with oxygen. In our work, conformational changes of secondary structures coupled to ET appear to be more substantial than expected from previous FTIR investigations, however, in agreement with high-resolution crystallography data and resulting MD calculations. (39,41) The shift of E^0 to negative values versus known midpoint potentials has been confirmed as well as the magnitude of the electrochemical rate constant of electronic wiring of the C*c*O to the electrode.

The negative shift has tentatively been explained in terms of the hypothetical metastable high-energy configuration of the binuclear center.

ACKNOWLEDGEMENT

We are grateful to Prof. Martin Neumann, University of Vienna, for helpful discussions and for providing expertise in all questions related to the Markov chain Monte Carlo simulations. We also gratefully acknowledge the constant support from Prof. Shelagh Ferguson-Miller, and Carrie Hiser, Michigan State University, who provided us with high-quality preparations of C*c*O from *R. sphaeroides*. Partial support for this work was provided by ZIT, Center of Innovation and Technology of Vienna.

ABBREVIATIONS

ATR, attenuated total reflection; C*c*O, cytochrome c oxidase; CV, cyclic voltammetry; ET, electron transfer; FWHM, full width at half maximum; FTIR, fourier transform infrared spectroscopy; IR, infrared; MD, molecular dynamics; PBS, phosphate buffered saline; PSD, phase sensitive detection; ptBLM, protein tethered bilayer lipid membrane; SERRS, surface enhanced resonance Raman spectroscopy; SEIRAS, surface enhanced infrared absorption spectroscopy; SHE, standard hydrogen electrode; tr, time resolved; UV/VIS, ultra violet/visible; 2D, two dimensional;

SUPPORTING CITATIONS

References (42-47) appear in the Supporting Material.

REFERENCES

1. Bailey, J. A., F. L. Tomson, S. L. Mecklenburg, G. M. MacDonald, A. Katsonouri, A. Puustinen, R. B. Gennis, W. H. Woodruff, and R. B. Dyer. 2002. Time-resolved step-scan Fourier transform infrared spectroscopy of the CO adducts of bovine cytochrome c oxidase and of cytochrome bo(3) from Escherichia coli. *Biochemistry* 41:2675-2683.
2. Heitbrink, D., H. Sigurdson, C. Bolwien, P. Brzezinski, and J. Heberle. 2002. Transient Binding of CO to CuB in Cytochrome c Oxidase Is Dynamically Linked to Structural Changes around a Carboxyl Group: A Time-Resolved Step-Scan Fourier Transform Infrared Investigation. *Biophys. J.* 82:1-10.
3. Pinakoulaki, E., U. Pfitzner, B. Ludwig, and C. Varotsis. 2002. The role of the cross-link His-Tyr in the functional properties of the binuclear center in cytochrome c oxidase. *The Journal of biological chemistry* 277:13563-13568.
4. Stavrakis, S., K. Koutsoupakis, E. Pinakoulaki, A. Urbani, M. Saraste, and C. Varotsis. 2002. Decay of the Transient CuB−CO Complex Is Accompanied by Formation of the Heme

Fe−CO Complex of Cytochrome cbb3−CO at Ambient Temperature: Evidence from Time-Resolved Fourier Transform Infrared Spectroscopy. *J. Am. Chem. Soc.* 124:3814-3815.

5. Koutsoupakis, C., E. Pinakoulaki, S. Stavrakis, V. Daskalakis, and C. Varotsis. 2004. Time-resolved step-scan Fourier transform infrared investigation of heme-copper oxidases: implications for O2 input and H2O/H+ output channels. *Biochim. Biophys. Acta, Bioenerg.* 1655:347-352.
6. Nyquist, R. M., D. Heitbrink, C. Bolwien, R. B. Gennis, and J. Heberle. 2003. Direct observation of protonation reactions during the catalytic cycle of cytochrome c oxidase. *Proc. Natl. Acad. Sci. U.S.A.* 100:8715-8720.
7. Okuno, D., T. Iwase, K. Shinzawa-Itoh, S. Yoshikawa, and T. Kitagawa. 2003. FTIR Detection of Protonation/Deprotonation of Key Carboxyl Side Chains Caused by Redox Change of the CuA-Heme a Moiety and Ligand Dissociation from the Heme a3-CuB Center of Bovine Heart Cytochrome c Oxidase. *J. Am. Chem. Soc.* 125:7209-7218.
8. Rost, B., J. Behr, P. Hellwig, O. M. H. Richter, B. Ludwig, H. Michel, and W. Mantele. 1999. Time-resolved FT-IR studies on the CO adduct of Paracoccus denitrificans cytochrome c oxidase: Comparison of the fully reduced and the mixed valence form. *Biochemistry* 38:7565-7571.
9. McMahon, B. H., M. Fabian, F. Tomson, T. P. Causgrove, J. A. Bailey, F. N. Rein, R. B. Dyer, G. Palmer, R. B. Gennis, and W. H. Woodruff. 2004. FTIR studies of internal proton transfer reactions linked to inter-heme electron transfer in bovine cytochrome c oxidase. *Biochim. Biophys. Acta, Bioenerg.* 1655:321-331.
10. Tomson, F., J. A. Bailey, R. B. Gennis, C. J. Unkefer, Z. H. Li, L. A. Silks, R. A. Martinez, R. J. Donohoe, R. B. Dyer, and W. H. Woodruff. 2002. Direct infrared detection of the covalently ring linked His-Tyr structure in the active site of the heme-copper oxidases. *Biochemistry* 41:14383-14390.
11. Nyquist, R. M., D. Heitbrink, C. Bolwien, T. A. Wells, R. B. Gennis, and J. Heberle. 2001. Perfusion-induced redox differences in cytochrome c oxidase: ATR/FT-IR spectroscopy. *FEBS Lett.* 505:63-67.
12. Prutsch, A., K. Vogtt, C. Ludovici, and M. Lübben. 2002. Electron transfer at the low-spin heme b of cytochrome bo3 induces an environmental change of the catalytic enhancer glutamic acid-286. *Biochim. Biophys. Acta, Bioenerg.* 1554:22-28.
13. Gorbikova, E. A., N. P. Belevich, M. Wikström, and M. I. Verkhovsky. 2007. Time-Resolved ATR-FTIR Spectroscopy of the Oxygen Reaction in the D124N Mutant of Cytochrome c Oxidase from Paracoccus denitrificans†. *Biochemistry* 46:13141-13148.
14. Giess, F., M. Friedrich, J. Heberle, R. Naumann, and W. Knoll. 2004. The Protein-Tethered Lipid Bilayer: A Novel Mimic of the Biological Membrane. *Biophys. J.* 87:3213-3220.
15. Friedrich, M. G., F. Gie, R. Naumann, W. Knoll, K. Ataka, J. Heberle, J. Hrabakova, D. H. Murgida, and P. Hildebrandt. 2004. Active site structure and redox processes of cytochrome c oxidase immobilised in a novel biomimetic lipid membrane on an electrode. *Chem. Commun.*:2376-2377.
16. Friedrich, M. G., J. W. F. Robertson, D. Walz, W. Knoll, and R. L. C. Naumann. 2008. Electronic Wiring of a Multi-Redox Site Membrane Protein in a Biomimetic Surface Architecture. *Biophys. J.* 94:3698-3705.

17. Nowak, C., M. G. Santonicola, D. Schach, J. Zhu, R. B. Gennis, S. Ferguson-Miller, D. Baurecht, D. Walz, W. Knoll, and R. L. C. Naumann. 2010. Conformational transitions and molecular hysteresis of cytochrome c oxidase: Varying the redox state by electronic wiring. *Soft Matter* 6:5523-5532.
18. Nowak, C., D. Schach, J. Gebert, M. Grosserueschkamp, R. B. Gennis, S. Ferguson-Miller, W. Knoll, D. Walz, and R. L. C. Naumann. 2011. Oriented immobilization and electron transfer to the cytochrome c oxidase. *J. Solid State Electrochem.* 15:105-114.
19. Schach, D., C. Nowak, R. B. Gennis, S. Ferguson-Miller, W. Knoll, D. Walz, and R. L. C. Naumann. 2010. Modeling direct electron transfer to a multi-redox center protein: Cytochrome c oxidase. *J. Electroanal. Chem.* 649:268-276.
20. Nowak, C., T. Laredo, J. Gebert, J. Lipkowski, R. B. Gennis, S. Ferguson-Miller, W. Knoll, and R. L. C. Naumann. 2011. 2D-SEIRA spectroscopy to highlight conformational changes of the cytochrome c oxidase induced by direct electron transfer. *Metallomics* 3:619-627.
21. Srajer, J., A. Schwaighofer, D. M. Hildenbrandt, A. Kibrom, and R. L. C. Naumann. 2013. A kinetic model of proton transport in a multi-redox centre protein: cytochrome coxidase. *Prog. React. Kinet. Mech.* 38:32-47.
22. Schwaighofer, A., S. Ferguson-Miller, R. L. C. Naumann, W. Knoll, and C. Nowak. 2013. Phase Sensitive Detection in Modulation Excitation Spectroscopy applied to potential induced electron transfer in Cytochrome c Oxidase. *Appl. Spectrosc.* in press.
23. Gorbikova, E. A., K. Vuorilehto, M. Wikstrom, and M. I. Verkhovsky. 2006. Redox titration of all electron carriers of cytochrome c oxidase by Fourier transform infrared spectroscopy. *Biochemistry* 45:5641-5649.
24. Nowak, C., C. Luening, W. Knoll, and R. L. C. Naumann. 2009. A Two-Layer Gold Surface with Improved Surface Enhancement for Spectro-Electrochemistry Using Surface-Enhanced Infrared Absorption Spectroscopy. *Appl. Spectrosc.* 63:1068-1074.
25. Nowak, C., C. Luening, D. Schach, D. Baurecht, W. Knoll, and R. L. C. Naumann. 2009. Electron Transfer Kinetics of Cytochrome C in the Submillisecond Time Regime Using Time-Resolved Surface-Enhanced Infrared Absorption Spectroscopy. *J. Phys. Chem. C* 113:2256-2262.
26. Hiser, C., D. A. Mills, M. Schall, and S. Ferguson-Miller. 2001. C-terminal truncation and histidine-tagging of cytochrome c oxidase subunit II reveals the native processing site, shows involvement of the C-terminus in cytochrome c binding, and improves the assay for proton pumping. *Biochemistry* 40:1606-1615.
27. Schach, D. 2011. Direct Electron Transfer to the Cytochrome c Oxidase investigated by Electrochemistry and Time-Resolved Surface-Enhanced Infrared Absorption Spectroscopy. Ph.D Thesis, Johannes Gutenberg Universität Mainz.
28. Haario, H., M. Laine, A. Mira, and E. Saksman. 2006. DRAM: Efficient adaptive MCMC. *Stat Comput* 16:339-354.
29. Hellwig, P., S. Grzybek, J. Behr, B. Ludwig, H. Michel, and W. Mantele. 1999. Electrochemical and Ultraviolet/Visible/Infrared Spectroscopic Analysis of Heme a and a3 Redox Reactions in the Cytochrome c Oxidase from Paracoccus denitrificans: Separation of Heme a and a3 Contributions and Assignment of Vibrational Modes. *Biochemistry* 38:1685-1694.

30. Goormaghtigh, E., V. Cabiaux, and J.-M. Ruysschaert. 1990. Secondary structure and dosage of soluble and membrane proteins by attenuated total reflection Fourier-transform infrared spectroscopy on hydrated films. *Eur. J. Biochem.* 193:409-420.
31. Stuart, B. 1997. Biological Applications of Infrared Spectroscopy. New York: Wiley.
32. Grosserueschkamp, M., C. Nowak, W. Knoll, and R. L. C. Naumann. 2010. Time-resolved surface-enhanced resonance Raman spectro-electrochemistry of heme proteins. *Spectroscopy* 24:125-129.
33. Wikstrom, M. 2012. Active site intermediates in the reduction of O-2 by cytochrome oxidase, and their derivatives. *Biochim. Biophys. Acta, Bioenerg.* 1817:468-475.
34. Wikstrom, M. and M. I. Verkhovsky. 2006. Towards the mechanism of proton pumping by the haem-copper oxidases. *Biochim. Biophys. Acta, Bioenerg.* 1757:1047-1051.
35. Bard, A. J., R. Parsons, and J. Jordan. 1985. Standard Potentials in Aqueous Solutions: IUPAC (Marcel Dekker), New York, USA,.
36. Wikstrom, M. 2004. Cytochrome c oxidase: 25 years of the elusive proton pump. *Biochim. Biophys. Acta, Bioenerg.* 1655:241-247.
37. Osawa, M. 2001. Surface-enhanced infrared absorption. *Near-Field Optics and Surface Plasmon Polaritons* 81:163-187.
38. Nedelkovski, V., A. Schwaighofer, C. Wraight, C. Nowak, and R. L. C. Naumann. 2013. Surface-Enhanced Infrared Absorption Spectroscopy (SEIRAS) of Light-Activated Photosynthetic Reaction Centers from Rhodobacter sphaeroides. *J. Phys. Chem. C* DOI: 10.1021/jp4056347.
39. Buhrow, L., S. Ferguson-Miller, and Leslie A. Kuhn. 2012. From Static Structure to Living Protein: Computational Analysis of Cytochrome c Oxidase Main-chain Flexibility. *Biophys. J.* 102:2158-2166.
40. Jian, L., Q. Ling, and S. Ferguson-Miller. 2011. Crystallographic and online spectral evidence for role of conformational change and conserved water in cytochrome oxidase proton pump. *Proc. Natl. Acad. Sci. U.S.A.* 108:1284-1289.
41. Ferguson-Miller, S., C. Hiser, and J. Liu. 2012. Gating and regulation of the cytochrome c oxidase proton pump. *Biochim. Biophys. Acta, Bioenerg.* 1817:489-494.
42. Calvetti, D. and E. Somersalo. 2007. Introduction to Bayesian Scientific Computing. Berlin: Springer Science+Business Media.
43. Gelman, A., J. B. Carlin, H. S. Stern, and D. B. Rubin. 2004. Bayesian data analysis. London: Chapman and Hall/CRC.
44. Robert, C. P. 2007. The Bayesian Choice. Berlin: Springer Science+Business Media
45. hdp, R. p. T. http://rss.acs.unt.edu/Rdoc/library/TeachingDemos/html/hpd.html.
46. Metropolis, N., A. Rosenbluth, M. Rosenbluth, A. Teller, and E. Teller. 1953. Equation of State Calculations by Fast Computing Machines. *The Journal of Chemical Physics* 21:1087-1092.
47. matlab toolbox: Marko Laine, University of Helsinki. http://helios.fmi.fi/~lainema/mcmc/.

Supplementary Information

Time-Resolved Surface-Enhanced IR-Absorption Spectroscopy of direct Electron Transfer to Cytochrome *c* Oxidase

Andreas Schwaighofer,[†#] Christoph Steininger,[†#] David M. Hildenbrandt,[†#] Johannes Srajer,[† §] Shelagh Ferguson-Miller,[‡] Christoph Nowak[†§] , Wolfgang Knoll[†] and Renate L.C. Naumann[†*]

Transformation of the CcO into the activated state using cyclic voltammetry

The CcO from *Rhodobacter sphaeroides* with the his-tag attached to subunit II [22] was immobilized on a gold film deposited on the ATR crystal of an IR spectrometer [17] and reconstituted into a ptBLM [23,15]. In this orientation, electrons were transferred to the redox centers of the protein via Cu_A, the first electron acceptor. This was deduced from cyclic voltammograms taken under strictly anaerobic conditions, showing peaks in the range 200 to 600 mV (Fig. S1A), corresponding to midpoint potentials of redox centers[7]. Changing to an air-saturated solution, the enzyme started to work under turnover conditions[15]. Two peaks appeared in the negative potential range, slightly shifting in the positive direction with successive scans (Fig. S1B). Finally, peak potentials under steady state conditions of –242 mV and –530 mV were reached. These peaks have previously been attributed to repeated electron and proton transfer, characterized by the amplified current density[15]. Surprisingly, upon returning to anaerobic conditions, the peak potential of the cyclic voltammogram of CcO was shifted by more than 400 mV in the negative direction[15] (Fig. S1C). We deduced from these results that the enzyme undergoes a gradual transition from a non-activated to an activated conformational state when the enzyme, under aerobic conditions, passes through a number of redox cycles (Fig. 1B). This is equivalent to the transition from the resting to the pulsed state when the CcO reconstituted in liposomes is subjected to oxygen pulses.[20,24,25]

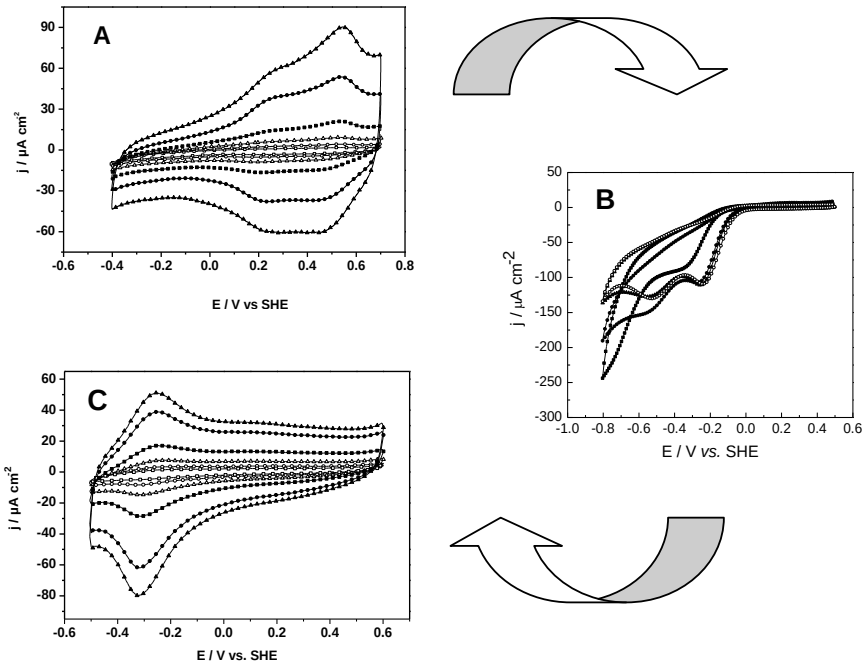

Fig. S1: Cyclic voltammograms of CcO immobilized via His-tag on subunit II, i.e. with Cu_A directed towards the electrode (cf. Fig.1A) (A) under anaerobic conditions before activation (scan rate/Vs^{-1} 0.05, 0.1, 02, 0.4, 0.8, 1.6) (B) upon evolution of the protein catalytic activity under aerobic conditions, i.e. activation (1st, 5th, 10th, and 20th scan with scan rate 0.05 V s^{-1}), and (C) under anaerobic conditions after activation (scan rate/V s^{-1} 0.05, 0.1, 0.2, 0.3, 0.4, 0.5, and 1V).

Principle of electrochemically modulated tr-SEIRAS

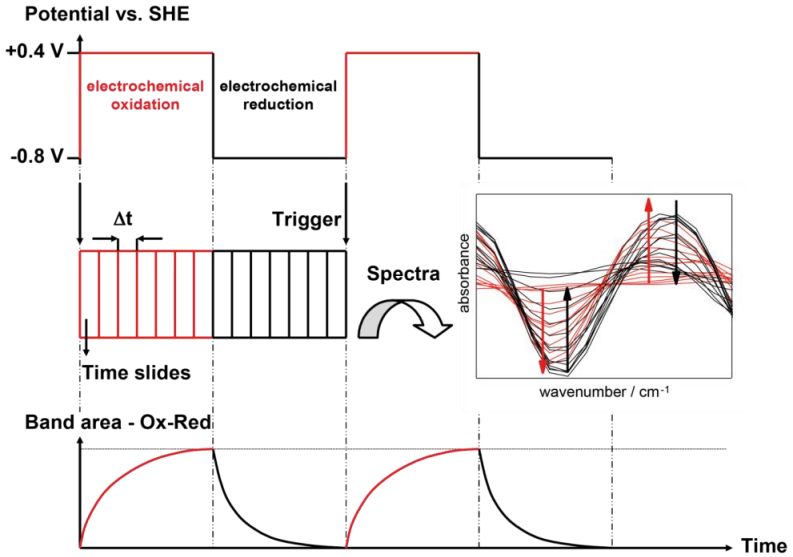

Fig. S2 Principle of electrochemically modulated tr-SEIRAS. Positive and negative potential pulses are periodically applied to the electrode, which is also the sensor surface. Spectra are recorded

in the step-scan mode at different time slides (50 per period). Band amplitudes oscillate between reduced and oxidized state.

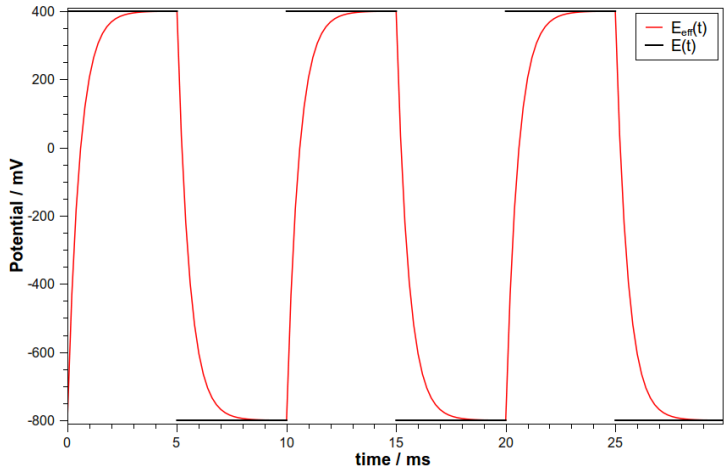

Figure S3: Applied, E, and effective Potentials, E_{eff}, calculated using eq (2) and the parameter value of τ = 0.55 ms obtained from the fitting routine described below, table S4.

Kinetic Model

According to the kinetic model presented in (21), the temporal evolution of the system of redox states of the enzyme (Fig. 1) is governed by the master equation

$$\frac{d}{dt}P_i = \sum_{j \neq i} k_{ij}P_i - k_{ji}P_j,$$

where k_{ij} and k_{ji} are the forward and backward reaction rates for the transition from redox state i into state j. The relation between these reaction rates is defined by the equilibrium constant $K=\frac{k_{ij}}{k_{ji}}$. Since we are dealing with a single complex, the condition

$$\sum_{i=1}^{16} P_i = 1$$

holds at any time.
Hence, the overall probabilities for the *i* th center in the reduced and oxidized state are, respectively,

$$p_{i,red} = \sum_k P_{k|i,red} \quad , \qquad p_{i,ox} = 1 - p_{i,red}$$

where $P_{k|i,red}$ denotes the probability of the kth conformation with the ith center reduced. The relation for $p_{i,ox}$ follows from these equations.

According to Beer-Lambert's law the contributions of the redox states to the absorbance A_i at wavenumber $\bar{\nu}$ and time t for a band associated with the ith center are proportional to the overall probabilities of the oxidized and the reduced state (27, p 59f)

$$A_i(\bar{\nu}, t) = k_{i,ox}(\bar{\upsilon})p_{i,ox}(t) + k_{i,red}(\bar{\upsilon})p_{i,red}(t) = k_{i,ox}(\bar{\upsilon}) + \Delta A_i(\bar{\upsilon})p_{i,red}(t)$$

With

$$\Delta A_i(\bar{\upsilon}) = k_{i,red}(\bar{\upsilon}) - k_{i,ox}(\bar{\upsilon}).$$

The proportionality constants $k_{i,\mathrm{red}}(\bar{\nu})$ and $k_{i,\mathrm{ox}}(\bar{\nu})$ are products of the effective optical path length, the concentration of protein, and the respective molar extinction coefficients. Since the absorbance $A_i(\bar{\nu}, 0)$ at the beginning of a potential pulse is chosen as a reference the change in absorbance with time becomes

$$\Delta A_i(\bar{\upsilon}, t) = \Delta A_i(\bar{\upsilon}) \cdot \left[p_{i,red}(t) - p_{i,red}(0)\right] + A_{i0}(\bar{\nu})$$

The term $A_{i0}(\bar{\nu})$ is added to account for a possible deviation of $A_i(\bar{\nu}, 0)$ due to experimental scatter. In order to reduce the effect of experimental scatter for A_i at individual wavenumbers $\Delta A_i(\bar{\nu}, t)$ is integrated over $\bar{\nu}$ thus yielding the band area $B_{i,\tilde{\nu}}(t)$:

$$B_{i,\tilde{\nu}}(t) = \int_{\nu_{\min}}^{\nu_{\max}} \Delta A_i(\bar{\upsilon}, t)\, d\bar{\upsilon}$$

The constants $\tilde{\nu}$, $\nu_{\min}$ and $\nu_{\max}$ refer to the peak wavenumber and to the outer boundaries of the band, respectively.

It follows that

$$B_{i,\tilde{\nu}}(t) = \left[p_{i,red}(t) - p_{i,red}(0)\right] \int_{\nu_{\min}}^{\nu_{\max}} \Delta A_i(\bar{\upsilon})\, d\bar{\upsilon} + \int_{\nu_{\min}}^{\nu_{\max}} \Delta A_{i0}(\bar{\upsilon})\, d\bar{\upsilon}$$

and we define

$$\overline{\Delta A_i}(\tilde{\nu}) \coloneqq \int_{\nu_{\min}}^{\nu_{\max}} \Delta A_i(\bar{\upsilon})\, d\bar{\upsilon}$$

$$\overline{\Delta A_{i0}}(\tilde{\nu}) \coloneqq \int_{\nu_{\min}}^{\nu_{\max}} \Delta A_{i0}(\bar{\nu})\, d\bar{\nu}\ .$$

The transition between redox states l and m is defined as a second order reaction expressed in terms of total species (protonated and unprotonated)

$$[r_l^t] + [o_m^t] \rightleftharpoons [o_l^t] + [r_m^t],$$

whose equilibrium constant follows to

$$K = \frac{k_{lm}}{k_{ml}} = \ e^{\frac{nF(E_m^0 - E_l^0)}{RT}}\ \frac{(1+10^{pK_l^o - pH})}{(1+10^{pK_l^r - pH})}\frac{(1+10^{pK_m^r - pH})}{(1+10^{pK_m^o - pH})}$$

With E^0 the standard redox potential of the centers and pK^r and pK^o, the pK values of the respective reduced and oxidized state and k_{lm} and k_{ml}, the forward and backward rate constant. The flow of electrons J_{lm} between centers l and m can be calculated, once the forward reaction rate has been identified, e.g. by independent measurements,

$$\mathrm{J_{lm}} = \Gamma\ \mathrm{A}\left(\mathrm{k_{lm}P_i} - \mathrm{k_{lm}}\ \mathrm{e}^{\frac{\mathrm{nF(E_l^0 - E_m^0)}}{\mathrm{RT}}}\ \frac{(1+10^{\mathrm{pK_l^r - pH}})}{(1+10^{\mathrm{pK_l^o - pH}})}\frac{(1+10^{\mathrm{pK_m^o - pH}})}{(1+10^{\mathrm{pK_m^r - pH}})}\mathrm{P_j}\right)$$

The treatment so far is only applicable to second order chemical reactions. In the case of Cu_A, however, the rate of electron transfer depends on the applied potential according to the Butler-Volmer equation, modified with respect to pK^r and pK^o. Hence the current i^e resulting from the electron transfer to Cu_A follows to

$$i^e = -FAk_e\Gamma \sum_{i\neq j}\left(P_i e^{\frac{F\alpha(E_1^0 - E)}{RT}}\left(\frac{1+10^{pK_1^r - pH}}{1+10^{pK_1^o - pH}}\right)^{\alpha} - P_j e^{\frac{-F(1-\alpha)(E_1^0 - E)}{RT}}\left(\frac{1+10^{pK_1^r - pH}}{1+10^{pK_1^o - pH}}\right)^{-(1-\alpha)}\right)$$

with k_e, the electrochemical rate constant and Γ, the surface coverage of proteins and A, the electrode area.

Table S1 : Fixed parameters.

$k_{12}\ (s^{-1})$	23411
$k_{23}\ (s^{-1})$	5759469
$k_{34}\ (s^{-1})$	20300649
$\overline{A_{10}}\ (\mathrm{cm}^-1)$	-0.0014
$\overline{A_{20}}\ (\mathrm{cm}^-1)$	0.002
$\overline{A_{30}}\ (\mathrm{cm}^-1)$	0.0025

Parameter Estimation

Likelihood

Let $\mathbf{m} = (m_{t=0}, \ldots, m_{t=T})$ be a data point vector containing *N* measured points each taken at a specific point in time $t_i \in (t_0, t_1, \ldots, t_n)$ and $\boldsymbol{\theta}$ a vector of the assembled parameters of interest used in our computational model.

A likelihood function is a function of the form

$$L(\boldsymbol{\theta}; \mathbf{m}) = f(\mathbf{m}|\boldsymbol{\theta}).$$

We choose a Gaussian distribution for f and assume that the conditional probability for each point in time is statistically independent from each other. The likelihood function then amounts to

$$L(\boldsymbol{\theta}|\mathbf{m}) = \frac{1}{(2\pi\tilde{\sigma})^{N/2}} \prod_{i=1}^{N} \exp\left(-\frac{1}{2\sigma_i^2}(\mathrm{m}_i - s_i(\boldsymbol{\theta}))^2\right)$$

with $s_i(\boldsymbol{\theta})$ denoting the output of our computational model at time t_i for a set of parameters $\boldsymbol{\theta}$ and *N* =147 data points in total (see Fig 4). The likelihood parameter $\tilde{\sigma} = 9.6217 \,.\, 10^{-6}$ was derived from local maximum of the likelihood function found in a trial run

$$\left(\frac{\text{mean square error}}{\text{number of data points}}\right).$$

An estimator of $\boldsymbol{\theta}$

$$\hat{\theta} = \mathrm{argsup}_{\theta} L(\boldsymbol{\theta}|\mathbf{m})$$

is called “maximum likelihood estimator” (MLE) and yields the set of parameters of $\boldsymbol{\theta}$ that maximizes *L* (See for example ref (1) , p 31 ff.).

Bayesian Inference

In Bayesian statistical analysis unknown parameters are treated as random variables of a k-dimensional parameter space $\boldsymbol{\Theta}$ and (conditional) probability densities for $\boldsymbol{\theta}$ can be defined on it. Inference on unknown parameters is justified through Bayes' Theorem, which we apply for continuous probability densities:

$$\rho(\boldsymbol{\theta}|\mathbf{m}) = \frac{f(\mathbf{m}|\boldsymbol{\theta})\rho(\boldsymbol{\theta})}{\int f(\mathbf{m}|\boldsymbol{\theta})\rho(\boldsymbol{\theta})d\boldsymbol{\theta}}$$

The function $\rho(\boldsymbol{\theta}|\mathbf{m})$ is called *posterior distribution* and we identify f with our previously defined likelihood function. The so-called *prior distribution* $\rho(\boldsymbol{\theta})$ constitutes a summary of *a-priori* available knowledge about the parameters. In our case

$$\rho(\boldsymbol{\theta}) = \begin{cases} 1 & \text{for} \quad \boldsymbol{\theta} \in \bar{\boldsymbol{\Theta}} \subset \boldsymbol{\Theta} \\ 0 & \text{otherwise} \end{cases}$$

where the subset $\bar{\boldsymbol{\Theta}}$ is defined as

$$\bar{\boldsymbol{\Theta}} = \left\{ \boldsymbol{\theta} \in \boldsymbol{\Theta} | (\boldsymbol{\theta}_{min} \leq \boldsymbol{\theta} \leq \boldsymbol{\theta}_{max}) \wedge (\boldsymbol{\theta}_{pK_i^r} > \boldsymbol{\theta}_{pK_i^o}) \right\}.$$

This restriction of parameter space arises due to

1. Choice of parameter boundaries $\boldsymbol{\theta}_{min}$, $\boldsymbol{\theta}_{max}$ to explore physically plausible regions of $\boldsymbol{\Theta}$.
2. $pK_i^r > pK_i^o$ due to electrostatic reasons.

For the posterior distribution function then follows:

$$\rho(\boldsymbol{\theta}|\mathbf{m}) = \frac{\exp\left(\sum_{i=1}^{N} -\frac{1}{2\sigma_i^2}(\mathrm{m}_i - s_i(\boldsymbol{\theta}))^2\right)}{\int_{\bar{\boldsymbol{\Theta}}} \exp\left(\sum_{i=1}^{N} -\frac{1}{2\sigma_i^2}(\mathrm{m}_i - s_i(\boldsymbol{\theta}))^2\right) d\boldsymbol{\theta}}$$

We define χ^2, the sum of squared deviations between measured and computer-generated data points:

$$\chi^2 = \sum_{i=1}^{N} (\mathrm{m}_i - s_i(\boldsymbol{\theta}))^2$$

A vector of parameters $\boldsymbol{\theta}$ that minimizes χ^2, also maximizes our likelihood as well as the posterior distribution function.

Marginal posterior density

Given a posterior of a vector of parameters, one way to draw conclusions about a single parameter is to average over all the others (See ref (2), p. 75 f.).

$$\rho(\boldsymbol{\theta}_i|\mathbf{m}) = \int_{\boldsymbol{\theta}_{min}}^{\boldsymbol{\theta}_{max}} \mathrm{d}\,\boldsymbol{\theta}_1 \mathrm{d}\boldsymbol{\theta}_2 \ldots \mathrm{d}\boldsymbol{\theta}_{i-1} \mathrm{d}\boldsymbol{\theta}_{i+1} \ldots \mathrm{d}\boldsymbol{\theta}_n \rho(\boldsymbol{\theta}|\mathbf{m})$$

Computing the marginal posterior density $\rho(\boldsymbol{\theta}_i|\mathbf{m})$ is not a trivial matter, especially for high-dimensional joint posteriors. A commonly used technique to generate samples from the posterior density, Markov chain Monte Carlo Simulation, was employed in this work. After obtaining a sufficiently large enough sample distributed according to the joint posterior we constructed histograms (Fig S4 – Fig S11) for each variable parameter. These histograms constitute an approximation of the marginal posterior densities of the respective parameters.

Point estimates and credible regions

To characterize the distributions depicted in the histograms, point estimates like the maximum likelihood estimate (MLE) as well as the maximum a posteriori estimate of the marginal density (MMAP) are listed in Table S4.

Histograms were generated for all of the parameters listed in Table S4, however, not all of them show distributions with clearly distinguishable peaks. Some parameters seem to be uniformly distributed within the examined intervals. In those cases every value within the boundaries seems be almost equally probable and our sample from the posterior distribution does not provide more information (about probable regions of parameters) than our prior function.

For the six non-uniformly distributed parameters ($E_1^0, E_2^0, E_3^0, E_4^0, pK_4^r, \tau$), 95 % highest posterior density regions (HPD: See for example ref. (3) p 260 ff.) were calculated using the function „emp.hpd()“ contained in the R package „TeachingDemos“ (4) and listed in Table S4 as well. The histograms of those parameters were combined with box and whisker plots, where the whiskers enclose the entire examined interval, while the box represents the 25 % and 75 % quantiles, respectively.

MCMC Simulation details

To generate samples from the posterior density, the Metropolis Algorithm (5)with symmetric proposal density was implemented in MATLAB R2010b with help of a toolbox provided by Marko Laine (6).

Metropolis Algorithm

1) Choose arbitrary initial value $\boldsymbol{\theta}_{m=0}$ and for m=0,1,2,...
2) Sample a new proposal $\boldsymbol{\theta'}$ from the proposal distribution $\rho(\boldsymbol{\theta'}|\boldsymbol{\theta_m})$
3) Calculate the ratio of the posteriors $\frac{\boldsymbol{\rho_{new}}}{\boldsymbol{\rho_{old}}} : \alpha = \frac{\boldsymbol{\rho(\theta'|\mathrm{m})}}{\boldsymbol{\rho(\theta_m|\mathrm{m})}}$
4) Set

$$\boldsymbol{\theta}_{m+1} = \begin{cases} \boldsymbol{\theta'} & \text{with probability } P = \min(\alpha, 1) \\ \boldsymbol{\theta_m} & \text{otherwise} \end{cases}$$

(See ref. (2), p 296 f.)

Gaussian proposal density

$$q(\boldsymbol{\theta'}|\boldsymbol{\theta}) = \frac{1}{(2\pi)^{14/2}|S|^{1/2}} \exp\left(-\frac{1}{2}(\boldsymbol{\theta'}-\boldsymbol{\theta})^T S^{-1}(\boldsymbol{\theta'}-\boldsymbol{\theta})\right),$$

where

$$S = \begin{pmatrix} \sigma_1^2 & 0 & 0 & \dots & 0 \\ 0 & \sigma_2^2 & 0 & \dots & 0 \\ 0 & 0 & \sigma_3^2 & \dots & 0 \\ \vdots & \vdots & \vdots & \ddots & \vdots \\ 0 & 0 & 0 & \dots & \sigma_{14}^2 \end{pmatrix}$$

Table S2: Parameter boundaries and random walk step sizes.

$\boldsymbol{\theta}$	$[\boldsymbol{\theta}_{\min}, \boldsymbol{\theta}_{\max}]$	σ_i
pK_1^r	[3,11]	0.44
pK_1^o	[1,5]	0.2
pK_2^r	[9,11]	0.11
pK_2^o	[2,6]	0.2
pK_3^r	[3,9]	0.4
pK_3^o	[0,2]	0.13
pK_4^r	[0,4]	0.22
pK_4^o	[0,2]	0.15
E_1^0 (V)	[-0.25,-0.1]	$8.33 \cdot 10^{-3}$
E_2^0 (V)	[-0.35,-0.15]	$12 \cdot 10^{-3}$
E_3^0 (V)	[-0.2,-0.05]	$9 \cdot 10^{-3}$
E_4^0 (V)	[-0.45,-0.25]	$11.11 \cdot 10^{-3}$
k_e (s^{-1})	[200,700]	20
τ (ms)	[0.45,0.6]	$6.8 \cdot 10^{-6}$

For a randomly selected 15 % of the steps of the Markov chain we increased the step sizes σ_i in $q(\boldsymbol{\theta}'|\boldsymbol{\theta})$ to $2.5 * \sigma_i$ in an effort to reduce inefficiencies in the sampling process.

Apart from the 14 parameters altered each iteration by the Metropolis algorithm, there are the two previously defined (integrated) absorbance constants $\overline{\Delta A_i}$ for each center, listed in Table S4. In order to reduce the number of parameters and thus dimensions and complexity, $\overline{\Delta A_{i0}}$ were fixed (see Table S1) and $\overline{\Delta A_i}$ were adapted dynamically depending on to solution of the master equation for a particular set of parameters. We adjust the height of the solution curve $\boldsymbol{s}(\boldsymbol{\theta})$ to the height of the measured curve $\boldsymbol{m}$ by setting $\overline{\Delta A_i}$ proportional to the ratio of the minima of both curves and make the ansatz:

$$\overline{\Delta A_i} = a_i \frac{\min(\boldsymbol{m})}{\min\left(\boldsymbol{s}(\boldsymbol{\theta})\right)} + b_i$$

The constants a_i , b_i were chosen arbitrarily and determined during test runs, solving the master equation for different parameter combinations within the pre-defined boundaries.

$$\overline{\Delta A_1} = 0.86 \frac{\min\left(\boldsymbol{m}_{\mathbf{Cu_A}}\right)}{\min\left(\boldsymbol{s}(\boldsymbol{\theta})_{\mathbf{Cu_A}}\right)}$$

$$\overline{\Delta A_2} = 0.999 \frac{\min(\boldsymbol{m}_{\mathbf{heme\ a}})}{\min(\boldsymbol{s}(\boldsymbol{\theta})_{\mathbf{heme\ a}})}$$

$$\overline{\Delta A_3} = \frac{\min\left(\boldsymbol{m}_{\mathbf{heme\ a_3}}\right)}{\min\left(\boldsymbol{s}(\boldsymbol{\theta})_{\mathbf{heme\ a_3}}\right)} + 0.0016$$

Convergence:

To determine convergence of the Markov chain(s), we used a method recommended by Gelman et al ((2), p 301 ff.). This approach involves multiple chains run from different initial values $\boldsymbol{\theta}_0$ (See Table S3). These starting values are points near local maxima of the likelihood function, gathered in previously conducted test runs.

Table S3: Starting values.

$\boldsymbol{\theta}$	chain 1	chain 2	chain 3	chain 4	chain 5	chain 6	chain 7	chain 8
pK_1^r	5.337	6.9	6.497	7.768	4.566	6.728	7.001	6.476
pK_1^o	4.466	1.146	3.344	1.52	2.632	3.358	2.748	2.569
pK_2^r	9.802	9.331	9.486	9.236	10.01	10.81	10.29	10.34
pK_2^o	5.752	2.752	3.444	2.416	3.017	4.305	4.167	5.148
pK_3^r	5.814	6.811	4.621	3.802	6.261	6.1	6.66	6.414
pK_3^o	1.88	0.6029	0.8352	0.2928	0.53	1.68	0.655	1.366
pK_4^r	2.418	1.788	2.185	2.996	1.661	2.573	2.198	1.896
pK_4^o	1.14	1.802	0.2477	1.216	0.2514	0.7154	1.082	1.531
E_1^0 (V)	-0.1722	-0.1711	-0.1673	-0.1911	-0.1758	-0.1642	-0.1623	-0.1786
E_2^0 (V)	-0.2148	-0.1866	-0.2487	-0.219	-0.2202	-0.2647	-0.2503	-0.2479
E_3^0 (V)	-0.1309	-0.1177	-0.1314	-0.1297	-0.1312	-0.1248	-0.1155	-0.1311
E_4^0 (V)	-0.3875	-0.4043	-0.4077	-0.4279	-0.4054	-0.4268	-0.3197	-0.3959
k_e (s^{-1})	456.8	414.1	696.3	232.1	630.2	432	337.2	389.6
τ (ms)	0.514	0.534	0.589	0.468	0.588	0.532	0.52	0.548

For every parameter of interest $\boldsymbol{\theta}$, the second halves of $\boldsymbol{m}$ = 8 parallel chains, each of length n = 40,000are assembled into a matrix $\boldsymbol{\theta}_{ij}$ and, according to Gelman et al (2), we define the „between- and within-sequence variances“

$$B \coloneqq \frac{n}{m-1}\sum_{j=1}^{m}\left(\overline{\boldsymbol{\theta}}_{\boldsymbol{j}} - \overline{\boldsymbol{\theta}}\right)^2, where\ \overline{\boldsymbol{\theta}}_{\boldsymbol{j}} = \frac{1}{\mathrm{n}}\sum_{j=1}^{m}\boldsymbol{\theta}_{ij}, \quad \overline{\boldsymbol{\theta}} = \frac{1}{\mathrm{m}}\sum_{j=1}^{m}\overline{\boldsymbol{\theta}}_{\boldsymbol{j}}$$

$$W \coloneqq \frac{1}{m}\sum_{j=1}^{m}s_j^2, \ \ where\ s_j^2 = \frac{1}{\mathrm{n}-1}\sum_{i=1}^{n}\left(\boldsymbol{\theta}_{ij} - \overline{\boldsymbol{\theta}}_j\right)^2.$$

Furthermore, a weighted average of W and B is defined to approximate the marginal posterior variance of $\boldsymbol{\theta}$:

$$\widehat{var}^{+}(\boldsymbol{\theta}|m) = \frac{n-1}{n}W + \frac{1}{n}B$$

As recommended by Gelman et al. (p 304) (2), we then monitor convergence by estimating the scale reduction factor $\hat{R}$

$$\hat{R} = \sqrt{\frac{\widehat{var}^{+}(\boldsymbol{\theta}|m)}{W}},$$

which decreases to 1 for $n \to \infty$. As long as $\hat{R}$ is not near 1, the simulation is being continued. As a rule of thumb, once $\hat{R} < 1.1$ for all parameters of interest, we collect the second halves of all the chains and consider them as a sample from the target distribution. These final scale factors for all parameters are listed in Table S4.

Table S4: Results.

$\boldsymbol{\theta}$	MMAP	MLE	HPD_{min}	HPD_{max}	median	$\hat{R}$
pK_1^r	4.95	8.092	-	-	6.235	1.053502
pK_1^o	1.175	2.479	-	-	2.662	1.060104
pK_2^r	10.375	9.288	-	-	10.098	1.032156
pK_2^o	5.375	5.382	-	-	4.143	1.011017
pK_3^r	8.45	4.514	-	-	5.845	1.069696
pK_3^o	1.925	1.837	-	-	1.072	1.054094
pK_4^r	3.075	1.487	0.956	3.999	2.587	1.023582
pK_4^o	0.925	0.776	-	-	0.939	1.050650
E_1^0 (V)	-0.169	-0.19208	-0.2463	-0.144	-0.1763	1.041318
E_2^0 (V)	-0.2275	-0.2023	-0.3174	-0.1725	-0.2463	1.042709
E_3^0 (V)	-0.131	-0.1277	-0.19	-0.0959	-0.1362	1.009292
E_4^0 (V)	-0.4275	-0.4437	-0.4498	-0.2897	-0.3743	1.020213
k_e (s^{-1})	475	536.36	-	-	448.7	1.031495
τ (ms)	0.525	0.5504	0.465	0.588	0.530	1.072409
$\overline{\Delta A_1}$ (cm^{-1})*	0.02219	0.02219	-	-	0.02219	-
$\overline{\Delta A_2}$ (cm^{-1})*	0.03657	0.03285	-	-	0.03286	-
$\overline{\Delta A_3}$ (cm^{-1})*	0.01983	0.01849	-	-	0.01849	-
χ^2 (cm^{-2})	0.0034042	0.00140709	-	-	0.0014647	-
$\sqrt{\chi^2}/N$ (cm^{-1})	$3.969 \cdot 10^{-4}$	$2.552 \cdot 10^{-4}$	-	-	$2.604 \cdot 10^{-4}$	-

Note: Absorbance parameters marked with an asterisk were not directly altered in the course of the MCMC Simulation procedure but indirectly depend on the solution of the master equation in each step, as described above. The term $\sqrt{\chi^2}/N$ refers to the average deviation of the computer-simulated band area graphs per measured data point.

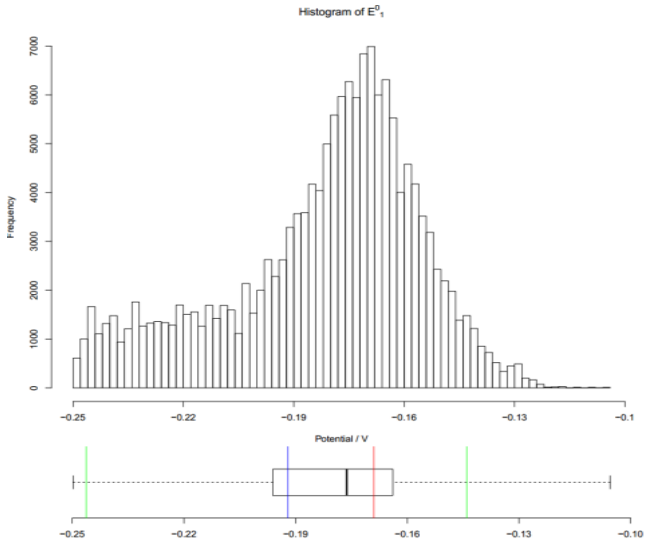

Figure S4: Histogram and Box and Whisker Plot of E_1^0; Red line: MMAP, Blue line: MLE, Green lines: HPD.

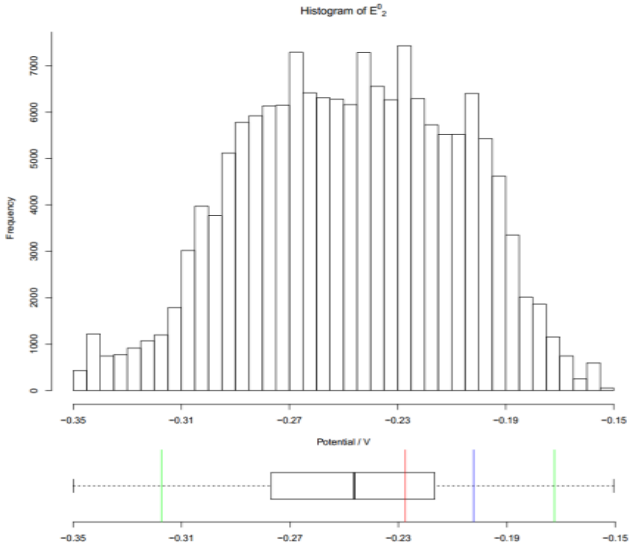

Figure S5:Histogram and Box and Whisker Plotof E_2^0; Red line: MMAP, Blue line: MLE, Green lines: HPD.

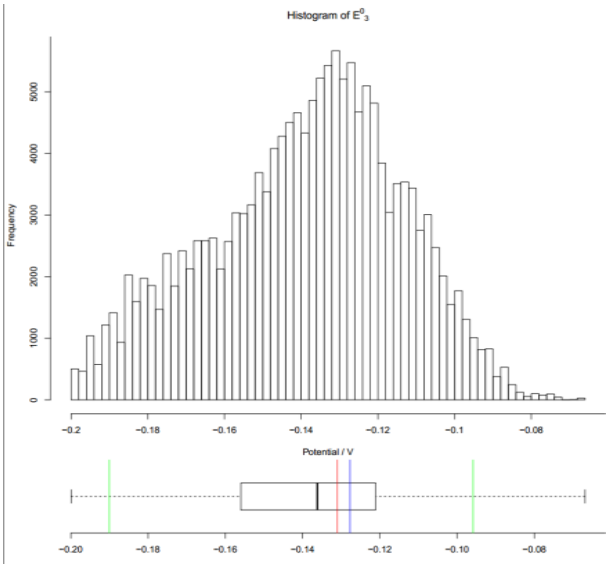

Figure S6:Histogram and Box and Whisker Plot of E_3^0; Red line: MMAP, Blue line: MLE, Green lines: HPD.

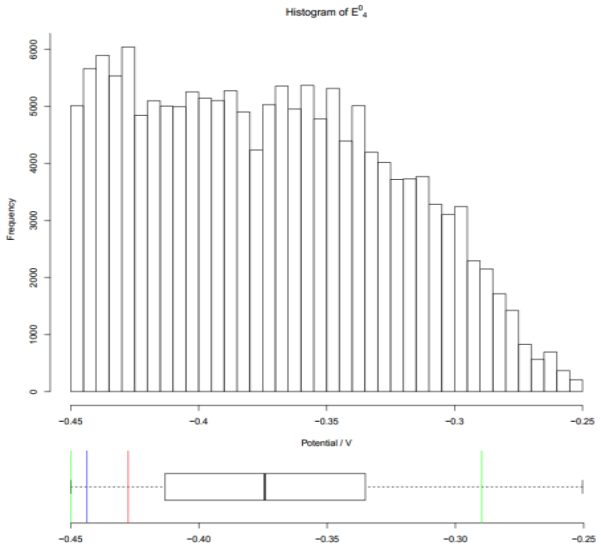

Figure S7:Histogram and Box and Whisker Plotof E_4^0; Red line: MMAP, Blue line: MLE, Green lines: HPD.

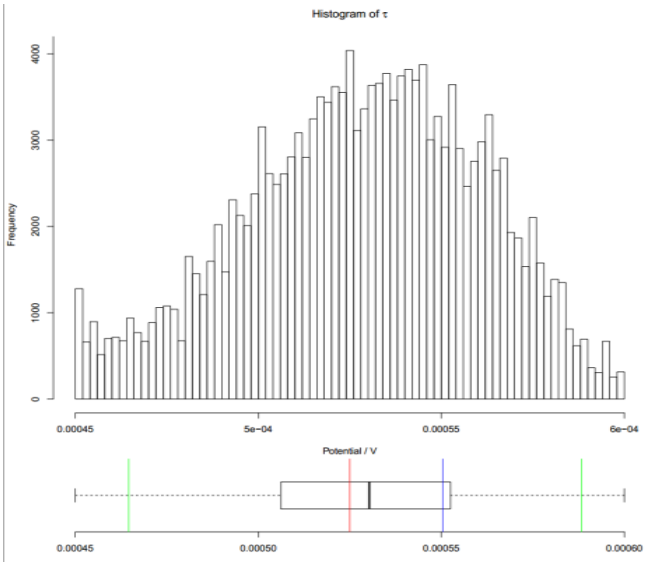

Figure S8:Histogram and Box and Whisker Plot of τ; Red line: MMAP, Blue line: MLE, Green lines: HPD.

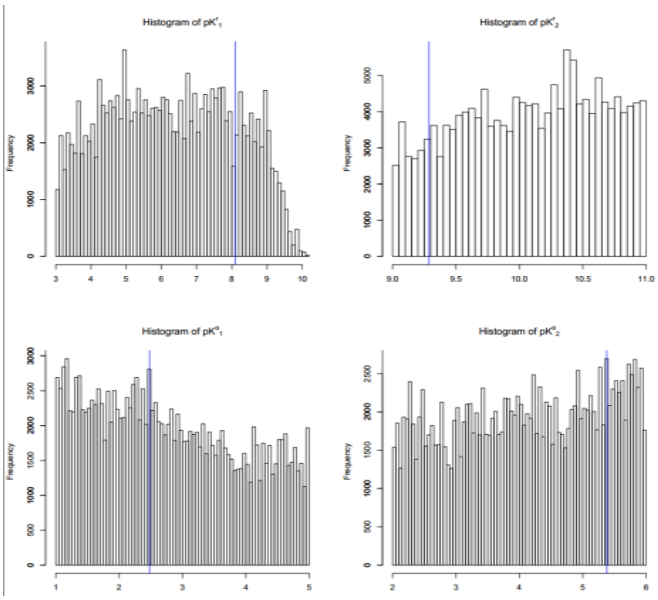

Figure S9:Histograms of nuisance Parameters ($pK_1^r, pK_2^r, pK_1^o, pK_2^o$). Blue line: MLE.

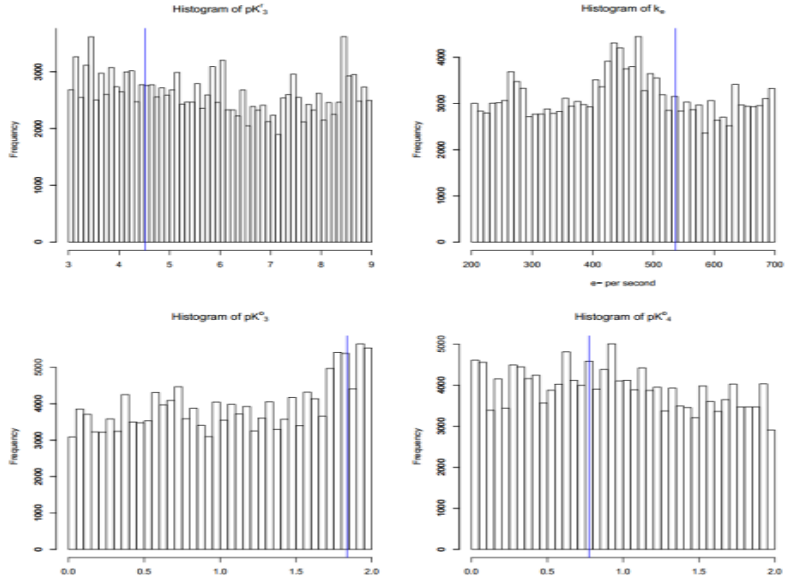

Figure S10:Histograms of nuisance Parameters ($pK_3^r, k_e, pK_3^o, pK_4^o$). Blue line: MLE.

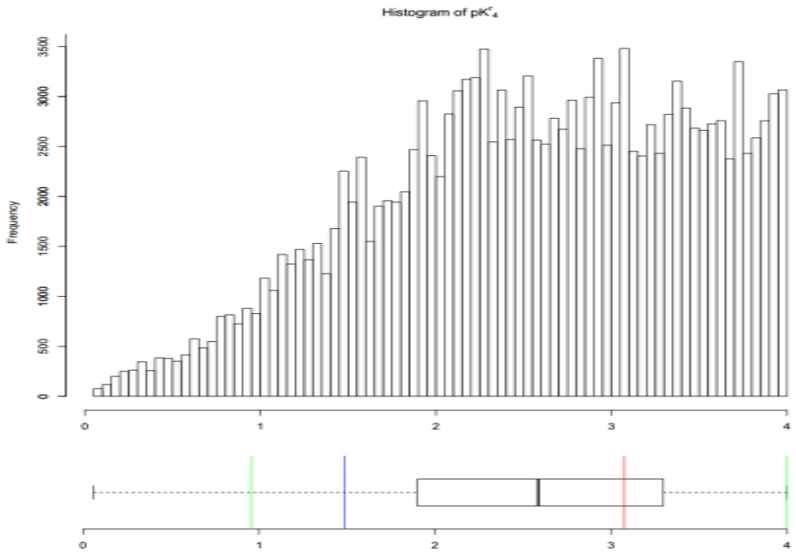

Figure S11:Histogram and Box and Whisker Plot of pK_4^r; Red line: MMAP, Blue line: MLE, Green lines: HPD.

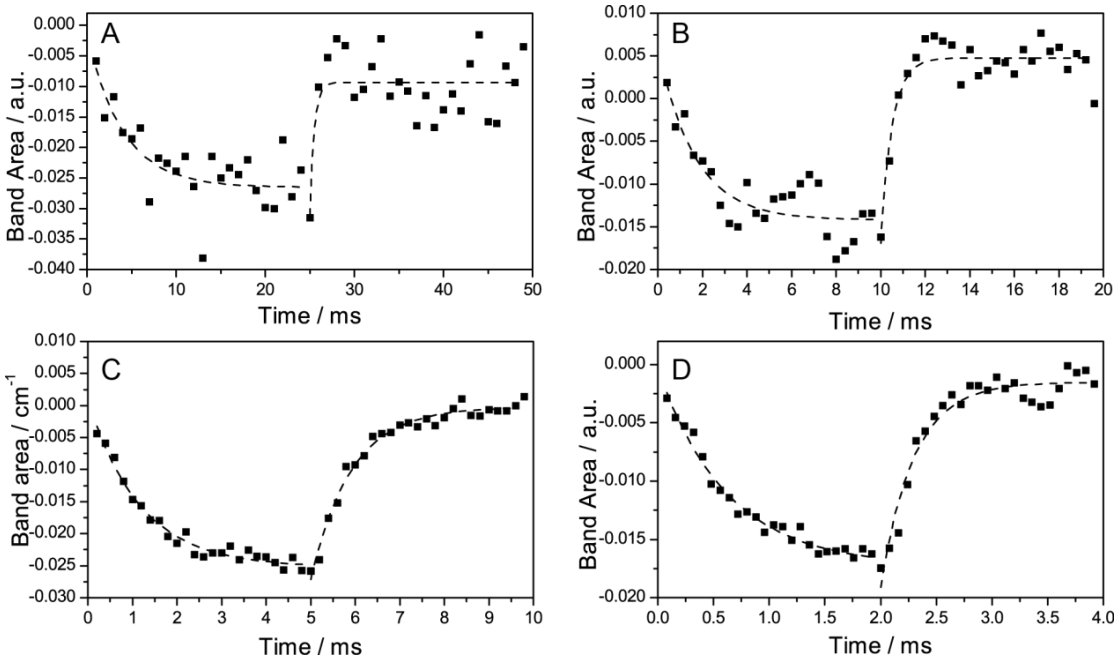

Figure S12: Time-evolution of the deconvoluted band at 1603 cm^{-1}, SEIRA spectra taken at different excitation frequencies (A) 20 Hz, (B) 50 Hz, (C) 100 Hz and (D) 250 Hz. The black, dashed line is an exponential fit that guides the eye.

Principle of Phase Sensitive Detection

Phase sensitive detection (PSD) is a mathematical method to separate signal from noise, which is particularly useful in modulation spectroscopy. It is able to selectively detect signals that show the same frequency as the stimulation. By evaluation of the phase lag of individual bands (i.e. the phase difference between the excitation trigger and the response of the system), PSD permits the isolation of overlapping components in a broad band. In our particular case, PSD also allows the subtraction of the H_2O bending band that interferes with the amide I band in the IR spectrum (see Fig. S13). The band parameters of the H_2O bending band (position, band width) were determined by an independent measurement of the buffer solution included into the fitting routine. Different components are then identified by their individual phase lags increasing as a function of excitation frequencies.

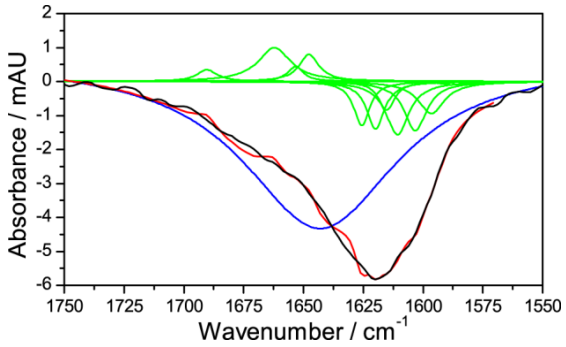

Fig. S13: Deconvoluted bands in the amide I region attributed to secondary structures and redox centers (green) after subtraction of the water band (blue). The sum of all fitted bands (red) is in good agreement with the measured IR spectrum at 100 Hz (black).

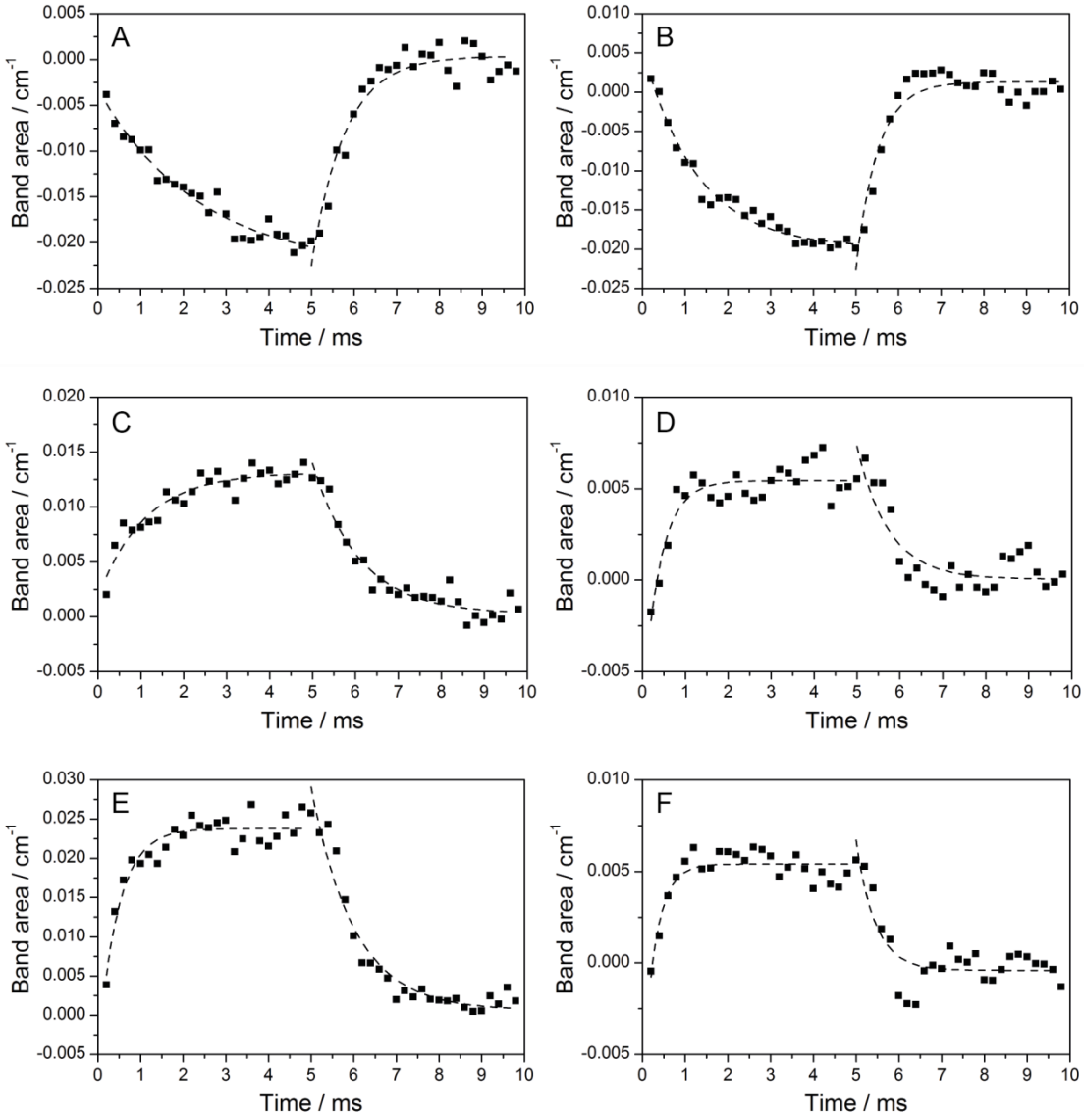

Figure S14: Time-Evolution of deconvoluted bands not used for fitting routine at (A)1596 cm^{-1}, (B) 1619 cm^{-1}, (C), 1647 cm^{-1}, (D) 1653 cm^{-1}, (E) 1662 cm^{-1}, (F) 1690 cm^{-1} taken at 100 Hz excitation frequency with an exponential fit that guides the eye (dashed line) .

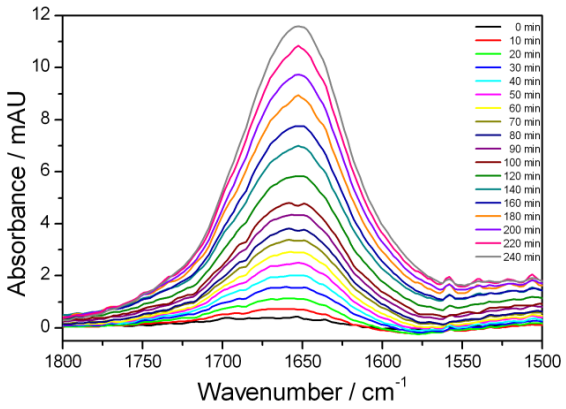

Figure S15: Immobilization spectra of C*c*O.

References:

1. Calvetti, D. and E. Somersalo. 2007. Introduction to Bayesian Scientific Computing. Berlin: Springer Science+Business Media.
2. Gelman, A., J. B. Carlin, H. S. Stern, and D. B. Rubin. 2004. Bayesian data analysis. London: Chapman and Hall/CRC.
3. Robert, C. P. 2007. The Bayesian Choice. Berlin: Springer Science+Business Media
4. hdp, R. p. T. http://rss.acs.unt.edu/Rdoc/library/TeachingDemos/html/hpd.html.
5. Metropolis, N., A. Rosenbluth, M. Rosenbluth, A. Teller, and E. Teller. 1953. Equation of State Calculations by Fast Computing Machines. The Journal of Chemical Physics 21:1087-1092.
6. matlab toolbox: Marko Laine, University of Helsinki. http://helios.fmi.fi/~lainema/mcmc/.

THE JOURNAL OF PHYSICAL CHEMISTRY C

Article

pubs.acs.org/JPCC

Surface-Enhanced Infrared Absorption Spectroscopy (SEIRAS) of Light-Activated Photosynthetic Reaction Centers from *Rhodobacter sphaeroides* Reconstituted in a Biomimetic Membrane System

Vedran Nedelkovski,[†] Andreas Schwaighofer,[†] Colin A. Wraight,[‡] Christoph Nowak,[†,§] and Renate L. C. Naumann[†,*]

[†]Austrian Institute of Technology GmbH, AIT, Donau-City Str. 1, 1220 Vienna, Austria

[‡]Department of Biochemistry and Center for Biophysics and Computational Biology, University of Illinois, Urbana, Illinois 61801, United States

[§]Center of Electrochemical Surface Technology, CEST, Viktor-Kaplan-Straße 2, 2700 Wiener Neustadt, Austria

Supporting Information

ABSTRACT: Surface-enhanced IR absorption spectroscopy (SEIRAS) in the ATR configuration has been performed on reaction centers (RCs) from *R. sphaeroides*. Surface-enhancement is achieved by a thin, structured gold film present on the surface of an ATR crystal. Purified RCs are immobilized as a monolayer on top of the gold film via a poly his-tag engineered to the C-terminal end of the M subunit. Subsequently, the RCs are reconstituted into a lipid bilayer by in situ dialysis. Light-minus-dark absorbance spectra were recorded under continuous illumination using the spectrum in the dark as the reference. A number of strong bands have been observed indicating the excitation of the special pair as well as alterations of quinone/quinol species. Spectra were recorded at different time intervals with and without liposoluble Q_{10} coreconstituted into the lipid phase. A steady (photostationary) state was approached slowly and bands were found to increase or decrease reversibly on illumination and relaxation. Tentative assignments were made for some bands, based on previous FTIR measurements. The long time scale of these processes was tentatively explained in terms of interprotein reactions of RC molecules.

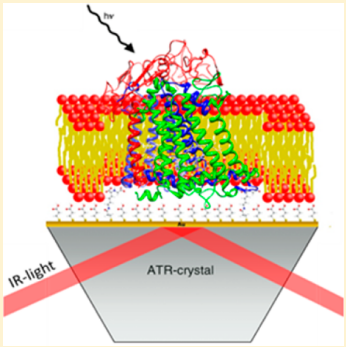

INTRODUCTION

FTIR spectroscopy is well suited to investigate photoexcitation of bacterial reaction centers (RCs). RCs have been investigated either in chromatophores[1] of the respective bacteria or in purified and solubilized form, mostly as a rehydrated thin film between two CaF_2 windows.[2−8] Marker bands for quinol formation were identified, obtained from the quinone/quinol pool present within chromatophores or added to solubilized RCs. Steady-state, light-minus-dark difference absorbance spectra under continuous illumination[5,9−12] and time-resolved spectra[1,3,4,7,13] have been measured. In the majority of these studies, the RCs have been observed in the presence of an electron donor to reduce the oxidized primary electron donor, $P870^+$.[1,7−9,12,14] Other redox active compounds have also been added as redox mediators.[1,7,9,12,14]

We use a different strategy using surface-enhanced IR absorption spectroscopy (SEIRAS) according to which FTIR spectra are measured in the ATR configuration, with a thin structured gold film on the ATR crystal to achieve enhancement of the IR signal. Purified RCs can be immobilized as a monolayer on the surface of the gold film via his-tag, a technology also used for the measurement of photocurrents.[15−18] In previous SEIRAS studies of cytochrome *c* oxidase (C*c*O), we had extended this strategy by in situ dialysis of the protein monolayer in the presence of lipid micelles. The protein is thus reconstituted in a lipid bilayer to form a protein-tethered bilayer lipid membrane (ptBLM) (Figure 1).[19,20] As a benefit of this structure, liposoluble Q_{10} can be coreconstituted into the lipid phase, while the protein is preserved in a fully functional form.

MATERIALS AND METHODS

Solvents and Chemicals. Deionized water was used from a Sartorius-Stedim system (Goettingen, Germany) with a resistivity of 18 MΩ cm. Argon 4.8 was obtained from Linde Gas GmbH (Stadl-Paura, Austria). 3-Mercaptopropyltrimethoxysilane (MPTES, 95%) was purchased from ABCR GmbH (Karlsruhe, Germany). Gold granules (99.99%) for evaporation were obtained from Mateck GmbH (Juelich, Germany). Biobeads (20−50 mesh) were purchased from Bio-Rad Laboratories GmbH (Vienna, Austria). 1,2-Diphytanoyl-*sn*-glycero-3-phosphocholine (DiPhyPC, >99%) was provided by Avanti Polar Lipids (Alabaster, AL). Dithiobis (nitriloacetic acid butylamidyl propionate) (DTNTA, ≥95.0%) was obtained from Dojindo Laboratories (Kumamoto, Japan). Hydroxylamine hydrochloride ($NH_2OH.HCl$, 99%), gold(III) chloride

Received: June 7, 2013
Revised: July 11, 2013

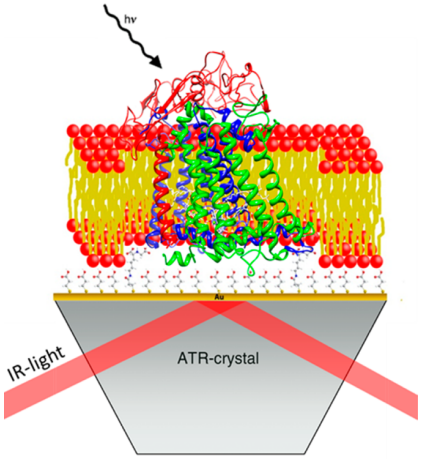

Figure 1. Setup of RCs immobilized on NTA-functionalized gold surface and reconstituted in the ptBLM. RCs are immobilized with the special pair oriented toward the surface of a silicon ATR crystal, covered with a two-layer gold film.

hydrate ($HAuCl_4 \cdot xH_2O$, 99.999%), dimethyl sulfoxide (DMSO, puriss., dried over molecular sieve), 3,3′-dithiodipropionic acid (DTP, 99%), dodecyl-β-D-maltoside (DDM, ≥98%), nickel(II) chloride ($NiCl_2$, 98%), D-(+)-glucose ($C_6H_{12}O_6$, ≥99.5%), glucose oxidase (GOx), and catalase, as well as Coenzyme Q_{10} (Q-2, diisoprenyl-ubiquinone) were purchased from Sigma-Aldrich (Steinheim, Germany). All chemicals were used as purchased.

Preparation of the Two-Layer Gold Surface on the ATR Crystal. Preparation was done as previously described by Nowak et al.[21] A polished silicon attenuated total reflection (ATR) crystal was immersed in a 10% ethanolic solution of MPTES for 60 min to anchor the gold layer. After rinsing with ethanol, the crystal was dried under a stream of argon and annealed at 100 °C for 60 min. The crystal was allowed to cool to room temperature, then immersed in water for 10 min, and dried under a stream of argon. A 25 nm gold film was then deposited onto the ATR crystal by electrochemical evaporation (HHV Edwards Auto 306, Crawley, U.K.). Gold nanoparticles were grown on the gold film by immersing the crystal in 50 mL of an aqueous solution of hydroxylamine hydrochloride (0.4 mM), to which 500 μL of an aqueous solution of gold(III) chloride hydrate (0.3 mM) was added five times at 2 min intervals. After that, the Au surface clearly showed protruding structures ranging in diameter from 43 to 60 nm (average 57 nm) with an aspect ratio of around 12. Finally, the crystal was rinsed with water and dried under a stream of argon.

Immobilization of the Protein. Wild-type *Rhodobacter sphaeroides* RCs with a genetically engineered 7-his-tag at the C-terminus of the M-subunit were expressed from a strain kindly provided by S.G. Boxer.[22] RCs were purified according to a modification of the original method.[23] The immobilization of RC on either the template stripped gold (TSG) surface (see Supporting Information, SI) or the ATR crystal was performed according to a method described by Nowak et al.[24] and references therein. TSG was used for Surface Plasmon Resonance (SPR) Spectroscopy and Electrochemical Impedance Spectroscopy (EIS) (see SI). Briefly, the gold surface was immersed in a solution of 2.5 mM DTNTA and 7.5 mM DTP in dry DMSO for 20 h. After rinsing with ethanol and purified water, the surface was immersed in 40 mM $NiCl_2$ in acetate buffer (50 mM, pH 5.5) for 30 min, followed by thorough rinsing with purified water to remove excess $NiCl_2$. The surface was dried under a stream of argon prior to assembly in the measuring cell and rehydrated with DDM-DPK buffer (0.05 M K_2HPO_4, 0.1 M KCl, pH 8, 0.1% DDM) before starting the SEIRA measurements. SEIRA spectra (Figure 2) were taken

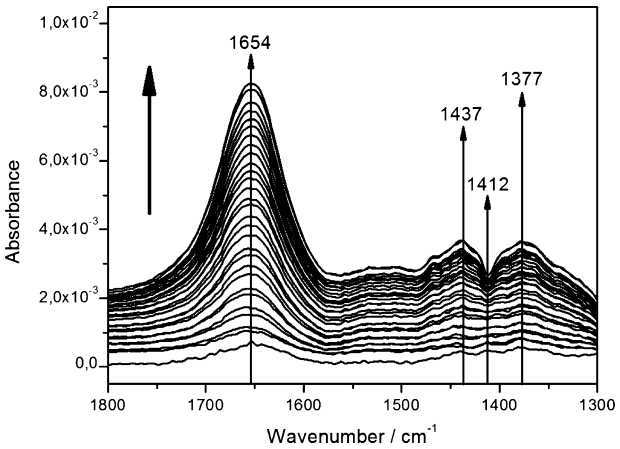

Figure 2. SEIRA spectra of RCs in the course of their immobilization on the gold film as a function of adsorption time. Total adsorption time was 4 h, intervals between spectra were 10 min. The spectrum of the functionalized gold surface was used as the reference.

while RCs dissolved in DDM-DPK were adsorbed to the NTA-functionalized gold surface at a final concentration of 100 nM. After 4 h time of adsorption carried out at 28 °C, the cell was rinsed with DDM-DPK to remove unspecifically adsorbed and bulk protein. Thereafter, DDM-DPK was replaced by a DiPhyPC/DDM-DPK solution (40 μM DiPhyPC in DDM-DPK). In the case of additional ubiquinone, Q_{10} was solubilized together with DiPhyPC (6 μM Q_{10} in DiPhyPC/DDM-DPK). In both cases, DDM was removed by adding Biobeads to the lipid-detergent solution.

ATR-SEIRA-Spectroscopy. The electrochemical cell was mounted on top of a trapezoid single reflection silicon ATR crystal. The IR beam of the FTIR spectrometer (VERTEX 70v, from Bruker, Ettlingen, Germany) was coupled into the crystal at an angle of incidence Θ = 60° by using the custom-made setup described previously.[21] All spectra were measured with parallel polarized light. Because the ATR element surface is coated with an electrical conductor, perpendicularly polarized light is unable to effectively penetrate the conducting layer. The total reflected IR beam intensity was measured with a liquid nitrogen-cooled photovoltaic mercury cadmium telluride (MCT) detector. IR measurements were done under aerobic conditions at 28 °C. The sample unit was purged with dry, carbon dioxide-free air. FTIR spectra were recorded at 4 cm^{-1} resolution using Blackham-Harris 3-term apodization and a zero filling factor of 2. The interferograms were measured in double-sided mode and transformed into spectra using the Power phase correction mode. Spectra were analyzed using the software package OPUS 7 and OriginLab's Origin software.

Illumination was performed with white light from a Fiber-Lite DC950 illuminator (150 W, quartz halogen lamp) provided with an optical fiber obtained from Dolan-Jenner (Boxborough, MA) with a light intensity of 0.2 W/cm^{-1} (at a wavelength of 800 nm).

dx.doi.org/10.1021/jp4056347 | J. Phys. Chem. C XXXX, XXX, XXX−XXX

RESULTS AND DISCUSSION

Formation of the ptBLM. Immobilization of the RCs and subsequent formation of the ptBLM followed by Surface Plasmon Resonance (SPR) and Electrochemical Impedance Spectroscopy (EIS) is shown in Figures S1 and S2A,B, respectively of the SI. Optical thickness and electrical parameters are given in Table S1 of the SI correspond to the respective data found in the case of C*c*O, where the surface concentration was determined to be ~6 pMol cm^{-2}, in agreement with the calculated value for a densely packed monolayer from the crystal structure of C*c*O from *R. sphaeroides.*[19,24,25] We conclude that a monolayer of RCs of a similar packing density had been formed on the gold film, with only small voids left between single proteins to be filled with a lipid bilayer.

SEIRAS Measurements. SEIRA spectra were recorded as a function of time in the course of the binding of the RCs via his-tag attached to the P side of the protein (Figure 2).

Vibrational components of α-helices in the amide I region can be recognized at 1654 cm^{-1}, as well as two bands at 1437 and 1377 cm^{-1}. The negative band at 1412 cm^{-1} may be due to changes in the NTA structure/orientation during complex formation with the his-tag.[26] No amide II bands are seen in the spectra. This can be explained in terms of the theory of SEIRAS, predicting that dipoles oriented perpendicular to the surface are subject to a particularly high surface-enhancement effect, while dipoles pointing in other directions are not detected.[27] Moreover, the enhancement decreases with distance from the metal film. The RCs are arranged on the surface with the α-helices pointing in the z-direction, giving rise to the relatively high absorbance of the amide I band. The transition dipole moment for the amide II mode is roughly orthogonal to this, with negligible SEIRA enhancement and consequently much weaker absorbance.

Next, light-minus-dark difference spectra were recorded under continuous illumination of the RC reconstituted in the ptBLM, first without any additional Q_{10}. A total of 1000 scans were recorded and averaged for every spectrum. Surprisingly, a steady state was not obtained on the seconds time scale, as described by Breton,[6] for example. Instead, absorbances of many bands increased over a much longer time scale. The first spectrum taken after 5 min illumination time, with no additional Q_{10}, is shown in Figure 3. Next, spectra were recorded at 5 min intervals, also without additional Q_{10} (Figure 4), and band areas of selective peaks were plotted as a function of time (Figure 5A). A steady state is approached after >20 min.

As seen in the spectra, a number of positive bands appear at 1234, 1282, 1360, 1434, 1507, 1642, and a negative band at 1685 cm^{-1}. Between the bands at 1360 and 1434 cm^{-1}, a small negative band is buried at 1389 cm^{-1} but is seen in the second derivative spectrum also shown in Figure 3B. Broad negative and positive bands appear at 3400 and 3629 cm^{-1}, respectively. The most prominent band at 1434 cm^{-1} is strongly indicative of a band assigned to QH_2 by FTIR,[1,2,4,7] although associated bands at 1491, 1470, and 1375 cm^{-1} are not seen. An FTIR band at 1389 cm^{-1} is also attributed to QH_2,[1,7] but the negative sign here is not consistent with the generation of QH_2 indicated by the positive band at 1434 cm^{-1}. The band at 1282 cm^{-1} is an FTIR marker band of P^+.[28−30] A band at approximately 1360 cm^{-1} has been assigned to the δCH_3 vibration of the methyl group at the 5-position of the ring in the semiquinone difference spectra, between Q_A^- and Q_A and Q_B^- and Q_B.[11,31]

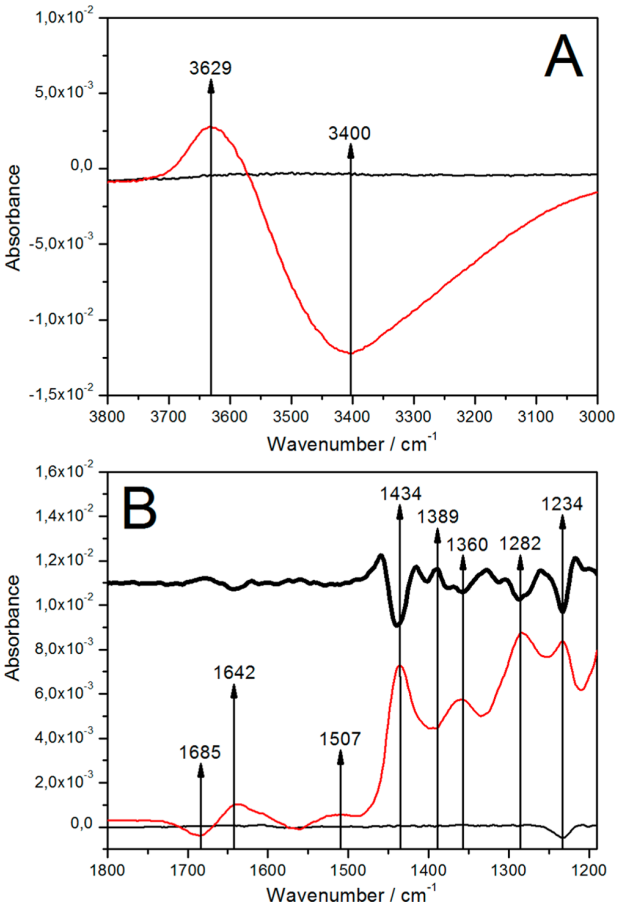

Figure 3. Light-minus-dark absorption spectra of RCs immobilized in the ptBLM after 5 min illumination time (red line), with the spectrum in the upper (A) and lower (B) wavenumber region. The reference spectrum in each is dark-minus-dark, which did not change as a function of time without illumination. The bold line in (B) represents the second-derivative spectrum showing a negative band appearing at 1389 cm^{-1} between the 1434 and 1360 cm^{-1} bands. The second derivative also shows that the band at 1642 cm^{-1} is an overlap of a variety of bands, which, however, cannot be resolved into single bands.

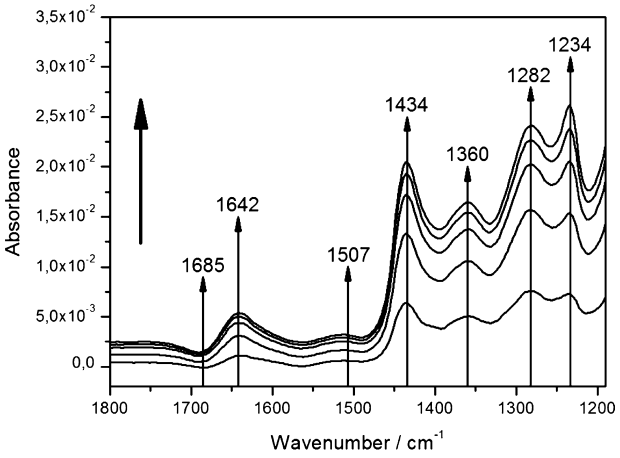

Figure 4. Time evolution of light-minus-dark absorption spectra of RCs immobilized in the ptBLM without added Q_{10} during the course of continuous illumination. Difference spectra were recorded every 5 min.

dx.doi.org/10.1021/jp4056347 | J. Phys. Chem. C XXXX, XXX, XXX−XXX

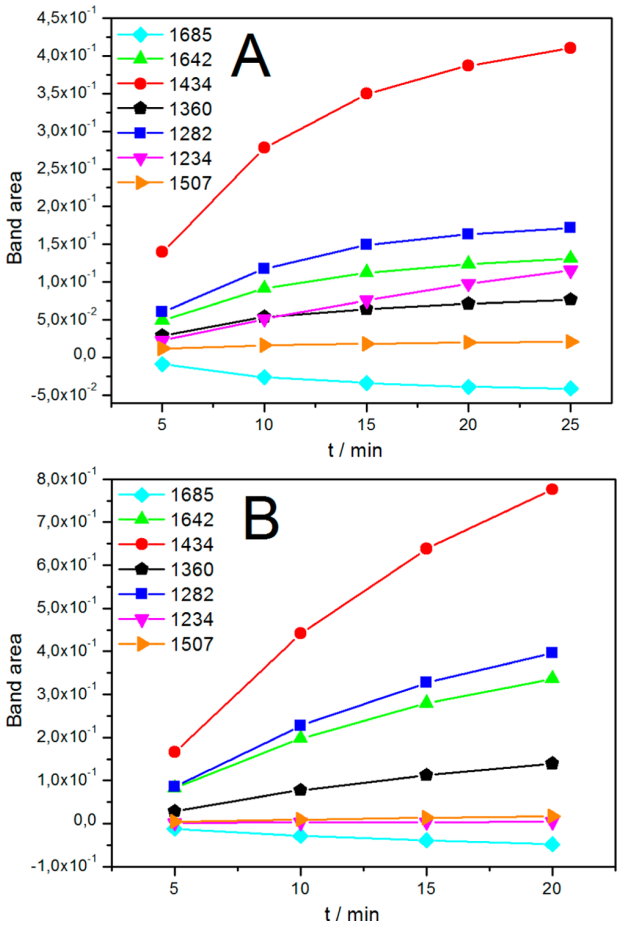

Figure 5. Band areas of absorbances of characteristic bands under continuous illumination of RCs in the ptBLM taken at different time intervals without (A) and with added Q_{10} (B).

FTIR bands indicating semiquinone were reported to occur at 1446 and 1479 cm^{-1}, which we do not see in our spectra.[11,31] The band at 1642 cm^{-1} may be an overlap of several bands in the region of the amide I band of α-helices and H−O−H bending vibration of water, and the C═O stretching vibration of Q_B is also assigned in this region.[4−6,29,32,33] Negative evolution of the band at 1685 cm^{-1} attributed to the C═O stretching vibration of the 9-keto group of P[4,30] is consistent with a decrease in the concentration of P.

Broad positive and negative bands in the region 3800−3000 cm^{-1} in FTIR were interpreted by Iwata et al.[14] as water stretching vibrations associated with formation of either semiquinone, Q_A^- or Q_B^-. Given the orientation of the RC in the ptBLM, with P facing the gold surface, oriented water(s) close to P/P^+ are also a likely a source of these bands. It is noteworthy that the spectra exhibit a well-defined isosbestic point.

An assignment for the band at 1507 cm^{-1} could not be found in the literature. A band at 1234 cm^{-1} also could not be found in the literature dealing with RCs, but lies in the region of C−O stretching modes of carboxylic acids.[34] The latter, however, is a prominent recurrent band, which also remains after relaxation of all others (see below). It could not be correlated to any kind of alteration, for example addition of Q_{10}, time of illumination or relaxation, etc.

Tentative band assignments from previous FTIR measurements are collected in Table 1.

The origin of the bands discussed above was supported by spectra recorded with liposoluble Q_{10} coreconstituted into the lipid phase. The absorbance of the strong bands was shown to increase under illumination and to decrease during dark relaxation (Figures 6, 7, and 8). Absorbances also increased when Q_{10} was coreconstituted (Figures 5B and 6), showing that the evolution of these bands is affected by the quinone/quinol pool. In summary, in the approach to steady state under continuous illumination, we detected the evolution of QH_2 and P^+ occurring in the time scale of minutes, which is fully reversible after switching of the light. The long time scale of the reactions will be discussed further below.

CONCLUSIONS

Many of the bands found in our spectra can be correlated with bands reported in previous FTIR work (see Table 1). However, the overall appearance of the spectra is strikingly different from FTIR difference spectra found in the literature, which are usually composed of narrow peaks and troughs changing in the μs to s time scale.[29] Some of the unfamiliar features of our spectra can be explained by the theory of SEIRAS, notably the high sensitivity of vibrational components in close proximity to the surface, and the strong dependence on the orientation of the transition dipole moments, which must be oriented perpendicular to the surface.[27,35] This means that the same component present in different orientations may be strongly represented or not at all. This largely accounts for the different sensitivities of bands associated with the same functional group, e.g., bands that represent QH_2 at 1434, 1491, 1470 cm^{-1}, of which only 1434 cm^{-1} is definitively seen here. This effect is enhanced by the preorientation of the RC molecules within the ptBLM. Furthermore, the extreme dominance of positive bands throughout the spectrum may indicate a strong effect of the large, internal dipole moment of the RC in the charge-separated state. The theory of SEIRAS, however, is not able to explain other features of our spectra, such as the substantial

Table 1. Possible Assignments of SEIRAS Bands for RCs Reconstituted in the ptBLM under Continuous Illumination

band (cm^{-1})			tentative assignment	
experimental	fwhm	literature	species	component
1282	77.5	1282[28−30]	P^+	(complex)
1360	34.7	1355,[11] 1365[32]	Q_A	δCH_3
1434	25.7	1433[1,2,4,7]	QH_2	
1643	66.7	1640,[5,29]1641,[6,32,33]1642[4]	quinone Q_A Q_B	C═O
1685	35.2	1682,[30]1683[4]	9-keto group of P	C═O
3400	312.7	3485[14]	Q_B^-/Q_B or P^+	H_2O
3629	194.5	3632[14]	Q_B^-/Q_B or P^+	H_2O

dx.doi.org/10.1021/jp4056347 | J. Phys. Chem. C XXXX, XXX, XXX−XXX

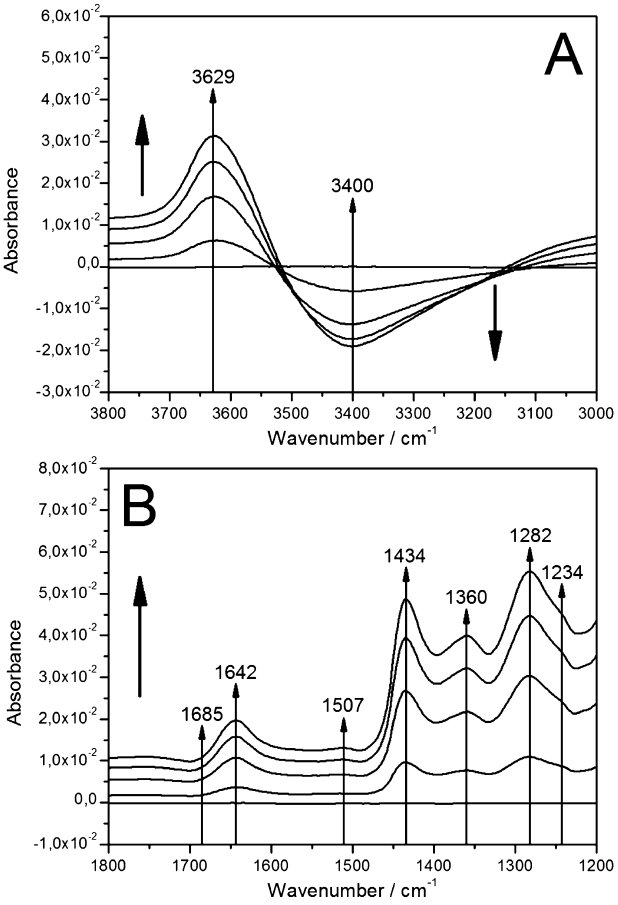

Figure 6. Light-minus-dark spectra of RCs in the ptBLM under continuous illumination with coreconstituted Q_{10}, with the spectrum in the dark as the reference, in the upper (A) and lower (B) wavenumber region. Difference spectra were recorded every 5 min.

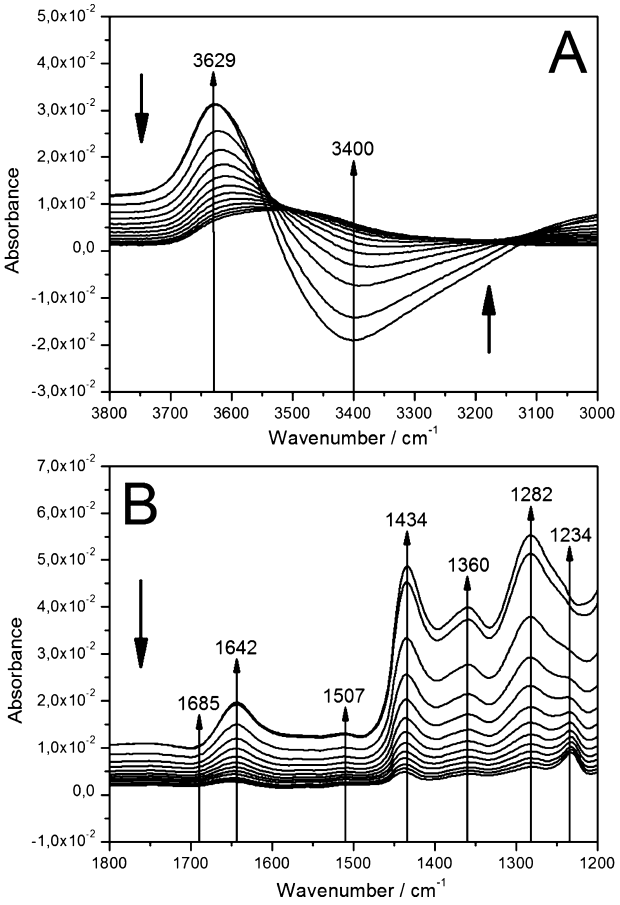

Figure 7. Relaxation of the bands of RC in the ptBLM with coreconstituted Q_{10} after termination of continuous illumination in the upper (A) and lower (B) wavenumber region. Total relaxation time is 1 h, difference spectra were recorded every 5 min.

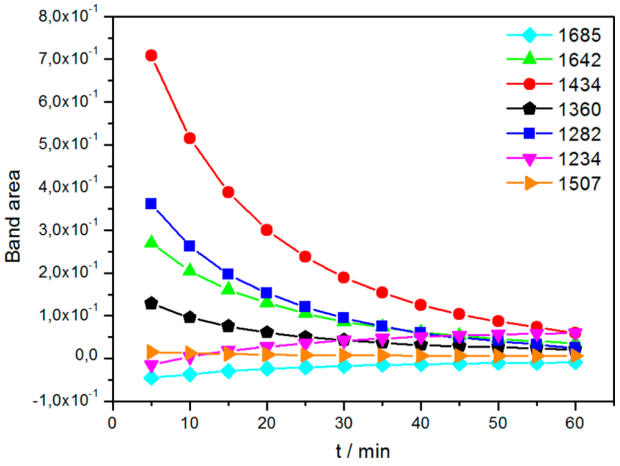

Figure 8. Kinetics of characteristic bands during relaxation. All band areas decrease during relaxation except for bands at 1234 and 1685 cm^{-1}, which increase.

enhancement in bandwidth, although this is also observed in other membrane proteins and we have speculated previously on possible origins.[36]

The long time scale of the evolution of the SEIRA spectra, which we take to represent species such as P^+ and QH_2, is unexpected. In FTIR, the light-driven electron transfers to form Q_A^- and Q_B^- (and even Q_B^{2-} or Q_BH_2) have been studied extensively in the μs to s time range. However, the release of QH_2 from its binding pocket and its replacement by a quinone molecule from the quinone pool have received attention only relatively recently.[37−39] Multiple saturating flashes or continuous illumination of chromatophores from *R. sphaeroides* have revealed the slow accumulation of QH_2, but in the presence of ascorbate and other redox mediators.[1] This investigation was later extended to look at intermediate RC states, using rapid scan FTIR spectroscopy of detergent micelles of RCs.[7] Kinetic traces were analyzed in terms of a model taking into account the slow quinone exchange between RC micelles and pure detergent micelles, taking place in the time scale of seconds.[7,40,41]

In all of these studies, however, multiple excitations were possible because of the presence of electron donors to restore P^+ back to P. These are absent in our experiments. The slow time scale of the formation of species such as QH_2 (and/or Q_BH_2) and P^+ (as indicated by probable assignments from FTIR marker bands), in the absence of an electron donor, suggests the following possible explanation. Due to the high density of RCs, interprotein quinone/semiquinone exchange may become possible, allowing release of quinol into the

dx.doi.org/10.1021/jp4056347 | J. Phys. Chem. C XXXX, XXX, XXX−XXX

membrane. Under normal circumstances the states $P^+Q_A^-$ and $P^+Q_B^-$ recombine in 0.1−1 s and these would represent the only detectable states, depending on light intensity. At the high protein densities used here, however, it may be possible for some cross reactivity to occur, i.e., $P^+Q_B^- + P^+Q_B^- \rightarrow P^+Q_B + P^+Q_B^{2-}$, followed by protonation of Q_B^{2-} and release as QH_2 into the membrane, with rebinding of Q_B from the quinone pool. The resulting states, P^+Q_B and QH_2 can be expected to be quite long-lived and to accumulate slowly over time. The fact that all or most of the light-induced SEIRA bands exhibit similar kinetics is supportive of this model. During relaxation, restoration of the dark adapted state would mostly likely be associated with direct reduction of P^+ by QH_2, yielding a short-lived semiquinone that would reduce another P^+. However, reversal of the original disproportion is also possible: $2P^+Q_B + QH_2 \rightarrow P^+Q_B^{2-} + P^+Q_B \rightarrow P^+Q_B^- + P^+Q_B^-$.

Another characteristic of the SEIRA spectra is the full width at half-maximum (fwhm) of the bands, which is significantly larger than that of the sharp bands found in the FTIR literature.[29] The fwhm is generally related to the freedom of movement of the structure associated with the particular component.[42−44] In previous studies, the protein was investigated either in the presence of an electron donor, or even an entire cocktail of mediators. In a previous SEIRAS study of cytochrome *c* oxidase, we observed the narrowing of fwhm in the presence of mediators.[24,36] The effect might be explained in terms of the internal dipole potential of the naturally activated charge-separated state being markedly different from that after equilibration between mediators and redox sites.

The positive and negative bands in the region 3800−3000 cm^{-1} should be due to highly ordered water molecules,[14] which are known to have particularly strong transition dipole moments. Remarkable in this context is a clear isosbestic point for these bands indicating that only *two* species vary in concentration to contribute to the absorption. The near-constancy of the isosbestic point also indicates that temperature effects should be small in this region.

In summary, SEIRAS of RCs present within a ptBLM yields a number of strong bands at wavelengths that correlate them with FTIR marker bands of photoexcitation. Weaker signals may be buried underneath the strong bands, potentially contributing to the large, apparent fwhm of the major bands. The time-evolution of the SEIRA spectra is, however, unusually slow and not as observed in other experimental setups. The long time scale is consistent with the idea of an interprotein disproportionation reaction followed by QH_2/Q exchange, which is diffusional. Reversal of the disproportionation accounts for the almost complete reversibility of the reactions observed under the experimental conditions used here.

■ ASSOCIATED CONTENT

Supporting Information

Additional Information about preparation of Template Stripped Gold (TSG), Surface Plasmon Resonance Spectroscopy (SPR) measurements, and Electrochemical Impedance Spectroscopy (EIS) used to monitor the immobilization of the protein and membrane formation. This material is available free of charge via the Internet at http://pubs.acs.org.

■ AUTHOR INFORMATION

Corresponding Author

*Phone: 0043 664 6207708, e-mail: Renate.Naumann@ait.ac.at.

Notes

The authors declare no competing financial interest.

■ ACKNOWLEDGMENTS

C.A.W. gratefully acknowledges support by NSF Grant MCB 08-18121.

■ REFERENCES

(1) Mezzetti, A.; Leibl, W.; Breton, J.; Nabedryk, E. Photoreduction of the quinone pool in the bacterial photosynthetic membrane: identification of infrared marker bands for quinol formation. *FEBS Lett.* **2003**, *537*, 161−165.

(2) Mezzetti, A.; Blanchet, L.; Juan, A.; Leibl, W.; Ruckebusch, C. Ubiquinol formation in isolated photosynthetic reaction centres monitored by time-resolved differential FTIR in combination with 2D correlation spectroscopy and multivariate curve resolution. *Anal. Bioanal. Chem.* **2010**, *399*, 1999−2014.

(3) Hermes, S.; Stachnik, J. M.; Onidas, D.; Remy, A.; Hofmann, E.; Gerwert, K. Proton uptake in the reaction center mutant L210DN from *Rhodobacter sphaeroides* via protonated water molecules. *Biochemistry* **2006**, *45*, 13741−13749.

(4) Brudler, R.; Gerwert, K. Step-Scan FTIR Spectroscopy Resolves the Q(A)(−)Q(B)-> Q(A)Q(B)(−) Transition in *Rb-sphaeroides* R26 Reaction Centres. *Photosynth. Res.* **1998**, *55*, 261−266.

(5) Breton, J.; Thibodeau, D. L.; Berthomieu, C.; Mantele, W.; Vermeglio, A.; Nabedryk, E. Probing the Primary Quinone Environment in Photosynthetic Bacterial Reaction Centers by Light-Induced FTIR Difference Spectroscopy. *FEBS Lett.* **1991**, *278*, 257−260.

(6) Breton, J. Steady-State FTIR Spectra of the Photoreduction of Q(A) and Q(B) in *Rhodobacter sphaeroides* Reaction Centers Provide Evidence against the Presence of a Proposed Transient Electron Acceptor X between the Two Quinones. *Biochemistry* **2007**, *46*, 4459−4465.

(7) Mezzetti, A.; Leibl, W. Investigation of Ubiquinol Formation in Isolated Photosynthetic Reaction Centers by Rapid-Scan Fourier Transform IR Spectroscopy. *Eur. Biophys. J.* **2005**, *34*, 921−936.

(8) Brudler, R.; Degroot, H. J. M.; Vanliemt, W. B. S.; Gast, P.; Hoff, A. J.; Lugtenburg, J.; Gerwert, K. Ftir Spectroscopy Shows Weak Symmetrical Hydrogen-Bonding of the Q(B) Carbonyl Groups in Rhodobacter-Sphaeroides R26 Reaction Centers. *FEBS Lett.* **1995**, *370*, 88−92.

(9) Breton, J.; Berthomieu, C.; Thibodeau, D. L.; Nabedryk, E. Probing the Secondary Quinone (QB) Environment in Photosynthetic Bacterial Reaction Centers by Light-Induced FTIR Difference Spectroscopy. *FEBS Lett.* **1991**, *288*, 109−113.

(10) Breton, J.; Burie, J. R.; Boullais, C.; Berger, G.; Nabedryk, E. Binding Sites of Quinones in Photosynthetic Bacterial Reaction Centers Investigated by Light-Induced FTIR Difference Spectroscopy: Binding of Chainless Symmetrical Quinones to the QA Site of *Rhodobacter sphaeroides*. *Biochemistry* **1994**, *33*, 12405−12415.

(11) Breton, J.; Boullais, C.; Burie, J. R.; Nabedryk, E.; Mioskowski, C. Binding-Sites of Quinones in Photosynthetic Bacterial Reaction Centers Investigated by Light-Induced Ftir Difference Spectroscopy—Assignment of the Interactions of Each Carbonyl of Q(a) in *Rhodobacter sphaeroides* Using Site-Specific C-13-Labeled Ubiquinone. *Biochemistry* **1994**, *33*, 14378−14386.

(12) Breton, J.; Burie, J. R.; Berthomieu, C.; Berger, G.; Nabedryk, E. The Binding-Sites of Quinones in Photosynthetic Bacterial Reaction Centers Investigated by Light-Induced Ftir Difference Spectroscopy—Assignment of the Q(a) Vibrations in *Rhodobacter sphaeroides* Using O-18-Labeled or C-13-Labeled Ubiquinone and Vitamin-K-1. *Biochemistry* **1994**, *33*, 4953−4965.

(13) Mezzetti, A.; Blanchet, L.; de Juan, A.; Leibl, W.; Ruckebusch, C. Ubiquinol Formation in Isolated Photosynthetic Reaction Centres Monitored by Time-Resolved Differential FTIR in Combination with 2D Correlation Spectroscopy and Multivariate Curve Resolution. *Anal. Bioanal. Chem.* **2011**, *399*, 1999−2014.
(14) Iwata, T.; Paddock, M. L.; Okamura, M. Y.; Kandori, H. Identification of FTIR Bands Due to Internal Water Molecules around the Quinone Binding Sites in the Reaction Center from *Rhodobacter sphaeroides*. *Biochemistry* **2009**, *48*, 1220−1229.
(15) Trammell, S. A.; Wang, L.; Zullo, J. M.; Shashidhar, R.; Lebedev, N. Orientated Binding of Photosynthetic Reaction Centers on Gold Using Ni-NTA Self-Assembled Monolayers. *Biosens. Bioelectron.* **2004**, *19*, 1649−1655.
(16) Trammell, S. A.; Griva, I.; Spano, A.; Tsoi, S.; Tender, L. M.; Schnur, J.; Lebedev, N. Effects of Distance and Driving Force on Photoinduced Electron Transfer between Photosynthetic Reaction Centers and Gold Electrodes. *J. Phys. Chem. C* **2007**, *111*, 17122−17130.
(17) Lebedev, N.; Trammell, S. A.; Spano, A.; Lukashev, E.; Griva, I.; Schnur, J. Conductive Wiring of Immobilized Photosynthetic Reaction Center to Electrode by Cytochrome *c*. *J. Am. Chem. Soc.* **2006**, *128*, 12044−12045.
(18) Lebedev, N.; Trammell, S. A.; Tsoi, S.; Spano, A.; Kim, J. H.; Xu, J.; Twigg, M. E.; Schnur, J. M. Increasing Efficiency of Photoelectronic Conversion by Encapsulation of Photosynthetic Reaction Center Proteins in Arrayed Carbon Nanotube Electrode. *Langmuir* **2008**, *24*, 8871−8876.
(19) Friedrich, M. G.; Robertson, J. W. F.; Walz, D.; Knoll, W.; Naumann, R. L. C. Electronic Wiring of a Multi-Redox Site Membrane Protein in a Biomimetic Surface Architecture. *Biophys. J.* **2008**, *94*, 3698−3705.
(20) Giess, F.; Friedrich, M. G.; Heberle, J.; Naumann, R. L.; Knoll, W. The Protein-Tethered Lipid Bilayer: A Novel Mimic of the Biological Membrane. *Biophys. J.* **2004**, *87*, 3213−3220.
(21) Nowak, C.; Luening, C.; Knoll, W.; Naumann, R. L. C. A Two-Layer Gold Surface with Improved Surface Enhancement for Spectro-Electrochemistry Using Surface-Enhanced Infrared Absorption Spectroscopy. *Appl. Spectrosc.* **2009**, *63*, 1068−1074.
(22) Goldsmith, J. O.; Boxer, S. G. Rapid Isolation of Bacterial Photosynthetic Reaction Centers with an Engineered Poly-Histidine Tag. *Biochim. Biophys. Acta, Bioenerg.* **1996**, *1276*, 171−175.
(23) Kirmaier, C.; Laible, P. D.; Czarnecki, K.; Hata, A. N.; Hanson, D. K.; Bocian, D. F.; Holten, D. Comparison of M-Side Electron Transfer in *Rb. sphaeroides* and *Rb. capsulatus* Reaction Centers. *J. Phys. Chem. B* **2002**, *106*, 1799−1808.
(24) Nowak, C.; Schach, D.; Gebert, J.; Grosserueschkamp, M.; Gennis, R. B.; Ferguson-Miller, S.; Knoll, W.; Walz, D.; Naumann, R. L. C. Oriented Immobilization and Electron Transfer to the Cytochrome *c* Oxidase. *J. Solid State Electrochem.* **2011**, *15*, 105−114.
(25) Schach, D.; Nowak, C.; Gennis, R. B.; Ferguson-Miller, S.; Knoll, W.; Walz, D.; Naumann, R. L. C. Modeling Direct Electron Transfer to a Multi-Redox Center Protein Cytochrome *c* Oxidase. *J. Electroanal. Chem.* **2010**, *649*, 268−276.
(26) Ataka, K.; Giess, F.; Knoll, W.; Naumann, R.; Haber-Pohlmeier, S.; Richter, B.; Heberle, J. Oriented Attachment and Membrane Reconstitution of His-Tagged Cytochrome *c* Oxidase to a Gold Electrode: In Situ Monitoring by Surface-Enhanced Infrared Absorption Spectroscopy. *J. Am. Chem. Soc.* **2004**, *126*, 16199−16206.
(27) Osawa, M. Surface-Enhanced Infrared Absorption. *Top. Appl. Phys.* **2001**, *81*, 163−187.
(28) Mäntele, W.; Nabedryk, E.; Tavitian, B. A.; Kreutz, W.; Breton, J. Light-Induced Fourier Transform Infrared (FTIR) Spectroscopic Investigations of the Primary Donor Oxidation in Bacterial Photosynthesis. *FEBS Lett.* **1985**, *187*, 227−232.
(29) Remy, A.; Gerwert, K. Coupling of Light-Induced Electron Transfer to Proton Uptake in Photosynthesis. *Nat. Struct. Biol.* **2003**, *10*, 637−644.
(30) Leonhard, M.; Mantele, W. Fourier-Transform Infrared-Spectroscopy and Electrochemistry of the Primary Electron-Donor in *Rhodobacter sphaeroides* and *Rhodopseudomonas viridis* Reaction Centers—Vibrational-Modes of the Pigments Insitu and Evidence for Protein and Water Modes Affected by P+ Formation. *Biochemistry* **1993**, *32*, 4532−4538.
(31) Breton, J.; Boullais, C.; Berger, G.; Mioskowski, C.; Nabedryk, E. Binding Sites of Quinones in Photosynthetic Bacterial Reaction Centers Investigated by Light-Induced FTIR Difference Spectroscopy: Symmetry of the Carbonyl Interactions and Close Equivalence of the QB Vibrations in *Rhodobacter sphaeroides* and *Rhodopseudomonas viridis* Probed by Isotope Labeling. *Biochemistry* **1995**, *34*, 11606−11616.
(32) Nabedryk, E.; Breton, J. Coupling of Electron Transfer to Proton Uptake at the QB Site of the Bacterial Reaction Center: A Perspective from FTIR Difference Spectroscopy. *Biochim. Biophys. Acta, Bioenerg.* **2008**, *1777*, 1229−1248.
(33) Breton, J.; Nabedryk, E. Protein-Quinone Interactions in the Bacterial Photosynthetic Reaction Center: Light-Induced FTIR Difference Spectroscopy of the Quinone Vibrations. *Biochim. Biophys. Acta, Bioenerg.* **1996**, *1275*, 84−90.
(34) Stuart, B. *Biological Applications of Infrared Spectroscopy*; John Wiley & Sons, Ltd: New York, 1997.
(35) Jiang, X.; Zaitseva, E.; Schmidt, M.; Siebert, F.; Engelhard, M.; Schlesinger, R.; Ataka, K.; Vogel, R.; Heberle, J. Resolving Voltage-Dependent Structural Changes of a Membrane Photoreceptor by Surface-Enhanced IR Difference Spectroscopy. *Proc. Natl. Acad. Sci. U. S. A.* **2008**, *105*, 12113−12117.
(36) Nowak, C.; Santonicola, M. G.; Schach, D.; Zhu, J.; Gennis, R. B.; Ferguson-Miller, S.; Baurecht, D.; Walz, D.; Knoll, W.; Naumann, R. L. C. Conformational Transitions and Molecular Hysteresis of Cytochrome *c* Oxidase: Varying the Redox State by Electronic Wiring. *Soft Matter* **2010**, *6*, 5523−5532.
(37) Nabedryk, E.; Breton, J.; Okamura, M. Y.; Paddock, M. L. Proton Uptake by Carboxylic Acid Groups upon Photoreduction of the Secondary Quinone (Q(B)) in Bacterial Reaction Centers from *Rhodobacter sphaeroides*: FTIR Studies on the Effects of Replacing Glu H173. *Biochemistry* **1998**, *37*, 14457−14462.
(38) Graige, M. S.; Paddock, M. L.; Bruce, J. M.; Feher, G.; Okamura, M. Y. Mechanism of Proton-Coupled Electron Transfer for Quinone (Q(B)) Reduction in Reaction Centers of *Rb-sphaeroides*. *J. Am. Chem. Soc.* **1996**, *118*, 9005−9016.
(39) McPherson, P. H.; Schonfeld, M.; Paddock, M. L.; Okamura, M. Y.; Feher, G. Protonation and Free Energy Changes Associated with Formation of QBH2 in Native and Glu-L212 → Gln Mutant Reaction Centers from *Rhodobacter sphaeroides*. *Biochemistry* **1994**, *33*, 1181−1193.
(40) Shinkarev, V. P.; Wraight, C. A. The Interaction of Quinone and Detergent with Reaction Centers of Purple Bacteria 0.1. Slow Quinone Exchange between Reaction Center Micelles and Pure Detergent Micelles. *Biophys. J.* **1997**, *72*, 2304−2319.
(41) Blanchet, L.; Mezzetti, A.; Ruckebusch, C.; Huvenne, J. P.; de Juan, A. Multivariate Curve Resolution of Rapid-Scan FTIR Difference Spectra of Quinone Photoreduction in Bacterial Photosynthetic Membranes. *Anal. Bioanal. Chem.* **2007**, *387*, 1863−1873.
(42) Mantsch, H. H.; McElhaney, R. N. Phospholipid Phase-Transitions in Model and Biological-Membranes as Studied by Infrared-Spectroscopy. *Chem. Phys. Lipids* **1991**, *57*, 213−226.
(43) Arrondo, J. L. R.; Castresana, J.; Valpuesta, J. M.; Goni, F. M. Structure and Thermal-Denaturation of Crystalline and Noncrystalline Cytochrome-Oxidase as Studied by Infrared-Spectroscopy. *Biochemistry* **1994**, *33*, 11650−11655.
(44) Casal, H. L.; Cameron, D. G.; Smith, I. C. P.; Mantsch, H. H. *Acholeplasma laidlawii* Membranes: A Fourier Transform Infrared Study of the Influence of Protein on Lipid Organization and Dynamics. *Biochemistry* **1980**, *19*, 444−451.

Supplementary Information

Marker Bands of Light-Activated Photosynthetic Reaction Centers from *Rhodobacter sphaeroides* by Surface-Enhanced Infrared Absorption Spectroscopy (SEIRAS)

Vedran Nedelkovski[†], Andreas Schwaighofer[†], Colin Wraight[‡], Renate L. C. Naumann[†], and Christoph Nowak[†,§,]*

[†] Austrian Institute of Technology GmbH, AIT, Donau-City Str. 1, 1220 Vienna, Austria

[‡] University of Illinois, Urbana, IL 61801, USA

[§] Center of Electrochemical Surface Technology, CEST, Viktor-Kaplan-Straße 2, 2700 Wiener Neustadt, Austria

Preparation of Template Stripped Gold (TSG) Surface. The preparation of TSG slides was performed as previously described by Naumann et al[1]. Gold films (43nm thick) were deposited by electrothermal evaporation (rate 0.1 nm/s, 1.7 x 10^{-7} mbar) silicon wafers, which had been cleaned by immersion in a solution (1:1:5) of ammonium hydroxide 25%, hydrogen peroxide 33%, H_2O at 80 C[1] for 10 minutes, rinsed in copious amounts of water and ethanol and dried in a stream of nitrogen. The gold surface was then glued with EPO-TEK 353ND (n=1.5694 @ 589 nm) (Epoxy Technology, Billerica, MA) to microscope glass slides and cured for 30 min at 120°C. After cooling, the slides were detached from the silicon wafers to expose the TSG film, which was then directly immersed into the thiolipid (DTNTA/DTP) solution.

Surface Plasmon Resonance Spectroscopy (SPR). SPR was performed in the Kretschmann-configuration using a home-built measuring cell designed for simultaneous measurement of SPR and electrochemistry[2]. The glass slide was optically matched (Index match n=1.7, Cargille Laboratories, Cedar Grove, NJ (USA)) to the base of a 90° glass prism (LaSFN9, from Helma Optics, Jena, Germany, n=1.85 @ 632.8 nm). Surface plasmons were excited by monochromatic light from a He-Ne Laser (10 mW, λ=632.8 nm from Uniphase, Milpitas, CA (USA)), which was directed through the prism and collected by a custom-made photodiode detector. Recording the change of reflectivity at a fixed angle in the linear regime of the SPR curve as a function of time yields the time course of protein immobilization and reconstitution in the ptBLM (Fig. S1). SPR spectra were simulated according to the Fresnel equations and the transfer-matrix method in the software Winspall (Max Planck Institute for Polymer Research in Mainz, Germany) using a four-layer model representing the prism glass, gold,

protein and lipid. By holding the refractive index constant one can obtain the optical layer-thickness. The simulated data are collected in Table S1.

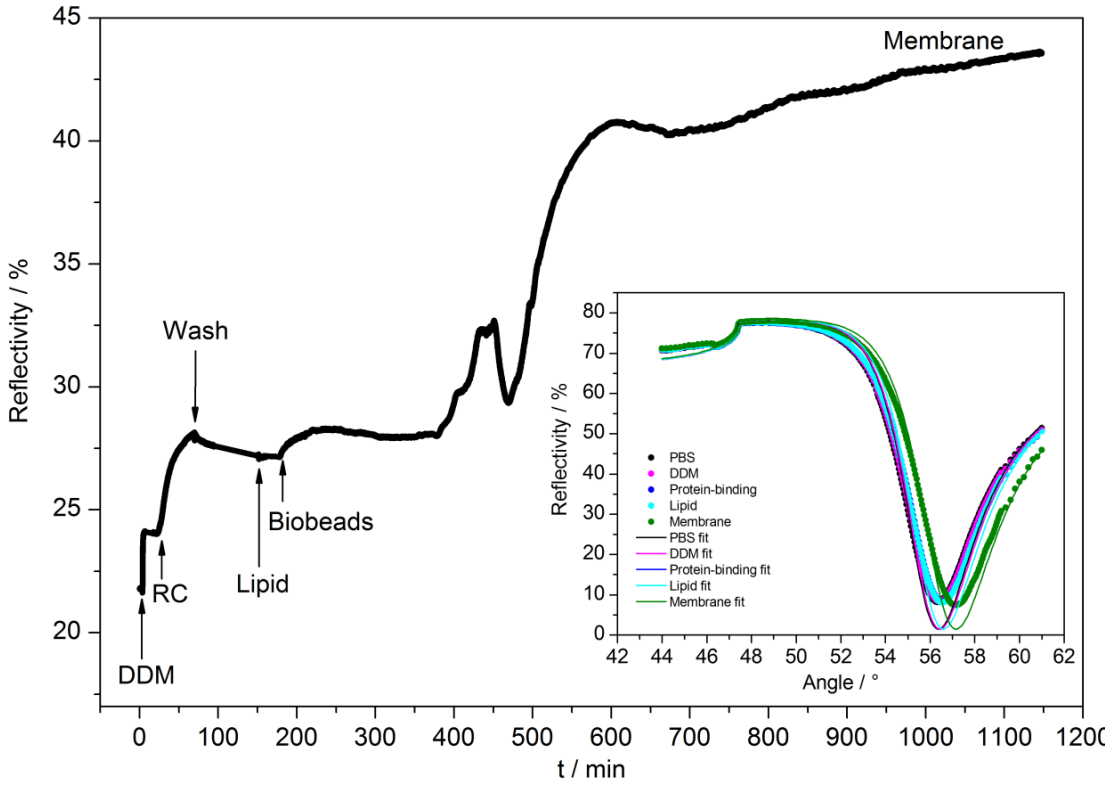

Figure S1. SPR Kinetic trace recorded during the immobilization of RCs on the NTA-functionalized gold and subsequent reconstitution in the ptBLM at a constant angle of incidence (55°). The respective SPR reflectivity scans as a function of angle of incidence are shown in the inset. Full circles represent the measured data, full lines represent the respective simulated curves.

Table S1. Optical layer-thickness values obtained from the simulated SPR spectra after protein-immobilization and reconstitution in the ptBLM, respectively.

	Layer thickness [nm]	**Refractive index n**
Protein	1.2	1.434
Membrane	6.1	1.434

Electrochemical Impedance Spectroscopy (EIS). Impedance measurements were carried out using an Autolab instrument (PGSTAT302 from Metrohm Autolab B.V., Utrecht, The Netherlands). Measurements were taken in a phosphate buffer solution (0.05 M K_2PO_4, 0.1 M KCl, pH=8) using a three-electrode configuration with TSG as the working electrode, a Ag/AgCl,KCl_{sat} reference electrode and a platinum wire as the counter electrode. Impedance spectra were recorded in a frequency range from 100 kHz to 10 mHz with an excitation amplitude of 10 mV, firstly after immobilization of RCs and then after reconstitution in the ptBLM (Fig. S2). Data were subsequently analyzed by the fitting algorithm using an equivalent circuit (Fig. S3), based on the Boukamp model, supplied in the data processing software package Nova (Version 1.7). Parameters obtained from the fitted data are collected in Table S2.

An increase in the resistance of the layer on the gold surface can be observed in the Bode plot (Fig. 2A) after formation of the ptBLM, indicating that the voids between the proteins are filled with a lipid bilayer, thus impeding the flow of ions. Furthermore, there is a substantial decrease in the capacitance of the layer after reconstitution (Fig. 2B), which can be understood in terms of the smaller dielectric constant of lipid than that of water molecules, thus confirming the formation of the ptBLM.

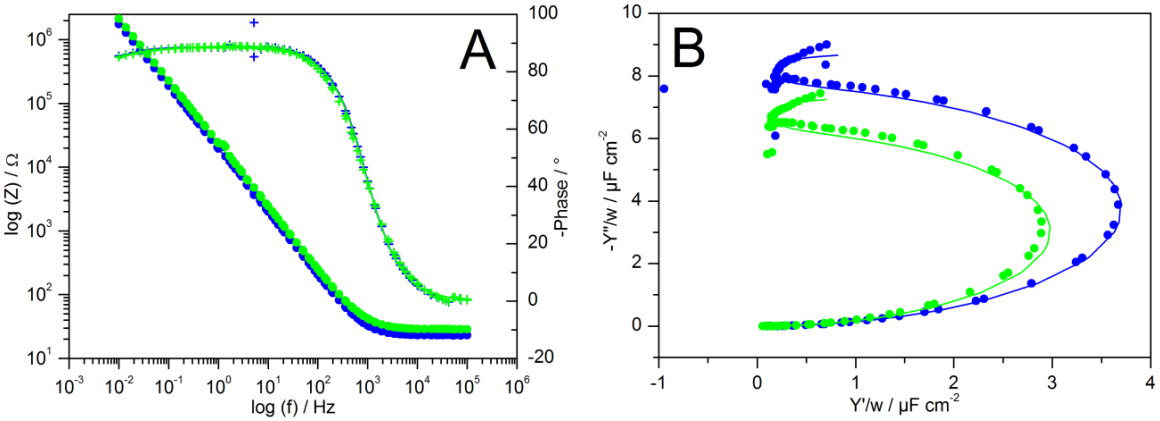

Figure S2. Impedance spectra of RCs immobilized on the NTA-functionalized gold surface (green data) and after reconstitution in the ptBLM (blue data). Full circles and crosses represent the measured data, full lines represent the fitted curves. A-Bode plot, B-Frequency-normalized

Table S2. Parameters obtained from the fitted impedance data of the protein layer before and after reconstitution in the ptBLM using the equivalent circuit from Fig. S3.

	R_M / MΩ cm^{-2}	CPE / µF cm^{-2}	α
Protein	25.3	8.34	0.986
Membrane	31.7	6.91	0.983

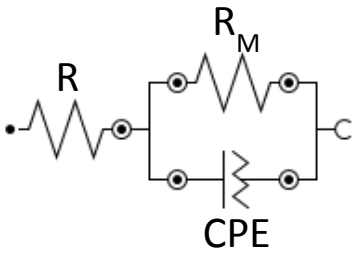

Figure S3. Equivalent electrochemical circuit used for fitting of impedance spectra of RCs reconstituted in the ptBLM. R represents the resistance of the submembrane space, R_M the resistance of the Protein/ptBLM layer. CPE is a constant phase element..

References

1. R. Naumann, S. M. Schiller, F. Giess, B. Grohe, K. B. Hartman, I. Karcher, I. Koper, J. Lubben, K. Vasilev and W. Knoll, *Langmuir*, 2003, **19**, 5435-5443.
2. F. Giess, M. G. Friedrich, J. Heberle, R. L. Naumann and W. Knoll, *Biophysical Journal*, 2004, **87**, 3213-3220.

Honey bee Odorant Binding Protein 14: Effects on Thermal Stability upon Odorant Binding revealed by FT-IR Spectroscopy and CD Measurements

Andreas Schwaighofer[†], Caroline Kotlowski[‡], Can Araman[§], Nam Chu[§], Rosa Mastrogiacomo[‖], Christian Becker[§], Paolo Pelosi,[‖] Wolfgang Knoll[†], Melanie Larisika[†], and Christoph Nowak[†,‡,*]

[†]Austrian Institute of Technology GmbH, AIT, Donau-City Str. 1, 1220 Vienna, Austria

[‡]Center of Electrochemical Surface Technology, CEST, Viktor-Kaplan-Straße 2, 2700 Wiener Neustadt, Austria

[§]Institut für Biologische Chemie, Universität Wien, Währinger Straße 38, 1090 Wien, Austria

[‖]Department of Agriculture, Food and Environment, University of Pisa, Via del Borghetto 80, 56124 Pisa, Italy

Corresponding author:
Dr. Christoph Nowak
Biosensor Technologies
AIT Austrian Institute of Technology
Muthgasse 11
1190 Vienna / Austria
Tel.: +43(0) 50550-4430

Abstract In the present work, we study the effect of odorant binding on the thermal stability of odorant binding protein 14 (OBP14) of the honey bee (*Apis mellifera* L.). Thermal denaturation of the protein in the absence and presence of different odorant molecules was monitored by Fourier transform infrared spectroscopy (FT-IR) and circular dichroism (CD). FT-IR spectra show characteristic bands for intermolecular aggregation through formation of intermolecular β-sheets during the heating process. Transition temperatures in the FT-IR spectra were evaluated using moving-window 2D correlation maps and confirmed by CD measurements. The obtained results reveal an increase of the denaturation temperature of the protein when bound to an odorant molecule. We could also discriminate between high and low affinity odorants using transition temperatures, as demonstrated independently by the two applied methodologies. The increased thermal stability in the presence of ligands is attributed to a stabilizing effect of non-covalent interactions between OBP14 and the odorant molecule.

Keywords Odorant binding protein, *Apis mellifera*, Infrared spectroscopy, circular dichroism, ligand binding, moving window 2D spectroscopy

Introduction

Odorant binding proteins (OBPs) are the object of growing interest as biosensing elements for the fabrication of odorant sensors based on the olfactory system (Park et al. 2012a; Persaud 2012; Glatz and Bailey-Hill 2011; Lee et al. 2012b). Applications are manifold and include disease diagnostics (Sankaran et al. 2011), food safety (Di Pietrantonio et al. 2013), and environmental monitoring (Misawa et al. 2010; Capone et al. 2011). Currently, so-called "electronic noses" are based on metal oxides and conducting polymers, but biomimetic sensors promise to show higher sensitivity and selectivity combined with lower detection limits and faster response time (Sankaran et al. 2012; Park et al. 2012b; Lee et al. 2012a; Jin et al. 2012). OBPs are small acidic proteins (~13-16 kDa) present in very high concentrations at the interface between olfactory receptors and external environment (Pelosi 1994; Tegoni et al. 2000; Bohbot and Vogt 2005; Pelosi et al. 2006). Their physiological role has not yet been clarified yet, but they have been associated with transfer of the odorant molecules to the receptor proteins. Odorants commonly are lipophilic molecules and need to be carried through the aqueous olfactory mucus of vertebrates respectively the sensillar lymph of insects to the membrane-bound olfactory receptors (Sankaran et al. 2011). The number of OBP subtypes is different for each species suggesting a role in discriminating semiochemicals.

Despite a common name, OBPs of vertebrates and those of insects are completely different in structure. Vertebrates OBPs are folded into 8 antiparallel β-strands and a short α-helical segment, in the typical β-barrel structure of lipocalins (Bianchet et al. 1996; Tegoni et al. 1996). OBPs of insects, instead, contain six α-helical domains arranged in a very compact and stable structure. The stability of these proteins is further increased by the presence of three interlocked

disulphide bonds (Leal et al. 1999; Scaloni et al. 1999). In the honey bee (*Apis mellifera* L.), 21 genes encode proteins of the OBP family (Foret and Maleszka 2006). OBP14 which is the subject of this study has been identified in different tissues of adult bees, as well as in larvae (Iovinella et al. 2011). Using binding fluorescence studies, affinities of several odorants have been determined for this OBP, geraniol being identified as a representative of low affinity ligands and eugenol as high affinity ligand. A crystallographic study of the three-dimensional structure of this protein and its complexes with some ligands, supports the ligand-binding experiments (Iovinella et al. 2011; Spinelli et al. 2012).

Stabilizing effects of proteins upon ligand binding have been reported for a large variety of systems (Celej et al. 2005; Moreau et al. 2010; Celej et al. 2003). Weak non-covalent forces such as hydrogen bonds as well as hydrophobic and aromatic interactions have been identified to play an important role in increasing the structural stability of the protein-ligand complexes (Williams et al. 2004; Bissantz et al. 2010; Stepanenko et al. 2008; Kumar et al. 2000). Thermal denaturation measurements employing differential scanning calorimetry or isothermal denaturation are a commonly used way to study the stability of proteins (Moreau et al. 2010). However, these methods lack the ability to provide structural information of the protein during the heating process.

Fourier-transform infrared (FT-IR) spectroscopy is an established and powerful method for investigating the structure and dynamics of proteins (Barth 2007). In combination with thermal denaturation experiments, FT-IR was extensively used to reveal structural changes of proteins induced by increasing temperatures (Pedone et al. 2003; Zhang et al. 1998; Arrondo et al. 2005), including the thermal transitions of the β-barrel structure of vertebrae OBPs (Marabotti et al. 2008a; Marabotti et al. 2008b; Paolini et al. 1999; Scire et al. 2009). Unlike previously used

evaluation methods, we use moving-window two-dimensional (MW2D) correlation maps to highlight the transition points in the FT-IR spectra. MW2D correlation maps are an extension to generalized 2D correlation (2D-COS) spectroscopy but here, the spectral information is sub-divided into slices along the perturbation range and the autocorrelation intensity is plotted versus the perturbation variable. Interpretation of MW2D correlations maps is more intuitive compared to the rather complex evaluation algorithms of 2D-COS spectra and it has been proven to be an excellent tool for analyzing spectral changes caused by external perturbation (Ashton and Blanch 2010; Thomas and Richardson 2000; Du et al. 2010). Further, circular dichroism (CD) is a convenient method for studying the structure of proteins in solution (Kelly et al. 2005). To the best of our knowledge, this is the first report applying FT-IR studies to insect OBPs. We investigated the changes of thermal stability upon odorant binding of low- and high-affinity ligands to OBP14. To address this question, FT-IR and CD have been adopted to study the structural changes of the protein induced by thermal denaturation, both in the presence and in absence of odorants. The denaturation temperatures in the FT-IR spectra were visualized by MW2D correlation maps and corroborated by CD measurements.

Materials and methods

Materials

Deuterium oxide (D_2O, 99.9% D), geraniol (2,6-Dimethyl-trans-2,6-octadien-8-ol, 98%) and eugenol (4-Hydroxy-3-methoxy-1-allyl-benzol, 99%) were provided by Sigma-Aldrich (Steinheim, Germany). Dithiobis (nitriloacetic acid butylamidyl propionate) (DTNTA, ≥95.0%) was obtained from Dojindo Laboratories (Kumamoto, Japan).

Expression and purification of OBP14

The nucleotide sequence encoding OBP14 and flanked by restriction sites NdeI and BamHI, was ligated into the expression vector pET15b (Novagen, Darmstadt, Germany), which provides a His-tag at the N-terminus of the protein. Bacterial expression was performed along with established protocols (Dani et al. 2010; Iovinella et al. 2011) and purification was accomplished using conventional chromatographic techniques (Ban et al. 2003; Calvello et al. 2003). The purity of the protein was checked by SDS-PAGE.

Infrared Spectroscopy

Infrared absorption measurements were performed using a Bruker 70v FTIR spectrometer (Karlsruhe, Baden-Württemberg, Germany), equipped with a Harrick Horizon attenuated total reflection (ATR) measuring unit with a temperature-controlled liquid sample cell (400 µL), containing a ZnSe ATR crystal (angle of incidence θ = 45°, 12.5 active reflections). OBP14 from *E. coli* with a His-tag engineered on the N-terminus was expressed as described by Iovinella et al. (Iovinella et al. 2011). ATR crystals were immersed in a solution of 5 mM DTNTA and 5 mM 3,3'-dithiodipropionic acid (DTP) in dry DMSO for 20 h. After rinsing with purified water, the crystals were immersed in 40 mM $NiCl_2$ in acetate buffer (50 mM, pH 5.5) for 30 minutes, followed by thorough rinsing with purified water to remove excess $NiCl_2$. OBP14 dissolved in phosphate buffer (140 mM NaCl, 3 mM KCl, 10 mM Na_2HPO_4, 2 mM KH_2PO_4, pH 8) was adsorbed at 25 °C onto the NTA-functionalized surface at a final concentration of 20 µM. After 4-h adsorption time, the cell was rinsed with phosphate buffer. Hydrogen/deuterium (H/D) exchange was initiated by exchanging the buffer in the measurement cell by D_2O-phosphate buffer (pD=8.0, corresponds to the pH meter reading + 0.4),(Glasoe and

Long 1960) followed by pumping the deuterated buffer through the sample cell for 20 h at 0.15 mL/min. For measurements in the presence of odorants, the protein was incubated in 100 µM odorant solution in D_2O-buffer for 1 h. In thermal-denaturation experiments, the temperature was raised by 5 °C steps from 25-90 °C. Spectra were obtained after a 5 min equilibration time for stabilizing the cell temperature.

During FT-IR measurements, the sample chamber was continuously purged with dry carbon dioxide-free air, and the total reflected IR beam intensity was measured using a liquid nitrogen-cooled photovoltaic mercury cadmium telluride (MCT) detector. Spectra were recorded with a spectral resolution of 4 cm^{-1} in double-sided acquisition mode, the mirror velocity was set to 80 kHz. At least 1000 scans were taken for each spectrum, which was calculated using a Blackman-Harris 3-term apodization function and a zero filling factor of 2. Spectra were analyzed using the software package OPUS 6.5 and OriginLab's Origin software.

Moving-Window 2D correlation Spectroscopy

MW2D correlation spectra were calculated using the difference spectra after baseline correction with the freely available 2Dshige software (available at http://sci-tech.ksc.kwansei.ac.jp/~ozaki/2D-shige.htm) with a window size of 2m+1=11.

Circular Dichroism

Far UV (260-195 nm) CD measurements were carried out using an Applied Photophysics Chirascan plus (Leatherhead, Surrey, United Kingdom) spectrophotometer equipped with a temperature control unit (Quantum TC125) in a 1 mm quartz cell at 1 nm resolution. Purified protein solutions (0.5 mg/mL; 41.8 µM) were prepared in phosphate buffer, pH 8. For static

measurements, ten spectra with the acquisition time of 0.5 s were taken at room temperature and the results were averaged. To study the effect of odorants on OBP14, the protein was incubated in 200 μM odorant solution for 1 h. In temperature-controlled experiments, spectra were taken in the range of 20-85 °C (ΔT=5 °C) with an acquisition time of 0.2 s after an equilibration time of 30 s at each temperature step.

Results and discussion

Infrared spectroscopy

OBP14 engineered with a His-tag at its N-terminus was immobilized on the NTA-linker functionalized on the ZnSe crystal (see Fig. S1 in the Supporting Information). Because of the increased noise level in the amide I region due to the high absorption of the OH-bending band of water in this area, H/D-exchange was performed to permit secondary structure determination. During exchange of the aqueous buffer with deuterated buffer solution (not shown), the amide II (~1550 cm^{-1}) band, primarily consisting of N-H bending modes, decreased and shifted to the amide II' band (~1450 cm^{-1}), that partly overlaps with the HOD vibration (1450 cm^{-1}) (Walrafen 1972). Since the N-H bending vibration only marginally contributes to the amide I band, it only exhibits a smaller shift to lower wavenumbers upon H/D exchange (Wu et al. 2001; Barth 2007; Barth and Zscherp 2002). Fig. 1 shows a FT-IR spectrum in the amide I' region of the immobilized OBP14 after H/D exchange. A curve-fit with Gaussian line shapes was performed to estimate components of the secondary structure. The measured spectrum (black line) is in good agreement with the sum of fitted lines (dashed red line). The band at 1648 cm^{-1} was attributed to α-helix, whose band position is slightly shifted to lower wavenumbers in D_2O

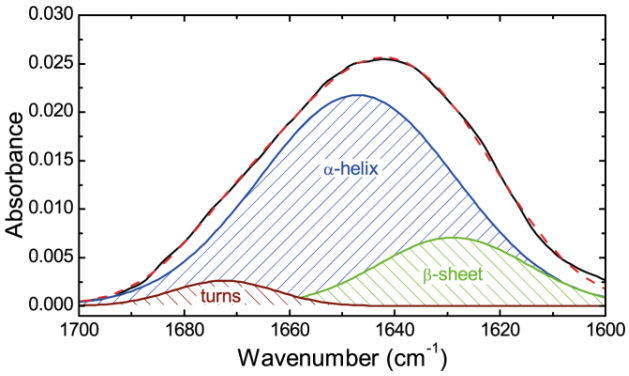

Fig. 1 FT-IR spectrum of immobilized OBP14 after H/D exchange with Gaussian curve-fits. The sum of fits (dashed red line) is in good agreement with the measured spectrum (black line)

puffer compared to aqueous buffer solution (Barth 2007; Arrondo et al. 1993; Pelton and McLean 2000). Bands at 1628.9 cm^{-1} and 1672.4 cm^{-1} were assigned to β-sheets and turns, respectively (Barth and Zscherp 2002). Evaluation of the band areas shows that the protein consists of 76.3 % α-helix, 18.9 % β-sheets and 4.8 % turns. This is in good agreement with X-ray diffraction studies that showed a high abundance of α-helix (Spinelli et al. 2012), in particular when considering that curve-fitting tends to overestimate β-sheets of overly α-helical proteins at the cost of α-helix (Oberg et al. 2004; Byler and Susi 1986). For measurements in complex with geraniol and eugenol, the odorants were incubated with the protein. IR absorbance spectra of OBP14 in the presence of ligands do not show significant differences in the amide I' region compared to the spectra of the protein alone (see Fig. S2 in the Supporting Information). This indicates that the binding of the odorant does not considerably modify the secondary structure in the protein, as reported previously for odorant binding proteins of other species (Scire et al. 2009; Paolini et al. 1999; Vincent et al. 2000).

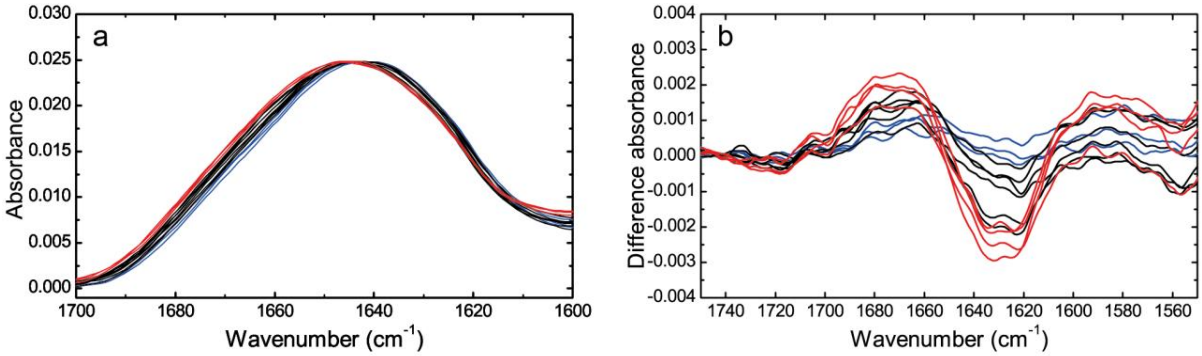

Fig. 2 (a) FT-IR spectra of OBP14 in the absence of an odorant at temperatures from 25-90 °C in the amide I' region. Spectra in blue are taken at low temperatures (30-40 °C), black spectra denote intermediate temperatures (45-70 °C) and red spectra indicate high temperatures (75-90 °C). The amide I' band shifts to higher frequencies with increasing temperature. (b) Difference spectra with the spectrum at 25 °C as a reference

The effect of odorant binding on the thermal stability of honey bee OBP14 were determined by monitoring the amide I' band, both in the absence and presence of geraniol and eugenol during the heating process. Fig. 2a shows the changes of the amide I' band while rising the temperature from 25 to 90 °C. With increasing temperature, the band shifts to higher frequencies. In spectroscopic methods, a band shift usually is the cumulative effect of the decrease of intensity at one vibration frequency combined with the increase of intensity at another vibration frequency. To study the structural changes during thermal denaturation in greater detail, difference spectra of OBP14 at various temperatures are shown in Fig. 2b. At lower temperatures up to 40 °C (blue lines), there are only minor changes in the spectra. Significant changes occur at temperatures between 40 and 70 °C (black spectra) with an increase of absorbance between 1670 and 1680 cm^{-1} and a decreasing band intensity around 1630 cm^{-1}. At high temperatures between 75 and 90 °C, only small changes take place and its seems that the structural changes upon thermal

denaturation are completed. Similar behavior has been found for other α-helix-rich proteins, in particular serum albumin (Saguer et al. 2012). The negative band at ~1630 cm^{-1} is assigned to the loss of native β-sheet structure. Increasing bands in the high-frequency region can be attributed to evolving turns (~1670 cm^{-1}) and intermolecular β–sheets (~1680 cm^{-1}) due to heat induced aggregation (Saguer et al. 2012). These bands attributed to intermolecular aggregation are known to occur at high-temperature treatment for proteins with various native secondary structures (Bai and Dong 2009; Pedone et al. 2003).

For visualization of the transition temperature in FT-IR spectra, MW2D correlation maps have been employed. In these maps, the FT-IR spectrum is plotted versus the perturbation coordinate, i.e. temperature. This method is particularly useful for the identification of spectral changes along the perturbation axis (Noda 2010). The temperature ranges where the largest spectral changes occur, are the regions where thermal denaturation takes place and are indicated by a peak in the correlation maps (Thomas and Richardson 2000). Fig. 3 shows the MW2D correlation maps for the thermal denaturation measurements of OBP14 in the absence or the presence odorants of present, monitored by FT-IR spectroscopy. In Fig. 3a, a sharp peak appears at 55 °C indicating that the major part of denaturation mainly takes place at this temperature. The spectral region of ~1630 cm^{-1} is attributed to native β-sheets, as discussed above. For OBP14 + geraniol, the peak for this structural feature is located at 60 °C (Fig. 3b), and for OBP14 + eugenol at a temperature of 65 °C (Fig. 3c). These results indicate, that the presence of odorants increases the thermal stability of the protein, and that strong ligands, such as eugenol, are more effective than weak ligands, as geraniol.

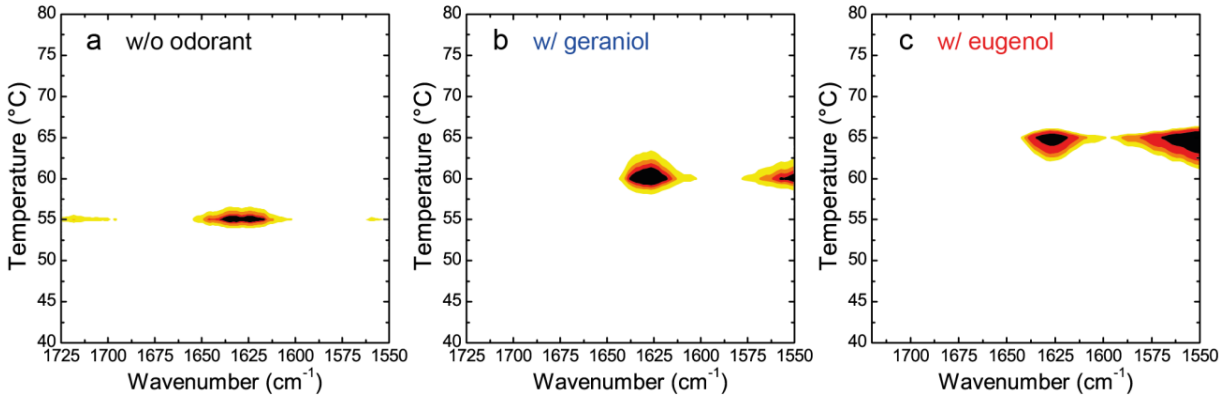

Fig. 3 MW2D correlation maps for OBP14 alone (a), or incubated with geraniol (b) and with eugenol (c)

Similar effects of ligands on the thermal stability of porcine (Paolini et al. 1999) and bovine (Marabotti et al. 2008a) OBPs have been reported, with increase of denaturation temperature of up to 15 °C. The structure of vertebrae OBPs features an 8-stranded β-barrel and is different from that of insect OBPs. The higher thermal stability is attributed to non-covalent forces such as hydrophobic and aromatic interactions as well as hydrogen bonds between OBP14 and the odorant molecule. Furthermore, correlation maps of OBP14 in the presence of odorants (Fig. 3b,c) display an additional peak at ~1550 cm^{-1}, that is not present in the map of OBP14 alone (Fig. 3a). Bands in this spectral region are assigned to H/D exchange. Their appearance at elevated temperatures indicates that H/D exchange has not been complete at room temperature or that prior buried structural features were exposed upon odorant binding (Paolini et al. 1999). This is in agreement with previous findings, which showed that the binding site of OBP14 performs geometry changes with small displacements of helices upon ligand binding that are subject of further H/D exchange (Spinelli et al. 2012). Particularly for eugenol, it was reported that strong

hydrogen bonds are involved in protein-odorant interaction (Spinelli et al. 2012). which accounts for the higher intensity of this peak.

Circular Dichroism

CD measurements of OBP14 with and without odorants are shown in Fig. S3 in the Supporting Information. The spectra display two negative peaks centered at 208 nm and 222 nm, which is a clear indication of high α-helical content (Yang et al. 2011; Briand et al. 2002; Kelly and Price 2000). Hence, assignment of secondary structure of OBP14 by CD is in agreement with X-ray diffraction and IR spectroscopy, as discussed above. As in FT-IR measurements, there is no significant change of secondary structure in CD measurements at room temperature due to ligand binding.

Effects on thermal stability of OBP14 due to odorant binding were investigated by acquiring CD spectra while increasing the temperature between 20 and 85 °C in 5 °C steps (see Fig. S4 in the Supporting Information). CD measurements of the buffer and odorant solutions without protein are shown in Fig. S5 in the Supporting Information and do not reveal any changes with increasing temperatures. Thermal denaturation of the protein was followed by evaluation of the CD signal at 222 nm which is particularly sensitive to changes of the secondary structure (Staiano et al. 2007; Kelly et al. 2005). Fig. 4 shows the ellipticity at 222 nm plotted versus temperature for OBP14 with and without odorants present. The data points were fitted with a Boltzmann function for sigmoidal lineshapes (dashed line). The points of inflection i.e. the temperature of maximum change for OBP14 alone, with geraniol and with eugenol are 55, 60 and 65 °C, respectively. These results agree very well with the data obtained by FT-IR spectroscopy, thus providing another tool to demonstrate that thermal stability of the OBP14, and

likely other insect OBPs, is higher in the presence of ligands and depends on the strength of binding (Spinelli et al. 2012).

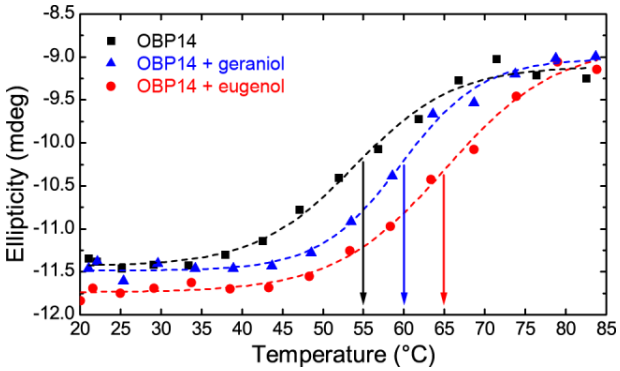

Fig. 4 Ellipticity at a wavelength of 222 nm of OBP14 in the absence and presence of odorants (data points). Dashed lines indicate a Boltzmann fit for sigmoidal lineshapes

Conclusions

In conclusion, we have shown that the interaction of honey bee OBP14 with its ligands leads to an increase of thermal stability of the protein. This finding is corroborated by two independent analytical methods, FT-IR spectroscopy and circular dichroism. The absence of significant changes in secondary structure upon ligand binding suggests that weaker forces such as hydrogen bonds and hydrophobic interactions are involved, as previously reported for OBP14 (Spinelli et al. 2012). Low-affinity and high-affinity odorants can be discriminated by their effect on the denaturation temperature that represents the different binding strengths and affinities for the tested odorants. Further, our measurements demonstrate the thermostability of OBP14 under ambient temperature until up to 45°C. This is of great interest with regard to possible uses of this protein for the fabrication of biosensors.

Acknowledgements

Partial support for this work was provided by the European Science Foundation (ESF), the Austrian Science Fund (FWF) (I681-N24) and the Austrian Federal Ministry for Transport, Innovation and Technology (GZ BMVIT-612.166/0001-III/I1/2010).

References

Arrondo JLR, Muga A, Castresana J, Goñi FM (1993) Quantitative studies of the structure of proteins in solution by fourier-transform infrared spectroscopy. Prog Biophys Mol Biol 59 (1):23-56.

Arrondo JLR, Pacios M, Iloro I, Goni FM (2005) Protein stability studied by 2D-infrared spectroscopy. Biophys J 88 (1):561a-562a.

Ashton L, Blanch EW (2010) pH-induced conformational transitions in alpha-lactalbumin investigated with two-dimensional Raman correlation variance plots and moving windows. J Mol Struct 974 (1-3):132-138.

Bai S, Dong A (2009) Effects of immobilization onto aluminum hydroxide particles on the thermally induced conformational behavior of three model proteins. Int J Biol Macromol 45 (1):80-85.

Ban L, Scaloni A, Brandazza A, Angeli S, Zhang L, Yan Y, Pelosi P (2003) Chemosensory proteins of Locusta migratoria. Insect Mol Biol 12 (2):125-134.

Barth A (2007) Infrared spectroscopy of proteins. Biochim Biophys Acta, Bioenerg 1767 (9):1073-1101.

Barth A, Zscherp C (2002) What vibrations tell about proteins. Q Rev Biophys 35 (04):369-430.

Bianchet MA, Bains G, Pelosi P, Pevsner J, Snyder SH, Monaco HL, Amzel LM (1996) The three-dimensional structure of bovine odorant binding protein and its mechanism of odor recognition. Nat Struct Biol 3 (11):934-939.

Bissantz C, Kuhn B, Stahl M (2010) A Medicinal Chemist's Guide to Molecular Interactions. J Med Chem 53 (14):5061-5084.

Bohbot J, Vogt RG (2005) Antennal expressed genes of the yellow fever mosquito (Aedes aegypti L.); characterization of odorant-binding protein 10 and takeout. Insect Biochem Mol Biol 35 (9):961-979.

Briand L, Swasdipan N, Nespoulous C, Bézirard V, Blon F, Huet J-C, Ebert P, Pernollet J-C (2002) Characterization of a chemosensory protein (ASP3c) from honeybee (Apis melliferaL.) as a brood pheromone carrier. Eur J Biochem 269 (18):4586-4596.

Byler DM, Susi H (1986) Examination of the secondary structure of proteins by deconvolved FTIR spectra. Biopolymers 25 (3):469-487.

Calvello M, Guerra N, Brandazza A, D'Ambrosio C, Scaloni A, Dani FR, Turillazzi S, Pelosi P (2003) Soluble proteins of chemical communication in the social wasp Polistes dominulus. Cell Mol Life Sci 60 (9):1933-1943.

Capone S, Pascali C, Francioso L, Siciliano P, Persaud KC, Pisanelli AM (2011) Odorant Binding Proteins as Sensing Layers for Novel Gas Biosensors: An Impedance Spectroscopy Characterization. In: Neri G, Donato N, d'Amico A, Di Natale C (eds) Sensors and Microsystems, vol 91. Lecture Notes in Electrical Engineering. Springer Netherlands, pp 317-324.

Celej MS, Dassie SA, Freire E, Bianconi ML, Fidelio GD (2005) Ligand-induced thermostability in proteins: thermodynamic analysis of ANS-albumin interaction. Biochim Biophys Acta 1750 (2):122-133.

Celej MS, Montich GG, Fidelio GD (2003) Protein stability induced by ligand binding correlates with changes in protein flexibility. Protein Sci 12 (7):1496-1506.

Dani FR, Iovinella I, Felicioli A, Niccolini A, Calvello MA, Carucci MG, Qiao HL, Pieraccini G, Turillazzi S, Moneti G, Pelosi P (2010) Mapping the Expression of Soluble Olfactory Proteins in the Honeybee. J Proteome Res 9 (4):1822-1833.

Di Pietrantonio F, Cannata D, Benetti M, Verona E, Varriale A, Staiano M, D'Auria S (2013) Detection of odorant molecules via surface acoustic wave biosensor array based on odorant-binding proteins. Biosens Bioelectron 41:328-334.

Du HY, Zhou T, Zhang JH, Liu XY (2010) Moving-window two-dimensional correlation infrared spectroscopy study on structural variations of partially hydrolyzed poly(vinyl alcohol). Anal Bioanal Chem 397 (7):3127-3132.

Foret S, Maleszka R (2006) Function and evolution of a gene family encoding odorant binding-like proteins in a social insect, the honey bee (Apis mellifera). Genome Res 16 (11):1404-1413.

Glasoe PK, Long FA (1960) Use of glass electrodes to measure acidities in deuterium oxide. J Phys Chem 64 (1):188-190.

Glatz R, Bailey-Hill K (2011) Mimicking nature's noses: from receptor deorphaning to olfactory biosensing. Prog Neurobiol 93 (2):270-296.

Iovinella I, Dani FR, Niccolini A, Sagona S, Michelucci E, Gazzano A, Turillazzi S, Felicioli A, Pelosi P (2011) Differential expression of odorant-binding proteins in the mandibular glands of the honey bee according to caste and age. J Proteome Res 10 (8):3439-3449.

Jin HJ, Lee SH, Kim TH, Park J, Song HS, Park TH, Hong S (2012) Nanovesicle-based bioelectronic nose platform mimicking human olfactory signal transduction. Biosens Bioelectron 35 (1):335-341.

Kelly SM, Jess TJ, Price NC (2005) How to study proteins by circular dichroism. Biochim Biophys Acta, Proteins Proteomics 1751 (2):119-139.

Kelly SM, Price NC (2000) The Use of Circular Dichroism in the Investigation of Protein Structure and Function. Curr Protein Pept Sci 1 (4):349-384.

Kumar S, Tsai C-J, Nussinov R (2000) Factors enhancing protein thermostability. Protein Eng 13 (3):179-191.

Leal WS, Nikonova L, Peng GH (1999) Disulfide structure of the pheromone binding protein from the silkworm moth, Bombyx mori. FEBS Lett 464 (1-2):85-90.

Lee SH, Jin HJ, Song HS, Hong S, Park TH (2012a) Bioelectronic nose with high sensitivity and selectivity using chemically functionalized carbon nanotube combined with human olfactory receptor. J Biotechnol 157 (4):467-472.

Lee SH, Kwon OS, Song HS, Park SJ, Sung JH, Jang J, Park TH (2012b) Mimicking the human smell sensing mechanism with an artificial nose platform. Biomaterials 33 (6):1722-1729.

Marabotti A, Lefevre T, Staiano M, Crescenzo R, Varriale A, Rossi M, Pezolet M, D'Auria S (2008a) Mutant bovine odorant-binding protein: Temperature affects the protein stability and dynamics as revealed by infrared spectroscopy and molecular dynamics simulations. Proteins: Struct, Funct, Genet 72 (2):769-778.

Marabotti A, Scire A, Staiano M, Crescenzo R, Aurilla V, Tanfani F, D'Auria S (2008b) Wild-Type and Mutant Bovine Odorant-Binding Proteins To Probe the Role of the Quaternary Structure Organization in the Protein Thermal Stability. J Proteome Res 7 (12):5221-5229.

Misawa N, Mitsuno H, Kanzaki R, Takeuchi S (2010) Highly sensitive and selective odorant sensor using living cells expressing insect olfactory receptors. Proc Natl Acad Sci 107 (35):15340-15344.

Moreau MJ, Morin I, Schaeffer PM (2010) Quantitative determination of protein stability and ligand binding using a green fluorescent protein reporter system. Mol Biosyst 6 (7):1285-1292.

Noda I (2010) Two-dimensional correlation spectroscopy - Biannual survey 2007-2009. J Mol Struct 974 (1-3):3-24.

Oberg KA, Ruysschaert JM, Goormaghtigh E (2004) The optimization of protein secondary structure determination with infrared and circular dichroism spectra. Eur J Biochem 271 (14):2937-2948.

Paolini S, Tanfani F, Fini C, Bertoli E, Paolo P (1999) Porcine odorant-binding protein: structural stability and ligand affinities measured by Fourier-transform infrared spectroscopy and fluorescence spectroscopy. Biochim Biophys Acta, Protein Struct Mol Enzymol 1431 (1):179-188.

Park J, Lim JH, Jin HJ, Namgung S, Lee SH, Park TH, Hong S (2012a) A bioelectronic sensor based on canine olfactory nanovesicle-carbon nanotube hybrid structures for the fast assessment of food quality. Analyst 137 (14):3249-3254.

Park SJ, Kwon OS, Lee SH, Song HS, Park TH, Jang J (2012b) Ultrasensitive flexible graphene based field-effect transistor (FET)-type bioelectronic nose. Nano Lett 12 (10):5082-5090.

Pedone E, Bartolucci S, Rossi M, Pierfederici FM, Scire A, Cacciamani T, Tanfani F (2003) Structural and thermal stability analysis of Escherichia coli and Alicyclobacillus acidocaldarius thioredoxin revealed a molten globule-like state in thermal denaturation pathway of the proteins: an infrared spectroscopic study. Biochem J 373:875-883.

Pelosi P (1994) Odorant-Binding Proteins. Crit Rev Biochem Mol 29 (3):199-228.

Pelosi P, Zhou JJ, Ban LP, Calvello M (2006) Soluble proteins in insect chemical communication. Cell Mol Life Sci 63 (14):1658-1676.

Pelton JT, McLean LR (2000) Spectroscopic methods for analysis of protein secondary structure. Anal Biochem 277 (2):167-176.

Persaud KC (2012) Biomimetic Olfactory Sensors. IEEE Sens J 12 (11):3108-3112.

Saguer E, Alvarez P, Ismail AA (2012) Heat-induced denaturation/aggregation of porcine plasma and its fractions studied by FTIR spectroscopy. Food Hydrocolloids 27 (1):208-219.

Sankaran S, Khot LR, Panigrahi S (2012) Biology and applications of olfactory sensing system: A review. Sens Actuator B-Chem 171:1-17.

Sankaran S, Panigrahi S, Mallik S (2011) Odorant binding protein based biomimetic sensors for detection of alcohols associated with Salmonella contamination in packaged beef. Biosens Bioelectron 26 (7):3103-3109.

Scaloni A, Monti M, Angeli S, Pelosi P (1999) Structural analysis and disulfide-bridge pairing of two odorant-binding proteins from Bombyx mori. Biochem Biophys Res Commun 266 (2):386-391.

Scire A, Marabotti A, Staiano M, Briand L, Varriale A, Bertoli E, Tanfani F, DAuria S (2009) Structure and Stability of a Rat Odorant-Binding Protein: Another Brick in the Wall. J Proteome Res 8 (8):4005-4013.

Spinelli S, Lagarde A, Iovinella I, Legrand P, Tegoni M, Pelosi P, Cambillau C (2012) Crystal structure of Apis mellifera OBP14, a C-minus odorant-binding protein, and its complexes with odorant molecules. Insect Biochem Mol Biol 42 (1):41-50.

Staiano M, D'Auria S, Varriale A, Rossi M, Marabotti A, Fini C, Stepanenko OV, Kuznetsova IM, Turoverov KK (2007) Stability and dynamics of the porcine odorant-binding protein. Biochemistry 46 (39):11120-11127.

Stepanenko OV, Marabotti A, Kuznetsova IM, Turoverov KK, Fini C, Varriale A, Staiano M, Rossi M, D'Auria S (2008) Hydrophobic interactions and ionic networks play an important role in thermal stability and denaturation mechanism of the porcine odorant-binding protein. Proteins: Struct, Funct, Genet 71 (1):35-44.

Tegoni M, Pelosi P, Vincent F, Spinelli S, Campanacci V, Grolli S, Ramoni R, Cambillau C (2000) Mammalian odorant binding proteins. Biochim Biophys Acta-Protein Struct Molec Enzymol 1482 (1-2):229-240.

Tegoni M, Ramoni R, Bignetti E, Spinelli S, Cambillau C (1996) Domain swapping creates a third putative combining site in bovine odorant binding protein dimer. Nat Struct Biol 3 (10):863-867.

Thomas M, Richardson HH (2000) Two-dimensional FT-IR correlation analysis of the phase transitions in a liquid crystal, 4'-n-octyl-4-cyanobiphenyl (8CB). Vib Spectrosc 24 (1):137-146.

Vincent F, Spinelli S, Ramoni R, Grolli S, Pelosi P, Cambillau C, Tegoni M (2000) Complexes of porcine odorant binding protein with odorant molecules belonging to different chemical classes. J Mol Biol 300 (1):127-139.

Walrafen GE (1972) Raman and infrared spectral investigations of water structure. In: Franks F (ed) Water A Comprehensive Treatise, vol 1. Plenum Press, New York, pp 151-214.

Williams DH, Stephens E, O'Brien DP, Zhou M (2004) Understanding Noncovalent Interactions: Ligand Binding Energy and Catalytic Efficiency from Ligand-Induced Reductions in Motion within Receptors and Enzymes. Angew Chem, Int Ed 43 (48):6596-6616.

Wu Y, Murayama K, Ozaki Y (2001) Two-Dimensional Infrared Spectroscopy and Principle Component Analysis Studies of the Secondary Structure and Kinetics of Hydrogen-Deuterium Exchange of Human Serum Albumin. J Phys Chem B 105 (26):6251-6259.

Yang G, Winberg G, Ren H, Zhang SG (2011) Expression, purification and functional analysis of an odorant binding protein AaegOBP22 from Aedes aegypti. Protein Expres Purif 75 (2):165-171.

Zhang HM, Ishikawa Y, Yamamoto Y, Carpentier R (1998) Secondary structure and thermal stability of the extrinsic 23 kDa protein of photosystem II studied by Fourier transform infrared spectroscopy. Febs Letters 426 (3):347-351.

Supplementary Data

Honey bee Odorant Binding Protein 14: Effects on Thermal Stability upon Odorant Binding revealed by FT-IR Spectroscopy and CD Measurements

Andreas Schwaighofer[†], *Caroline Kotlowski*[‡], *Can Araman*[§], *Nam Chu*[§], *Rosa Mastrogiacomo*[‖], *Christian Becker*[§], *Paolo Pelosi,*[‖] *Wolfgang Knoll*[†], *Melanie Larisika*[†], *and Christoph Nowak*[†,‡,*]

[†]Austrian Institute of Technology GmbH, AIT, Donau-City Str. 1, 1220 Vienna, Austria

[‡]Center of Electrochemical Surface Technology, CEST, Viktor-Kaplan-Straße 2, 2700 Wiener Neustadt, Austria

[§]Institut für Biologische Chemie, Universität Wien, Währinger Straße 38, 1090 Wien, Austria

[‖]Department of Biology of Agriculture, Food and Environment, University of Pisa, Via del Borghetto 80, 56124 Pisa, Italy

*Author to whom correspondence should be addressed: Christoph Nowak, c.nowak@ait.ac.at

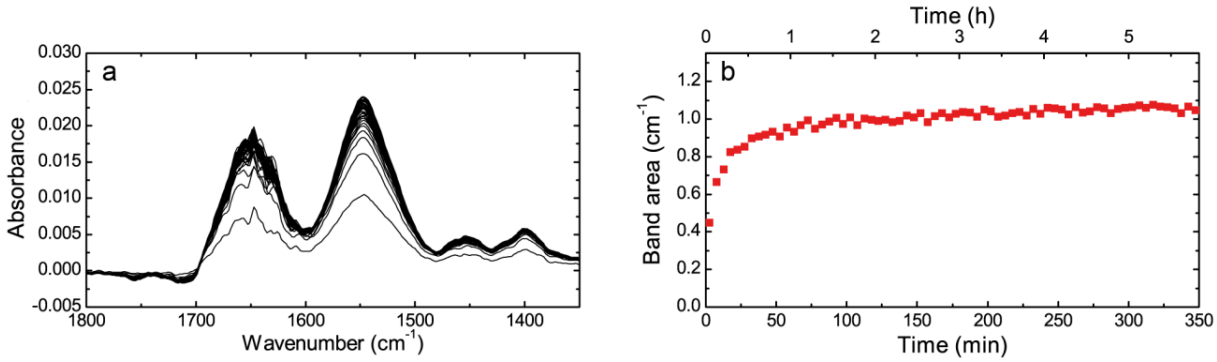

Supplementary Fig. 1 (A) FT-IR difference spectra of OBP14 in the amide I and II region recorded as a function of time. Spectra are taken every 5 mins. The reference spectrum of the DTNTA-modified ZnSe ATR crystal was taken before adsorption of the protein. The high noise in the amide I region is attributed to the high absorption of the OH-bending band of water. (B) Area of the amide II band plotted versus adsorption time

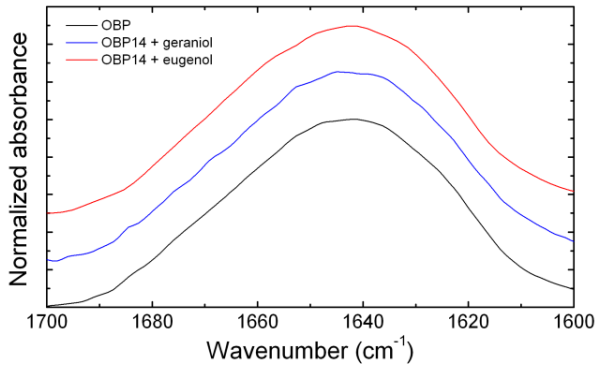

Supplementary Fig. 2 FT-IR spectra in the amide I' region of OBP14 (black), OBP14 incubated with geraniol (blue) and OBP14 incubated with eugenol (red) taken at 25 °C

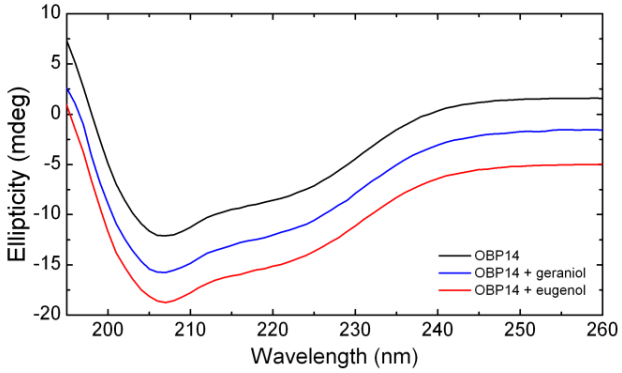

Supplementary Fig. 3 CD spectra obtained at 25 °C of OBP14 (black), OBP14 incubated with geraniol (blue) and OBP14 incubated with eugenol (red)

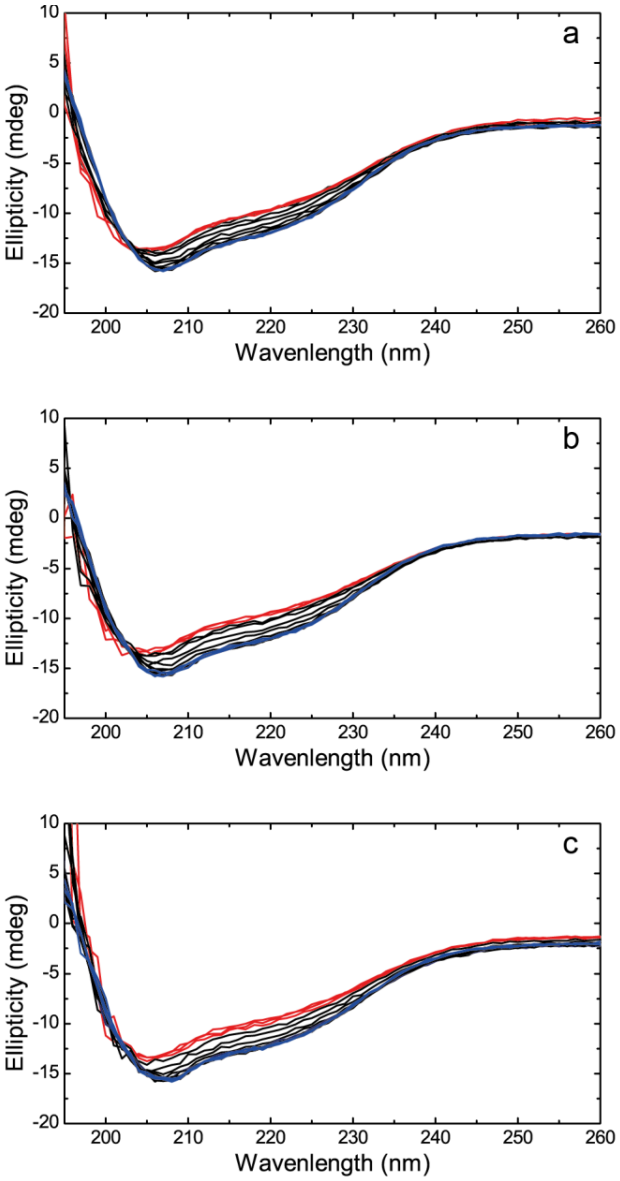

Supplementary Fig. 4: Circular dichroism measurements of (A) OBP14, (B) OBP14 + geraniol, (C) OBP14 + eugenol at temperatures between 20-85 °C. Spectra in blue are taken at low temperatures and red lines indicate spectra recorded at high temperatures

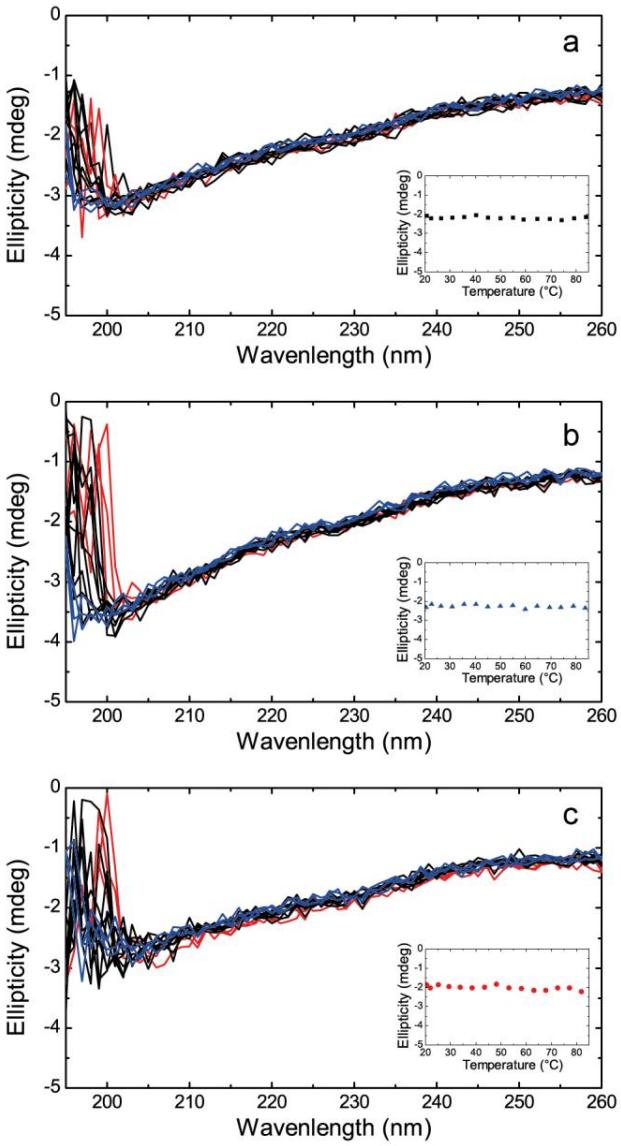

Supplementary Fig. 5 Circular dichroism measurements of (A) phosphate buffer, (B) 200 µM geraniol in phosphate buffer, (C) 200 µM eugenol in phosphate buffer at temperatures between 20-85 °C. Spectra in blue are taken at low temperatures and red lines indicate spectra recorded at high temperatures. Insets show changes of the ellipticity at 222 nm with increasing temperature

Biomedical Spectroscopy and Imaging 2 (2013) 51–71
DOI 10.3233/BSI-120034
IOS Press

Review

Surface-enhanced Raman spectroscopy for biomedical diagnostics and imaging

Johannes Srajer [a,*], Andreas Schwaighofer [a,*] and Christoph Nowak [a,b,**]
[a] *Austrian Institute of Technology GmbH, Vienna, Austria*
[b] *Center of Electrochemical Surface Technology, CEST, Wiener Neustadt, Austria*

Abstract. Surface-enhanced Raman spectroscopy (SERS) is an analytical technique exploiting plasmonic effects that enhance sensitivity significantly, compared to conventional Raman spectroscopy. Progress in nanotechnology led to new fabrication methods for nanostructures and nanoparticles over the last decade. Besides increased comprehension of mechanisms that cause the signal enhancement, computational methods have been developed to tailor analyte-specific nanostructures efficiently. The ability to control the size, shape, and material of surfaces has facilitated the widespread application of SERS in biomedical analytics and clinical diagnostics. In this review, a brief excerpt of such SERS applications is shown, with special focus on cancer diagnostics, glucose detection and *in vivo* imaging applications. Simulation techniques are discussed to show that electrodynamic theory can be used to predict the characteristics of nanostructure arrangements. Different fabrication methods, such as nanoparticle synthesis, their immobilization and lithographic methods are reviewed in brief.

Keywords: Surface-enhanced Raman spectroscopy, SERS, glucose, cancer, *in vivo*, nanostructure fabrication, lithography, nanoparticles, plasmonics, Mie theory, DDA, FDTD, imaging

1. Introduction

During the last decade, the evolving field of life sciences has led to a growing need of sensitive optical techniques for biosensing, biomedical diagnostics, pathogen detection, gene mapping and DNA sequencing [147,148]. Nanostructures are powerful analytical tools based on two of their inherent key features. Firstly, the local field enhancement around the nanostructures allows detection of very few molecules, enabling low limits of detection down to single molecules. Secondly, substrates decorated with nanoparticles (NPs) provide much larger surface areas than their macroscopic dimensions indicate and therefore provide an improved sensitivity. Surface-enhanced Raman spectroscopy (SERS) became popular within the scientific community, because of its non-invasive nature and varied applications for *in vivo* assemblies. For example, it allows simultaneous detection of multiple analytes (multiplexing) and reduces the need for labeling markers [48,148].

In general, Raman spectroscopy is an analytical method to detect chemical and biological samples. It is based on inelastic scattering of laser light on atoms or molecules [124]. Compared to other analyt-

[*] These authors contributed equally to the work.
[**] Corresponding author: Dr. Christoph Nowak, Austrian Institute of Technology GmbH, AIT, Donau-City Str. 1, 1220 Vienna, Austria. Tel.: +43 50550 4430; E-mail: c.nowak@ait.ac.at.

ical methods, Raman spectroscopy suffers from an inherently small cross-section (e.g. 10^{-30} cm^2 per molecule) thus reducing the possibility of detecting analytes in low concentrations [148]. During the last three decades, much effort has been put into finding ways to overcome this deficit. In the early 1970s, Fleischmann et al. observed enhanced signal intensity when analyzing pyridine adsorbed onto electrochemically roughened silver electrodes. After this enhancement was confirmed by Jeanmaire et al. and Albrecht et al., it became evident that NPs also enhance Raman signals [6,53,77]. This enhancement is caused by excitation of localized surface plasmon resonances (LSPR), which are electromagnetic waves that enhance the electromagnetic field near to the metallic nanostructures [70,112,120]. In the 1980s, electrodynamical models have been developed to predict optical properties of substrates which can be used for SERS. Further, the first analytical applications of SERS, like the detection of cyanopyridines, have been developed [114,127,135]. Major achievements in analytics were the single molecule detection and DNA based SERS probes for medical diagnosis in the mid-1990s [90,115,146]. The growing popularity of SERS applications in biomedical research is shown by a hundredfold increase of yearly publications from 1991 to 2011 (searching for "SERS" in the literature meta database 'Pubmed').

This review will address SERS applications like glucose sensors, cancer detection and *in vivo* applications used for biological imaging and medical diagnostics. Fabrication methods from NP synthesis and their immobilization on surfaces, to lithographic methods and combinations thereof, will also be discussed. Finally, the most commonly used simulation techniques, including a very short introduction to the electromagnetic theory on LSPR, are reviewed in brief. In order to cover a wide spectrum from the fabrication of substrates to the latest biomedical applications, the authors can only provide a very concise outline to each single topic.

2. SERS applications

Today's applications of SERS techniques are manifold. For applications in the general field of analytical chemistry, we refer the reader to recent reviews [49,92]. In bioanalytical applications, SERS substrates are used with and without the need for labeling in genetics and proteomics [11,26]. Beside the above applications, recognition of biomarkers released from bacterial spores [28–31], DNA or RNA analysis [10,139,144], medical diagnostics [72,73,76,121,148] and the detection of biological warfare agents [38,117,121,131,163] can be found.

The SERS effect is not substrate-bound, but can also be used in form of soluble silver or gold NPs of various sizes, for example in analytical chemistry [129,174]. In DNA biosensors, NPs allow label-free detection [8,45,119]. In biochemical analysis, NPs are used as labels for biomolecules functionalized with reporter molecules (e.g. dyes) [16,17,19,93,157], or with antibodies enabling the specific linking to binding sites [63,132,133]. Modification of the SERS labels with protective layers such as hydrophilic molecules [132], silica shells [19,93] or layer-by-layer deposited polyelectrolyte [87] has achieved robust sensing devices. An upcoming field for applications of NPs is the *in vivo* diagnosis of cancer [14,105, 111,123,130] and related imaging techniques [86,106,176].

The following sections focus on SERS applications for glucose sensing, cancer diagnostics and *in vivo* applications for imaging in more detail.

2.1. Towards in vivo glucose detection with SERS sensors

An intriguing application of SERS in biomedical sensing is the real-time and quantitative detection of drugs and hormones. Especially *in vivo* diagnostics of glucose experienced considerable progress during

the last few years. A significant healthcare challenge of the 21st century is the growing incidence of diabetes mellitus, a metabolic disease characterized by the patient's high blood sugar level. Two types of diabetes are known, either the body does not produce its own insulin (Type I), or cells do not respond to the insulin that is produced (Type II). Successful treatment makes it necessary to quantitatively monitor the blood sugar level over time to determine the right dosage of medication. The currently most prevalent but invasive "finger-stick" method is based on the electrochemical detection of hydrogen peroxide, the redox species produced by enzymatic reduction of glucose by glucose oxidase [143,154]. Other indirect techniques relying on protein–glucose interaction [118,128] have similar limitations i.e. finite protein stability [137] and liability to false positives by interfering analytes [101,143,154]. For direct detection of glucose, a number of laboratory techniques are established [41,60]. Unfortunately, these methods are limited for application in medical diagnostics, in particular for everyday clinical or personal use because of their size and cost.

Optical techniques for the direct glucose determination, like polarimetric [23,88], infrared [57,107] and Raman scattering methods [13,46] have been developed. The polarimetric methods lack specificity due to interferences of other chiral molecules [102]. In IR spectroscopy, the competing absorbance of water and difficulties in producing miniaturized broad-band light sources are the challenges for routine application. The initial drawbacks of Raman scattering methods, such as long acquisition times and high powers not feasible in biomedical applications have been overcome with the employment of SERS [134].

The Van Duyne group showed recently that SERS is applicable for real-time *in vivo* analysis of a complex biological matrix under varying conditions. In order to monitor glucose levels over time, an *in vivo* glucose sensor needs to be specific, reversible and stable. To accurately determine physiologically relevant glucose concentrations, a fast temporal response of the sensor is necessary. In 2003, the first *in vitro* glucose sensor based on SERS was introduced, using a Ag film over a nanospheres architecture (AgFON) [134]. Because of the low intrinsic affinity of glucose towards noble metal surfaces, a self-assembled monolayer (SAM) was used to preconcentrate glucose within the range of electromagnetic enhancement. Initially, alkanethiol monolayers were used, but the SAM composition was optimized later on as described below [168]. Since the SAM layer acts like a stationary phase in chromatography, it partitions and also departitions glucose on AgFON, thus providing reversible conditions for long term measurements [137]. By avoiding direct contact of analytes with the metal surface, the nanostructures are prevented from fouling. A quantitative real-time analysis of glucose at physiological levels has been achieved in presence of interfering analytes and bovine plasma using multivariate analysis [101]. Transferring an *in vitro* technique to the living object generally poses a challenging task and was addressed by implanting the AgFON nanostructure in the interstitial space between muscle and dermis of a Sprague–Dawley rat as a live animal model [138]. Difficulties in this approach were the surgical placement of the implant without causing damage to the host or sensor surface as well as interfering effects on the sensor immersed in the biological milieu. Non-target molecules such as clotting factors and other blood constituents may create interfering signals and noise while blocking the analyte from accessing the sensor surface. These problems were solved by developing a mixed SAM consisting of decanethiole (DT) and mercaptohexanol (MH). Thus creating a stable, biocompatible surface that can be used as internal standard and resists non-specific binding of proteins [100,138,158]. The accuracy of blood glucose concentration in the interstitial fluid acquired by SERS using an optical window is comparable to that of commercial glucometers [42,138].

The latest developments of *in vivo* glucose sensors were achieved by combining the AgFON DT/MH sensor and spatially offset Raman spectroscopy (SORS). Unlike in conventional Raman spectroscopy,

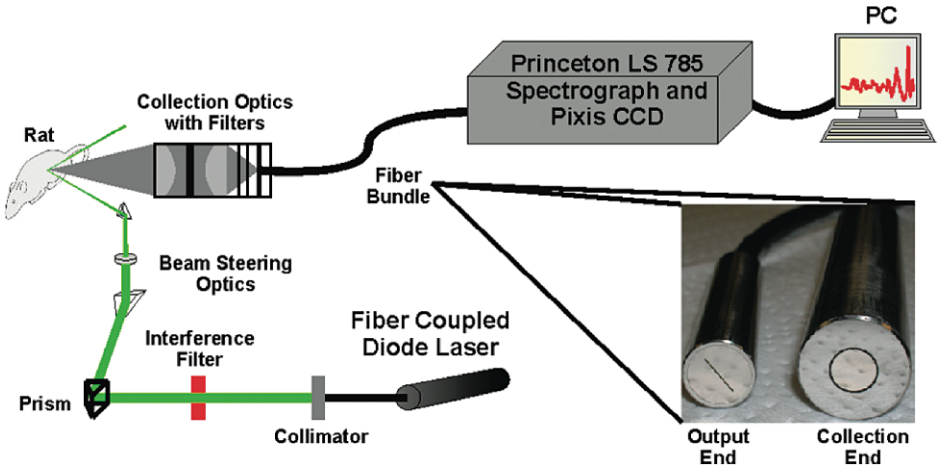

Fig. 1. Scheme of the surface-enhanced spatially offset Raman spectroscopy (SESORS) device. The inset shows the annular fiber bundle used to achieve offset collection. Reprinted with permission from [171]. Copyright © 2010 American Chemical Society. (Colors are visible in the online version of the article; http://dx.doi.org/10.3233/BSI-120034.)

where the points of excitation and collection are coincident, the Raman scattered light is collected from regions offset from the laser excitation area in SORS [108]. SORS highlights the spectral features of underlying layers compared to the actual surface that gives a greater contribution in the Raman spectrum. The combination of highly sensitive SERS and the depth resolution of SORS led to the new transcutaneous glucose sensor, shown in Fig. 1 [171]. Long term stability of up to 17 days without calibration and a lower limit of detection than clinically required have been shown for this technique [103].

2.2. SERS-based cancer diagnostics

The use of nanostructures and nanoparticles for cancer-related diagnostics has become an extremely active field during the last few years. With cancer posing one of the most challenging medical problems, it is expected that the development of nanoparticle-based technologies improves cancer diagnosis and treatment. Methods for diagnosis of cancer using conventional Raman spectroscopy have been reported previously, but these are based on investigation of cancerous tissues after the disease has advanced [36, 39,67,116,142]. Different from normal Raman spectroscopy that provides molecular information of the entire cell, SERS techniques allow the detection and identification of single molecules under ambient conditions [24,89], thus enabling cancer detection at an earlier stage. The high signal intensity and sensitivity qualifies SERS for application in read out immunoassays and biomarker detection. Immunoassays have become the dominant test method for detection of tumor markers i.e. specific proteins that are released by the tumor into the circulation system. Conventional fluorescence detection via molecular labels is used to identify a specific antigen–antibody interaction in an immunoassay. Concentrations of tumor markers are associated with different stages of cancer. Accordingly, reliable and sensitive quantification of these molecules is significant for early clinical diagnosis of cancer [125]. Advantages of SERS are the absence of photobleaching and its narrow band width (10–100 times narrower than that of fluorescence), which leads to exceptional multiplexing capability [150,152]. Another point is the low limit of detection accompanied by the inherent surface selectivity. Yan et al. employed this feature by performing SERS

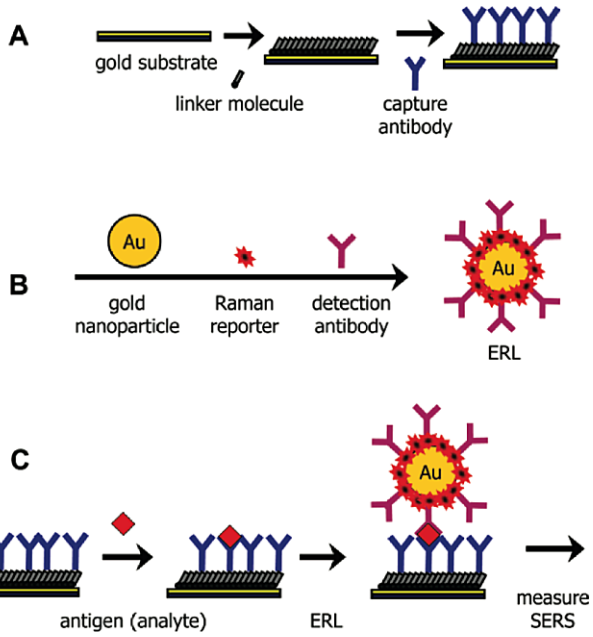

Fig. 2. General SERS-based immunoassay chip design and assay. (A) substrate functionalized with a self-assembled monolayer of linker molecules to specifically extract and concentrate antigens from solution; (B) Au NPs surface functionalized with a Raman reporter and detection antibodies (ERL), to bind to captured antigens selectively and generate intense SERS signals; (C) sandwich immunoassay with SERS readout. Reprinted with permission from [152]. Copyright © 2011 American Chemical Society. (Colors are visible in the online version of the article; http://dx.doi.org/10.3233/BSI-120034.)

on cell surfaces of tumor and non-tumor cell lines on Ag NP agglomerate substrates [162]. The aim is to detect changes of the lipid bilayer, glycoproteins and morphology of the cell which are all associated with carcinogenesis.

For biomarker detection, Au or Ag NPs are usually labeled with Raman reporter molecules that exhibit a strong and specific signal. The outer surface of the probes is functionalized with specific targeting molecules such as antibodies (see Fig. 2(B)). Yang et al. utilized receptor-mediated endocytosis of these extrinsic Raman labels (ERL) for distinguishing breast cancer cells from normal cells [164]. In a pioneering work, Qian et al. decorated the ERL with thiolated polyethylene glycol to increase the biocompatibility and achieve non-invasive cancer targeting under *in vivo* conditions in living animals [123].

Using ERL in combination with a capture substrate (Fig. 2(A)), Wang et al. developed a SERS-based immunoassay to detect a pancreatic cancer marker molecule in serum samples (see Fig. 2(C)) [152]. Recently, the SERS-based immunoassay technique was used to design an optofluidic chip to analyze alpha-fetoprotein, an indicator of hepatocellular carcinoma [95]. Besides the immunoassay approach, SERS-based detection was also used on nucleic acid assays to diagnose breast cancer [7,145,150].

An entirely different approach is applied by employing the direct measurement of body fluids like blood or saliva [52,81,97,98]. Nanoparticles without any functionalization are used for signal enhancement. Olivo et al. developed a Au NPs surface that allowed detection of oral cancer by evaluating spectral features of saliva samples [81]. The facile sample preparation of just mixing Au NPs with blood serum enabled Lin et al. to differentiate between colorectal cancer patients and healthy individuals after rigorous application of principal component analysis and linear discriminant analysis (PCA-LDA) on the SERS data [98].

2.3. In vivo applications for SERS imaging

Within the fast growing and advancing field of SERS, there has been an explosion in the number of publications reporting on SERS imaging applications, in particular employing *in vivo* imaging in living animal models. General progress in SERS imaging has been extensively reviewed recently [18,166,175,178,179], so the following section concerns exclusively *in vivo* imaging applications. In the field of non-invasive *in vivo* imaging, several different modalities have been used for medical diagnostics, such as nuclear imaging, magnetic resonance imaging (MRI), computer tomography, ultrasound imaging bioluminescence and fluorescence imaging [15]. In this animate area of activity, *in vivo* imaging with SERS has gained significant interest during the last years and is about to become a predominant imaging modality [84]. Advantages over other imaging methods include low detectable amounts of targeted molecules, employment of multiplex imaging due to the narrow peak shapes and low toxicity because of the inert nature of NPs [166].

Modifications of NPs with reporter molecules (e.g. dyes) that exhibit a strong, unique Raman spectrum allow the detection of multiple NPs (functionalized with different Raman reporters) simultaneously. Gambhir et al. demonstrated multiplexing capabilities in a living mouse by intravenously administering differently tagged NPs and observing their natural accumulation in the liver [86,176]. Figure 3 shows the transcutaneously acquired SERS spectra and images with penetration depth of up to 5 mm. Deconvolution of the SERS image (Fig. 3(B)), according to the unique SERS spectra of the Raman reporters (Fig. 3(A)) allowed the separate evaluation of the accumulation of each functionalized nanoparticle type (Fig. 3(C)). Further functionalization of NPs with targeting ligands (e.g. peptides, proteins, antibodies) is the predominant approach for tumor targeting. This technique can also be applied to *in vivo* imaging. Following the early work of Nie et al. [123], a growing number of *in vivo* studies involving functionalized SERS-tags were reported over the last years [149]. Recently, Maiti et al. demonstrated multiplexed targeted *in vivo* cancer detection, employing modified Au NPs with Raman reporters and anti-epidermal growth factor (EGFR) antibodies [105,106]. EGFR overexpression has been related to various solid tumor types such as head, neck, lung and bladder cancer. Current investigations are headed towards designing contrast agents for multimodal imaging, thus overcoming the shortcomings of one imaging method with the advantages of the other [37,79,153]. MRI offers high image resolution, but suffers from poor sensitivity and low detection limit. To combine MRI with the high sensitivity yet low resolution of SERS, Yigit et al. reported on nanotags based on MRI-active superparamagnetic iron oxide nanoparticles. These NPs are stably complexed with SERS-active gold nanoparticles and were successfully tested *in vivo* [167].

3. Surface shapes and fabrications

Various techniques have been reported on manufacturing structures which support the excitation of LSPR and further lead to the surface-enhancement effect [22,61]. Research on nanostructures for SERS shows extensive possibilities for optimization, since the maximum field enhancement depends strongly on the shape, size and arrangement of the metallic nanostructures [85]. While average enhancement factors range between 10^4 and 10^5, enhancement factors as high as 10^{10} have been reported [75]. It is crucial to keep in mind, that there is no single standard procedure for determining enhancement factors. A comprehensive overview on this topic is given in a review by Le Ru et al. [94].

Beside the aim of maximal signal intensity, other requirements are inexpensive and easy production, as well as reproducibility. A common compromise is to employ fabrication methods that have average

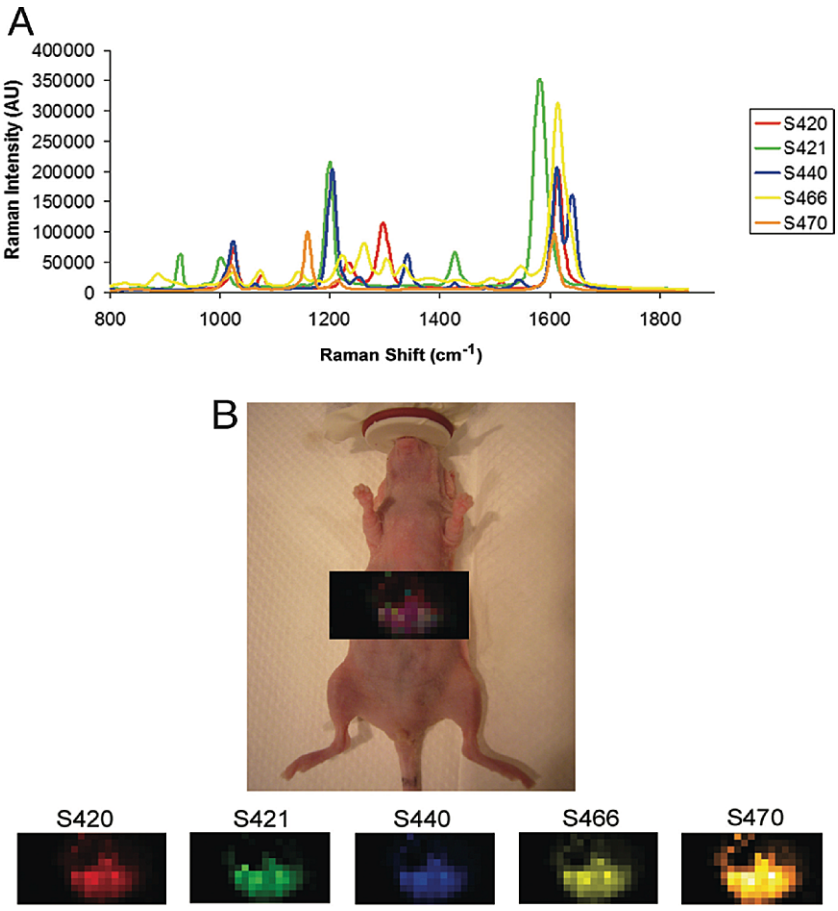

Fig. 3. Demonstration of deep-tissue multiplexed imaging of five unique SERS nanoparticle batches simultaneously. (A) Graph depicting the Raman spectra of the five individual SERS batches. (B) Raman image of liver overlaid on digital photo of mouse, showing accumulation of all five sorts of NPs accumulating in the liver. Panels below depict separate channels associated with each of the injected SERS nanoparticle batches. Individual colors have been assigned to each channel. All NPs show accumulation in the liver, while their distribution is not homogeneous [176]. Reproduced with permission by the author. (Colors are visible in the online version of the article; http://dx.doi.org/10.3233/BSI-120034.)

enhancement, but provide good reproducibility. For a facile overview, we discuss the manufacturing methods for nanostructure arrangements as follows: firstly, chemical production of NPs and their immobilization onto substrates and secondly, fabricated nanostructures using lithographic methods and combinations of nanoparticles with lithographic methods.

3.1. Nanoparticles and immobilization

The process of creating SERS substrates that employ NPs starts with solution-phase synthesis of metal nanocrystals. Here, formation of small clusters of atoms, i.e. nucleation, plays a major role [47, 56]. During this synthesis, citric acid can be used to establish a controllable coagulation of NPs [47,62, 80]. When the nuclei reach a critical size, they show a relatively stable crystallinity and well defined crystallographic facets, so-called seeds [161]. The shape of the resulting seeds depends on the minimal surface energy, a distinct property of the materials in use. A common crystallographic defect within

these seeds is called twinning. It occurs under low temperatures and can be understood in terms of minimization of the surface energy [5]. While the twinned seeds are of almost spherical shape, several different shapes of nanocrystals can be grown. The shape depends on the growth rate along the different directions of the crystal structure, as shown in Fig. 4 [159,160].

In the next step, the metallic nanoparticles have to be deposited onto the substrate. The most commonly used method is the self-assembly of nanoparticles using bifunctional molecules, primarily reported by the Natan group [55]. Amine or thiol groups are commonly used as bifunctional anchor molecules that bind to the substrate on the one side and to the NPs on the other [50,113]. This self-assembly method also works for non-flat materials, as demonstrated using 4-aminobenzenethiol to immobilize Ag NPs onto Ag nanowires [96]. The latest developments showed that 3D structures, made out of multiple self-assembled NP layers show a SERS signal that is about two orders of magnitude higher than that of single NP layers [2,3,48]. Besides these more common methods, other modification methods have been established. For instance using silane-chemistry is used to increase sample-to-sample reproducibility [25,80]. Self-assembly due to electrostatic interaction of polymers and biomolecules such as proteins, antigens and nucleic acid systems has also been reported [9,27,65,170,177].

3.2. Nanolithographic methods and combinations

The ongoing miniaturization in semiconductor technologies made it possible to develop lithographic methods that provide resolutions far below the 100 nm mark. Nowadays nanolithographic methods are manifold and span atomic force microscope nanolithography, neutral particle lithography, photo- and X-ray lithography [151,155,172]. By far the most common fabrication methods are photo- and electron-beam nanolithography. Both are based on chemical resists sensitive to the exposure of the incident light- or electron-beam. Positive and negative resists are available. For the positive resist, areas exposed to the beam will be soluble in the developer, so that the resist will be rinsed away in these areas during the following washing step. Negative resists work the opposite way. The most used positive resist in electron beam lithography is poly-methyl methacrylate [49]. There are two different methods of fabricating substrates, the lift-off technique and reactive ion etching. Nanoparticle arrays are normally created using the lift-off-method, while linear and crossed gratings are typically transferred onto a substrate by reactive ion etching method (see Fig. 5) [49]. In performance evaluation of both methods for gold, the continuous film approach lead to better results than the isolated NPs substrate [82].

The most important advantage of lithography is the possibility to control NP size, shape and arrangement with great accuracy. Numerous studies on distance and shape dependency of the plasmon resonance positions, and differences between NP gratings and nanohole gratings can be found in literature [66,99,169]. In highly ordered arrangements of NPs, plasmonic grating resonances, also called propagating surface plasmons (PSP), can be excited in addition to LSPR. PSP generation depends on the size and environment of the NPs. Substrates combining both, PSP and LSPR have been reported to provide enhancement factors of up to 8.4×10^8 [32,33,51,54]. However, even if substrates prepared by photo- or electron-beam lithography show the highest reproducibility, these methods are not suitable for mass-production because of their high cost.

A promising approach is the usage of templates that allow deposition of metals in a controllable way. A good example for that is nanosphere lithography (NSL), which was developed by Van Duyne's group [68]. In NSL, self-assembled monolayers of nanospheres are used as templates for vapor deposition of metals. After the metal is directly deposited on the nanosphere layer, the nanosphere mask is removed. This leads to a periodic structure of triangles or hexagons. The final structure depends on the

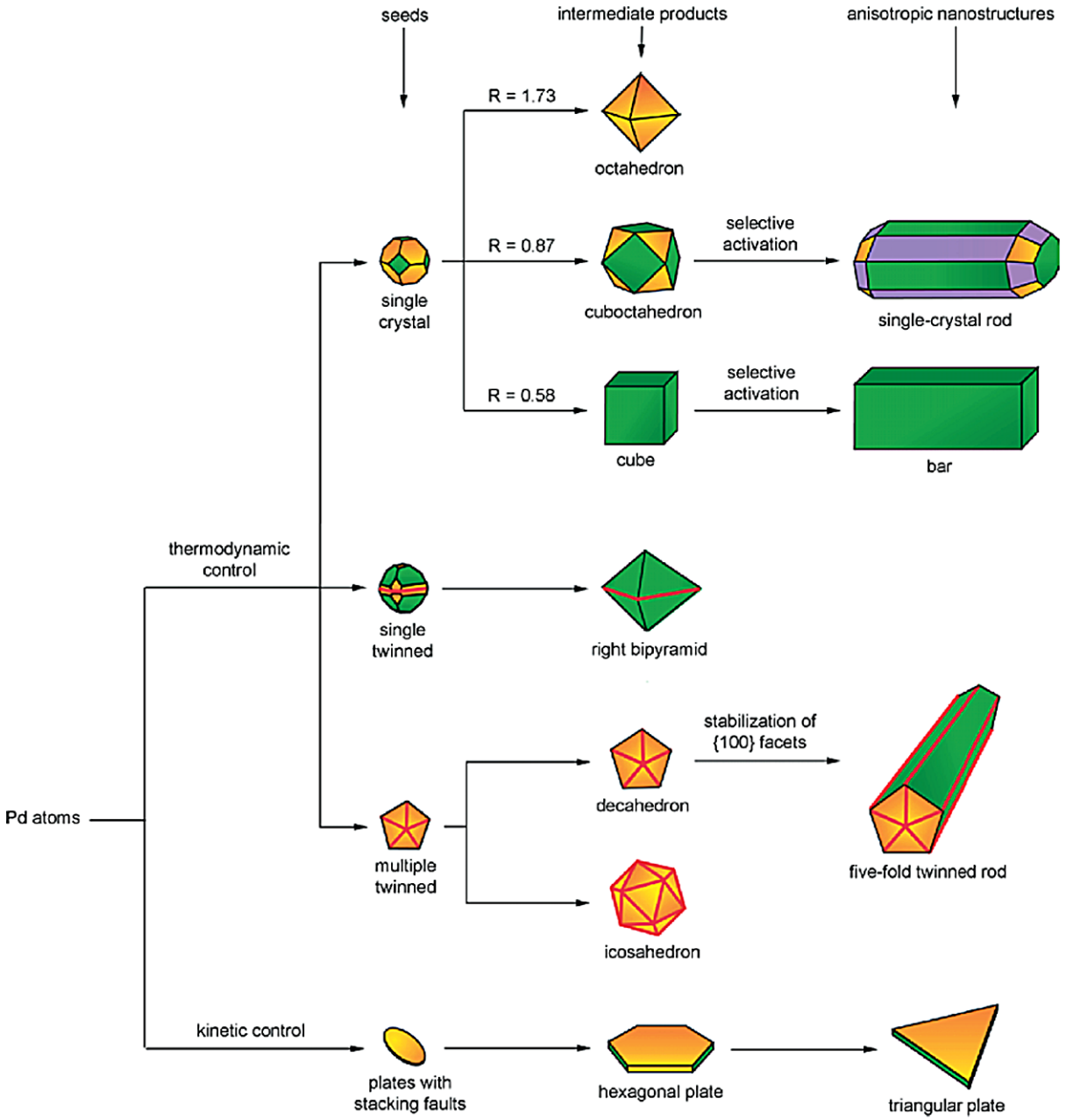

Fig. 4. Illustration of reaction pathways that lead to differently shaped NP using Pd. Once the nuclei have grown past a certain size, the seeds become single or multiple twinned, or single crystalloid, respectively. The colors green, orange, and purple represent the different crystallographic facets ⟨100⟩, ⟨111⟩ and ⟨110⟩. Twinning planes are marked in red, and R is defined as ratio between the growth rates along the ⟨100⟩ and ⟨111⟩ direction. From [161], Copyright © 2007 by John Wiley & Sons, Inc. Reprinted by permission of John Wiley & Sons, Inc. (Colors are visible in the online version of the article; http://dx.doi.org/10.3233/BSI-120034.)

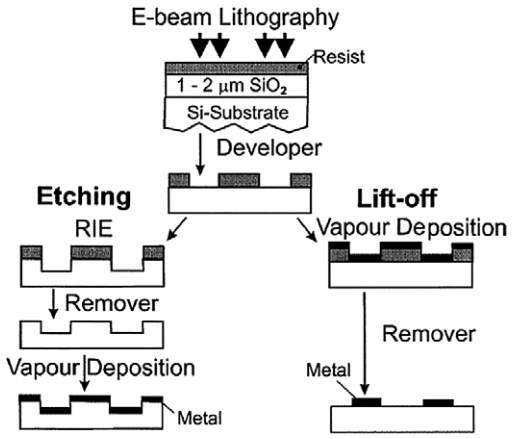

Fig. 5. Scheme of etching and lift-off fabrication strategies for SERS substrates. In the etching process, the substrate is covered with metal on the whole surface. Using lift-off, the substrate presents a series of isolated NPs, after the removal of the resist. From [82]; Copyright © 1998 Elsevier B.V. Reprinted by permission of Elsevier B.V.

number of nanosphere layers deposited onto the substrate [74,78]. Immobilization of the nanospheres is again performed using methods described in the previous section. Using NSL, Van Duyne et al. examined the relationship between localized plasmon excitation and the SERS enhancement factor, reaching a maximum enhancement factor of 10^8 [69]. Based on NSL, nanocrescents and crescent shaped nanoholes have been developed, which exhibit multiple localized surface plasmon resonances form the visible to the infrared region [20,21,156].

4. Theoretical background

Simulation techniques are typically used to adapt nano-structured geometries for biosensing applications to develop made-to-measure devices. Several excellent reviews on the theoretical background are available [91,104,180]. The following section describes the theory behind the interaction of light with free electrons at a metal–dielectric interface, approximate solutions and numerical simulation methods.

Even though surface plasmon polaritons are named in a way that sounds similar to quantum quasiparticles, the classical description based on Maxwell equations is suitable to describe the electron waves resulting from interactions between electrons and photons at interfaces [104]. In a review from Gustav Mie on the optics of metallic colloidal solutions, the scattering problem of a polarized plane wave on a spherical metal-particle in a non-conductive solution has been addressed [110]. The usage of spherical coordinates helped Mie to find the first approximation to the scattering problem for NPs in solution. The resulting wave can be developed in an infinite series, similar to multipole expansion in electric fields. The accuracy of the predicted wavelengths of the plasmon resonances, when compared to scattering experiments, made "Mie scattering" to an eponym for elastic scattering at spherical particles in the size range of the wavelength of the exciting light. This theory was then extended to spheroidal particles, taking into account oblate and prolate particles by Gans [58].

Since modern computing techniques facilitate the simulation of light scattered on objects of any shape, we will only discuss the simple example of a plane wave on the flat interface between a metal and a dielectric material, as shown in Fig. 6. Surface plasmons propagating along this interface can be described as a transverse magnetic wave, which leads to the following equations [1]. For the two sides of the

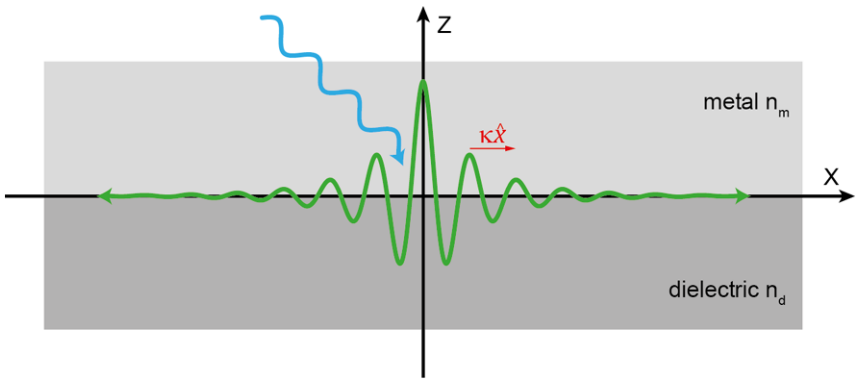

Fig. 6. Scheme of a plasmonic resonance at a metal–dielectric interface. Through an external stimulation (blue), a standing electromagnetic wave (green) can be generated, called surface plasmon resonance. The propagation length is predefined by the complex wavenumber κ. For long range propagation, the complex value of κ diminishes. (The colors are visible in the online version of the article; http://dx.doi.org/10.3233/BSI-120034.)

interface, the magnetic field $\vec{H}$ is given by

$$\vec{H} = \hat{y} A_d \exp(\mathrm{i}\kappa\hat{x} + \alpha_d z), \quad z < 0, \tag{1}$$

$$\vec{H} = \hat{y} A_m \exp(\mathrm{i}\kappa\hat{x} - \alpha_m z), \quad z > 0 \tag{2}$$

with the wavevector $\kappa\hat{x}$ and its lateral wavenumber κ, the transverse wavenumbers α_d and α_m and the coefficients A_d and A_m, which have to be determined. The condition for real transverse wavenumbers can be written as

$$\alpha_d^2 = \kappa^2 - \left(\frac{2\pi n_d}{\lambda}\right)^2, \qquad \alpha_m^2 = \kappa^2 - \left(\frac{2\pi n_m}{\lambda}\right)^2 \tag{3}$$

using the free space wavelength λ and the complex refractive indices n_d and n_m of the dielectric material and the metal, respectively. In order to satisfy the boundary conditions for the electric and magnetic fields at the interface ($z = 0$), the Maxwell equations lead to the dispersion relation (i.e. the energy-momentum relation)

$$\alpha_m n_d^2 + \alpha_d n_m^2 = 0, \tag{4}$$

which is typically written in the form of

$$\kappa = \frac{2\pi}{\lambda}\sqrt{\frac{\varepsilon_d \varepsilon_m}{\varepsilon_m + \varepsilon_d}}. \tag{5}$$

The latter equation is assuming materials where the relation between the complex refractive index n and the relative permittivity ε is given by $n = \sqrt{\varepsilon}$, assuming a relative permeability $\mu = 1$, which is a common expectation for metals at optical frequencies [136]. A few conclusions can be drawn from this simple example. One condition for a plasmon wave to exist is that the real parts of the permittivities of the metal and the dielectric need to have opposite signs. Since the permittivity functions are usually

complex, the wavevector is also complex, leading to a finite propagation length of the wave. For long range propagation, for which the complex values of κ are diminishing, the condition $\varepsilon_d < -\varepsilon_m$ must hold.

Current methods for calculating the electromagnetic properties of NPs make use of different numerical techniques in order to simulate the influence of adsorbed molecules on metal films, different shapes of nanoparticles and coupling effects of regular gratings. In the following sections, the three most common simulation techniques are discussed in brief.

4.1. Finite difference time domain (FDTD)

In 1966, Kane Yee published a method, where he replaced Maxwell equations with a set of finite difference equations [165]. In principle, the finite difference time domain method (FDTD) is based on discretization of geometries into calculation grids, in which the three components of the electric and magnetic field are stored at different positions of a single voxel (i.e. volumetric pixel element). Even though Yee already proposed a stability criterion, a general stability condition was introduced later by Taflove et al. [141]. Based on this criterion, the first validated simulation of a electromagnetic wave penetrating a metal cavity was performed [140]. The acronym FDTD reflects that the temporal evolution of the fields is calculated in this method, while the frequency domain spectra of nanoparticles have to be calculated through Fourier transformations. FDTD advanced rapidly during the last few decades. A major milestone was the development of the so-called perfectly matched layers, which mimic an open boundary condition where electromagnetic waves are not or only barely reflected [12,83]. This effective boundary technique has been improved later by uniaxial perfectly matched layers and convolutional perfectly matched layers [59,126]. The latest development in FDTD is an unconditionally, numerically stable algorithm, which was introduced by DeRaedt and further improved by Ahmed et al. [4,40].

Correlations between measured and simulated spectra from reflectance, transmission, fluorescence and SPR-measurements, have proven the ability of this method to properly describe reality [32,33,51,54].

4.2. Discrete dipole approximation (DDA)

Another popular method for computing the optical spectrum from near field distributions of NPs is the discrete dipole approximation (DDA). Hereby, arbitrary geometries are mapped on a cubic array of voxels representing electric dipoles, each with its own polarizability function. Even if methods using individual polarizabilities to describe compositions can be traced back to Lorentz, the first de-facto DDA simulation was performed by Purcell and Pennypacker [122]. They validated their model of a spherical colloid, consisting of 136 polarizable elements, using Mie theory. Since then, several attempts to improve accuracy, numerical stability, data analysis and material assumptions have been undertaken. We kindly refer the interested reader to the review of Yurkin and Hoekstra [173].

For a long time, field strength patterns were exclusively accessible through simulations. Recently, the correlation between the intensity in electron energy loss spectroscopy and the electric field density, which is equivalent to the photonic density of states, showed that the simulated and real field patterns are in good agreement. As an example, Fig. 7 shows how field pattern calculated using the DDA method behave compared to electron energy loss measurements.

The most commonly used DDA code is DDSCAT, written in FORTRAN 90, which includes functions of various target geometries and periodic structures [44]. Recently, C based codes as well as Matlab based codes have been published [43,109,173].

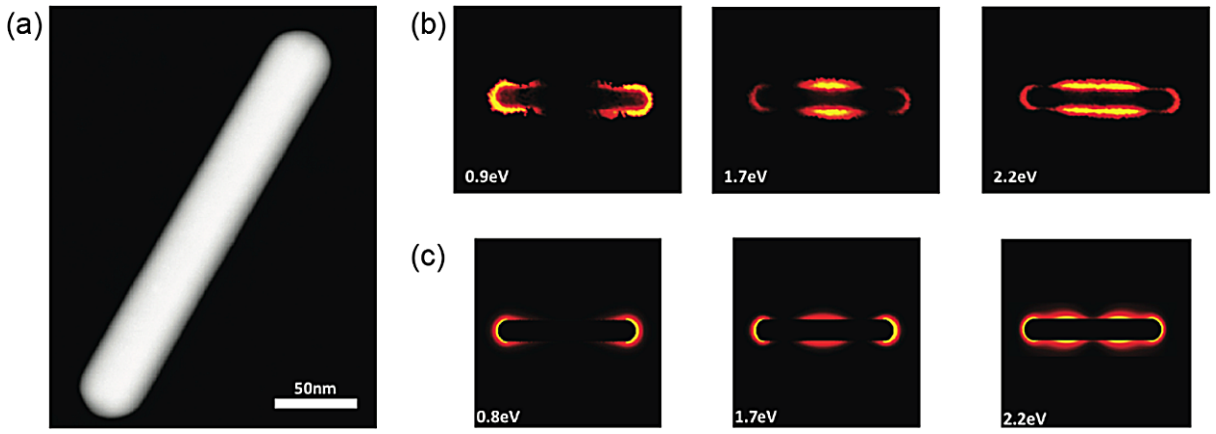

Fig. 7. Comparison between measured and simulated field strength pattern. (a) shows the geometry of the Ag nanorods, (b) illustrates the intensity image form electron energy loss spectroscopy at three different energies and (c) shows the simulated field strength of the electric field using a DDA method. Adapted with permission from [64], Copyright © 2011 American Chemical Society. (Colors are visible in the online version of the article; http://dx.doi.org/10.3233/BSI-120034.)

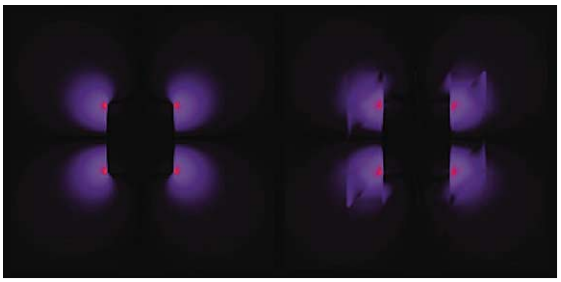

Fig. 8. Field patterns of scattered light of a cubic nanoparticle with 50 nm edge length. The left side shows the FDTD simulations and the right side the FEM simulation, respectively. Adapted with permission from [180], Copyright © 2008 American Chemical Society. (Colors are visible in the online version of the article; http://dx.doi.org/10.3233/BSI-120034.)

4.3. Finite elements method (FEM)

A method particularly interesting for complex geometries is the finite elements method (FEM). It was first outlined by Courant [35]. A result is obtained by using the variational principle to find solutions, where every element of the mesh satisfies Gauss' law and the appropriate boundary conditions on the surface of the element [180]. A variety of mesh generation software to divide the domain into a fine grid of elements, on which the partial differential equations are solved, is available online [71]. Since FEM is also very popular for solving fluid mechanics and structural mechanics, there are many software tools for solving electro-dynamic problems as well. A review on FEM applied to electromagnetic problems was published by Coccioli et al. [34].

A comparison between field patterns calculated by FDTD and FEM is shown in Fig. 8. The FEM results show some small artifacts, but they agree well with the FDTD results. FDTD is more accurate, but it consumes much more computation power. In the shown example the FDTD simulation took 2058 CPU hours (á 2.8 GHz), while the FEM simulation only took four CPU hours (á 3.4 GHz) [180].

Several software packages, from open-source and freeware to proprietary codes, are available. Most open-source codes are command line based, using C++ or FORTRAN libraries, while most of the

commercial software packages have a graphical user interface. Due to the wide variety, an application-oriented analysis of which software satisfies the user's requirements is advisable before deciding on any simulation software. All discussed simulation methods can be used to predict the wavelengths of LSPR excitations and therefore fasten the development of new SERS applications.

5. Conclusions

In applications involving the diagnosis of cancerous lesions, the current standard is surgical resection and analysis by histopathology. Since this procedure is invasive, expensive and time-consuming, the availability of rapid, non-invasive analytical techniques is very desirable. SERS applications have shown their great potential to become the future standard. This is not only true for cancer diagnostics but also for glucose detection. The growing number of applications in DNA sequencing using multiplexed SERS sensors, as well as progress in *in vivo* glucose detection, show that SERS has finally matured to levels of reproducibility and dependability that are needed for routine applications.

These advances also result from the rapid development of new fabrication techniques during the last decade. Thanks to lithography, the possibilities in creating new geometries are manifold. The fast evolving field of template based lithography opens the door for high-throughput analysis and minimizes expenses. The development time of new SERS applications can be further reduced by accompanying experiments with numerical simulations. Various commercial, as well as non-commercial modeling techniques are available. Knowledge of the near field behavior of a substrate is crucial for tailoring new devices.

The number of publication on SERS exploded in the past years; therefore this review only covers a fraction of those publications. Even with the high research activity on SERS, a unanimous definition of a general enhancement factor has not yet been found. In order to rate and compare different SERS techniques, a uniform definition for the enhancement factor would be highly desirable.

Acknowledgements

The authors acknowledge the contribution of B. Siebenhofer and K. Mahajan. Partial support for this work was provided by ZIT, Centre of Innovation and Technology of Vienna.

References

[1] I. Abdulhalim, M. Zourob and A. Lakhtakia, Surface plasmon resonance for biosensing: a mini-review, *Electromagnetics* **28** (2008), 214–242.
[2] C.J. Addison and A.G. Brolo, Nanoparticle-containing structures as a substrate for surface-enhanced Raman scattering, *Langmuir* **22** (2006), 8696–8702.
[3] C.J. Addison, S.O. Konorov, A.G. Brolo, M.W. Blades and R.F.B. Turner, Tuning gold nanoparticle self-assembly for optimum coherent anti-stokes Raman scattering and second harmonic generation response, *J. Phys. Chem. C* **113** (2009), 3586–3592.
[4] I. Ahmed, C. Eng-Kee, L. Er-Ping and C. Zhizhang, Development of the three-dimensional unconditionally stable LOD-FDTD method, *IEEE Trans. Antennas Propag.* **56** (2008), 3596–3600.
[5] P.M. Ajayan and L.D. Marks, Quasimelting and phases of small particles, *Phys. Rev. Lett.* **60** (1988), 585–587.
[6] M.G. Albrecht and J.A. Creighton, Anomalously intense Raman spectra of pyridine at a silver electrode, *J. Am. Chem. Soc.* **99** (1977), 5215–5217.

[7] L.R. Allain and T. Vo-Dinh, Surface-enhanced Raman scattering detection of the breast cancer susceptibility gene BRCA1 using a silver-coated microarray platform, *Anal. Chim. Acta* **469** (2002), 149–154.
[8] J.N. Anker, W.P. Hall, O. Lyandres, N.C. Shah, J. Zhao and R.P. Van Duyne, Biosensing with plasmonic nanosensors, *Nat. Mater.* **7** (2008), 442–453.
[9] R.F. Aroca, P.J.G. Goulet, D.S. dos Santos, R.A. Alvarez-Puebla and O.N. Oliveira, Silver nanowire layer-by-layer films as substrates for surface-enhanced Raman scattering, *Anal. Chem.* **77** (2004), 378–382.
[10] A. Barhoumi, D. Zhang, F. Tam and N.J. Halas, Surface-enhanced Raman spectroscopy of DNA, *J. Am. Chem. Soc.* **130** (2008), 5523–5529.
[11] H.T. Beier, C.B. Cowan, I.H. Chou, J. Pallikal, J.E. Henry, M.E. Benford, J.B. Jackson, T.A. Good and G.L. Cote, Application of surface-enhanced Raman spectroscopy for detection of beta amyloid using nanoshells, *Plasmonics* **2** (2007), 55–64.
[12] J.-P. Berenger, A perfectly matched layer for the absorption of electromagnetic waves, *J. Comput. Phys.* **114** (1994), 185–200.
[13] A.J. Berger, T.W. Koo, I. Itzkan, G. Horowitz and M.S. Feld, Multicomponent blood analysis by near-infrared Raman spectroscopy, *Appl. Opt.* **38** (1999), 2916–2926.
[14] M.S. Bergholt, W. Zheng and Z.W. Huang, Characterizing variability in *in vivo* Raman spectroscopic properties of different anatomical sites of normal tissue in the oral cavity, *J. Raman Spectrosc.* **43** (2012), 255–262.
[15] R.G. Blasberg, Imaging update: New windows, new views, *Clin. Cancer Res.* **13** (2007), 3444–3448.
[16] S. Boca, D. Rugina, A. Pintea, L. Barbu-Tudoran and S. Astilean, Flower-shaped gold nanoparticles: synthesis, characterization and their application as SERS-active tags inside living cells, *Nanotechnology* **22** (2011), 055702.
[17] C.I. Brady, N.H. Mack, L.O. Brown and S.K. Doorn, Self-assembly approach to multiplexed surface-enhanced Raman spectral-encoder beads, *Anal. Chem.* **81** (2009), 7181–7188.
[18] M.C. Breitkreitz and R.J. Poppi, Trends in Raman chemical imaging, *Biomedical Spectroscopy and Imaging* **1** (2012), 159–183.
[19] L.O. Brown and S.K. Doorn, A controlled and reproducible pathway to dye-tagged, encapsulated silver nanoparticles as substrates for SERS multiplexing, *Langmuir* **24** (2008), 2277–2280.
[20] R. Bukasov, T.A. Ali, P. Nordlander and J.S. Shumaker-Parry, Probing the plasmonic near-field of gold nanocrescent antennas, *ACS Nano* **4** (2010), 6639–6650.
[21] R. Bukasov and J.S. Shumaker-Parry, Highly tunable infrared extinction properties of gold nanocrescents, *Nano Letters* **7** (2007), 1113–1118.
[22] J.P. Camden, J.A. Dieringer, J. Zhao and R.P. Van Duyne, Controlled plasmonic nanostructures for surface-enhanced spectroscopy and sensing, *Acc. Chem. Res.* **41** (2008), 1653–1661.
[23] B.D. Cameron, H. Gorde and G.L. Cote, Development of an optical polarimeter for *in vivo* glucose monitoring, *Proc. SPIE* **3599** (1999), 43–49.
[24] A. Campion and P. Kambhampati, Surface-enhanced Raman scattering, *Chem. Soc. Rev.* **27** (1998), 241–250.
[25] C. Caro, C. López-Cartes, P. Zaderenko and J.A. Mejías, Thiol-immobilized silver nanoparticle aggregate films for surface enhanced Raman scattering, *J. Raman Spectrosc.* **39** (2008), 1162–1169.
[26] J.W. Chen, X.P. Liu, K.J. Feng, Y. Liang, J.H. Jiang, G.L. Shen and R.Q. Yu, Detection of adenosine using surface-enhanced Raman scattering based on structure-switching signaling aptamer, *Biosens. Bioelectron.* **24** (2008), 66–71.
[27] H.-W. Cheng, W.-Q. Luo, G.-L. Wen, S.-Y. Huan, G.-L. Shen and R.-Q. Yu, Surface-enhanced Raman scattering based detection of bacterial biomarker and potential surface reaction species, *Analyst* **135** (2010), 2993–3001.
[28] H.W. Cheng, Y.Y. Chen, X.X. Lin, S.Y. Huan, H.L. Wu, G.L. Shen and R.Q. Yu, Surface-enhanced Raman spectroscopic detection of *Bacillus subtilis* spores using gold nanoparticle based substrates, *Anal. Chim. Acta* **707** (2011), 155–163.
[29] H.W. Cheng, S.Y. Huan, H.L. Wu, G.L. Shen and R.Q. Yu, Surface-enhanced Raman spectroscopic detection of a bacteria biomarker using gold nanoparticle immobilized substrates, *Anal. Chem.* **81** (2009), 9902–9912.
[30] H.W. Cheng, S.Y. Huan and R.Q. Yu, Nanoparticle-based substrates for surface-enhanced Raman scattering detection of bacterial spores, *Analyst* **137** (2012), 3601–3608.
[31] H.W. Cheng, W.Q. Luo, G.L. Wen, S.Y. Huan, G.L. Shen and R.Q. Yu, Surface-enhanced Raman scattering based detection of bacterial biomarker and potential surface reaction species, *Analyst* **135** (2010), 2993–3001.
[32] Y. Chu, M.G. Banaee and K.B. Crozier, Double-resonance plasmon substrates for surface-enhanced Raman scattering with enhancement at excitation and Stokes frequencies, *ACS Nano* **4** (2010), 2804–2810.
[33] Y.Z. Chu and K.B. Crozier, Experimental study of the interaction between localized and propagating surface plasmons, *Opt. Lett.* **34** (2009), 244–246.
[34] R. Coccioli, T. Itoh, G. Pelosi and P.P. Silvester, Finite-element methods in microwaves: a selected bibliography, *IEEE Antennas Propag. Mag.* **38** (1996), 34–48.
[35] R. Courant, Variational methods for the solution of problems of equilibrium and vibrations, *Bull. Amer. Math. Soc.* **49** (1943), 1–23.

[36] P. Crow, B. Barrass, C. Kendall, M. Hart-Prieto, M. Wright, R. Persad and N. Stone, The use of Raman spectroscopy to differentiate between different prostatic adenocarcinoma cell lines, *Brit. J. Cancer* **92** (2005), 2166–2170.
[37] Y. Cui, X.-S. Zheng, B. Ren, R. Wang, J. Zhang, N.-S. Xia and Z.-Q. Tian, Au@organosilica multifunctional nanoparticles for the multimodal imaging, *Chem. Sci.* **2** (2011), 1463–1469.
[38] J.K. Daniels, T.P. Caldwell, K.A. Christensen and G. Chumanov, Monitoring the kinetics of *Bacillus subtilis* endospore germination via surface-enhanced Raman scattering spectroscopy, *Anal. Chem.* **78** (2006), 1724–1729.
[39] B.W.D. de Jong, T.C. Bakker, K. Maquelin, T. van der Kwast, C.H. Bangma, D.J. Kok and G.J. Puppels, Discrimination between nontumor bladder tissue and tumor by Raman spectroscopy, *Anal. Chem.* **78** (2006), 7761–7769.
[40] H. De Raedt, K. Michielsen, J.S. Kole and M.T. Figge, Solving the Maxwell equations by the Chebyshev method: a one-step finite-difference time-domain algorithm, *IEEE Trans. Antennas Propag.* **51** (2003), 3155–3160.
[41] M.L. Di Gioia, A. Leggio, A. Le Pera, A. Liguori, A. Napoli, C. Siciliano and G. Sindona, Quantitative analysis of human salivary glucose by gas chromatography–mass spectrometry, *J. Chromatogr., B: Anal. Technol. Biomed. Life Sci.* **801** (2004), 355–358.
[42] J.A. Dieringer, A.D. McFarland, N.C. Shah, D.A. Stuart, A.V. Whitney, C.R. Yonzon, M.A. Young, X.Y. Zhang and R.P. Van Duyne, Surface enhanced Raman spectroscopy: new materials, concepts, characterization tools, and applications, *Faraday Discuss.* **132** (2006), 9–26.
[43] J.M. Donald, A. Golden and S.G. Jennings, Opendda: a novel high-performance computational framework for the discrete dipole approximation, *Int. J. High Perform. C* **23** (2009), 42–61.
[44] B.T. Draine and P.J. Flatau, Discrete-dipole approximation for periodic targets: theory and tests, *J. Opt. Soc. Am. A* **25** (2008), 2693–2703.
[45] T. Endo, K. Kerman, N. Nagatani, Y. Takamura and E. Tamiya, Label-free detection of peptide nucleic acid–DNA hybridization using localized surface plasmon resonance based optical biosensor, *Anal. Chem.* **77** (2005), 6976–6984.
[46] A.M.K. Enejder, T.W. Koo, J. Oh, M. Hunter, S. Sasic, M.S. Feld and G.L. Horowitz, Blood analysis by Raman spectroscopy, *Opt. Lett.* **27** (2002), 2004–2006.
[47] B.V. Enustun and J. Turkevich, Coagulation of colloidal gold, *J. Am. Chem. Soc.* **85** (1963), 3317–3328.
[48] M. Fan and A.G. Brolo, Self-assembled Au nanoparticles as substrates for surface-enhanced vibrational spectroscopy: optimization and electrochemical stability, *Chemphyschem* **9** (2008), 1899–1907.
[49] M.K. Fan, G.F.S. Andrade and A.G. Brolo, A review on the fabrication of substrates for surface enhanced Raman spectroscopy and their applications in analytical chemistry, *Anal. Chim. Acta* **693** (2011), 7–25.
[50] T. Felicia, B. Monica, B. Lucian and A. Simion, Controlling gold nanoparticle assemblies for efficient surface-enhanced Raman scattering and localized surface plasmon resonance sensors, *Nanotechnology* **18** (2007), 255702.
[51] N. Felidj, S.L. Truong, J. Aubard, G. Levi, J.R. Krenn, A. Hohenau, A. Leitner and F.R. Aussenegg, Gold particle interaction in regular arrays probed by surface enhanced Raman scattering, *J. Chem. Phys.* **120** (2004), 7141–7146.
[52] S.Y. Feng, R. Chen, J.Q. Lin, J.J. Pan, Y.A. Wu, Y.Z. Li, J.S. Chen and H.S. Zeng, Gastric cancer detection based on blood plasma surface-enhanced Raman spectroscopy excited by polarized laser light, *Biosens. Bioelectron.* **26** (2011), 3167–3174.
[53] M. Fleischmann, P.J. Hendra and A.J. McQuillan, Raman spectra of pyridine adsorbed at a silver electrode, *Chem. Phys. Lett.* **26** (1974), 163–166.
[54] P. Frank, J. Srajer, A. Schwaighofer, A. Kibrom and C. Nowak, Double-layered nanoparticle stacks for spectroelectrochemical applications, *Opt. Lett.* **37** (2012), 3603–3605.
[55] R.G. Freeman, K.C. Grabar, K.J. Allison, R.M. Bright, J.A. Davis, A.P. Guthrie, M.B. Hommer, M.A. Jackson, P.C. Smith, D.G. Walter and M.J. Natan, Self-assembled metal colloid monolayers: An approach to SERS substrates, *Science* **267** (1995), 1629–1632.
[56] G. Frens, Particle size and sol stability in metal colloids, *Kolloid Z. Z. Polym.* **250** (1972), 736–741.
[57] I. Gabriely and H. Shamoon, Transcutaneous glucose measurement using near-infrared spectroscopy during hypoglycemia, *Diabetes Care* **23** (2000), 1209–1210.
[58] R. Gans, Über die Form ultramikroskopischer Goldteilchen, *Ann. Phys.* **342** (1912), 881–900.
[59] S.D. Gedney, An anisotropic perfectly matched layer-absorbing medium for the truncation of FDTD lattices, *IEEE Trans. Antennas Propag.* **44** (1996), 1630–1639.
[60] D.B. Gomis, D.M. Tamayo and J.M. Alonso, Determination of monosaccharides in cider by reversed-phase liquid chromatography, *Anal. Chim. Acta* **436** (2001), 173–180.
[61] R. Gordon, D. Sinton, K.L. Kavanagh and A.G. Brolo, A new generation of sensors based on extraordinary optical transmission, *Acc. Chem. Res.* **41** (2008), 1049–1057.
[62] M. Grosserueschkamp, C. Nowak, D. Schach, W. Schaertl, W. Knoll and R.L.C. Naumann, Silver surfaces with optimized surface enhancement by self-assembly of silver nanoparticles for spectroelectrochemical applications, *J. Phys. Chem. C* **113** (2009), 17698–17704.
[63] N. Guarrotxena, B. Liu, L. Fabris and G.C. Bazan, Antitags: Nanostructured tools for developing SERS-based ELISA analogs, *Adv. Mater.* **22** (2010), 4954–4958.

[64] B.S. Guiton, V. Iberi, S. Li, D.N. Leonard, C.M. Parish, P.G. Kotula, M. Varela, G.C. Schatz, S.J. Pennycook and J.P. Camden, Correlated optical measurements and plasmon mapping of silver nanorods, *Nano Lett.* **11** (2011), 3482–3488.
[65] R. Gunawidjaja, E. Kharlampieva, I. Choi and V.V. Tsukruk, Bimetallic nanostructures as active Raman markers: gold-nanoparticle assembly on 1D and 2D silver nanostructure surfaces, *Small* **5** (2009), 2460–2466.
[66] L. Gunnarsson, E.J. Bjerneld, H. Xu, S. Petronis, B. Kasemo and M. Kall, Interparticle coupling effects in nanofabricated substrates for surface-enhanced Raman scattering, *Appl. Phys. Lett.* **78** (2001), 802–804.
[67] A.S. Haka, Z. Volynskaya, J.A. Gardecki, J. Nazemi, R. Shenk, N. Wang, R.R. Dasari, M. Fitzmaurice and M.S. Feld, Diagnosing breast cancer using Raman spectroscopy: prospective analysis, *J. Biomed. Opt.* **14** (2009), 054023.
[68] C.L. Haynes and R.P. Van Duyne, Nanosphere lithography: A versatile nanofabrication tool for studies of size-dependent nanoparticle optics, *J. Phys. Chem. B* **105** (2001), 5599–5611.
[69] C.L. Haynes and R.P. Van Duyne, Plasmon-sampled surface-enhanced Raman excitation spectroscopy, *J. Phys. Chem. B* **107** (2003), 7426–7433.
[70] R.M. Hexter and M.G. Albrecht, Metal surface Raman spectroscopy: Theory, *Spectrochim. Acta A* **35** (1979), 233–251.
[71] K. Ho-Le, Finite element mesh generation methods: a review and classification, *Comput. Aided Des.* **20** (1988), 27–38.
[72] J. Hu, P.C. Zheng, J.H. Jiang, G.L. Shen, R.Q. Yu and G.K. Liu, Electrostatic interaction based approach to thrombin detection by surface-enhanced Raman spectroscopy, *Anal. Chem.* **81** (2009), 87–93.
[73] J. Hu, P.C. Zheng, J.H. Jiang, G.L. Shen, R.Q. Yu and G.K. Liu, Sub-attomolar HIV-1 DNA detection using surface-enhanced Raman spectroscopy, *Analyst* **135** (2010), 1084–1089.
[74] J.C. Hulteen, D.A. Treichel, M.T. Smith, M.L. Duval, T.R. Jensen and R.P. Van Duyne, Nanosphere lithography: size-tunable silver nanoparticle and surface cluster arrays, *J. Phys. Chem. B* **103** (1999), 3854–3863.
[75] J.B. Jackson and N.J. Halas, Surface-enhanced Raman scattering on tunable plasmonic nanoparticle substrates, *Proc. Natl. Acad. Sci. USA* **101** (2004), 17930–17935.
[76] R.M. Jarvis and R. Goodacre, Characterisation and identification of bacteria using SERS, *Chem. Soc. Rev.* **37** (2008), 931–936.
[77] D.L. Jeanmaire and R.P. Van Duyne, Surface Raman spectroelectrochemistry: Part I. Heterocyclic, aromatic, and aliphatic amines adsorbed on the anodized silver electrode, *J. Electroanal. Chem. Interfacial Electrochem.* **84** (1977), 1–20.
[78] T.R. Jensen, M.D. Malinsky, C.L. Haynes and R.P. Van Duyne, Nanosphere lithography: tunable localized surface plasmon resonance spectra of silver nanoparticles, *J. Phys. Chem. B* **104** (2000), 10549–10556.
[79] L. Jiang, J. Qian, F. Cai and S. He, Raman reporter-coated gold nanorods and their applications in multimodal optical imaging of cancer cells, *Anal. Bioanal. Chem.* **400** (2011), 2793–2800.
[80] L. Jiang, Y. Sun, C. Nowak, A. Kibrom, C. Zou, J. Ma, H. Fuchs, S. Li, L. Chi and X. Chen, Patterning of plasmonic nanoparticles into multiplexed one-dimensional arrays based on spatially modulated electrostatic potential, *ACS Nano* **5** (2011), 8288–8294.
[81] J.C.Y. Kah, K.W. Kho, C.G.L. Lee, C.J.R. Sheppard, Z.X. Shen, K.C. Soo and M.C. Olivo, Early diagnosis of oral cancer based on the surface plasmon resonance of gold nanoparticles, *Int. J. Nanomed.* **2** (2007), 785–798.
[82] M. Kahl, E. Voges, S. Kostrewa, C. Viets and W. Hill, Periodically structured metallic substrates for SERS, *Sens. Actuators B* **51** (1998), 285–291.
[83] D.S. Katz, E.T. Thiele and A. Taflove, Validation and extension to three dimensions of the Berenger PML absorbing boundary condition for FD-TD meshes, *IEEE Microw. Guided Wave Lett.* **4** (1994), 268–270.
[84] S. Kaur, G. Venktaraman, M. Jain, S. Senapati, P.K. Garg and S.K. Batra, Recent trends in antibody-based oncologic imaging, *Cancer Lett.* **315** (2012), 97–111.
[85] K.L. Kelly, E. Coronado, L.L. Zhao and G.C. Schatz, The optical properties of metal nanoparticles: the influence of size, shape, and dielectric environment, *J. Phys. Chem. B* **107** (2002), 668–677.
[86] S. Keren, C. Zavaleta, Z. Cheng, A. de la Zerda, O. Gheysens and S.S. Gambhir, Noninvasive molecular imaging of small living subjects using Raman spectroscopy, *Proc. Natl. Acad. Sci. USA* **105** (2008), 5844–5849.
[87] K. Kim, H.S. Lee, H.D. Yu, H.K. Park and N.H. Kim, A facile route to stabilize SERS-marker molecules on mu Ag particles: Layer-by-layer deposition of polyelectrolytes, *Colloids Surf. A* **316** (2008), 1–7.
[88] D.C. Klonoff, Noninvasive blood glucose monitoring, *Diabetes Care* **20** (1997), 433–437.
[89] J. Kneipp, H. Kneipp and K. Kneipp, SERS – a single-molecule and nanoscale tool for bioanalytics, *Chem. Soc. Rev.* **37** (2008), 1052–1060.
[90] K. Kneipp, Y. Wang, H. Kneipp, L.T. Perelman, I. Itzkan, R.R. Dasari and M.S. Feld, Single molecule detection using surface-enhanced Raman scattering (SERS), *Phys. Rev. Lett.* **78** (1997), 1667–1670.
[91] W. Knoll, Interfaces and thin films as seen by bound electromagnetic waves, *Annu. Rev. Phys. Chem.* **49** (1998), 569–638.
[92] A. Kudelski, Analytical applications of Raman spectroscopy, *Talanta* **76** (2008), 1–8.

[93] B. Kustner, M. Gellner, M. Schutz, F. Schoppler, A. Marx, P. Strobel, P. Adam, C. Schmuck and S. Schlucker, SERS labels for red laser excitation: Silica-encapsulated SAMs on tunable gold/silver nanoshells, *Angew. Chem., Int. Ed.* **48** (2009), 1950–1953.
[94] E.C. Le Ru, E. Blackie, M. Meyer and P.G. Etchegoin, Surface enhanced Raman scattering enhancement factors: a comprehensive study, *J. Phys. Chem. C* **111** (2007), 13794–13803.
[95] M. Lee, K. Lee, K.H. Kim, K.W. Oh and J. Choo, SERS-based immunoassay using a gold array-embedded gradient microfluidic chip, *Lab. Chip.* **12** (2012), 3720–3727.
[96] S.J. Lee, J.M. Baik and M. Moskovits, Polarization-dependent surface-enhanced Raman scattering from a silver-nanoparticle-decorated single silver nanowire, *Nano Lett.* **8** (2008), 3244–3247.
[97] X.Z. Li, T.Y. Yang and J.X. Lin, Spectral analysis of human saliva for detection of lung cancer using surface-enhanced Raman spectroscopy, *J. Biomed. Opt.* **17** (2012), 037003.
[98] D. Lin, S.Y. Feng, J.J. Pan, Y.P. Chen, J.Q. Lin, G.N. Chen, S.S. Xie, H.S. Zeng and R. Chen, Colorectal cancer detection by gold nanoparticle based surface-enhanced Raman spectroscopy of blood serum and statistical analysis, *Opt. Express* **19** (2011), 13565–13577.
[99] Y.J. Liu, Z.Y. Zhang, Q. Zhao and Y.P. Zhao, Revisiting the separation dependent surface enhanced Raman scattering, *Appl. Phys. Lett.* **93** (2008), 173106–3.
[100] A. Loren, J. Engelbrektsson, C. Eliasson, M. Josefson, J. Abrahamsson and K. Abrahamsson, Self-assembled monolayer coating for normalization of surface enhanced Raman spectra, *Nano Lett.* **4** (2004), 309–312.
[101] O. Lyandres, N.C. Shah, C.R. Yonzon, J.T. Walsh, M.R. Glucksberg and R.P. Van Duyne, Real-time glucose sensing by surface-enhanced Raman spectroscopy in bovine plasma facilitated by a mixed decanethiol/mercaptohexanol partition layer, *Anal. Chem.* **77** (2005), 6134–6139.
[102] O. Lyandres, J.M. Yuen, N.C. Shah, R.P. VanDuyne, J.T. Walsh and M.R. Glucksberg, Progress toward an *in vivo* surface-enhanced Raman spectroscopy glucose sensor, *Diabetes Technol. Ther.* **10** (2008), 257–265.
[103] K. Ma, J.M. Yuen, N.C. Shah, J.T. Walsh, M.R. Glucksberg and R.P. Van Duyne, *In vivo*, transcutaneous glucose sensing using surface-enhanced spatially offset Raman spectroscopy: multiple rats, improved hypoglycemic accuracy, low incident power, and continuous monitoring for greater than 17 days, *Anal. Chem.* **83** (2011), 9146–9152.
[104] S.A. Maier, *Plasmonics: Fundamentals and Applications*, Springer, New York, 2007.
[105] K.K. Maiti, U.S. Dinish, C.Y. Fu, J.J. Lee, K.S. Soh, S.W. Yun, R. Bhuvaneswari, M. Olivo and Y.T. Chang, Development of biocompatible SERS nanotag with increased stability by chemisorption of reporter molecule for *in vivo* cancer detection, *Biosens. Bioelectron.* **26** (2010), 398–403.
[106] K.K. Maiti, U.S. Dinish, A. Samanta, M. Vendrell, K.S. Soh, S.J. Park, M. Olivo and Y.T. Chang, Multiplex targeted *in vivo* cancer detection using sensitive near-infrared SERS nanotags, *Nano Today* **7** (2012), 85–93.
[107] L.A. Marquardt, M.A. Arnold and G.W. Small, Near-infrared spectroscopic measurement of glucose in a protein matrix, *Anal. Chem.* **65** (1993), 3271–3278.
[108] P. Matousek, I.P. Clark, E.R.C. Draper, M.D. Morris, A.E. Goodship, N. Everall, M. Towrie, W.F. Finney and A.W. Parker, Subsurface probing in diffusely scattering media using spatially offset Raman spectroscopy, *Appl. Spectrosc.* **59** (2005), 393–400.
[109] M.D. McMahon, Effects of geometrical order on the linear and nonlinear optical properties of metal nanoparticles, Dissertation, Vanderbilt University, Nashville, Tennessee, 2006.
[110] G. Mie, Beiträge zur Optik trüber Medien, speziell kolloidaler Metallösungen, *Ann. Phys.* **330** (1908), 377–445.
[111] A.M. Mohs, M.C. Mancini, S. Singhal, J.M. Provenzale, B. Leyland-Jones, M.D. Wang and S.M. Nie, Hand-held spectroscopic device for *in vivo* and intraoperative tumor detection: contrast enhancement, detection sensitivity, and tissue penetration, *Anal. Chem.* **82** (2010), 9058–9065.
[112] M. Moskovits, Surface roughness and the enhanced intensity of Raman scattering by molecules adsorbed on metals, *J. Chem. Phys.* **69** (1978), 4159–4161.
[113] M. Muniz-Miranda, B. Pergolese, A. Bigotto and A. Giusti, Stable and efficient silver substrates for SERS spectroscopy, *J. Colloid Interface Sci.* **314** (2007), 540–544.
[114] F. Ni, H. Feng, L. Gorton and T.M. Cotton, Electrochemical and SERS studies of chemically modified electrodes – Nile blue-a, a mediator for Nadh oxidation, *Langmuir* **6** (1990), 66–73.
[115] S. Nie and S.R. Emory, Probing single molecules and single nanoparticles by surface-enhanced Raman scattering, *Science* **275** (1997), 1102–1106.
[116] Y. Oshima, H. Shinzawa, T. Takenaka, C. Furihata and H. Sato, Discrimination analysis of human lung cancer cells associated with histological type and malignancy using Raman spectroscopy, *J. Biomed. Opt.* **15** (2010), 017009.
[117] W.F. Pearman and A.W. Fountain, Classification of chemical and biological warfare agent simulants by surface-enhanced Raman spectroscopy and multivariate statistical techniques, *Appl. Spectrosc.* **60** (2006), 356–365.
[118] J.H. Pei, F. Tian and T. Thundat, Glucose biosensor based on the microcantilever, *Anal. Chem.* **76** (2004), 292–297.
[119] H.I. Peng and B.L. Miller, Recent advancements in optical DNA biosensors: Exploiting the plasmonic effects of metal nanoparticles, *Analyst* **136** (2011), 436–447.

[120] B. Pettinger, U. Wenning and H. Wetzel, Surface plasmon enhanced Raman scattering frequency and angular resonance of Raman scattered light from pyridine on Au, Ag and Cu electrodes, *Surf. Sci.* **101** (1980), 409–416.
[121] O.M. Primera-Pedrozo, J.I. Jerez-Rozo, E. De la Cruz-Montoya, T. Luna-Pineda, L.C. Pacheco-Londono and S.P. Hernandez-Rivera, Nanotechnology-based detection of explosives and biological agents simulants, *IEEE Sens. J.* **8** (2008), 963–973.
[122] E.M. Purcell and C.R. Pennypacker, Scattering and absorption of light by nonspherical dielectric grains, *Astrophys. J.* **186** (1973), 705–714.
[123] X.M. Qian, X.H. Peng, D.O. Ansari, Q. Yin-Goen, G.Z. Chen, D.M. Shin, L. Yang, A.N. Young, M.D. Wang and S.M. Nie, *In vivo* tumor targeting and spectroscopic detection with surface-enhanced Raman nanoparticle tags, *Nat. Biotechnol.* **26** (2008), 83–90.
[124] C.V. Raman and K.S. Krishnan, A new type of secondary radiation, *Nature* **121** (1928), 501–502.
[125] P.C. Ray, S.A. Khan, A.K. Singh, D. Senapati and Z. Fan, Nanomaterials for targeted detection and photothermal killing of bacteria, *Chem. Soc. Rev.* **41** (2012), 3193–3209.
[126] J.A. Roden and S.D. Gedney, Convolution PML (CPML): An efficient FDTD implementation of the CFS–PML for arbitrary media, *Microw. Opt. Techn. Let.* **27** (2000), 334–339.
[127] J.C. Rubim, Surface-enhanced Raman scattering (SERS) on silver electrodes as a technical tool in the study of the electrochemical reduction of cyanopyridines and in quantitative analysis, *J. Electroanal. Chem. Interfacial Electrochem.* **220** (1987), 339–350.
[128] R.J. Russell, M.V. Pishko, C.C. Gefrides, M.J. McShane and G.L. Cote, A fluorescence-based glucose biosensor using concanavalin A and dextran encapsulated in a poly(ethylene glycol) hydrogel, *Anal. Chem.* **71** (1999), 3126–3132.
[129] K. Saha, S.S. Agasti, C. Kim, X.N. Li and V.M. Rotello, Gold nanoparticles in chemical and biological sensing, *Chem. Rev.* **112** (2012), 2739–2779.
[130] A. Samanta, K.K. Maiti, K.S. Soh, X.J. Liao, M. Vendrell, U.S. Dinish, S.W. Yun, R. Bhuvaneswari, H. Kim, S. Rautela, J.H. Chung, M. Olivo and Y.T. Chang, Ultrasensitive near-infrared Raman reporters for SERS-based *in vivo* cancer detection, *Angew. Chem. Int. Ed.* **50** (2011), 6089–6092.
[131] J.P. Scaffidi, M.K. Gregas, B. Lauly, J.C. Carter, S.M. Angel and T. Vo-Dinh, Trace molecular detection via surface-enhanced Raman scattering and surface-enhanced resonance Raman scattering at a distance of 15 meters, *Appl. Spectrosc.* **64** (2010), 485–492.
[132] M. Schutz, D. Steinigeweg, M. Salehi, K. Kompe and S. Schlucker, Hydrophilically stabilized gold nanostars as SERS labels for tissue imaging of the tumor suppressor p63 by immuno-SERS microscopy, *Chem. Commun.* **47** (2011), 4216–4218.
[133] M.Y. Sha, H.X. Xu, M.J. Natan and R. Cromer, Surface-enhanced Raman scattering tags for rapid and homogeneous detection of circulating tumor cells in the presence of human whole blood, *J. Am. Chem. Soc.* **130** (2008), 17214–17215.
[134] K.E. Shafer-Peltier, C.L. Haynes, M.R. Glucksberg and R.P. Van Duyne, Toward a glucose biosensor based on surface-enhanced Raman scattering, *J. Am. Chem. Soc.* **125** (2003), 588–593.
[135] R. Sheng, F. Ni and T.M. Cotton, Determination of purine bases by reversed-phase high-performance liquid chromatography using real-time surface-enhanced Raman spectroscopy, *Anal. Chem.* **63** (1991), 437–442.
[136] G. Shvets and Y.A. Urzhumov, Electric and magnetic properties of sub-wavelength plasmonic crystals, *J. Opt. A: Pure Appl. Opt.* **7** (2005), S23–S31.
[137] D.A. Stuart, C.R. Yonzon, X. Zhang, O. Lyandres, N.C. Shah, M.R. Glucksberg, J.T. Walsh and R.P. Van Duyne, Glucose sensing using near-infrared surface-enhanced Raman spectroscopy: Gold surfaces, 10-day stability, and improved accuracy, *Anal. Chem.* **77** (2005), 4013–4019.
[138] D.A. Stuart, J.M. Yuen, N.S.O. Lyandres, C.R. Yonzon, M.R. Glucksberg, J.T. Walsh and R.P. Van Duyne, *In vivo* glucose measurement by surface-enhanced Raman spectroscopy, *Anal. Chem.* **78** (2006), 7211–7215.
[139] Y.H. Sun, R.M. Kong, D.Q. Lu, X.B. Zhang, H.M. Meng, W.H. Tan, G.L. Shen and R.Q. Yu, A nanoscale DNA–Au dendrimer as a signal amplifier for the universal design of functional DNA-based SERS biosensors, *Chem. Commun.* **47** (2011), 3840–3842.
[140] A. Taflove, Application of the finite-difference time-domain method to sinusoidal steady-state electromagnetic-penetration problems, *IEEE Trans. Electromagn. Compat.* **EMC-22** (1980), 191–202.
[141] A. Taflove and M.E. Brodwin, Numerical solution of steady-state electromagnetic scattering problems using the time-dependent Maxwell's equations, *IEEE Trans. Microw. Theory Techn.* **23** (1975), 623–630.
[142] Q. Tu and C. Chang, Diagnostic applications of Raman spectroscopy, *Nanomed.-Nanotechnol. Biol. Med.* **8** (2012), 545–558.
[143] A.P.F. Turner, B.N. Chen and S.A. Piletsky, *In vitro* diagnostics in diabetes: Meeting the challenge, *Clin. Chem.* **45** (1999), 1596–1601.
[144] T. Vo-Dinh, Nanobiosensing using plasmonic nanoprobes, *IEEE J. Sel. Top. Quantum Electron.* **14** (2008), 198–205.
[145] T. Vo-Dinh, L.R. Allain and D.L. Stokes, Cancer gene detection using surface-enhanced Raman scattering (SERS), *J. Raman Spectrosc.* **33** (2002), 511–516.

[146] T. Vo-Dinh, K. Houck and D.L. Stokes, Surface-enhanced Raman gene probes, *Anal. Chem.* **66** (1994), 3379–3383.
[147] T. Vo-Dinh, H.N. Wang and J. Scaffidi, Plasmonic nanoprobes for SERS biosensing and bioimaging, *J. Biophotonics* **3** (2010), 89–102.
[148] T. Vo-Dinh, F. Yan and M.B. Wabuyele, Surface-enhanced Raman scattering for medical diagnostics and biological imaging, *J. Raman Spectrosc.* **36** (2005), 640–647.
[149] G. von Maltzahn, A. Centrone, J.H. Park, R. Ramanathan, M.J. Sailor, T.A. Hatton and S.N. Bhatia, SERS-coded gold nanorods as a multifunctional platform for densely multiplexed near-infrared imaging and photothermal heating, *Adv. Mater.* **21** (2009), 3175–3180.
[150] M.B. Wabuyele, F. Yan and T. Vo-Dinh, Plasmonics nanoprobes: detection of single-nucleotide polymorphisms in the breast cancer BRCA1 gene, *Anal. Bioanal. Chem.* **398** (2010), 729–736.
[151] B.A. Wacaser, M.J. Maughan, I.A. Mowat, T.L. Niederhauser, M.R. Linford and R.C. Davis, Chemomechanical surface patterning and functionalization of silicon surfaces using an atomic force microscope, *Appl. Phys. Lett.* **82** (2003), 808–810.
[152] G.F. Wang, R.J. Lipert, M. Jain, S. Kaur, S. Chakraboty, M.P. Torres, S.K. Batra, R.E. Brand and M.D. Porter, Detection of the potential pancreatic cancer marker MUC4 in serum using surface-enhanced Raman scattering, *Anal. Chem.* **83** (2011), 2554–2561.
[153] Y. Wang, L. Chen and P. Liu, Biocompatible Triplex Ag@SiO2@mTiO2 core–shell nanoparticles for simultaneous fluorescence-SERS bimodal imaging and drug delivery, *Chemistry* **18** (2012), 5935–5943.
[154] G.S. Wilson and Y.B. Hu, Enzyme based biosensors for *in vivo* measurements, *Chem. Rev.* **100** (2000), 2693–2704.
[155] J.C. Wolfe and B.P. Craver, Neutral particle lithography: a simple solution to charge-related artefacts in ion beam proximity printing, *J. Phys. D: Appl. Phys.* **41** (2008), 024007.
[156] L.Y. Wu, B.M. Ross and L.P. Lee, Optical properties of the crescent-shaped nanohole antenna, *Nano Letters* **9** (2009), 1956–1961.
[157] M. Xiao, J. Nyagilo, V. Arora, P. Kulkarni, D.S. Xu, X.K. Sun and D.P. Dave, Gold nanotags for combined multi-colored Raman spectroscopy and X-ray computed tomography, *Nanotechnology* **21** (2010), 035101.
[158] Z. Xiaoyu, N.C. Shah and R.P. Van Duyne, Sensitive and selective chem/bio sensing based on surface-enhanced Raman spectroscopy (SERS), *Vib. Spectrosc.* **42** (2006), 2–88.
[159] Y. Xiong, H. Cai, B.J. Wiley, J. Wang, M.J. Kim and Y. Xia, Synthesis and mechanistic study of palladium nanobars and nanorods, *J. Am. Chem. Soc.* **129** (2007), 3665–3675.
[160] Y. Xiong, J.M. McLellan, J. Chen, Y. Yin, Z.-Y. Li and Y. Xia, Kinetically controlled synthesis of triangular and hexagonal nanoplates of palladium and their SPR/SERS properties, *J. Am. Chem. Soc.* **127** (2005), 17118–17127.
[161] Y. Xiong and Y. Xia, Shape-controlled synthesis of metal nanostructures: the case of palladium, *Adv. Mater.* **19** (2007), 3385–3391.
[162] B. Yan and B.M. Reinhard, Identification of tumor cells through spectroscopic profiling of the cellular surface chemistry, *J. Phys. Chem. Lett.* **1** (2010), 1595–1598.
[163] F. Yan and T. Vo-Dinh, Surface-enhanced Raman scattering detection of chemical and biological agents using a portable Raman integrated tunable sensor, *Sens. Actuators B* **121** (2007), 61–66.
[164] J. Yang, Z.Y. Wang, S.F. Zong, C.Y. Song, R.H. Zhang and Y.P. Cui, Distinguishing breast cancer cells using surface-enhanced Raman scattering, *Anal. Bioanal. Chem.* **402** (2012), 1093–1100.
[165] K. Yee, Numerical solution of initial boundary value problems involving maxwell's equations in isotropic media, *IEEE Trans. Antennas Propag.* **14** (1966), 302–307.
[166] M.V. Yigit and Z. Medarova, *In-vivo* and *ex-vivo* applications of gold nanoparticles for biomedical SERS imaging, *Am. J. Nucl. Med. Mol. Imaging* **2** (2012), 232–241.
[167] M.V. Yigit, L. Zhu, M.A. Ifediba, Y. Zhang, K. Carr, A. Moore and Z. Medarova, Noninvasive MRI-SERS imaging in living mice using an innately bimodal nanomaterial, *ACS Nano* **5** (2011), 1056–1066.
[168] C.R. Yonzon, C.L. Haynes, X. Zhang, J.T. Walsh and R.P. Van Duyne, A glucose biosensor based on surface-enhanced Raman scattering: improved partition layer, temporal stability, reversibility, and resistance to serum protein interference, *Anal. Chem.* **76** (2003), 78–85.
[169] Q. Yu, P. Guan, D. Qin, G. Golden and P.M. Wallace, Inverted size-dependence of surface-enhanced Raman scattering on gold nanohole and nanodisk arrays, *Nano Letters* **8** (2008), 1923–1928.
[170] W. Yuan and C.M. Li, Direct modulation of localized surface plasmon coupling of Au nanoparticles on solid substrates via weak polyelectrolyte-mediated layer-by-layer self assembly, *Langmuir* **25** (2009), 7578–7585.
[171] J.M. Yuen, N.C. Shah, J.T. Walsh, Jr., M.R. Glucksberg and R.P. Van Duyne, Transcutaneous glucose sensing by surface-enhanced spatially offset Raman spectroscopy in a rat model, *Anal. Chem.* **82** (2010), 8382–8385.
[172] V. Yuli, B. Antony, V. Olga, J. Wenlong and L. Quinn, Demagnification in proximity x-ray lithography and extensibility to 25 nm by optimizing Fresnel diffraction, *J. Phys. D: Appl. Phys.* **32** (1999), L114.
[173] M.A. Yurkin and A.G. Hoekstra, The discrete dipole approximation: An overview and recent developments, *J. Quant. Spectrosc. Radiat. Transfer* **106** (2007), 558–589.

[174] F.P. Zamborini, L.L. Bao and R. Dasari, Nanoparticles in measurement science, *Anal. Chem.* **84** (2012), 541–576.
[175] C.L. Zavaleta, M.F. Kircher and S.S. Gambhir, Raman's "effect" on molecular imaging, *J. Nucl. Med.* **52** (2011), 1839–1844.
[176] C.L. Zavaleta, B.R. Smith, I. Walton, W. Doering, G. Davis, B. Shojaei, M.J. Natan and S.S. Gambhir, Multiplexed imaging of surface enhanced Raman scattering nanotags in living mice using noninvasive Raman spectroscopy, *Proc. Natl. Acad. Sci. USA* **106** (2009), 13511–13516.
[177] J. Zeng, H. Jia, J. An, X. Han, W. Xu, B. Zhao and Y. Ozaki, Preparation and SERS study of triangular silver nanoparticle self-assembled films, *J. Raman Spectrosc.* **39** (2008), 1673–1678.
[178] Y. Zhang, H. Hong and W.B. Cai, Imaging with Raman spectroscopy, *Curr. Pharm. Biotechnol.* **11** (2010), 654–661.
[179] Y. Zhang, H. Hong, D.V. Myklejord and W.B. Cai, Molecular imaging with SERS-active nanoparticles, *Small* **7** (2011), 3261–3269.
[180] J. Zhao, A.O. Pinchuk, J.M. McMahon, S. Li, L.K. Ausman, A.L. Atkinson and G.C. Schatz, Methods for describing the electromagnetic properties of silver and gold nanoparticles, *Acc. Chem. Res.* **41** (2008), 1710–1720.

Double-layered nanoparticle stacks for spectro-electrochemical applications

Pinar Frank,[1,†] Johannes Srajer,[1,†] Andreas Schwaighofer,[1] Asmorom Kibrom,[1,4] and Christoph Nowak[1,2,3,*]

[1]*Austrian Institute of Technology GmbH, AIT, Donau-City Str. 1, 1220 Vienna, Austria*

[2]*Center for Biomimetic Sensor Science, 50 Nanyang Drive, Singapore 637553, Singapore*

[3]*Center of Electrochemical Surface Technology, CEST, Viktor-Kaplan-Straße 2, 2700 Wiener Neustadt, Austria*

[4]*e-mail: Asmorom.Kibrom@ait.ac.at*

**Corresponding author: C.Nowak@ait.ac.at*

Received June 28, 2012; revised July 20, 2012; accepted July 20, 2012;
posted July 23, 2012 (Doc. ID 171345); published August 24, 2012

Here we present a surface based on double-layered nanoparticle stacks suitable for spectro-electrochemical applications. The structure is formed on a continuous gold layer by a two-dimensional periodic array of stacks of gold and tantalum pentoxide nanodisks. Reflection spectra in the visible wavelength region showed the multiple-resonant nature of surface plasmon (SP) excitations in the nanostructure, which is in good agreement with simulations based on a finite-difference-time-domain method. The multiple SP resonances can be tuned to various wavelength regions, which are required for simultaneous enhancement at excitation and emission wavelengths. Cyclic voltammetry measurements on the nanostructure proved the applicability of electrochemical methods involving interfacial redox processes.

OCIS codes: 240.6680, 260.3910.

Noble metal nanostructures have led to significant advancements in bio-sensing applications in terms of sensitivity and signal-to-noise ratio, particularly in the field of spectro-electrochemical investigation of structure and reaction mechanisms of redox enzymes attached to electrodes [1,2]. The benefit of metal nanostructures as conductive substrates is based on the strong near-field enhancement resulting from the excitation of collective oscillations of free electrons at the metal/dielectric interface termed as propagating surface plasmons (PSP) and localized surface plasmons (LSP) [3,4].

A common approach to fabricate nanostructured substrates is to arrange nanoparticles in a periodic array on a conducting surface [5–8]. Recently, a remarkable improvement in this direction has been achieved by insertion of a thin dielectric spacer layer between the nanoparticle array and the metallic surface [9–11]. This development enabled the simultaneous enhancement of excitation and emission or scattered light due to its multiple surface plasmon (SP) resonances. The resonance wavelengths can be tuned by varying the grating period and the size of the particles. The optical properties of such arrays can be understood in terms of strong coupling between LSP and PSP modes [12].

However, spectro-electrochemical applications involving interfacial redox processes at the electrode are not possible on structures with an electrically sealing, continuous dielectric layer. On the other side, a dielectric spacer layer is required in order to achieve tunable multiple SP resonances. Consequently, the main challenge is to fabricate nanostructured surfaces that not only show multiple SP resonances, but also facilitate electrochemical methods involving direct electron transfer between the analyte and the electrode.

In this Letter, we present a modified periodic structure (Fig. 1) made of a continuous gold film and a periodic array of disk stacks consisting of tantalum pentoxide (Ta_2O_5) and gold. Instead of a continuous dielectric layer, Ta_2O_5 is placed only on the areas underneath the gold nanoparticles, thereby allowing direct electron transfer at the uncovered metallic surface around the nanoparticles. Also, the nanostructure is tunable in its optical properties and shows multiple SP resonances.

Therefore, glass samples were prepared with a stack of continuous layers in the following order: 5 nm adhesive tantalum (Ta), 100 nm gold, 27 nm Ta_2O_5, and 40 nm gold. The coatings were prepared by direct current magnetron sputtering under an argon atmosphere. The disk-stack nanostructure was created by a top-down lithography process. First, the disk-stack pattern was defined by electron-beam (e-beam) exposure of a negative e-beam resist. After removal of the unexposed parts of the resist, the disk-array structure was formed by ion-beam etching.

To understand the optical properties of this structure, reflection spectra were measured and compared with a simulation model implemented using the MIT Electromagnetic Equation Propagation (MEEP) software package, which utilizes the finite-difference-time-domain (FDTD) method [13]. For proof of principle with regard to spectro-electrochemical applications, cyclic voltammetry measurements using potassium ferricyanide were performed.

The three-dimensional computational cell defines the Brillouin zone of the two-dimensional (2D) square lattice.

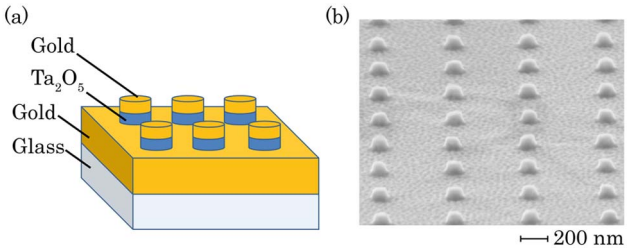

Fig. 1. (Color online) (a) Schematic of the structure geometry; and (b) scanning electron microscope image of the disc-stack array on the gold surface recorded under an angle of 75 deg.

0146-9592/12/173603-03$15.00/0

The cell consists of a single stack and an infinitely extended 2D array is mimicked by defining periodic boundary conditions at the side walls of the cell. Absorbing boundaries made of perfectly matched layers are inserted at the top and the bottom edges of the cell in order to avoid spurious reflections [14]. The optical properties of gold are defined using the Lorentz–Drude model for its permittivity. The parameters of this model are taken from [15]. The refractive index values of glass substrate and tantalum pentoxide are 1.517 and 2.1, respectively. A Gaussian-pulse source is placed over the structure, thereby simulating a linearly polarized light beam at normal incidence. All reflection spectra are normalized to the reflection spectrum of a plain gold layer and are depicted in Fig. 2 for grating period G from 450 nm to 750 nm and disc diameter d from 100 nm to 250 nm.

The computed spectra can be interpreted as follows: for all grating periods, the peaks located at 890 nm, 1092 nm, 1370 nm, and 1640 nm result from the LSP resonances of the nanoparticles with diameters of 100 nm, 150 nm, 200 nm, and 250 nm, respectively. For increasing grating periods, the PSP resonance sharpens and is red-shifted from 468 nm ($G = 450$ nm) to 769 nm ($G = 750$ nm).

Furthermore, for stacks with diameters of 200 nm and 250 nm, additional resonances were observed at 790 nm and 600 nm, which can be attributed to higher-order oscillation modes of LSPs. Hence, we can conclude that for disc-stack diameters >200 nm, the interaction between LSP and PSP shows a more complex behavior, which would be of further interest for future studies.

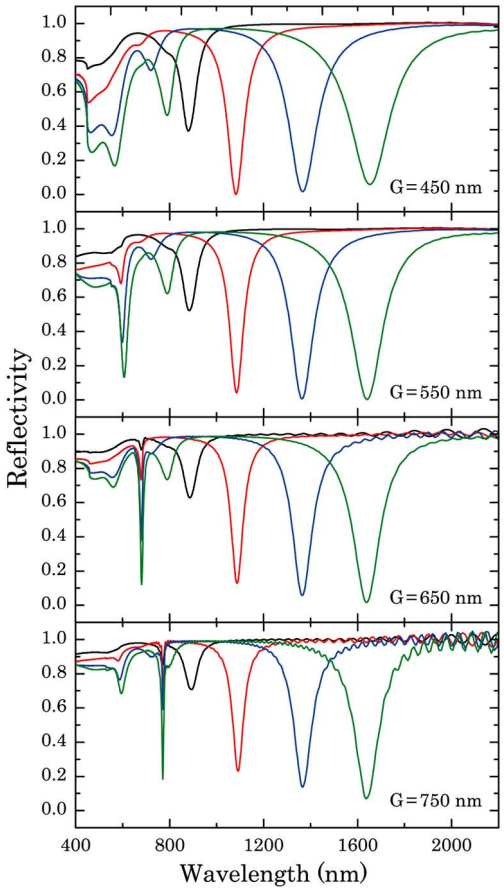

Fig. 2. (Color online) Computed reflection spectra of the nanostructure with varying disc diameters d (black = 100 nm, red = 150 nm, blue = 200 nm, green = 250 nm) and grating periods G.

To observe the resonance wavelengths experimentally, reflection measurements of two different structures [$G = 450$ nm, $d = 230$ nm, thickness of gold nanoparticles (h) = 43 nm; $G = 650$ nm, $d = 200$ nm, $h = 40$ nm] were studied. The square lattice of particles covered an area of 1000 μm × 1000 μm. The obtained spectra were normalized in the same manner as the simulated spectra. The structure was illuminated by a polarized collimated white light beam under normal incidence [Fig. 3(a)]. A beam splitter and fiber optics are used to direct the reflected light into the spectrometer. An iris was placed right after the light source to ensure that solely the structure is illuminated. The measured reflection spectra [Fig. 3(b)] are in good agreement with the calculated reflection spectra [Fig. 3(c)] obtained from FDTD simulations. Deviations between simulation and measurements are attributed to inhomogeneities in the thickness of sputtered layers and inaccuracies in the theoretical dielectric function of gold and in the refractive index of Ta_2O_5 used in the simulations.

To prove the applicability of this structure for electrochemical methods, potassium ferricyanide as a well-known standard redox compound was used for cyclic voltammetry (CV) measurements. CV is a common tool to study electron transfer between the electrode and a redox complex; further information is given in [16]. The CV measurements of 10 mM potassium ferricyanide at different scan rates were taken in a phosphate buffer solution (pH = 8) using an electrochemical cell with a three-electrode configuration: a Ag/AgCl, KCl_{sat} electrode as the reference, a platin wire as the counter, and the sample with the nanostructure as the working

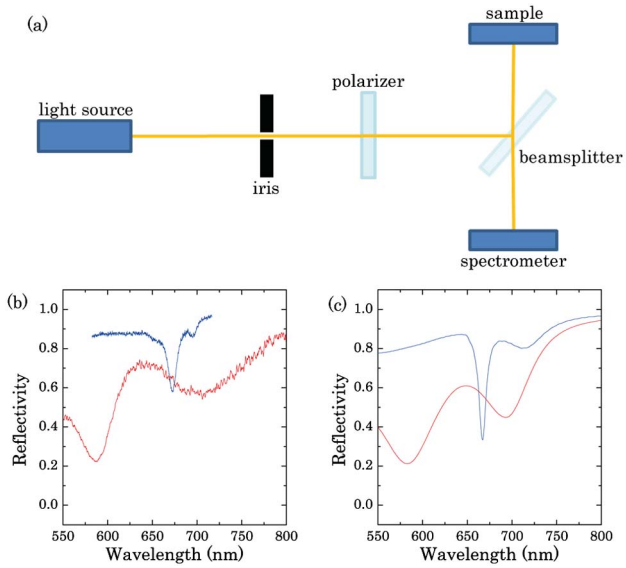

Fig. 3. (Color online) (a) Schematic of the experimental setup for reflection measurements; (b) measured and (c) computed reflection spectra of two different structures. The lower red curve represents the reflection measurement of a structure with $G = 450$ nm and $d = 230$ nm and the higher blue curve shows the spectrum of the structure with $G = 650$ nm and $d = 200$ nm.

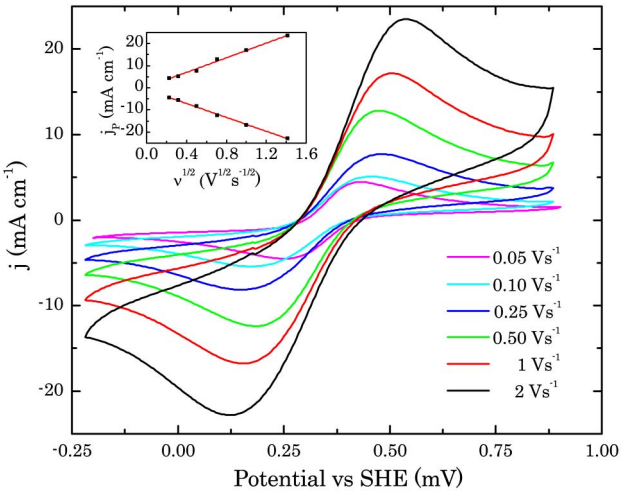

Fig. 4. (Color online) Cyclic voltammetry of 10 mM potassium ferricyanide in PBS (pH = 8) measured on top of the structure with a grating period of 450 nm and disk diameter of 200 nm. The inset shows the peak current densities j_p of the anodic and cathodic peaks plotted as a function of the square root of the scan rate ν.

electrode. A cathodic peak at 268 mV and an anodic peak at 439 mV versus a standard hydrogen electrode were observed in the cyclic voltammogram measured at a scan rate $\nu = 50$ mV s^{-1} (Fig. 4). The inset in Fig. 4 shows that the measured peak current densities j_p are depending linearly on the square root of the scan rate, which is consistent with diffusion-controlled processes. The reversibility of the system is therefore verified [16]. The resulting standard redox potential of potassium ferricyanide of 354 mV is in good agreement with literature values [17].

In summary, we have demonstrated a strategy for designing a plasmonic nanostructure with multiple SP resonances for simultaneous enhancement of excitation and emission or scattered light, respectively. Interfacial electron transfer at the electrode was verified by CV measurements of potassium ferricyanide. Therefore, we suggest that the structure presented here will be very useful for spectro-electrochemical applications for the investigation of structure and reaction mechanisms of redox enzymes attached to electrodes.

The authors acknowledge the IT support of Bilal Guenay from the Health and Environment Department from AIT. The research was supported under the Austrian Federal Ministry for Transport, Innovation and Technology (GZ BMVIT-612.166/0001-III/I1/2010). Partial support for this work was provided by ZIT, Center of Innovation and Technology of Vienna.

†Both authors contributed equally to this Letter.

References

1. C. Nowak, C. Luening, W. Knoll, and R. L. C. Naumann, Appl. Spectrosc. **63**, 1068 (2009).
2. M. Grosserueschkamp, C. Nowak, D. Schach, W. Schaertl, W. Knoll, and R. L. C. Naumann, J. Phys. Chem. C **113**, 17698 (2009).
3. Y. Chu, M. G. Banaee, and K. B. Crozier, ACS Nano **4**, 2804 (2010).
4. W.-D. Li, F. Ding, J. Hu, and S. Y. Chou, Opt. Express **19**, 3925 (2011).
5. N. Papanikolaou, Phys. Rev. B **75**, 235426 (2007).
6. V. G. Kravets, F. Schedin, and A. N. Grigorenko, Phys. Rev. Lett. **101**, 087403 (2008).
7. N. Felidj, S. L. Truong, J. Aubard, G. Levi, J. R. Krenn, A. Hohenau, A. Leitner, and F. R. Aussenegg, J. Chem. Phys. **120**, 7141 (2004).
8. N. Felidj, J. Aubard, G. Levi, J. R. Krenn, G. Schider, A. Leitner, and F. R. Aussenegg, Phys. Rev. B **66** (2002).
9. A. Ghoshal and P. G. Kik, J. Appl. Phys. **103**, 113111 (2008).
10. Y. Z. Chu and K. B. Crozier, Opt. Lett. **34**, 244 (2009).
11. J. Cesario, R. Quidant, G. Badenes, and S. Enoch, Opt. Lett. **30**, 3404 (2005).
12. S. A. Maier, *Plasmonics: Fundamentals and Applications* (Springer, 2007).
13. A. F. Oskooi, D. Roundy, M. Ibanescu, P. Bermel, J. D. Joannopoulos, and S. G. Johnson, Comput. Phys. Commun. **181**, 687 (2010).
14. J.-P. Berenger, J. Comput. Phys. **114**, 185 (1994).
15. A. D. Rakic, A. B. Djurisic, J. M. Elazar, and M. L. Majewski, Appl. Opt. **37**, 5271 (1998).
16. D. Pletcher, S. E. Group, R. Greff, R. Peat, and L. M. Peter, *Instrumental Methods in Electrochemistry* (Ellis Horwood, 2001).
17. D. W. H. Rankin, Crystallogr. Rev. **15**, 223 (2009).

submitted to *Nanoscale*

www.rsc.org/xxxxxx

Communication

Double-layered nanoparticle stacks for surface enhanced infrared absorption spectroscopy

Johannes Srajer,†[a,b] Andreas Schwaighofer,†[a] Georg Ramer,[c] Stefan Rotter,[d] Bilal Guenay,[a] Albert Kriegner,[a] Wolfgang Knoll,[a] Bernhard Lendl[c] and Christoph Nowak*[a,b]

Received (in XXX, XXX) XthXXXXXXXXX 20XX, Accepted Xth XXXXXXXXX 20XX
DOI: 10.1039/b000000x

We demonstrate that double layered stacks of gold and insulator nanoparticles dramatically enhance the sensitivity in absorption infrared microscopy. Through morphological variations of the nanoparticles, the frequency of the plasmon resonances can be tuned to match the frequency of the molecular vibration in the mid infrared. The results show that the nanostructures enhance the absorption signal of the molecules by a factor of up to ~2.2x10^6, while preserving their characteristic line-shape remarkably well.

The capability to efficiently convert photons into collective oscillations of electrons - plasmons - causes a growing interest in production and the applications of metallic nanostructures. Plasmons were first studied in the visible regime. There they led to the development of new spectroscopic techniques with extreme enhancement of sensitivity, allowing for instance single molecule detection.[1-4] Recently, the fabrication of nanostructures with plasmon excitations in the infrared region attracted special attention due to their possible application to improve infrared spectroscopic techniques.

Generally, infrared absorption spectroscopy is used to investigate vibrational modes associated with specific molecular bonds and chemical functional groups by measuring the absorption in the mid-infrared spectral region.[5] Most significant is the ability to identify conformational changes of proteins that reveal the molecular mechanisms of their functionality.[6-9] The technique is extremely powerful in substance identification, since chemical fingerprints of the most common functional groups can be found in the infrared region and it provides a responsive and almost non-destructive chemical analysis.

Despite such advantages, the moderate sensitivity is one of the major shortcomings that severely limit the application of infrared absorption spectroscopy. Especially in thin samples such as monolayers the absorption signals become prohibitively weak.[10] One way to overcome this fundamental deficit involves leveraging the strong light-matter interaction through enhancing the electromagnetic field in the vicinity of sub-wavelength metallic nanostructures. Enabled by plasmonic resonances in the infrared region, surface enhanced infrared absorption spectroscopy (SEIRAS)[11-15] was developed in analogy with surface enhanced Raman scattering (SERS)[2,16-18] and surface enhanced fluorescence (SEF).[19-21]

Herein, we demonstrate a enormous gain of sensitivity in infrared absorption spectroscopy using a self assembled monolayer of dodecanethiol, which shows characteristic symmetric and asymmetric stretching vibrations of the CH_2 and CH_3 groups in the mid-infrared region.[22] Recent studies show that strong enhancement in SEIRAS causes a significant distortion of the molecular signature, that complicates the evaluation of the obtained SEIRAS spectra. These distortions are often called Fano resonances.[15,23,24] Uniquely, our plasmonic system preserves the characteristic shape of the vibrational bands while providing extreme enhancement which enables the monitoring the absorption signal of a molecular monolayer. Additionally we found that under certain conditions our device can also suppress absorption of molecular vibrations, resulting in so-called window resonances or anti-absorption.[25] Often, theoretical models describe the interaction between molecule vibrations and plasmons through coupled oscillators, where constructive interference can lead to strong enhancement, but destructive interference can also damp certain vibrations.[24,26,27] Our results show that these effects are related to the relative position of frequencies of the molecular vibration and the plasmon. The scheme in Fig. 1 sums up the morphology of the nanostructure and the interaction between the plasmons and the dodecanethiol monolayer. Our nanostructures represent a transformative advancement in the compatibility of infrared absorption spectroscopy with modern sample preparation. The system allows targeted enhancement of molecular 'fingerprints' with high specificity and additionally can be used to suppress disruptive signals from other molecules within the experiment. As a first step, we prepared nanoparticle stacks using a lithographic approach and verified their plasmon resonances in the infrared. Therefore, glass samples were prepared with a stack of continuous layers in the following order: 5 nm adhesive tantalum (Ta), 100 nm gold (Au), 30 nm Ta_2O_5 and 42 nm gold. The coatings were prepared by direct current magnetron sputtering under argon atmosphere. The top-down lithographic process used to create the disk-stack nanostructure has been reported previously.[28] The regular arranged disk-stack pattern was defined by electron beam (e-beam) exposure of a negative e-beam resist. After removal of the unexposed parts of the resist, the stack-array structure was created by ion-beam etching. The remaining e-beam resist deposit on top of the disk-stacks was removed by sonication in piranha solution (1:3 H_2O_2:H_2SO_4).

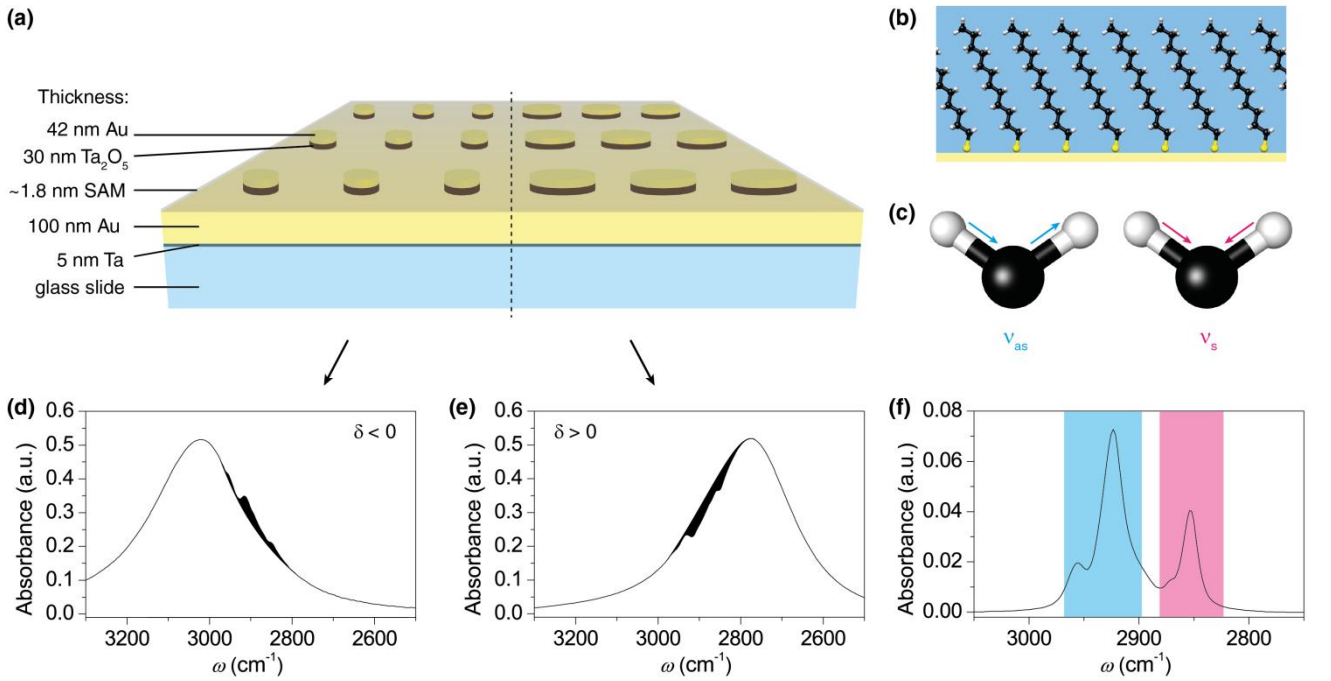

Fig. 1 (a) Scheme of two-dimensional arrays of Ta_2O_5/Au nanoparticles with different stack diameters and a self-assembled monolayer (SAM) of dodecanethiol molecules on the gold surface and on top of the nanoparticles. (b) Graphical representation of the self-assembled monolayer of dodecanethiol on gold. The hydrocarbon chains consisting of CH_2 groups and a CH_3 terminal group form a contact angle of 85° while sulfur is binding to the gold surface. (c) Asymmetric (blue) and symmetric (magenta) stretching modes of CH_2 vibrations. (d) Nanostructures with the plasmon at higher wavenumbers than the molecule vibrations ($\delta < 0$) enhance the molecular absorption. (e) Larger particle diameters (i.e. plasmon at lower wavenumber than the molecule vibration, $\delta > 0$) suppress the molecular vibrations which lowers the total absorbance. (f) ATR-IR measured absorption spectrum of solute dodecanethiol corresponding to stretching modes depicted in (c).

Further details on this crucial step are provided in the Supplementary Information, due to the fact that clean and resist-free disk-stacks are essential for the formation of self-assembled monolayers.

In order to understand the relation between the disk-stack diameter and the plasmon resonance frequency, infrared absorption measurements were performed on a dry-air purged infrared microscope (Bruker Hyperion 3000) coupled to a liquid-nitrogen cooled mercury-cadmium telluride detector. IR spectra of each structure were recorded in the spectral region between 8000 and 600 cm^{-1} and calculated as co-addition of 300 scans. The obtained spectra were compared with a simulation model implemented in the MIT Electromagnetic Equation Propagation software package, which utilizes the finite difference time domain (FDTD) method.[29] Further details on the simulations can be found in the Supplementary Information. Fig. 2 shows the absorption spectra of the uncoated disk-stack pattern for various diameters (250 – 700 nm). The strong absorption signals from the plasmons are in excellent agreement with the FDTD-simulations. The deviations between the measured resonance positions and the simulation are attributed to fabrication imperfections, which are also analyzed in the Supplementary Information in terms of scanning electron microscopy and focal plane array infrared absorption measurements.

For IR measurements of the monolayer, the diameters of the disk-stacks are adjusted to tune the plasmon resonances in the spectral region of the characteristic band positions of the CH stretching vibrations in the dodecanethiol molecules. The molecular signature of solute dodecanethiol was obtained from attenuated total reflection infrared (ATR-IR) measurements (see Fig. 1f). The spectra are dominated by the methylene (CH_2) group (symmetric stretching vibration ν_s: ~2850 cm^{-1} and asymmetric stretching vibration ν_{as}: ~2925 cm^{-1}).[22] The corresponding absorption of the terminal methyl (CH_3) group is also visible in the spectrum and appears at ~2870 cm^{-1} (ν_s) and ~2960 cm^{-1} (ν_{as}), respectively.

In the next step, the monolayer of dodecanethiol molecules was assembled onto the nanostructures. Therefore, the nanostructured samples were immersed in an ethanolic solution of 1 mM dodecanethiol (98%, Alfa Aeser) for 24 h before rinsing with pure ethanol and drying with nitrogen gas. The coated substrates were measured with the infrared microscope under the same conditions as the bare structures. Additionally we performed spatially-resolved IR microscope measurements within a single grating using a focal plane array (FPA) detector. The spatial resolution helped to monitor the quality of the fabrication and delivered additional information on the enhancement. The influence of the plasmon position on the enhancement factor was experimentally determined on nanostructures with various diameters. The resulting spectra show that the difference $\delta = \omega_m - \omega_p$ in the spectral position between the plasmon resonance (ω_p) and the molecule-bond vibration (ω_m) crucially influences the enhancement of the absorption signal. Fig. 3 illustrates that the distance parameter δ further determines, if the

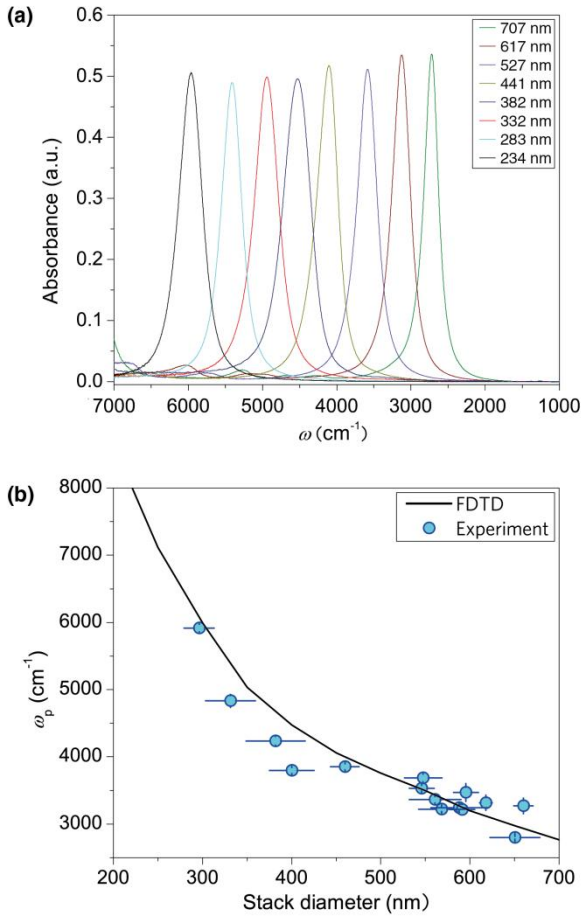

Fig. 2 (a) IR-absorption measurements of the double-layered nanoparticles show the tunability of the plasmon resonances by variation of the stack diameters. (b) Blue circles with error bars represent measured resonance positions of the nanostructured device without adsorbed molecules. The black line was calculated for a three dimensional model of the device using finite difference time domain (FDTD) simulations, which are in good agreement with the experimental data.

absorption of the molecular vibration is enhanced or suppressed. For negative values of δ, i.e. when the plasmon resonance is located at higher wavenumbers than the molecule vibration, the characteristic absorption of the molecule is enhanced. For positive values of δ, the effect reverses and the molecular absorbance is suppressed through the plasmon, in analogy to strong damping in coupled oscillator modes for destructive interference.[24,26,27] While the enhancement and suppression depend on the relative position of the frequencies of the molecule vibration and the plasmon, the efficiency of the enhancement or the suppression, related to the coupling strength of the oscillators, depends on the spectral distances between both frequencies. The coupling between plasmon excitation and molecule vibrations already starts at extreme distances. While infrared spectra of the molecular monolayer could not be measured on a flat gold substrate (i.e. when no plasmonic structures are present), nanoparticle-stacks with a plasmonic resonance in a spectral distance of ~1300 cm^{-1} to the molecule vibrations already allowed the detection of their characteristic absorption bands, as shown in the inset of Fig. 3b. To evaluate the coupling strengths for

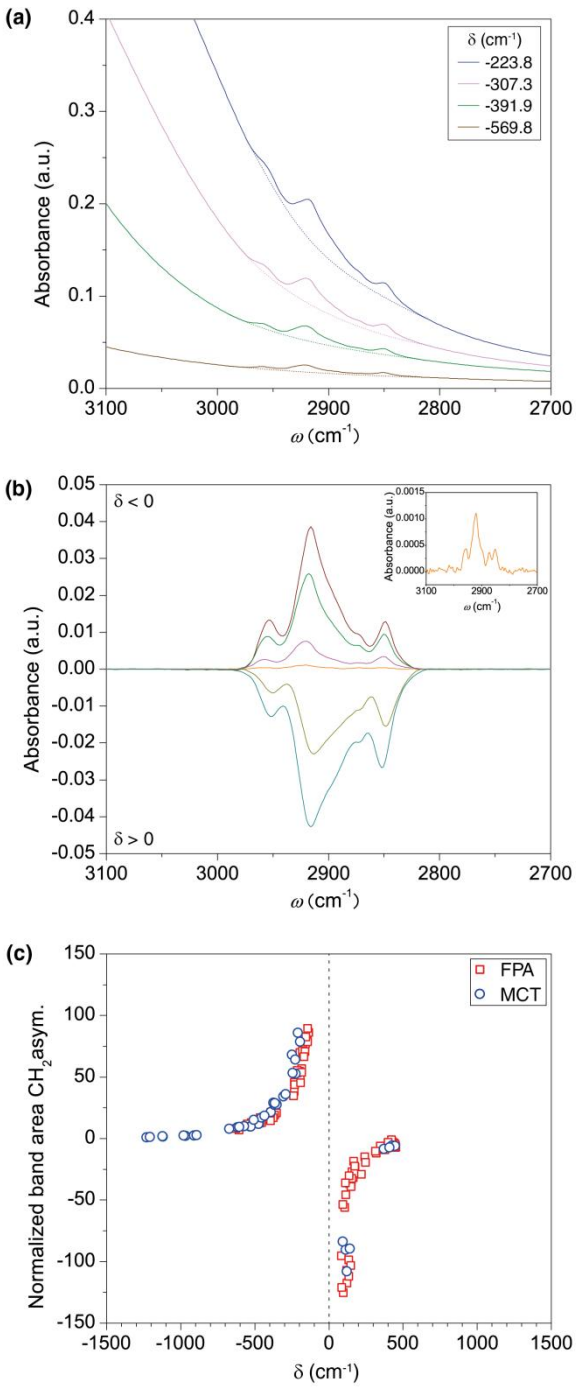

Fig. 3 (a) Infrared absorbance spectra of dodecanethiol monolayers adsorbed onto nanostacks. The intensities of methyl and methylene bands increase for lower δ values, i.e. the plasmon resonance is located closer to molecular vibrations. (b) Baseline-corrected IR spectra of C-H vibrations for selected δ values. Negative δ values lead to enhanced absorption, whereas positive δ values form window resonances. The inset shows the enlarged IR-spectrum of the nanostructure with δ=-1230 cm^{-1}, which was the largest distance where a characteristic CH_2-band pattern of the monolayer was recognizable. (c) Normalized band areas measured at various spectral distances between plasmon resonance and molecular vibrations. The inset spectrum of (b) was used for normalization to calculate the band area enhancement.

constructive and destructive interferences quantitatively, the band area from this weakly coupled case was used as a reference. Comparing the band area of the asymmetric stretching mode[30] at 2916 cm^{-1} for differently aligned plasmonic resonances to this reference revealed extremely strong growth in the band area. Fig. 3a shows the growth of resonances and window-resonances as a function of the spectral displacement between plasmon and molecule resonances. Reducing the distance from 1000 cm^{-1} to 80 cm^{-1} resulted in a maximal signal enhancement of the molecule vibration by a factor of ~125 (Fig. 3c). It is important to stress that this number is not an enhancement factor in the conventional sense, since it is normalized to an already enhanced absorbance signal. To estimate the conventional enhancement factor we compare the absorption of the monolayer to the absorption of solute dodecanethiol in the ATR-IR measurement. Based on the molecule area of ~20 $Å^2$, the monolayer on the disk-stacks contains $1.2x10^{11}$ molecules, resulting in an absorbance of 0.04 (see Fig.3b).[31] The number of molecules in the active area of the evanescent wave in the ATR-IR setup is approximately $1.5x10^{17}$ molecules, resulting in a absorbance of 0.07 (see Fig 1f). From that we calculated an effective enhancement factor of ~$2.2x10^6$. Interestingly, our results in Fig. 3b demonstrate that the shape of the characteristic absorptions of the molecules is approximately preserved for most of the enhancing nanostructures. The distortion of characteristic signal only becomes relevant for perfectly aligned resonances ($\delta \rightarrow 0$). For this case it was not possible to find the correct baseline, which made an evaluation of the enhancement obsolete. For plasmon resonances in a distance greater than ~50 cm^{-1}, distortion of the molecule signal reduces dramatically, for both the constructive and the destructive interference. As demonstrated in Fig. 3b, the window resonances in the molecule absorption, resulting from damped molecule vibrations, provide the same quality for monitoring as the enhanced absorption signals, see Fig 2c.

In summary, we have demonstrated tuning of the plasmon resonance in the infrared spectral region. The plasmon resonance position depends on the diameter of the disk-stacks and has a critical influence on the enhancement factor. We successfully demonstrated a strong enhancement of the infrared absorption by detecting a monolayer of dodecanethiol molecules on the nanostructures, while preserving the shape of the characteristic molecular signal. This presents a unique advantage in enhancing sensitivity in infrared absorption spectroscopy using plasmonic structures. Interestingly, we further observed a way to use plasmons to damp specific absorption signals of the molecules, which might be used to suppress disruptive signals from the experimental environment. The facile tunability of the plasmon position for selective signal enhancement poses a versatile and exceptional platform for the analysis of a wide range of molecular signals.

Acknowledgements

The authors acknowledge the contribution of B. Siebenhofer and thank F. Tai from Linköping University for her initial help and suggestions on infrared reflection measurements. We thank M. Faber and T. Pichler for very helpful discussions. Partial support for this work was provided by ZIT, Centre of Innovation and Technology of Vienna. Financial support by the Austrian Research Promotion Agency (FFG) within the COMET framework, by the Province of Lower Austria as well as by the Austrian Science Fund (FWF) through Project Nos. SFB IR-ON F25-14 and SFB NextLite F49-10 is gratefully acknowledged.

Notes and references

[a] *Austrian Institute of Technology GmbH, AIT, Donau-City Str. 1, 1220 Vienna, Austria. E-mail: C.Nowak@ait.ac.at*
[b] *Center of Electrochemical Surface Technology, CEST, Viktor-Kaplan-Straße 2, 2700 Wiener Neustadt, Austria*
[c] *Institute of Chemical Technologies and Analytics, Vienna University of Technology, Getreidemarkt 9/164 AC, 1060 Vienna, Austria*
[d] *Institute for Theoretical Physics, Vienna University of Technology,Wiedner Hauptstraße 8-10/136 A-1040 Vienna, Austria*
† *These authors contributed equally to this work*

Electronic Supplementary Information (ESI) available: [Experimental details, numerical simulations]. See DOI: 10.1039/b000000x/

1. B. Fazio, C. D'Andrea, F. Bonaccorso, A. Irrera, G. Calogero, C. Vasi, P. G. Gucciardi, M. Allegrini, A. Toma, D. Chiappe, C. Martella and F. B. de Mongeot, *Acs Nano*, 2011, **5**, 5945-5956.
2. K. Kneipp, Y. Wang, H. Kneipp, L. T. Perelman, I. Itzkan, R. R. Dasari and M. S. Feld, *Phys. Rev. Lett.*, 1997, **78**, 1667-1670.
3. K. M. Mayer, F. Hao, S. Lee, P. Nordlander and J. H. Hafner, *Nanotechnology*, 2010, **21**.
4. S. Nie and S. R. Emory, *Science*, 1997, **275**, 1102-1106.
5. P. Griffiths and J. A. Haseth, *Fourier Transform Infrared Spectrometry, 2nd Edition*, John Wiley and Sons, 2007.
6. V. Nedelkovski, A. Schwaighofer, C. A. Wraight, C. Nowak and R. L. C. Naumann, *J. Phys. Chem. C*, 2013, **117**, 16357-16363.
7. C. Nowak, M. G. Santonicola, D. Schach, J. Zhu, R. B. Gennis, S. Ferguson-Miller, D. Baurecht, D. Walz, W. Knoll and R. L. C. Naumann, *Soft Matter*, 2010, **6**, 5523-5532.
8. C. Nowak, D. Schach, J. Gebert, M. Grosserueschkamp, R. B. Gennis, S. Ferguson-Miller, W. Knoll, D. Walz and R. L. C. Naumann, *J. Solid State Electrochem.*, 2011, **15**, 105-114.
9. A. Schwaighofer, S. Ferguson-Miller, R. L. C. Naumann, W. Knoll and C. Nowak, *Appl. Spectrosc.*, 2013, **in press**.
10. K. Ataka, T. Kottke and J. Heberle, *Angew. Chem., Int. Ed. Engl.*, 2010, **49**, 5416-5424.
11. J. Bochterle, F. Neubrech, T. Nagao and A. Pucci, *Acs Nano*, 2012, **6**, 10917-10923.
12. C. D'Andrea, J. Bochterle, A. Toma, C. Huck, F. Neubrech, E. Messina, B. Fazio, O. M. Maragò, E. Di Fabrizio, M. Lamy de La Chapelle, P. G. Gucciardi and A. Pucci, *ACS Nano*, 2013, 3522-3531.
13. D. Enders and A. Pucci, *Appl. Phys. Lett.*, 2006, **88**, 184104.
14. O. Krauth, G. Fahsold and A. Pucci, *J. Chem. Phys.*, 1999, **110**, 3113-3117.
15. F. Neubrech, A. Pucci, T. W. Cornelius, S. Karim, A. Garcia-Etxarri and J. Aizpurua, *Phys. Rev. Lett.*, 2008, **101**, 157403.
16. J. A. Creighton, C. G. Blatchford and M. G. Albrecht, *J. Chem. Soc., Faraday Trans. 2*, 1979, **75**, 790-798.
17. M. Fleischmann, P. J. Hendra and A. J. McQuillan, *Chem. Phys. Lett.*, 1974, **26**, 163-166.
18. C. L. Haynes, C. R. Yonzon, X. Y. Zhang and R. P. Van Duyne, *J. Raman Spectrosc.*, 2005, **36**, 471-484.

19. F. Emmanuel and G. Samuel, *J. Phys. D: Appl. Phys.*, 2008, **41**, 013001.
20. P. J. Tarcha, J. Desaja-Gonzalez, S. Rodriguez-Llorente and R. Aroca, *Appl. Spectrosc.*, 1999, **53**, 43-48.
21. J. Zhang, J. Malicka, I. Gryczynski and J. R. Lakowicz, *J. Phys. Chem. B*, 2005, **109**, 7643-7648.
22. B. Stuart, *Biological Applications of Infrared Spectroscopy*, Wiley, New York, 1997.
23. R. Adato, A. A. Yanik, J. J. Amsden, D. L. Kaplan, F. G. Omenetto, M. K. Hong, S. Erramilli and H. Altug, *Proc. Natl. Acad. Sci.*, 2009, **106**, 19227-19232.
24. V. Giannini, Y. Francescato, H. Amrania, C. C. Phillips and S. A. Maier, *Nano Lett.*, 2011, **11**, 2835-2840.
25. F. Neubrech and A. Pucci, *IEEE J. Sel. Top. Quantum Electron.*, 2013, **19**, 4600809-4600809.
26. R. Adato, A. Artar, S. Erramilli and H. Altug, *Nano Lett.*, 2013, 2584-2591.
27. E. J. Osley, C. G. Biris, P. G. Thompson, R. R. F. Jahromi, P. A. Warburton and N. C. Panoiu, *Phys. Rev. Lett.*, 2013, **110**, 087402.
28. P. Frank, J. Srajer, A. Schwaighofer, A. Kibrom and C. Nowak, *Opt. Lett.*, 2012, **37**, 3603-3605.
29. A. F. Oskooi, D. Roundy, M. Ibanescu, P. Bermel, J. D. Joannopoulos and S. G. Johnson, *Comput. Phys. Commun.*, 2010, **181**, 687-702.
30. A. R. Noble-Luginbuhl and R. G. Nuzzo, *Langmuir*, 2001, **17**, 3937-3944.
31. W. D. Luedtke and U. Landman, *J. Phys. Chem. B*, 1998, **102**, 6566-6572.

Supplementary Information

Double-layered nanoparticle stacks for surface enhanced infrared absorption spectroscopy

*Johannes Srajer,[†, ‡, ¶] Andreas Schwaighofer, [†, ¶] Georg Ramer,[§] Stefan Rotter,[⊥] Bilal Guenay, [†] Albert Kriegner, [†] Wolfgang Knoll, [†] Bernhard Lendl, [§] Christoph Nowak [†, ‡, *]*

[†]Austrian Institute of Technology GmbH, AIT, Donau-City Str. 1, 1220 Vienna, Austria

[‡]Center of Electrochemical Surface Technology, CEST, Viktor-Kaplan-Straße 2, 2700 Wiener Neustadt, Austria

[§]Institute of Chemical Technologies and Analytics, Vienna University of Technology, Getreidemarkt 9/164 AC, 1060 Vienna, Austria

[⊥]Institute for Theoretical Physics, Vienna University of Technology, Wiedner Hauptstraße 8-10/136 A-1040 Vienna, Austria

Corresponding author, E-Mail address: *C.Nowak@ait.ac.at*

Removal of electron beam resist

Self-assembled monolayer formation on the surface of the metal nanoparticles requires complete removal of e-beam resist deposited on top of the cylindrical nanoparticles. A challenging task was to find removal settings for which the deposits wash off completely while geometry and disc shape are preserved.

We varied the duration of sample sonication in piranha solution and intermittently checked the resonance position via IR absorption measurements and the geometrical abrasion with scanning electron microscopic images. The optimal results were found at a duration of 6 h (sonicated

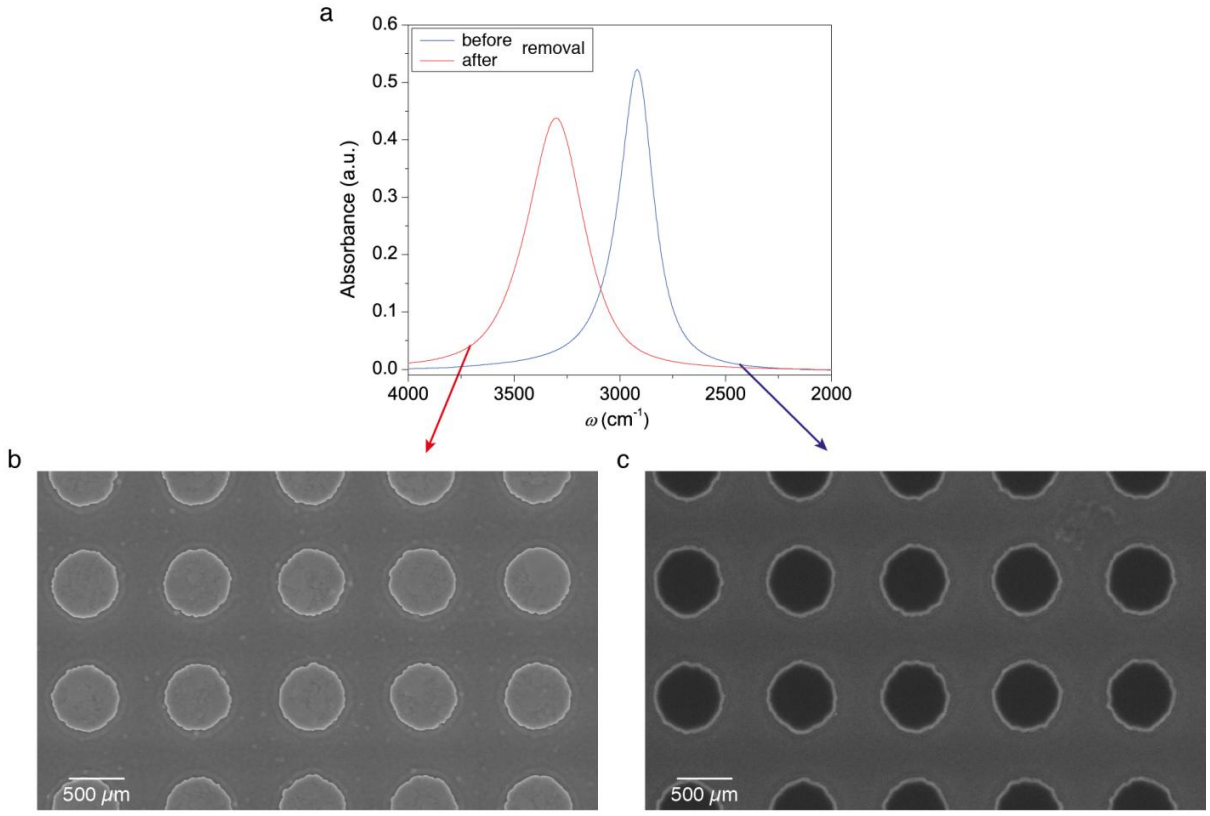

Figure S1. Preserving the structure while removing e-beam resist. (a) IR-spectrum of the plasmon resonance before and after removal of the e-beam resist. (b), (c) Scanning electron microscope images of the corresponding resonances show slight alterations of the geometry. E-beam resist deposits appear dark, due to their low conductivity.

in an upright position) at 40 °C. An average blue shift of the plamonic resonance position of 387 ± 28 cm^{-1} was found for the change in the dielectric environment through removing the deposit (see Supporting Figure 1a). We found a broadening of the plasmon peaks of about 27 cm^{-1}, which we attribute to small aberrations especially at the edges of the particles (see Supporting Figure S1 b, c).

Diameter variations in fabrication process

The correlation between disk-stack diameters and plasmon resonance positions has been proved using infrared microscopy. Each of the 200 x 200 µm² disk-stack pattern was monitored using focal plane array detection of the infrared spectra. Figure S2 shows the direct correlation between the infrared absorbance and the drop in diameter of the stacks at the boundary of the array.

FDTD-Simulations

We performed three dimensional finite difference time domain (FDTD) simulations using the open source software MEEP.[1] A uniform mesh size of 3.33 nm in all dimensions was used. The optical parameters of Au were taken from Rakic and coworkers.[2] The refractive indices used for glass and Ta_2O_5 were 1.517 and 1.74, respectively. The simulated data represent perfectly arranged monodisperse disc-stacks for which an unambiguous relation between the stack diameter and the plasmon resonance position is revealed (see Fig.2b in the manuscript).

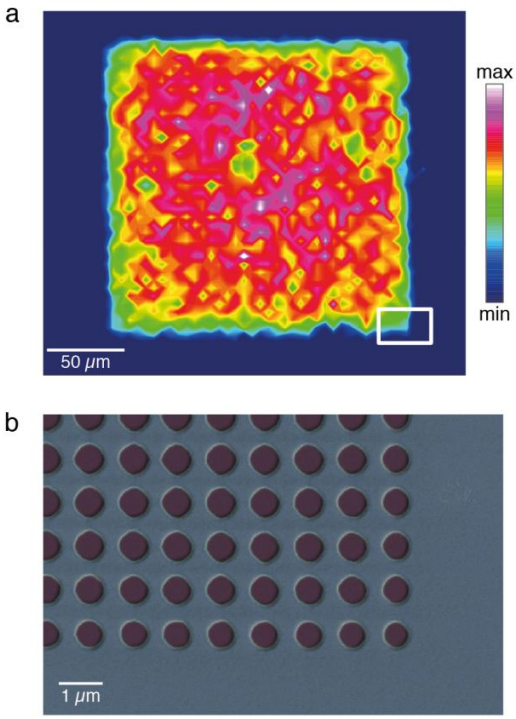

Figure S2. Focal plane array measurement of disc-stack array. (a) The two-dimensional map shows the intensity of the absorption at a frequency of 3020 cm^{-1} according to the plasmon resonance of this structure (disc-stack diameter: ~680 nm) with a spatial resolution of ~2.7 µm on a 200x200 µm² array. The lowered intensity at the borders of the array is attributed to a shift of the plasmon resonance due to a drop in the nanoparticle diameter. (b) Scanning electron microscope image (false color) shows a magnified view of the area in the white box in (a), with a clear decrease of the disc-stack diameter at the boundary of the grating.

References:

1. A. F. Oskooi, D. Roundy, M. Ibanescu, P. Bermel, J. D. Joannopoulos and S. G. Johnson, *Comput. Phys. Commun.*, 2010, **181**, 687-702.
2. A. D. Rakic, A. B. Djurisic, J. M. Elazar and M. L. Majewski, *Appl. Opt.*, 1998, **37**, 5271-5283.

Summary and Outlook

The aims of these studies were to investigate functional proteins tethered to the surface of an attenuated total reflection (ATR) crystal with Fourier transform infrared (FTIR) spectroscopy and to advance plasmonic nanostructures for signal enhancement using FTIR microscopy.

Cytochrome *c* Oxidase (C*c*O) genetically engineered with a his-tag was tethered to a two-layer gold film deposited on an ATR crystal and reconstituted into the protein-tethered bilayer lipid membrane (ptBLM). Time-resolved surface-enhanced infrared absorption (tr-SEIRA) spectra in the millisecond range were recorded under strictly anaerobic conditions during electrochemical excitation of the protein by periodic potential pulses. Application of multiple modulation frequencies allowed the utilization of phase sensitive detection for separating single components within the broad band of overlapping structural bands in the amide I region. Vibrational components thus identified were attributed to redox centers within the protein. A sequential four-electron transfer (ET) model based on protonation-dependent reaction kinetics was used to analyze tr-SEIRA spectra. This ET model was fitted to the temporal progression of the IR band areas in order to obtain the kinetic parameters of electron transfer. It was found that the secondary structures of C*c*O undergo substantial conformational changes upon oxidation and reduction of the redox centers. However, it was not possible to derive rate constants of ET between redox centers from tr-SEIRAS triggered by electrochemical modulation, because the overall ET is limited by electrochemical reduction of Cu_A. Therefore, in future experiments ET to C*c*O should be triggered by light-excitation that allows time-resolution in the millisecond time range. For this purpose, a Ruthenium-C*c*O complex is available. Light-excitation has already been demonstrated to be feasible utilizing the present FTIR setup with bacterial reaction centers incorporated in the ptBLM.

Further studies involved odorant binding protein 14 (OBP14) of the honey bee (*Apis mellifera*). This protein is of potential interest for fabrication of odorant sensors mimicking the biological olfactory system. For FTIR measurements, OBP14 genetically engineered with a his-tag was immobilized on an ATR crystal functionalized with a nitrilotriacetic (NTA) linker. ATR-FTIR spectra confirmed the high abundance of α-helical domains in insect OBPs previously identified by X-ray spectroscopy. Ligand binding of several odorants was monitored by FTIR spectroscopy and circular dichroism (CD). Since FTIR and CD spectra of OBP14 in the presence of ligands did not show significant differences compared to the spectra of the protein alone, effects of odorant binding on thermal stability were investigated. FTIR and CD spectra were recorded while increasing the temperature from 25 to 90 °C. Transition temperatures in the FTIR spectra were evaluated using moving-window 2D correlation maps confirmed by CD measurements. It was found that OBP14 is thermostable under ambient temperature up to 45 °C. This is of great interest with regard to possible applications of this protein for the fabrication of biosensors. Measurements in the presence of odorants indicate an increase of the denaturation temperature of the OBP-odorant complex. The higher thermal stability is attributed to non-covalent forces such as hydrophobic and aromatic interactions as well as hydrogen bonds between OBP14 and the odorant molecule. Evaluation of the transition temperatures enabled the discrimination between high and low affinity odorants, as demonstrated independently by the two applied methodologies. The introduced approach constitutes an easy and elegant alternative for roughly estimating an odorants affinity to an OBP by evaluating the changes of thermal stability upon ligand binding. In future experiments, this methodology will be used to analyze further odorants with OBP14. Of particular interest is the influence of an additional disulfide bridge introduced in a mutant of OBP14 on odorant affinity and thermal stability. For evaluation of the non-covalent interactions in the OBP-odorant complex, molecular dynamics simulations will be performed.

Finally, a plasmonic nanostructured surface was introduced for signal enhancement in IR microscopy. The nanostructure is composed of an array of insulator and gold discs on top of a continuous gold layer deposited on a glass slide. It was demonstrated that the resonance frequency of the plasmon can be tuned by varying the disc diameter while keeping the grating period constant. Signal enhancement was investigated by evaluating the IR bands in the CH_2 region of a dodecanethiol monolayer self-assembled

on the gold surface. Studies of the molecular monolayer on nanostructures with various disc diameters resulted in two significant findings. A first intriguing result was that the sign of the molecular absorbance depends on the relative location of the molecular vibration to the plasmonic resonance. In case the plasmon resonance is positioned at higher wavenumbers than the CH_2 band, the molecular absorbance adds up to the absorbance of the plasmon, yielding signal enhancement. When the plasmonic excitation is located at lower frequencies than the molecular vibration, CH_2 absorbances appear to be subtracted from the plasmonic signal, resulting in signal damping. Secondly, it was found that the magnitude of the signal enhancement depends on the distance between the molecular vibration and the plasmonic resonance in the IR spectrum. Signal enhancement occurs at the flanks of the plasmon band and is largest when the two resonances are located closely together, where the highest enhancement factors of up to $\sim$125 could be achieved. This relationship holds for both, signal enhancement and signal damping. Potential applications of this promising nanostructured surface are manifold due to the tunability of the plasmon resonance. Experiments are planned that involve immobilization of an antibody on the gold surface for sensing applications. Further studies will also involve elucidation of the nature of signal enhancement and damping.

References

[1] A. P. F. Turner. **Biosensors: sense and sensibility**. *Chemical Society Reviews*, **42**:3184–3196, 2013.

[2] S. Iwata, C. Ostermeier, B. Ludwig, and H. Michel. **Structure at 2.8 Å resolution of cytochrome *c* oxidase from *Paracoccus denitrificans***. *Nature*, **376**:660–669, 1995.

[3] B. Kadenbach. **Struktur und Evolution des Atmungsferments Cytochrom-*c*-Oxidase**. *Angewandte Chemie*, **95**:273–281, 1983.

[4] M. G. Friedrich, F. Giess, R. Naumann, W. Knoll, K. Ataka, J. Heberle, J. Hrabakova, D. H. Murgida, and P. Hildebrandt. **Active site structure and redox processes of cytochrome *c* oxidase immobilised in a novel biomimetic lipid membrane on an electrode**. *Chemical Communications*, **40**:2376–2377, 2004.

[5] M. G. Friedrich, J. W. F. Robertson, D. Walz, W. Knoll, and R. L. C. Naumann. **Electronic Wiring of a Multi-Redox Site Membrane Protein in a Biomimetic Surface Architecture**. *Biophysical Journal*, **94**:3698–3705, 2008.

[6] F. Giess, M. Friedrich, J. Heberle, R. Naumann, and W. Knoll. **The Protein-Tethered Lipid Bilayer: A Novel Mimic of the Biological Membrane**. *Biophysical Journal*, **87**:3213–3220, 2004.

[7] D. Schach, C. Nowak, R. B. Gennis, S. Ferguson-Miller, W. Knoll, D. Walz, and R. L. C. Naumann. **Modeling direct electron transfer to a multi-redox center protein: Cytochrome *c* oxidase**. *Journal of Electroanalytical Chemistry*, **649**:268–276, 2010.

[8] C. Nowak, C. Luening, W. Knoll, and R. L. C. Naumann. **A Two-Layer Gold Surface with Improved Surface Enhancement for Spectro-Electrochemistry Using Surface-Enhanced Infrared Absorption Spectroscopy**. *Applied Spectroscopy*, **63**:1068–1074, 2009.

[9] C. Nowak, D. Schach, J. Gebert, M. Grosserueschkamp, R. B. Gennis, S. Ferguson-Miller, W. Knoll, D. Walz, and R. L. C. Naumann. **Oriented**

immobilization and electron transfer to the cytochrome *c* oxidase. *Journal of Solid State Electrochemistry*, **15**:105–114, 2011.

[10] C. Nowak, M. G. Santonicola, D. Schach, J. Zhu, R. B. Gennis, S. Ferguson-Miller, D. Baurecht, D. Walz, W. Knoll, and R. L. C. Naumann. **Conformational transitions and molecular hysteresis of cytochrome *c* oxidase: Varying the redox state by electronic wiring**. *Soft Matter*, **6**:5523–5532, 2010.

[11] J. R. Winkler, B. G. Malmström, and H. B. Gray. **Rapid electron injection into multisite metalloproteins: intramolecular electron transfer in cytochrome oxidase**. *Biophysical Chemistry*, **54**:199–209, 1995.

[12] R. Glatz and K. Bailey-Hill. **Mimicking nature's noses: from receptor deorphaning to olfactory biosensing**. *Progress in Neurobiology*, **93**:270–96, 2011.

[13] S. H. Lee, O. S. Kwon, H. S. Song, S. J. Park, J. H. Sung, J. Jang, and T. H. Park. **Mimicking the human smell sensing mechanism with an artificial nose platform**. *Biomaterials*, **33**:1722–9, 2012.

[14] J. Park, J. H. Lim, H. J. Jin, S. Namgung, S. H. Lee, T. H. Park, and S. Hong. **A bioelectronic sensor based on canine olfactory nanovesicle-carbon nanotube hybrid structures for the fast assessment of food quality**. *Analyst*, **137**:3249–54, 2012.

[15] S. Sankaran, S. Panigrahi, and S. Mallik. **Odorant binding protein based biomimetic sensors for detection of alcohols associated with Salmonella contamination in packaged beef**. *Biosensors and Bioelectronics*, **26**:3103–9, 2011.

[16] F. Di Pietrantonio, D. Cannata, M. Benetti, E. Verona, A. Varriale, M. Staiano, and S. D'Auria. **Detection of odorant molecules via surface acoustic wave biosensor array based on odorant-binding proteins**. *Biosensors and Bioelectronics*, **41**:328–34, 2013.

[17] N. Misawa, H. Mitsuno, R. Kanzaki, and S. Takeuchi. **Highly sensitive and selective odorant sensor using living cells expressing insect olfactory receptors**. *Proceedings of the National Academy of Sciences*, **107**:15340–15344, 2010.

[18] H. J. Jin, S. H. Lee, T. H. Kim, J. Park, H. S. Song, T. H. Park, and S. Hong. **Nanovesicle-based bioelectronic nose platform mimicking human olfactory signal transduction**. *Biosensors and Bioelectronics*, **35**:335–41, 2012.

[19] S. Sankaran, L. R. Khot, and S. Panigrahi. **Biology and applications of olfactory sensing system: A review**. *Sensors and Actuators B: Chemical*, **171**:1–17, 2012.

[20] P. Pelosi. **Odorant-Binding Proteins**. *Critical Reviews in Biochemistry and Molecular Biology*, **29**:199–228, 1994.

[21] A. Marabotti, T. Lefevre, M. Staiano, R. Crescenzo, A. Varriale, M. Rossi, M. Pezolet, and S. D'Auria. **Mutant bovine odorant-binding protein: Temperature affects the protein stability and dynamics as revealed by infrared spectroscopy and molecular dynamics simulations**. *Proteins: Structure, Function, and Bioinformatics*, **72**:769–778, 2008.

[22] A. Marabotti, A. Scire, M. Staiano, R. Crescenzo, V. Aurilla, F. Tanfani, and S. D'Auria. **Wild-Type and Mutant Bovine Odorant-Binding Proteins To Probe the Role of the Quaternary Structure Organization in the Protein Thermal Stability**. *Journal of Proteome Research*, **7**:5221–5229, 2008.

[23] S. Paolini, F. Tanfani, C. Fini, E. Bertoli, and P. Paolo. **Porcine odorant-binding protein: structural stability and ligand affinities measured by Fourier-transform infrared spectroscopy and fluorescence spectroscopy**. *Biochimica Et Biophysica Acta-Protein Structure and Molecular Enzymology*, **1431**:179–188, 1999.

[24] A. Scire, A. Marabotti, M. Staiano, L. Briand, A. Varriale, E. Bertoli, F. Tanfani, and S. D'Auria. **Structure and Stability of a Rat Odorant-Binding Protein: Another Brick in the Wall**. *Journal of Proteome Research*, **8**:4005–4013, 2009.

[25] M. S. Celej, S. A. Dassie, E. Freire, M. L. Bianconi, and G. D. Fidelio. **Ligand-induced thermostability in proteins: thermodynamic analysis of ANS-albumin interaction**. *Biochimica Et Biophysica Acta*, **1750**:122–33, 2005.

[26] M. J. Moreau, I. Morin, and P. M. Schaeffer. **Quantitative determination of protein stability and ligand binding using a green fluorescent protein reporter system**. *Molecular BioSystems*, **6**:1285–92, 2010.

[27] T. Vo-Dinh, H. N. Wang, and J. Scaffidi. **Plasmonic nanoprobes for SERS biosensing and bioimaging**. *Journal of Biophotonics*, **3**:89–102, 2010.

[28] K. M. Mayer and J. H. Hafner. **Localized Surface Plasmon Resonance Sensors**. *Chemical Reviews*, **111**:3828–3857, 2011.

[29] S. M. Nie and S. R. Emery. **Probing single molecules and single nanoparticles by surface-enhanced Raman scattering**. *Science*, **275**:1102–1106, 1997.

[30] M. Osawa, K. Ataka, K. Yoshii, and Y. Nishikawa. **Surface-Enhanced Infrared-spectroscopy-The Origin of the Absorption Enhancement and Band Selection rule in Infrared-spectra of Molecules adsorbed on fine Metal Particles**. *Applied Spectroscopy*, **47**:1497–1502, 1993.

[31] D. Enders and A. Pucci. **Surface enhanced infrared absorption of octadecanethiol on wet-chemically prepared Au nanoparticle films**. *Applied Physics Letters*, **88**:184104, 2006.

[32] R. Adato and H. Altug. **In-situ ultra-sensitive infrared absorption spectroscopy of biomolecule interactions in real time with plasmonic nanoantennas**. *Nature Communications*, **4**, 2013.

[33] M. K. Fan, G. F. S. Andrade, and A. G. Brolo. **A review on the fabrication of substrates for surface enhanced Raman spectroscopy and their applications in analytical chemistry**. *Analytica Chimica Acta*, **693**:7–25, 2011.

[34] V. Liberman, R. Adato, T. H. Jeys, B. G. Saar, S. Erramilli, and H. Altug. **Rational design and optimization of plasmonic nanoarrays for surface enhanced infrared spectroscopy**. *Optics Express*, **20**:11953–11967, 2012.

[35] F. Le, D. W. Brandl, Y. A. Urzhumov, H. Wang, J. Kundu, N. J. Halas, J. Aizpurua, and P. Nordlander. **Metallic Nanoparticle Arrays: A Common Substrate for Both Surface-Enhanced Raman Scattering and Surface-Enhanced Infrared Absorption**. *ACS Nano*, **2**:707–718, 2008.

[36] R. Bukasov and J. S. Shumaker-Parry. **Highly Tunable Infrared Extinction Properties of Gold Nanocrescents**. *Nano Letters*, **7**:1113–1118, 2007.

[37] Y. Chu and K. B. Crozier. **Experimental study of the interaction between localized and propagating surface plasmons**. *Optics Letters*, **34**:244–246, 2009.

[38] D. A. Skoog, F. J. Holler, and S. R. Crouch. *Principles of instrumental analysis*. Thomson Learning, Belmont, CA, 6. edition, 2007.

[39] P. R. Griffiths. *Handbook of Vibrational Spectroscopy*, chapter "Introduction to Vibrational Spectroscopy". John Wiley & Sons, Ltd., Hoboken, NJ, 2006.

[40] B. Schrader. *Infrared and Raman Spectroscopy - Methods and Applications*. VCH Wiley, Weinheim, 1995.

[41] M. Buskühl. *Infrarotellipsometrische Untersuchungen zur Oberflächenverstärkten Infrarotabsorption*. PhD thesis, Humboldt-Universität zu Berlin, 2003.

[42] A. Barth. **Infrared spectroscopy of proteins**. *Biochimica Et Biophysica Acta-Bioenergetics*, **1767**:1073–1101, 2007.

[43] N. Kaun. *New Strategies for Time Resolved Infrared Spectroscopy of Chemical Reactions in Solution*. PhD thesis, Technische Universität Wien, 2006.

[44] W. D. Perkins. **Fourier transform-infrared spectroscopy: Part l. Instrumentation**. *Journal of Chemical Education*, **63**:A5, 1986.

[45] J. L. R. Arrondo, A. Muga, J. Castresana, and F. M. Goni. **Quantitative studies of the structure of proteins in solution by fourier-transform infrared spectroscopy**. *Progress in Biophysics and Molecular Biology*, **59**:23–56, 1993.

[46] J. W. Cooley and J. W. Tukey. **An Algorithm for Machine Calculation of Complex Fourier Series**. *Mathematics of Computation*, **19**:297–301, 1965.

[47] A. A. Michelson. **Visibility of interference-fringes in the focus of a telescope**. *London, Edinburgh and Dublin Philosophical Magazine and Journal of Science*, **5**:217–220, 1891.

[48] J. K. Kauppinen and J. O. Partanen. *Encyclopedia of Spectroscopy and Spectrometry*, chapter "High Resolution IR Spectroscopy (Gas Phase) Instrumentation". Academic Press, Ltd., San Diego, CA, 2000.

[49] A. Barth and C. Zscherp. **What vibrations tell about proteins**. *Quarterly Reviews of Biophysics*, **35**:369–430, 2002.

[50] B. Stuart. *Biological Applications of Infrared Spectroscopy*. Wiley, New York, 1. edition, 1997.

[51] D. Baurecht and U. P. Fringeli. **Quantitative modulated excitation Fourier transform infrared spectroscopy**. *Review of Scientific Instruments*, **72**:3782–3792, 2001.

[52] H. Fabian and W. Mäntele. *Handbook of Vibrational Spectroscopy*, chapter "Infrared Spectroscopy of Proteins". John Wiley & Sons, Ltd., Hoboken, NJ, 2006.

[53] D. K. Das, T. Mondal, U. Mandal, and K. Bhattacharyya. **Probing Deuterium Isotope Effect on Structure and Solvation Dynamics of Human Serum Albumin**. *ChemPhysChem*, **12**:814–822, 2011.

[54] J. L. R. Arrondo and F. M. Goni. **Structure and dynamics of membrane proteins as studied by infrared spectroscopy**. *Progress in Biophysics and Molecular Biology*, **72**:367–405, 1999.

[55] E. Rial, A. Muga, J. M. Valpuesta, J. L. R. Arrondo, and F. M. Goni. **Infrared spectroscopic studies of detergent-solubilized uncoupling protein from brown-adipose-tissue mitochondria**. *European Journal of Biochemistry*, **188**:83–89, 1990.

[56] A. Kohen and H. H. Limbach. *Isotope Effects In Chemistry and Biology*. CRC Press, Boca Raton, 2005.

[57] R. P. Sheridan, E. T. Knight, and L. C. Allen. **The effect of deuterium substitution on hydrogen bonds in redox proteins**. *Biopolymers*, **23**:195–200, 1984.

[58] O. Farver, J. D. Zhang, Q. J. Chi, I. Pecht, and J. Ulstrup. **Deuterium isotope effect on the intramolecular electron transfer in *Pseudomonas aeruginosa* azurin**. *Proceedings of the National Academy of Sciences*, **98**:4426–4430, 2001.

[59] J. Fahrenfort. **Attenuated Total Reflection - a New Principle for the Production of Useful Infra-Red Reflection Spectra of Organic Compounds**. *Spectrochimica Acta*, **17**:698–709, 1961.

[60] N. J. Harrick. **Surface Chemistry from Spectral Analysis of Totally Internally Reflected Radiation**. *Journal of Physical Chemistry*, **64**:1110–1114, 1960.

[61] G. Ramer and B. Lendl. *Encyclopedia of Analytical Chemistry*, chapter "Attenuated Total Reflection Fourier Transform Infrared Spectroscopy". John Wiley & Sons, Ltd, Hoboken, NJ, 2006.

[62] E. Goormaghtigh, V. Raussens, and J. M. Ruysschaert. **Attenuated total reflection infrared spectroscopy of proteins and lipids in biological membranes**. *Biochimica Et Biophysica Acta-Reviews on Biomembranes*, **1422**:105–185, 1999.

[63] M. Fringeli. *Internal Reflection Spectroscopy*, chapter "In Situ Infrared Attenuated Total Reflection Membrane Spectroscopy". Elsevier Academic Press Inc, San Diego, CA, 1992.

[64] V. U. Kirste. *Elektrochemisch gesteuerte zeitaufgelöste Infrarotspektroskopie an Redox-Membranproteinen in einer biomimetischen Membran-Architektur*. PhD thesis, Johannes-Gutenberg-Universität, 2007.

[65] J. Matijasevic. *Synthesis of biomimetic surfaces under permanent in situ FTIR ATR monitoring*. PhD thesis, Universität Wien, 2008.

[66] C. Nowak. *Spektroelektrochemische Untersuchungen mittels oberflächenverstärkter Infrarotabsorptionsspektroskopie (SEIRAS) an Multi-Redox-Center-Proteinen in einer biomimetischen Membranumgebung*. PhD thesis, Johannes-Gutenberg-Universität, 2010.

[67] F. Goos and H. Hänchen. **Ein neuer und fundamentaler Versuch zur Totalreflexion**. *Annalen der Physik*, **436**:333–346, 1947.

[68] S. Devouge, J. Conti, A. Goldsztein, E. Gosselin, A. Brans, M. Voue, J. De Coninck, F. Homble, E. Goormaghtigh, and J. Marchand-Brynaert. **Surface functionalization of germanium ATR devices for use in FTIR-biosensors**. *Journal of Colloid and Interface Science*, **332**:408–415, 2009.

[69] A. R. Noble-Luginbuhl and R. G. Nuzzo. **Assembly and Characterization of SAMs Formed by the Adsorption of Alkanethiols on Zinc Selenide Substrates**. *Langmuir*, **17**:3937–3944, 2001.

[70] M. Voue, E. Goormaghtigh, F. Homble, J. Marchand-Brynaert, J. Conti, S. Devouge, and J. De Coninck. **Biochemical interaction analysis on ATR devices: A wet chemistry approach for surface functionalization**. *Langmuir*, **23**:949–955, 2007.

[71] N. J. Harrick. *Internal reflection spectroscopy.* Interscience, New York; London, 1967.

[72] J. L. Tosi. **Photonics Handbook-Common Infrared Optical Materials** [online]. Available from: `http://www.photonics.com/Article.aspx?AID=25495` [last accessed: 09/25/2013].

[73] B. Stuart. *Infrared Spectroscopy: Fundamentals and Applications.* Wiley, New York, 1. edition, 2004.

[74] A. Hartstein, J. R. Kirtley, and J. C. Tsang. **Enhancement of the Infrared-Absorption from Molecular Monolayers with Thin Metal Overlayers**. *Physical Review Letters*, **45**:201–204, 1980.

[75] M. Osawa. *Handbook of Vibrational Spectroscopy*, chapter "Surface-enhanced Infrared Absorption Spectroscopy". John Wiley & Sons, Ltd., Hoboken, NJ, 2002.

[76] M. Osawa. *Near Field Optics and Surface Plasmon Polaritons*, chapter "Surface-enhanced Infrared Absorption Spectroscopy". Springer, Berlin, 2001.

[77] M. Osawa and M. Ikeda. **Surface-Enhanced Infrared-Absorption of Para-Nitrobenzoic Acid Deposited on Silver Island Films - Contributions of Electromagnetic and Chemical Mechanisms**. *Journal of Physical Chemistry*, **95**:9914–9919, 1991.

[78] M. Osawa. **Dynamic Processes in Electrochemical Reactions Studied by Surface-Enhanced Infrared Absorption Spectroscopy (SEIRAS)**. *Bulletin of the Chemical Society of Japan*, **70**:2861–2880, 1997.

[79] M. Osawa and K. Ataka. **Electromagnetic Mechanism of Enhanced Infrared-Absorption of Molecules Adsorbed on Metal Island Films**. *Surface Science*, **262**:L118–L122, 1992.

[80] V. P. Tolstoy, I. V. Chernyshova, and V. A. Skryshevsky. *Handbook of Infrared Spectroscopy of Ultrathin films.* John Wiley & Sons, Inc., Hoboken, NJ, 2003.

[81] G. D. Smith and R. A. Palmer. *Handbook of Vibrational Spectroscopy*, chapter "Fast time-resolved mid-infrared spectroscopy using an interferometer". John Wiley & Sons, Ltd., Hoboken, NJ, 2002.

[82] P. R. Griffiths, B. L. Hirsche, and C. J. Manning. **Ultra-rapid-scanning Fourier transform infrared spectrometry**. *Vibrational Spectroscopy*, **19**:165–176, 1999.

[83] Y. Qinghua, Z. Renkui, and Z. Baochang. **Novel moving-corner-cube-pair interferometer**. *Journal of Optics A: Pure and Applied Optics*, **11**:015505, 2009.

[84] Q. Yang. **Moving corner-cube mirror interferometer and reflection characteristic of corner-cube mirror**. *Applied Optics*, **49**:4088–4095, 2010.

[85] R. A. Palmer, J. L. Chao, R. M. Dittmar, V. G. Gregoriou, and S. E. Plunkett. **Investigation of Time-Dependent Phenomena by Use of Step-Scan FT-IR**. *Applied Spectroscopy*, **47**:1297–1310, 1993.

[86] M. Baker. **Making membrane proteins for structures: a trillion tiny tweaks**. *Nature Methods*, **7**:429–434, 2010.

[87] M. Almen, K. Nordstrom, R. Fredriksson, and H. Schioth. **Mapping the human membrane proteome: a majority of the human membrane proteins can be classified according to function and evolutionary origin**. *BMC Biology*, **7**:50–64, 2009.

[88] M. A. Yildirim, K.-I. Goh, M. E. Cusick, A.-L. Barabasi, and M. Vidal. **Drug-target network**. *Nature Biotechnology*, **25**:1119–1126, 2007.

[89] O. S. Andersen. **Ion Movement through Gramicidin-a Channels - Interfacial Polarization Effects on Single-Channel Current Measurements**. *Biophysical Journal*, **41**:135–146, 1983.

[90] O. Purrucker, H. Hillebrandt, K. Adlkofer, and M. Tanaka. **Deposition of highly resistive lipid bilayer on silicon-silicon dioxide electrode and incorporation of gramicidin studied by ac impedance spectroscopy**. *Electrochimica Acta*, **47**:791–798, 2001.

[91] T. H. Watts, H. E. Gaub, and H. M. Mcconnell. **T-Cell-Mediated Association of Peptide Antigen and Major Histocompatibility Complex Protein Detected by Energy-Transfer in an Evanescent Wave-Field**. *Nature*, **320**:179–181, 1986.

[92] S. A. Tatulian, P. Hinterdorfer, G. Baber, and L. K. Tamm. **Influenza Hemagglutinin Assumes a Tilted Conformation during Membrane-Fusion as Determined by Attenuated Total-Reflection FTIR Spectroscopy**. *Embo Journal*, **14**:5514–5523, 1995.

[93] S. Terrettaz, T. Stora, C. Duschl, and H. Vogel. **Protein-Binding to Supported Lipid-Membranes - Investigation of the Cholera-Toxin Ganglioside Interaction by Simultaneous Impedance Spectroscopy and Surface-Plasmon Resonance**. *Langmuir*, **9**:1361–1369, 1993.

[94] Y. Ebara and Y. Okahata. **A Kinetic-Study of Concanavalin-a Binding to Glycolipid Monolayers by Using a Quartz-Crystal Microbalance**. *Journal of the American Chemical Society*, **116**:11209–11212, 1994.

[95] W. Knoll, C. W. Frank, C. Heibel, R. Naumann, A. Offenhäusser, J. Rühe, E. K. Schmidt, W. W. Shen, and A. Sinner. **Functional tethered lipid bilayers**. *Reviews in Molecular Biotechnology*, **74**:137–158, 2000.

[96] M. Schaub, G. Wenz, G. Wegner, A. Stein, and D. Klemm. **Ultrathin Films of Cellulose on Silicon-Wafers**. *Advanced Materials*, **5**:919–922, 1993.

[97] S. M. Schiller, R. Naumann, K. Lovejoy, H. Kunz, and W. Knoll. **Archaea analogue thiolipids for tethered bilayer lipid membranes on ultrasmooth gold surfaces**. *Angewandte Chemie - International Edition*, **42**:208–211, 2003.

[98] O. Purrucker, A. Fortig, R. Jordan, and M. Tanaka. **Supported membranes with well-defined polymer tethers-incorporation of cell receptors**. *ChemPhysChem*, **5**:327–335, 2004.

[99] R. C. Naumann and W. Knoll. **Protein tethered lipid bilayer: An alternative mimic of the biological membrane**. *Biointerphases*, **3**:FA101–FA107, 2008.

[100] E. Hochuli, H. Dobeli, and A. Schacher. **New Metal Chelate Adsorbent Selective for Proteins and Peptides Containing Neighboring Histidine-Residues**. *Journal of Chromatography*, **411**:177–184, 1987.

[101] K. Ataka, F. Giess, W. Knoll, R. Naumann, S. Haber-Pohlmeier, B. Richter, and J. Heberle. **Oriented Attachment and Membrane Reconstitution of His-Tagged Cytochrome *c* Oxidase to a Gold Electrode: In Situ Monitoring by Surface-Enhanced Infrared Absorption Spectroscopy**. *Journal of the American Chemical Society*, **126**:16199–16206, 2004.

[102] M. G. Friedrich, V. U. Kirste, J. Zhu, R. B. Gennis, W. Knoll, and R. L. C. Naumann. **Activity of Membrane Proteins Immobilized on Surfaces as a Function of Packing Density**. *The Journal of Physical Chemistry B*, **112**:3193–3201, 2008.

[103] A. Schwaighofer, S. Ferguson-Miller, R. L. C. Naumann, W. Knoll, and C. Nowak. **Phase Sensitive Detection in Modulation Excitation Spectroscopy applied to potential induced electron transfer in Cytochrome *c* Oxidase**. *Applied Spectroscopy*, **accepted**, 2013.

[104] A. Schwaighofer, C. Steininger, D. M. Hildenbrandt, J. Srajer, C. Nowak, W. Knoll, and R. L. C. Naumann. **Time-Resolved Surface-Enhanced IR-Absorption Spectroscopy of direct Electron Transfer to Cytochrome *c* Oxidase from *R. sphaeroides***. *Biophysical Journal*, **under review**, 2013.

[105] V. Nedelkovski, A. Schwaighofer, C. A. Wraight, C. Nowak, and R. L. C. Naumann. **Surface-Enhanced Infrared Absorption Spectroscopy (SEIRAS) of Light-Activated Photosynthetic Reaction Centers from *Rhodobacter sphaeroides* Reconstituted in a Biomimetic Membrane System**. *The Journal of Physical Chemistry C*, **117**:16357–16363, 2013.

[106] R. L. C. Naumann, C. Nowak, and W. Knoll. **Proteins in biomimetic membranes: promises and facts**. *Soft Matter*, **7**:9535–9548, 2011.

[107] P. R. Rich and A. Marechal. **The mitochondrial respiratory chain**. *Essays in Biochemistry: Mitochondrial Function*, **47**:1–23, 2010.

[108] J. Koolman and K. H. Röhm. *Color Atlas of Biochemistry*. Thieme, 2004.

[109] Y. Hatefi. **The Mitochondrial Electron Transport and Oxidative Phosphorylation System**. *Annual Review of Biochemistry*, **54**:1015–1069, 1985.

[110] Donald J.; Voet and Judith G.; Voet. *Biochemistry*. John Wiley & Sons, Inc., Hoboken, NJ, 4. edition, 2011.

[111] A. Lehninger, D. Nelson, and M. Cox. *Lehninger Principles of Biochemistry*. W. H. Freeman, 5. edition, 2008.

[112] T. Yonetani. **Studies on Cytochrome Oxidase: III. Improved preparation and some properties**. *Journal of Biological Chemistry*, **236**:1680–1688, 1961.

[113] T. Tsukihara, H. Aoyama, E. Yamashita, T. Tomizaki, H. Yamaguchi, K. ShinzawaItoh, R. Nakashima, R. Yaono, and S. Yoshikawa. **The whole structure of the 13-subunit oxidized cytochrome *c* oxidase at 2.8 angstrom**. *Science*, **272**:1136–1144, 1996.

[114] M. Svensson-Ek, J. Abramson, G. Larsson, S. Tornroth, P. Brzezinski, and S. Iwata. **The X-ray crystal structures of wild-type and EQ(I-286) mutant cytochrome *c* oxidases from *Rhodobacter sphaeroides***. *Journal of Molecular Biology*, **321**:329–339, 2002.

[115] C. Ostermeier, A. Harrenga, U. Ermler, and H. Michel. **Structure at 2.7 angstrom resolution of the *Paracoccus denitrificans* two-subunit cytochrome *c* oxidase complexed with an antibody F_V fragment**. *Proceedings of the National Academy of Sciences*, **94**:10547–10553, 1997.

[116] J. Koepke, E. Olkhova, H. Angerer, H. Muller, G. H. Peng, and H. Michel. **High resolution crystal structure of *Paracoccus denitrificans* cytochrome *c* oxidase: New insights into the active site and the proton transfer pathways**. *Biochimica Et Biophysica Acta-Bioenergetics*, **1787**:635–645, 2009.

[117] O. M. H. Richter and B. Ludwig. *Cytochrome c oxidase structure, function, and physiology of a redox-driven molecular machine*, **Volume 147** of *Reviews of Physiology, Biochemistry and Pharmacology*, chapter 2, pages 47–74. Springer Berlin Heidelberg, 2003.

[118] A. F. Hollemann and E. Wiberg. *Lehrbuch der Anorganischen Chemie*. de Gruyter, New York, 101. edition, 1995.

[119] S. Yoshikawa, K. Muramoto, K. Shinzawa-Itoh, and M. Mochizuki. **Structural studies on bovine heart cytochrome *c* oxidase**. *Biochimica Et Biophysica Acta-Bioenergetics*, **1817**:579–589, 2012.

[120] H. Kass, F. MacMillan, B. Ludwig, and T. F. Prisner. **Investigation of the Mn binding site in cytochrome *c* oxidase from *Paracoccus denitrificans* by high-frequency EPR**. *Journal of Physical Chemistry B*, **104**:5362–5371, 2000.

[121] R. A. Marcus and N. Sutin. **Electron Transfers in Chemistry and Biology**. *Biochimica Et Biophysica Acta*, **811**:265–322, 1985.

[122] H. B. Gray and J. R. Winkler. **Electron transfer in proteins**. *Annual Review of Biochemistry*, **65**:537–561, 1996.

[123] C. C. Moser, J. M. Keske, K. Warncke, R. S. Farid, and P. L. Dutton. **Nature of Biological Electron-Transfer**. *Nature*, **355**:796–802, 1992.

[124] C. C. Page, C. C. Moser, X. X. Chen, and P. L. Dutton. **Natural engineering principles of electron tunnelling in biological oxidation-reduction**. *Nature*, **402**:47–52, 1999.

[125] I. Belevich and M. I. Verkhovsky. **Molecular mechanism of proton translocation by cytochrome *c* oxidase**. *Antioxidants & Redox Signaling*, **10**:1–29, 2008.

[126] L. M. Geren, J. R. Beasley, B. R. Fine, A. J. Saunders, S. Hibdon, G. J. Pielak, B. Durham, and F. Millett. **Design of a Ruthenium Cytochrome *c* Derivative to Measure Electron-Transfer to the Initial Acceptor in Cytochrome *c* Oxidase**. *Journal of Biological Chemistry*, **270**:2466–2472, 1995.

[127] Y. J. Zhen, C. W. Hoganson, G. T. Babcock, and S. Ferguson-Miller. **Definition of the interaction domain for cytochrome *c* on cytochrome *c* oxidase - I. Biochemical, spectral, and kinetic characterization of surface mutants in subunit II of *Rhodobacter sphaeroides* cytochrome aa_3**. *Journal of Biological Chemistry*, **274**:38032–38041, 1999.

[128] R. Mitchell and P. R. Rich. **Proton Uptake by Cytochrome *c* Oxidase on Reduction and on Ligand-Binding**. *Biochimica Et Biophysica Acta-Bioenergetics*, **1186**:19–26, 1994.

[129] M. I. Verkhovsky, I. Belevich, D. A. Bloch, and M. Wikström. **Elementary steps of proton translocation in the catalytic cycle of cytochrome oxidase**. *Biochimica Et Biophysica Acta-Bioenergetics*, **1757**:401–407, 2006.

[130] I. Belevich, D. A. Bloch, N. Belevich, M. Wikström, and M. I. Verkhovsky. **Exploring the proton pump mechanism of cytochrome *c* oxidase in real time**. *Proceedings of the National Academy of Sciences*, **104**:2685–2690, 2007.

[131] M. I. Verkhovsky, A. Tuukkanen, C. Backgren, A. Puustinen, and M. Wikström. **Charge translocation coupled to electron injection into oxidized cytochrome *c* oxidase from *Paracoccus denitrificans***. *Biochemistry*, **40**:7077–7083, 2001.

[132] D. Zaslavsky, R. C. Sadoski, K. F. Wang, B. Durham, R. B. Gennis, and F. Millett. **Single electron reduction of cytochrome *c* oxidase compound F: Resolution of partial steps by transient spectroscopy**. *Biochemistry*, **37**:14910–14916, 1998.

[133] I. Belevich. **Homepage of Molecular Physics Group, Biocenter Helsinki** [online]. Available from: `http://www.biocenter.helsinki.fi/bi/biophys/research_CcO.html` [last accessed: 05/25/2013].

[134] J. R. Fetter, J. Qian, J. Shapleigh, J. W. Thomas, A. Garciahorsman, E. Schmidt, J. Hosler, G. T. Babcock, R. B. Gennis, and S. Ferguson-Miller. **Possible Proton Relay Pathways in Cytochrome *c* Oxidase**. *Proceedings of the National Academy of Sciences*, **92**:1604–1608, 1995.

[135] J. P. Hosler, S. Ferguson-Miller, M. W. Calhoun, J. W. Thomas, J. Hill, L. Lemieux, J. X. Ma, C. Georgiou, J. Fetter, J. Shapleigh, M. M. J. Tecklenburg, G. T. Babcock, and R. B. Gennis. **Insight into the Active-Site Structure and Function of Cytochrome-Oxidase by Analysis of Site-Directed Mutants of Bacterial Cytochrome aa_3 and Cytochrome**. *Journal of Bioenergetics and Biomembranes*, **25**:121–136, 1993.

[136] J. W. Thomas, L. J. Lemieux, J. O. Alben, and R. B. Gennis. **Site-Directed Mutagenesis of Highly Conserved Residues in Helix VIII of Subunit-I of the Cytochrome *bo* Ubiquinol Oxidase from *Escherichia-Coli* - an Amphipathic Transmembrane Helix That May Be Important in Conveying Protons to the Binuclear Center**. *Biochemistry*, **32**:11173–11180, 1993.

[137] J. W. Thomas, A. Puustinen, J. O. Alben, R. B. Gennis, and M. Wikström. **Substitution of Asparagine for Aspartate-135 in Subunit-I of the Cytochrome *bo* Ubiquinol Oxidase of *Escherichia Coli* Eliminates Proton-Pumping Activity**. *Biochemistry*, **32**:10923–10928, 1993.

[138] J. Abramson, S. Riistama, G. Larsson, A. Jasaitis, M. Svensson-Ek, L. Laakkonen, A. Puustinen, S. Iwata, and M. Wikström. **The structure of the ubiquinol oxidase from *Escherichia coli* and its ubiquinone binding site**. *Nature Structural Biology*, **7**:910–917, 2000.

[139] V. R. I. Kaila, M. I. Verkhovsky, and M. Wikström. **Proton-Coupled Electron Transfer in Cytochrome Oxidase**. *Chemical Reviews*, **110**:7062–7081, 2010.

[140] I. Hofacker and K. Schulten. **Oxygen and proton pathways in cytochrome *c* oxidase**. *Proteins-Structure Function and Genetics*, **30**:100–107, 1998.

[141] M. Wikström, M. I. Verkhovsky, and G. Hummer. **Water-gated mechanism of proton translocation by cytochrome *c* oxidase**. *Biochimica Et Biophysica Acta-Bioenergetics*, **1604**:61–65, 2003.

[142] P. Adelroth, R. B. Gennis, and P. Brzezinski. **Role of the pathway through K(I-362) in proton transfer in cytochrome *c* oxidase from *R. sphaeroides***. *Biochemistry*, **37**:2470–2476, 1998.

[143] T. V. Vygodina, C. Pecoraro, D. Mitchell, R. Gennis, and A. A. Konstantinov. **Mechanism of inhibition of electron transfer by amino acid replacement K362M in a proton channel of *Rhodobacter sphaeroides* cytochrome *c* oxidase**. *Biochemistry*, **37**:3053–3061, 1998.

[144] M. Wikström, A. Jasaitis, C. Backgren, A. Puustinen, and M. I. Verkhovsky. **The role of the D- and K-pathways of proton transfer in the function of the haem-copper oxidases**. *Biochimica Et Biophysica Acta-Bioenergetics*, **1459**:514–520, 2000.

[145] P. Adelroth, M. S. Ek, D. M. Mitchell, R. B. Gennis, and P. Brzezinski. **Glutamate 286 in cytochrome aa_3 from *Rhodobacter sphaeroides* is involved in proton uptake during the reaction of the fully-reduced enzyme with dioxygen**. *Biochemistry*, **36**:13824–13829, 1997.

[146] A. A. Konstantinov, S. Siletsky, D. Mitchell, A. Kaulen, and R. B. Gennis. **The roles of the two proton input channels in cytochrome *c* oxidase from *Rhodobacter sphaeroides* probed by the effects of site-directed mutations on time-resolved electrogenic intraprotein proton transfer**. *Proceedings of the National Academy of Sciences*, **94**:9085–9090, 1997.

[147] A. Puustinen and M. Wikström. **Proton exit from the heme-copper oxidase of *Escherichia coli***. *Proceedings of the National Academy of Sciences*, **96**:35–37, 1999.

[148] S. Riistama, A. Puustinen, A. Garcia-Horsman, S. Iwata, H. Michel, and M. Wikström. **Channelling of dioxygen into the respiratory enzyme**. *Biochimica Et Biophysica Acta-Bioenergetics*, **1275**:1–4, 1996.

[149] S. Riistama, A. Puustinen, M. I. Verkhovsky, J. E. Morgan, and M. Wikström. **Binding of O_2 and its reduction are both retarded by replacement of valine 279 by isoleucine in cytochrome *c* oxidase from *Paracoccus denitrificans*.** *Biochemistry*, **39**:6365–6372, 2000.

[150] M. Wikström. **Identification of the electron transfers in cytochrome oxidase that are coupled to proton-pumping.** *Nature*, **338**:776–778, 1989.

[151] H. Michel. **Cytochrome *c* oxidase: Catalytic cycle and mechanisms of proton pumping - A discussion.** *Biochemistry*, **38**:15129–15140, 1999.

[152] M. Wikström. **Proton translocation by cytochrome *c* oxidase: A rejoinder to recent criticism.** *Biochemistry*, **39**:3515–3519, 2000.

[153] E. Antonini, M. Brunori, A. Colosimo, C. Greenwood, and M. T. Wilson. **Oxygen "pulsed" cytochrome *c* oxidase: functional properties and catalytic relevance.** *Proceedings of the National Academy of Sciences*, **74**:3128–3132, 1977.

[154] T. Nilsson. **Photoinduced Electron-Transfer from Tris(2,2'-Bipyridyl) Ruthenium to Cytochrome *c* Oxidase.** *Proceedings of the National Academy of Sciences*, **89**:6497–6501, 1992.

[155] M. Ruitenberg, A. Kannt, E. Bamberg, B. Ludwig, H. Michel, and K. Fendler. **Single-electron reduction of the oxidized state is coupled to proton uptake via the K pathway in *Paracoccus denitrificans* cytochrome *c* oxidase.** *Proceedings of the National Academy of Sciences*, **97**:4632–4636, 2000.

[156] A. J. Moody, U. Brandt, and P. R. Rich. **Single Electron Reduction of Slow and Fast Cytochrome *c* Oxidase.** *Febs Letters*, **293**:101–105, 1991.

[157] M. Fabian, W. W. Wong, R. B. Gennis, and G. Palmer. **Mass spectrometric determination of dioxygen bond splitting in the "peroxy" intermediate of cytochrome *c* oxidase.** *Proceedings of the National Academy of Sciences*, **96**:13114–13117, 1999.

[158] D. A. Proshlyakov, M. A. Pressler, and G. T. Babcock. **Dioxygen activation and bond cleavage by mixed-valence cytochrome *c* oxidase.** *Abstracts of Papers of the American Chemical Society*, **216**:U138–U138, 1998.

[159] M. Oliveberg, S. Hallen, and T. Nilsson. **Uptake and Release of Protons during the Reaction between Cytochrome *c* Oxidase and Molecular-Oxygen - a Flow-Flash Investigation.** *Biochemistry*, **30**:436–440, 1991.

[160] J. E. Morgan, M. I. Verkhovsky, G. Palmer, and M. Wikström. **Role of the P-R intermediate in the reaction of cytochrome *c* oxidase with O_2.** *Biochemistry*, **40**:6882–6892, 2001.

[161] P. Lappalainen, R. Aasa, B. G. Malmstrom, and M. Saraste. **Soluble Cu_A-binding Domain from the *Paracoccus* Cytochrome *c* Oxidase**. *Journal of Biological Chemistry*, **268**:26416–26421, 1993.

[162] D. Jancura, V. Berka, M. Antalik, J. Bagelova, R. B. Gennis, G. Palmer, and M. Fabian. **Spectral and kinetic equivalence of oxidized cytochrome *c* oxidase as isolated and "activated" by reoxidation**. *Journal of Biological Chemistry*, **281**:30319–30325, 2006.

[163] D. Bloch, I. Belevich, A. Jasaitis, C. Ribacka, A. Puustinen, M. I. Verkhovsky, and M. Wikström. **The catalytic cycle of cytochrome *c* oxidase is not the sum of its two halves**. *Proceedings of the National Academy of Sciences*, **101**:529–533, 2004.

[164] E. Fadda, C.-H. Yu, and R. Poms. **Electrostatic control of proton pumping in cytochrome *c* oxidase**. *Biochimica Et Biophysica Acta-Bioenergetics*, **1777**:277–284, 2008.

[165] J. E. Morgan, M. I. Verkhovsky, and M. Wikström. **The Histidine Cycle - a New Model for Proton Translocation in the Respiratory Heme-Copper Oxidases**. *Journal of Bioenergetics and Biomembranes*, **26**:599–608, 1994.

[166] S. Firestein. **How the olfactory system makes sense of scents**. *Nature*, **413**:211–218, 2001.

[167] B. S. Hansson and M. C. Stensmyr. **Evolution of Insect Olfaction**. *Neuron*, **72**:698–711, 2011.

[168] W. S. Leal. **Odorant reception in insects: roles of receptors, binding proteins, and degrading enzymes**. *Annual Review of Entomology*, **58**:373–391, 2013.

[169] S. Thuret, L. D. F. Moon, and F. H. Gage. **Therapeutic interventions after spinal cord injury**. *Nature Reviews Neuroscience*, **7**:628–643, 2006.

[170] U. B. Kaupp. **Olfactory signalling in vertebrates and insects: differences and commonalities**. *Nature Reviews Neuroscience*, **11**:188–200, 2010.

[171] L. B. Vosshall and R. E. Stocker. *Molecular architecture of smell and taste in Drosophila*, **Volume 30** of *Annual Review of Neuroscience*, pages 505–533. Annual Reviews, Palo Alto, CA, 2007.

[172] M. Bear, B. Connors, and M. Paradiso. *Neuroscience: Exploring the Brain*. Lippincott Williams & Wilkins, Baltimore, MD, 3. edition, 2006.

[173] R. L. Doty. **Olfaction**. *Annual Review of Psychology*, **52**:423–452, 2001.

[174] M. Stengl and N. Funk. **The role of the coreceptor Orco in insect olfactory transduction**. *Journal of Comparative Physiology A*, **199**:1–13, 2013.

[175] M. Pellegrino and T. Nakagawa. **Smelling the difference: controversial ideas in insect olfaction**. *Journal of Experimental Biology*, **212**:1973–1979, 2009.

[176] P. X. Xu, R. Atkinson, D. N. M. Jones, and D. P. Smith. **Drosophila OBP LUSH is required for activity of pheromone-sensitive neurons**. *Neuron*, **45**:193–200, 2005.

[177] K. Sato, M. Pellegrino, T. Nakagawa, T. Nakagawa, L. B. Vosshall, and K. Touhara. **Insect olfactory receptors are heteromeric ligand-gated ion channels**. *Nature*, **452**:1002–1009, 2008.

[178] D. Wicher, R. Schafer, R. Bauernfeind, M. C. Stensmyr, R. Heller, S. H. Heinemann, and B. S. Hansson. **Drosophila odorant receptors are both ligand-gated and cyclic-nucleotide-activated cation channels**. *Nature*, **452**:1007–1010, 2008.

[179] K. E. Kaissling. **Olfactory perireceptor and receptor events in moths: A kinetic model**. *Chemical Senses*, **26**:125–150, 2001.

[180] Y. Ishida and W. S. Leal. **Rapid inactivation of a moth pheromone**. *Proceedings of the National Academy of Sciences*, **102**:14075–14079, 2005.

[181] R. G. Vogt. *Molecular basis of pheromone detection in insects*, **Volume 3** of *Comprehensive Insect Physiology, Biochemistry, Pharmacology, and Molecular Biology*, pages 753–801. Elsevier, London, 2005.

[182] J. J. Zhou. *Odorant-Binding Proteins in Insects*, **Volume 83** of *Vitamins and Hormones*, pages 241–272. Elsevier Academic Press Inc, San Diego, CA, 2010.

[183] M. Tegoni, R. Ramoni, E. Bignetti, S. Spinelli, and C. Cambillau. **Domain swapping creates a third putative combining site in bovine odorant binding protein dimer**. *Nature Structural Biology*, **3**:863–867, 1996.

[184] B. H. Sandler, L. Nikonova, W. S. Leal, and J. Clardy. **Sexual attraction in the silkworm moth: structure of the pheromone-binding-protein-bombykol complex**. *Chemistry & Biology*, **7**:143–151, 2000.

[185] T. K. Györgyi, A. J. Roby-Shemkovitz, and M. R. Lerner. **Characterization and cDNA cloning of the pheromone-binding protein from the tobacco hornworm, Manduca sexta: a tissue-specific developmentally regulated protein**. *Proceedings of the National Academy of Sciences*, **85**:9851–9855, 1988.

[186] J. Fan, F. Francis, Y. Liu, J. L. Chen, and D. F. Cheng. **An overview of odorant-binding protein functions in insect peripheral olfactory reception**. *Genetics and Molecular Research*, **10**:3056–3069, 2011.

[187] R. G. Vogt, R. Rybczynski, and M. R. Lerner. **Molecular-Cloning and Sequencing of General Odorant Binding-Proteins GOBP1 and GOBP2 from the Tobacco Hawk Moth Manduca-Sexta - Comparisons with Other Insect OBPs and Their Signal Peptides**. *Journal of Neuroscience*, **11**:2972–2984, 1991.

[188] P. Pelosi and R. Maida. **Odorant-Binding Proteins in Vertebrates and Insects-Similarities and possible common Functions**. *Chemical Senses*, **15**:205–215, 1990.

[189] S. Foret and R. Maleszka. **Function and evolution of a gene family encoding odorant binding-like proteins in a social insect, the honey bee (*Apis mellifera*)**. *Genome Research*, **16**:1404–1413, 2006.

[190] I. Iovinella, F. R. Dani, A. Niccolini, S. Sagona, E. Michelucci, A. Gazzano, S. Turillazzi, A. Felicioli, and P. Pelosi. **Differential expression of odorant-binding proteins in the mandibular glands of the honey bee according to caste and age**. *Journal of Proteome Research*, **10**:3439–3449, 2011.

[191] S. Spinelli, A. Lagarde, I. Iovinella, P. Legrand, M. Tegoni, P. Pelosi, and C. Cambillau. **Crystal structure of *Apis mellifera* OBP14, a C-minus odorant-binding protein, and its complexes with odorant molecules**. *Insect Biochemistry and Molecular Biology*, **42**:41–50, 2012.

[192] A. Schwaighofer, C. Kotlowski, C. Amaran, N. Chu, R. Mastrogiacomo, C. Becker, P. Pelosi, W. Knoll, M. Larisika, and C. Nowak. **Honey bee Odorant Binding Protein 14: Effects on Thermal Stability upon Odorant Binding revealed by FT-IR Spectroscopy and CD Measurements**. *European Biophysical Journal*, **under review**, 2013.

List of Figures

List of Tables

Glossary

ATP	adenosine triphosphate
ATR	attenuated total reflection
BLM	black lipid membrane
BNC	binuclear center
C*c*O	cytochrome *c* oxidase
cAMP	cyclic 3,5-adenosine monophosphate
cGMP	cyclic 3',5'-guanosine monophosphate
CNG	cyclic nucleotide-gated
CV	cyclic voltammetry
cyt *c*	cytochrome *c*
EIS	electrochemical impedance spectroscopy
EPR	electron paramagnetic resonance
ET	electron transfer
FIR	far infrared
FPR	formyl peptide receptors
FTIR	Fourier transform infrared
G-protein	guanine nucleotide-binding protein
GPCR	G protein-coupled receptor
IMM	inner mitochondrial membrane
IMS	intermembrane space
IR	infrared

IRRAS infrared reflection absorption spectroscopy

MIR mid infrared

NADH nicotinamide adenine dinucleotide

NIR near infrared

NMR nuclear magnetic resonance

NTA nitrilotriacetic

OBP odorant binding protein

OR odorant receptor

Orco odorant receptor coreceptor

PLS proton-loading site

ptBLM protein-tethered bilayer lipid membrane

QCM quartz crystal microbalance

SEIRAS surface-enhanced infrared absorption spectroscopy

SERS surface-enhanced Raman spectroscopy

SLB supported lipid bilayer

SNR signal-to-noise ratio

SPR surface plasmon resonance

SU subunit

TAAR trace amine-associated receptor

tBLM tethered bilayer lipid membrane

TE transverse electric

TM transverse magnetic

tr-FTIR time-resolved Fourier transform infrared

UQ ubiquinone

UQH_2 ubiquinol